

DISSERTATION

**Nonequilibrium QCD in heavy-ion collisions:
Kinetic theory and jet modifications
during the initial stages**

Ausgeführt zum Zwecke der Erlangung des akademischen Grades eines
Doktors der Naturwissenschaften

unter der Leitung von

Priv.-Doz. Dr. Kirill Boguslavski
E136
Institut für Theoretische Physik

eingereicht an der Technischen Universität Wien
Fakultät für Physik

von

Dipl.-Ing. Florian Lindenbauer, BSc

Matrikelnummer: 01608107

Wien,
am 13.06.2025

Florian Lindenbauer
(Verfasser)

Priv.-Doz. Dr. Kirill Boguslavski
(Betreuer)

Prof. Dr. Charles Gale
(Gutachter)

Prof. Dr. Sören Schlichting
(Gutachter)

ABSTRACT

Heavy-ion collision experiments create a high-temperature plasma that is characterized by a deconfined state of quarks and gluons. It is described by the theory of the strong interaction: Quantum Chromodynamics (QCD). At high energies, QCD admits an effective kinetic description, which allows studying and simulating how the initially far-from-equilibrium plasma reaches thermal equilibrium, where the plasma can be described as a relativistic fluid. While many studies have focused on this fluid phase, the nonequilibrium stages before a fluid picture becomes applicable have recently received increased attention. In particular, they may be experimentally studied using highly energetic particles called jets.

This thesis focuses on how jets are modified by the nonequilibrium quark-gluon plasma. Its influence on their propagation is typically encoded in a single medium function which is referred to as the dipole cross section. Its small distance behavior is characterized by the jet quenching parameter \hat{q} , and we obtain its numerical value throughout the pre-equilibrium stage, finding values comparable in magnitude to the earlier Glasma stage, with also a similar anisotropy. We also compute the more general elastic collision kernel, obtained by Fourier transforming the dipole cross section. We observe that its small distance behavior is suppressed during the pre-fluid stages, implying a suppression of jet quenching during the initial stages. This constitutes an important step to facilitate the understanding of jet-medium interactions during the initial stages in heavy-ion collisions.

Additionally, this thesis improves our understanding of QCD equilibration in heavy-ion collisions. QCD kinetic theory simulations are improved by employing a more realistic (hard thermal loop) screening mechanism to incorporate medium effects, which we compare with simpler screening mechanisms. While the effect on isotropic systems is negligible, an expanding plasma realized in the initial stages of heavy-ion collisions exhibits a significantly reduced maximum anisotropy when using the improved screening prescription. We also quantify its effect on the specific shear viscosity η/s , finding that its numerical value decreases when using the improved screening prescription. Moreover, we investigate the gluon splitting rates used as input for kinetic theory simulations, which are typically obtained using an isotropic model for the collision kernel. Going beyond that approximation, we find that the splitting rates obtained from the nonequilibrium anisotropic kernel significantly differ from those used in QCD kinetic theory simulations, both in magnitude and qualitative time evolution. We further identify a novel type of attractor in this thesis, which can be observed in the ratio of the jet quenching parameter, and is obtained by extrapolating to vanishing coupling. This weak coupling limiting attractor is also identified in the pressure ratio. This improved kinetic theory description and novel limiting attractors contribute towards a more realistic modeling of the nonequilibrium QCD plasma and its equilibration and hydrodynamization process during the initial stages.

ZUSAMMENFASSUNG

In relativistischen Schwerionenkollisionen wird ein Hochtemperaturplasma erzeugt, das durch einen Zustand freier Quarks und Gluonen charakterisiert ist. Es wird durch die Theorie der starken Wechselwirkung beschrieben, die Quantenchromodynamik (QCD). Bei hohen Energien erlaubt diese eine effektive kinetische Beschreibung, die es ermöglicht, die Thermalisierung des anfänglich weit vom Gleichgewicht entfernten Plasmas aus Quarks und Gluonen zu simulieren. In der Nähe des Gleichgewichts kann das Plasma als eine relativistische Flüssigkeit beschrieben werden. Diese hydrodynamische Beschreibung dient als Grundlage vieler Studien zu Schwerionenkollisionen. Jedoch hat in letzter Zeit die vorhergehende Phase außerhalb des Gleichgewichts erhöhte Aufmerksamkeit erhalten, insbesondere, da sie möglicherweise experimentell mittels hochenergetischer Teilchen, genannt Jets, untersucht werden kann.

Diese Arbeit beschäftigt sich mit der Frage, wie Jets durch das Plasma fern des Gleichgewichts modifiziert werden. Diese Modifikation wird typischerweise durch eine einzige Funktion des Mediums beschrieben, die Dipol-Wirkungsquerschnitt genannt wird. Dessen Verhalten für kleine Entferungen wird durch den *Jet Quenching Parameter* \hat{q} beschrieben und wir berechnen dessen Werte in den frühen Nicht-Gleichgewichtsphasen von Schwerionenkollisionen. Insbesondere finden wir, dass dessen Werte in unseren Simulationen mit jenen Werten dieses Parameters vergleichbar sind, die in der noch früheren Glasma Phase berechnet wurden, sowohl in Größe als auch Richtungsabhängigkeit. Weiters extrahieren wir den allgemeineren Kollisionskernel durch Fourier-Transformation des Dipol-Wirkungsquerschnitts. Wir finden, dass dessen Werte bei kleinen Abständen kleiner sind als im thermischen Gleichgewicht, was zu einer Unterdrückung von Jet Quenching während der frühen Zeiten führt. Das Extrahieren dieser Größen stellt einen bedeutenden Schritt dar, um die Beschreibung von Jet-Medium Wechselwirkungen in den frühen Phasen von Schwerionenkollisionen besser zu verstehen.

Darüber hinaus verbessert diese Arbeit die zugrundeliegende kinetische Beschreibung durch die Verwendung eines realistischeren Abschirmmechanismus (mittels harter thermischer Schleifen), um die Effekte des Mediums zu berücksichtigen. Diesen vergleichen wir mit einfacheren Abschirmmechanismen. Für isotrope Systeme sind seine Effekte vernachlässigbar, wohingegen ein expandierendes Plasma, das in den frühen Zeiten von Schwerionenkollisionen existiert, eine deutlich geringere Anisotropie aufweist, wenn man den verbesserten Abschirmmechanismus verwendet. Wir quantifizieren diesen Effekt auch durch die Ermittlung der numerischen Werte der spezifischen Viskosität η/s , deren Wert durch die verbesserte Abschirmvorschrift verringert wird. Schließlich untersuchen wir die Spaltungsrate von Gluonen, die in kinetischen QCD Simulationen auf Basis einer isotropen Näherung verwendet werden. Wir stellen fest, dass sich die Spaltungsrate unter Verwendung des anisotropen Nicht-Gleichgewichts-Kernels deutlich von den genäherten Raten unterscheiden, und zwar sowohl in der Größe als auch im qualit-

tativen Zeitverhalten. Weiters identifizieren wir einen neuartigen Attraktor, der für das Verhältnis des Jet Quenching Parameters zwischen verschiedenen Richtungen relevant ist, und über die Extrapolation zu verschwindenden Kopplungen erhalten wird. Die Weiterentwicklung der kinetischen Theorie und diese neuartigen Attraktoren führen zu einem besseren Verständnis der Thermalisierung des Quark-Gluon Plasmas in Schwerionenkollisionen.

LIST OF PUBLICATIONS

This thesis is based on the following published papers [1–4] and conference proceedings [5], for which I am the corresponding author, and on a paper in preparation [6]:

- [1] Boguslavski, K., Kurkela, A., Lappi, T., Lindenbauer, F., & Peuron, J. (2024). Jet momentum broadening during initial stages in heavy-ion collisions. *Physics Letters B*, 850, 138525. <https://doi.org/10.1016/j.physletb.2024.138525>
- [2] Boguslavski, K., Kurkela, A., Lappi, T., Lindenbauer, F., & Peuron, J. (2024). Jet quenching parameter in QCD kinetic theory. *Physical Review D*, 110(3). <https://doi.org/10.1103/physrevd.110.034019>
- [3] Boguslavski, K., Kurkela, A., Lappi, T., Lindenbauer, F., & Peuron, J. (2024). Limiting attractors in heavy-ion collisions. *Physics Letters B*, 852, 138623. <https://doi.org/10.1016/j.physletb.2024.138623>
- [4] Boguslavski, K., & Lindenbauer, F. (2024). Soft-gluon exchange matters: Isotropic screening in QCD kinetic theory. *Physical Review D*, 110(7). <https://doi.org/10.1103/physrevd.110.074017>
- [5] Boguslavski, K., Kurkela, A., Lappi, T., Lindenbauer, F., & Peuron, J. (2024). Limiting attractors in heavy-ion collisions—The interplay between bottom-up and hydrodynamic attractors. *EPJ Web of Conferences*, 296, 10004. <https://doi.org/10.1051/epjconf/202429610004>
- Chapter 8 is based on a paper in preparation in collaboration with Alois Altenburger and Kirill Boguslavski [6].

Other publications not used in this thesis:

- [7] Boguslavski, K., Kurkela, A., Lappi, T., Lindenbauer, F., & Peuron, J. (2024). Heavy quark diffusion coefficient in heavy-ion collisions via kinetic theory. *Physical Review D*, 109(1). <https://doi.org/10.1103/physrevd.109.014025>
- [8] Peuron, J., Boguslavski, K., Kurkela, A., Lappi, T., & Lindenbauer, F. (2024). Heavy quark diffusion coefficient during hydrodynamization - non-equilibrium vs. equilibrium. In *Proceedings of 11th International Conference on Hard and Electromagnetic Probes of High-Energy Nuclear Collisions — PoS(HardProbes2023)* (p. 091). 11th International Conference on Hard and Electromagnetic Probes of High-Energy Nuclear Collisions. Sissa Medialab. <https://doi.org/10.22323/1.438.0091>
- [9] Boguslavski, K., Kurkela, A., Lappi, T., Lindenbauer, F., & Peuron, J. (2024). Heavy quark momentum diffusion coefficient during hydrodynamization via effective kinetic theory. *EPJ Web of Conferences*, 296, 09001. <https://doi.org/10.1051/epjconf/202429609001>

ACKNOWLEDGEMENTS

During the course of my PhD, I have met many people who I owe gratitude. First and foremost, I am grateful to my excellent supervisor Kirill Boguslavski, for introducing me to the exciting topic of heavy-ion collisions, and for his help and guidance, both on academic and bureaucratic topics; for saving me from digging too deep into maybe not so relevant aspects, and for motivating me to pursue what seemed interesting to me. Thank you for your support and for believing in me!

Furthermore, I am indebted to all the people I was lucky to collaborate with, who offered wisdom, guidance, and insights, without which this thesis would have never come about. Thank you to Aleksi Kurkela, Tuomas Lappi, and Jarkko Peuron for the collaboration on the projects this thesis is explicitly based on, and additionally to Alois Altenburger, João Barata, Sergio Barrera Cabodevila, Michal Heller, Lucas Hörl, Aleksas Mazeliauskas, Andrey Sadofyev, Michał Spaliński, Adam Takacs and Fabian Zhou for the collaboration on ongoing projects that unfortunately could not be included in this thesis and which have yet to see the light of the arXiv. Thank you not only for sharing ideas about research but also for providing advice and guidance on my journey through academia.

I had the wonderful privilege of being invited to research stays in Santiago de Compostela, Heidelberg, and Stavanger, and I would like to thank Andrey Sadofyev, Aleksas Mazeliauskas, and Aleksi Kurkela for being excellent hosts during my stays there.

I would like to thank fellow PhD students and postdocs that I met at various conferences and with whom I enjoyed enlightening or humorous discussions, dinners, lunches, snacks, or drinks, who made my PhD much more fun! Thank you to André, Bruno, Carlos, Clemens, Dana, Győző, Ismail, Jannis, János, Jean, Jendrik, Matisse, Orestis, Rachel, Sylwia, Viktoria, Victor, Xiaojian, and Xoán, and to the many more I surely failed to mention.

I want to thank my fellow PhD students at the institute, especially Paul, Markus, and Kayran, for the many shared lunches and discussions, for sharing rooms during various trips, and additionally, for their feedback on early drafts of parts of this thesis.

Finally, and perhaps most significantly, I would like to express my deepest gratitude to my girlfriend Liane for her unwavering support, for being present when it was most needed, and for helpful comments on early and not-so-early drafts of this thesis. Lastly, I would like to thank my parents for their constant and unconditional support during my studies.

I am a recipient of a DOC Fellowship of the Austrian Academy of Sciences at TU Wien (project 27203). I would also like to acknowledge support by the Austrian Science Fund (FWF) under Grant DOI 10.55776/P34455 and Grant DOI 10.55776/W1252.

CONTENTS

Abstract	3
Zusammenfassung	5
List of publications	7
Acknowledgements	9
1 INTRODUCTION	15
1.1 The fundamental forces and the Standard Model	15
1.2 Quantum Chromodynamics and the quark-gluon plasma	15
1.3 Heavy-ion collisions and thermalization	16
1.4 Jet quenching	18
1.5 Guiding questions	21
1.6 Outline	21
1.7 Conventions	22
2 JET ENERGY LOSS	23
2.1 How does an energetic gluon lose energy in a medium	23
2.2 AMY rate equations	25
2.3 Medium-induced radiation spectrum in a finite medium	26
2.3.1 Energy spectrum	26
2.3.2 Medium-induced radiation spectrum differential in transverse momentum	27
3 QCD KINETIC THEORY	29
3.1 Validity of QCD kinetic theory	29
3.2 The equations of QCD kinetic theory	30
3.3 Medium effects: Screening of soft modes	34
3.3.1 Where screening is needed	34
3.3.2 Debye-like screening	36
3.4 How kinetic theory emerges from quantum field theory	37
3.4.1 Kadanoff-Baym equations	37
3.4.2 Wigner transform	38
3.4.3 Quasiparticle approximation	39
3.4.4 Decay rate	40
3.4.5 Relation to the Boltzmann equation	44
3.5 What we know about QCD equilibration	44
3.5.1 Thermalization of isotropic systems	44
3.5.2 Thermalization of expanding systems	46
3.6 Performing QCD kinetic theory simulations	47
3.6.1 Symmetries of the distribution function	47
3.6.2 Boltzmann equation and initial condition	48
3.6.3 Observables and Landau matching	50
3.6.4 Time markers and time scales	50
3.6.5 Extrapolating EKT to large couplings	52
3.6.6 Numerical details and discretization artifacts	52
4 MOMENTUM BROADENING OF JETS	55

4.1	Obtaining the jet quenching parameter in QCD kinetic theory	55
4.1.1	Relation of jet quenching parameter and scattering rate	55
4.1.2	Coordinate systems	58
4.1.3	Formula for the jet quenching parameter for finite jet energy	60
4.1.4	Symmetries of \hat{q}^{ij}	62
4.1.5	Medium screening effects	62
4.1.6	Towards the limit $p \rightarrow \infty$: NLO terms in $1/p$	65
4.1.7	Limit $p \rightarrow \infty$ with a momentum cutoff	66
4.1.8	Limiting behavior for large cutoff	68
4.1.9	Interpreting the momentum cutoff	68
4.2	Analytical results for the jet quenching parameter in special cases	70
4.2.1	Thermal distribution	70
4.2.2	Toy models for bottom-up thermalization	78
4.3	Obtaining \hat{q} between Glasma and hydrodynamics	84
4.3.1	Results for a fixed momentum cutoff Λ_\perp	86
4.3.2	Results for realistic cutoff dependence	88
4.4	Concluding remarks	92
5	LIMITING ATTRACTORS IN HEAVY-ION COLLISIONS	95
5.1	Time scales and initial conditions	95
5.2	Limiting attractors in the pressure ratio	96
5.3	Limiting attractors for transport coefficients of hard probes	98
5.3.1	Jet quenching parameter and heavy-quark diffusion coefficient	98
5.3.2	Numerical results	100
5.4	Note on the time scales	102
5.5	Concluding remarks	104
6	IMPROVING QCD KINETIC THEORY SIMULATIONS	105
6.1	Recapitulate: Debye-like screening in QCD kinetic theory	105
6.2	Hard thermal loop propagator	106
6.2.1	Isotropic HTL gluon propagator in a linear gauge	106
6.2.2	IsoHTL screening	107
6.2.3	Debye-like screening as an approximation to isoHTL	108
6.2.4	Different Debye-like screening prescriptions	109
6.3	Thermalization of isotropic systems	110
6.4	Results with longitudinal expansion	112
6.4.1	Initial conditions, time markers and time scales	112
6.4.2	Comparison of Debye-like screening prescriptions	114
6.4.3	Comparison with isoHTL: Pressure ratio	114
6.4.4	Numerical extraction of the specific shear viscosity η/s	116
6.4.5	Simulations at the same specific shear viscosity η/s	120
6.4.6	Thermalization and hydrodynamization time	121
6.4.7	Impact of screening prescriptions on early-time dynamics	122
6.4.8	Evolution of the jet quenching parameter	124
6.5	Concluding remarks	125
7	COLLISION KERNEL AND AMY RATES OUT OF EQUILIBRIUM	127

7.1	Going beyond the jet quenching parameter: Elastic collision kernel	127
7.1.1	Generalizing the jet quenching parameter to obtain the collision kernel	127
7.1.2	Symmetries of the collision kernel	129
7.1.3	Analytic limits: Small and large momentum transfers	130
7.1.4	Numerical results	132
7.2	Dipole cross section	137
7.2.1	Small distance limit	138
7.2.2	Numerical results	141
7.3	Gluon radiation in an anisotropic medium	144
7.3.1	AMY rate equation	145
7.3.2	Solving the AMY rate equation numerically	146
7.3.3	Numerical results	147
7.4	Concluding remarks	151
8	SUMMARY, CONCLUSIONS AND OUTLOOK	153
A	QCD AND NONEQUILIBRIUM QUANTUM FIELD THEORY	157
A.1	QCD Lagrangian and notation	157
A.2	Correlation functions and closed time path	158
A.3	Perturbation theory and self-energy	161
A.4	Correlator relations and properties	162
A.5	Hard thermal loops	163
A.5.1	Hard thermal loop resummed gluon propagator	163
A.5.2	IsoHTL screening in the jet quenching parameter	164
A.5.3	IsoHTL screening in the elastic collision kernel	165
A.5.4	Sum rule	165
A.5.5	An analytic results for the dipole cross section	168
A.6	Scattering with soft gluon exchange	169
A.6.1	Quark scattering	170
A.6.2	Gluon scattering	171
B	NUMERICAL AND KINEMATIC DETAILS ON KINETIC THEORY SIMULATIONS	173
B.1	Discretization	173
B.2	Symmetrization of the collision terms	174
B.3	Coordinate system and Mandelstam variables	175
B.4	Inelastic collision term	176
B.5	Monte Carlo evaluation of the collision terms	176
B.6	Adaptive step size	177
B.7	Kinematic considerations	179
B.8	Dominance of small angle scatterings	180
B.9	Statistical averages	182
C	LARGE MOMENTUM LIMITS OF THE JET QUENCHING PARAMETER	183
C.1	The integrand of \hat{q} for large p	183
C.1.1	The large p limit of $\cos\theta_{qp}$	184
C.1.2	Matrix element for large $ \omega $	184
C.1.3	Integral over a more generic integrand	184
C.2	Behavior of \hat{q} for large p	186

C.2.1	Large p behavior combined with a transverse momentum cutoff	187
C.2.2	Large momentum cutoff Λ_\perp behavior	188
D	NUMERICAL DETAILS ON SOLVING THE AMY RATE EQUATIONS	191
D.1	Equations and boundary conditions	191
D.2	Numerical cross-checks	197
E	ADDITIONAL NUMERICAL RESULTS FOR BOTTOM-UP THERMALIZATION	199
F	NOTES ON NOTATIONAL CONVENTIONS HERE AND IN THE PAPERS	207
G	TOOLS USED	209

INTRODUCTION

1.1 THE FUNDAMENTAL FORCES AND THE STANDARD MODEL

Physics aims to describe, explain, and predict phenomena encountered in nature using mathematical models. The ultimate goal is to understand and answer fundamental questions about our universe, e.g., *what are the fundamental forces of nature?* or *What forces bind together the matter we are made of?* or *Can we probe nonequilibrium effects of the strong interaction using particle colliders?*

Perhaps needless to say, tremendous effort has gone into answering these questions over the past centuries. With the exception of gravity, all fundamental interactions are now conveniently combined in the *Standard Model of particle physics*. It is arguably the most well-tested physical theory today and the cornerstone of modern particle and collider physics, allowing predictions with astonishing precision and accuracy. Despite its compact mathematical formulation, which fits on a simple coffee mug (available for purchase at the European Organization for Nuclear Research (CERN)), it describes surprisingly complex dynamics and phenomena.

For instance, the Standard Model includes the *electromagnetic force*, perhaps the most important fundamental force in our everyday lives. It is essential for describing the stability of atoms¹, molecules and solids, while also describing light, electricity, and electromagnetic waves. In the Standard Model, it is neatly combined with the *weak interaction*, which describes how the building blocks of atoms, the protons and neutrons, decay.

The structure of the atomic nucleus itself is governed by the *strong interaction*, the force that binds protons and neutrons together. This interaction describes how protons and neutrons are not fundamental particles, but rather composed of even tinier constituents, the quarks and gluons. This thesis focuses on the mathematical theory of the strong interaction, *quantum chromodynamics* (QCD).

1.2 QUANTUM CHROMODYNAMICS AND THE QUARK-GLUON PLASMA

QCD was formulated over 50 years ago [10], and lives within the mathematical framework of quantum field theory, which combines special relativity with quantum mechanics. The fundamental ingredients of QCD are quarks and gluons. They have the important property that their interaction strength decreases for increasing

¹ Atoms are important for everyday life despite being banned in Austria per its constitution ("Bundesverfassungsgesetz für ein atomfreies Österreich", <https://www.ris.bka.gv.at/GeltendeFassung.wxe?Abfrage=Bundesnormen&Gesetzesnummer=10008058>)

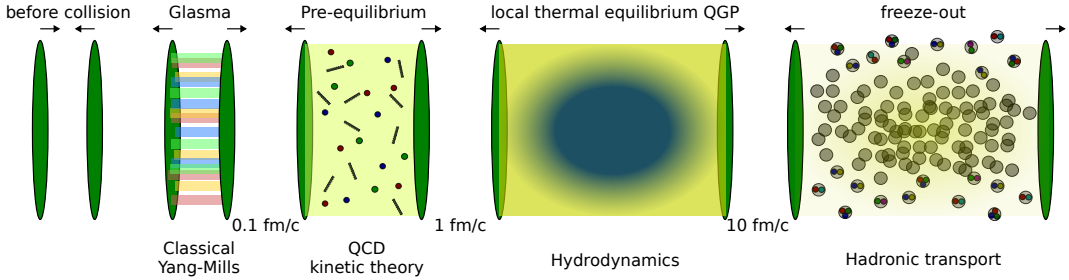


Figure 1.1: Schematic overview of the initial stages in heavy-ion collisions and their respective effective description.

energies, a property called *asymptotic freedom*. Thus, at weak coupling—or large energies—one may use perturbation theory to obtain properties of QCD. At lower energies, quarks and gluons are confined in ordinary hadrons, such as protons and neutrons making up most of the visible matter in the universe. For a QCD plasma in thermal equilibrium, numerical tools such as *Lattice QCD* are available and reveal a crossover phase transition between ordinary nuclear matter and a phase of deconfined quarks and gluons at very high temperatures: the quark-gluon plasma (QGP). This many-body system of quarks and gluons is also predicted to exist shortly after the Big Bang and can be produced experimentally in relativistic heavy-ion collision experiments. How a nonequilibrium QCD plasma equilibrates has been the context of intensive study and remains an important research question [11, 12]. Moreover, the theoretical and experimental study of this system in and out of equilibrium and its thermalization processes reveals intriguing phenomena and possesses also exciting interdisciplinary connections to other fields of physics, such as condensed matter, cosmology, and ultracold quantum gases [13].

1.3 HEAVY-ION COLLISIONS AND THERMALIZATION

As alluded to earlier, the equilibrium and nonequilibrium properties of the quark-gluon plasma can be studied experimentally in relativistic heavy-ion collisions, which are currently performed at the Relativistic Heavy Ion Collider (RHIC, soon to be phased out to make room for the new Electron-Ion Collider (EIC) at Brookhaven National Laboratory, and at the Large Hadron Collider (LHC) at CERN. There, heavy nuclei such as gold and lead are accelerated nearly to the speed of light and brought to collision. Their decay products are then studied in the detectors, similarly to the study of proton-proton collisions. These heavy-ion collisions create a droplet of QCD matter that is initially far from equilibrium. Analyzing the remnants of these collisions reveals that a deconfined state of matter is created, where quarks and gluons are no longer bound into hadrons, the quark-gluon plasma.

Currently, it is impossible to describe the time evolution of this out-of-equilibrium system using (numerical) first-principle simulations of QCD. Real-time Lattice QCD simulations, for example, suffer from the infamous sign problem [14–16], which prevents real-time simulations or simulations at finite density. Instead, the out-of-equilibrium QCD plasma is often described using a series of effective theories,

which are depicted schematically in Fig. 1.1. At sufficiently high energies and weak couplings, directly after the collision, the system is dominated by large classical gluon fields and can be described within the Color Glass Condensate [17]. The corresponding state (following a specific set of initial conditions) is referred to as the *Glasma*, and its time evolution can be obtained using classical statistical lattice simulations [18]. After a time of about $0.1 \text{ fm}/c \approx 3 \times 10^{-25} \text{ s}$, a quasiparticle description becomes applicable with gluons initially remaining the dominant degrees of freedom and the—still far from equilibrium—plasma can be described as a weakly-interacting gas of quarks and gluons using an effective kinetic theory [19, 20], where the time evolution of the system is dictated by a Boltzmann equation

$$\left(\frac{\partial}{\partial t} + \mathbf{v} \cdot \nabla \right) f(\mathbf{p}, \mathbf{x}, t) = -\mathcal{C}[f] \quad (1.1)$$

for the particle distribution function $f(\mathbf{p}, \mathbf{x}, t)$. Numerical implementations of this QCD kinetic theory allow tracking the system's time evolution towards equilibrium and to the later hydrodynamic stage [21–26], and are also commonly extrapolated to larger coupling values for phenomenological purposes [27–33].

Common QCD kinetic theory implementations [21–26] use a simple screening approximation to include medium effects in the simulations, approximating internal medium resummed propagators by a simple Debye-like screened propagator. Notably, this isotropic screening approximation neglects the effect of plasma instabilities that are present in anisotropic systems [34–39], but might be damped by collisions [40, 41]. However, they have been shown not to have very dramatic effects on the earliest stages [42, 43].

The nonequilibrium plasma hydrodynamizes when a hydrodynamic description becomes applicable. This description using relativistic hydrodynamics [44–47] has been successfully used to understand many experimentally observed collective phenomena. For example, when off-central collisions lead to an initial almond-shaped overlap region of the colliding nuclei, hydrodynamics predicts an elliptical-shaped particle distribution observed in the detectors, known and observed as *elliptic flow* [48]. Hydrodynamics is a macroscopic description where microscopic properties only enter via effective transport parameters. As such, hydrodynamics is applicable for both weakly and strongly coupled systems. However, it is typically formulated as a (gradient) expansion around local thermal equilibrium, limiting its applicability to systems close to equilibrium, while kinetic theory provides a genuine description of the microscopic dynamics of the system valid also out of equilibrium.

When the temperature of the fluid drops below a critical “freeze-out” temperature, the hydrodynamic evolution is stopped and the energy density is converted back into hadrons which are then measured in the detectors (after a subsequent stage of hadronic interactions) [48].

It should be noted that while hydrodynamics as an effective macroscopic theory is applicable for all values of the coupling constant, kinetic theory and the Glasma stage rely on a weak coupling picture. There is a parallel effort to investigate the features of strongly coupled effective models of QCD, which can be achieved using the holographic principle and the gauge/gravity duality [49–51]. There, one uses

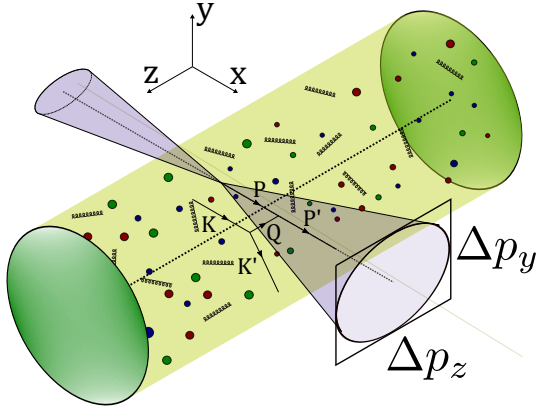


Figure 1.2: Schematic sketch of jet modification when traversing the quark-gluon plasma generated in a heavy-ion collision. Figure reused from [2].

the duality of a strongly coupled gauge theory to a weakly coupled gravitational theory, e.g., the AdS/CFT correspondence allows to probe $\mathcal{N} = 4$ supersymmetric Yang-Mills (SYM), which is used as a model for QCD at large temperatures. Heavy-ion collisions are studied in the dual gravitational theory by performing extensive numerical simulations of shock wave collisions [52–55].

Despite their different setups, comparing kinetic theory and holographic models of the pre-equilibrium stages reveals astonishing similarities [56, 57], such as the approach to a hydrodynamic attractor [58]. This attractor refers to the property that, for various initial conditions, the system's time evolution follows a universal curve characterized by a reduced number of parameters [59, 60]. These attractors have been observed in various formulations of hydrodynamics [57, 61], kinetic theory at weak couplings [22, 24, 26, 29, 62–66], and holographic models at strong couplings [56, 57, 67, 68]. In particular, this identified universal behavior in certain observables allows making predictions from the pre-hydrodynamic stages despite incomplete information about the initial conditions [29, 31, 32]. The notion of attractors in heavy-ion collisions and other theoretical setups has been the extensive subject of recent studies [64–66, 69–75].

Recently, there has been an increased interest to also consider the pre-hydrodynamic evolution and search for possible experimental observables of this stage [27, 30, 76–78]. This is thought to be even more important for light ion collisions and smaller collision systems which spend a larger fraction of their time before hydrodynamics is applicable. In particular, the upcoming lighter ions collision experiments, such as the planned oxygen-oxygen run at the LHC, will provide an environment in which nonequilibrium effects become more important [79, 80], making it now an ideal time to study nonequilibrium and pre-hydrodynamic effects in heavy-ion collisions.

1.4 JET QUENCHING

Experimentally accessible probes with potential contributions from the pre-hydrodynamic nonequilibrium stages are jets. They are observed as a collection of

collimated particles with large momenta and are experimentally reconstructed using jet clustering algorithms [81, 82].

Generally, they originate from a highly energetic parton (quark or gluon) created in the initial collision, and, thus, interact with the QCD plasma during all stages of its evolution. Hence, they may carry imprints of the nonequilibrium initial stages. Experimental evidence suggests that jets lose energy while traversing the plasma, which is referred to as *jet quenching* and is considered to be strong evidence for the formation of the quark-gluon plasma.

Experimentally, jet observables are typically compared to a corresponding observable measured in proton-proton collisions. For example, the nuclear modification factor is obtained by normalizing the yields or cross sections measured in nuclear collisions to their values in proton-proton collisions scaled by the number of binary collisions. If it is equal to one, there are no nuclear effects, i.e., the observable can be obtained as a superposition of proton-proton collisions, and is not modified by the medium generated in heavy-ion collisions.

Jet energy loss and jet quenching are dominated by the process of inelastic gluon emissions. Without going into much more detail (see Chapter 3), the probability for medium-induced gluon radiation and the gluon spectrum depend on an effective propagator in a potential given by the *dipole cross section* [83–88]

$$C(x) = \int \frac{d^2 q_\perp}{(2\pi)^2} C(q_\perp) (1 - e^{ix \cdot q_\perp}). \quad (1.2)$$

It depends on the elastic collision kernel $C(q_\perp)$ describing the probability per time of a jet particle to receive a momentum kick with transverse momentum q_\perp . Different jet quenching formalisms [83–98] (see Ref. [99] for a comparison) differ in how they approximate the propagator or dipole cross section. In the *harmonic oscillator approximation*, the small distance (small- $|x|$) behavior of the dipole cross section is encoded in the jet quenching parameter \hat{q} ,

$$C(x) = \frac{1}{4} \hat{q} x^2 + \mathcal{O}(x^4). \quad (1.3)$$

This parameter has the physical interpretation of quantifying the transverse momentum broadening per unit time,

$$\hat{q} = \frac{d\langle p_\perp^2 \rangle}{dt} = \int \frac{d^2 q_\perp}{(2\pi)^2} q_\perp^2 C(q_\perp). \quad (1.4)$$

Importantly, all the medium information is contained in the dipole cross section $C(x)$ or, in the small- $|x|$ limit, in the jet quenching parameter \hat{q} . They have been calculated analytically for a weakly-coupled plasma using perturbative QCD in thermal equilibrium at leading [100, 101] and next-to-leading order [102] in the coupling. Further thermal results exist also for strongly coupled systems using AdS/CFT [103–107], Lattice QCD [108], dimensionally reduced electrostatic QCD [109, 110], and quasiparticle models [111–113]. There exist also extractions of the jet quenching parameter \hat{q} from experimental data [114–117]. In thermal equilibrium, the evolution of jets has been studied using kinetic theory [33, 118–120]. For the radiation spectrum, formalisms have been developed to go beyond the small x limit of the dipole cross section by expanding in logarithms [101, 121–124] or using

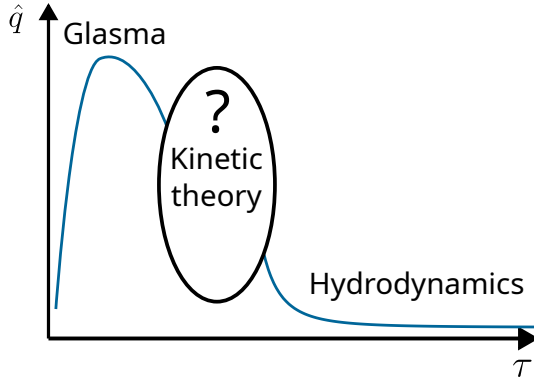


Figure 1.3: Schematic evolution of the jet quenching parameter \hat{q} : Its evolution has been obtained in the early Glasma stage and in the later hydrodynamic stage. Figure reused from [1].

the full kernel to obtain the gluon spectrum and splitting rate [97, 110, 125–129]. While these results have been obtained in equilibrium, there has been significant theoretical progress towards describing jet quenching also in inhomogeneous, anisotropic and flowing systems [130–139].

While many phenomenological models ignore or drastically simplify the time evolution of the plasma during these initial stages [76, 114, 115, 117, 128, 140–151], it has been argued that the pre-equilibrium evolution is important for the correct description of experimental observables [76, 148]. In particular, the jet quenching parameter \hat{q} has recently been extracted during the Glasma stage during the earliest times of the nonequilibrium evolution [152–157], and its value was found to be surprisingly large while other studies find \hat{q} should be negligible at early times to be compatible with experimental data [76]. However, different treatments of jet quenching during the initial stages reach partly different conclusions [76, 147, 148, 151]. This clearly highlights the need for a better theoretical understanding of jet quenching during the initial stages.

Although numerical simulations of the equilibration process in heavy-ion collisions using QCD kinetic theory have been performed [21–26], the value of the jet quenching parameter \hat{q} or the form of the collision kernel $C(\mathbf{q}_\perp)$ during the pre-equilibrium stages have not been established, as is sketched in Fig. 1.3. This will be the main focus of this thesis. We will discuss the extraction of the jet quenching parameter \hat{q} in Chapter 4.4, and argue that its anisotropy ratio follows a novel type of attractor, which is referred to as *limiting attractor*, in Chapter 6. Finally, we study the more general collision kernel $C(\mathbf{q}_\perp)$ in Chapter 8.

Another important topic of this thesis is the question of how to properly include medium effects, both for obtaining the jet quenching parameter \hat{q} and for QCD kinetic theory simulations. In the past, simple approximations have been used for the medium-resummed matrix elements in the collision kernels. The effect of these assumptions has never been fully studied and will be the topic of Chapter 6.4.8.

1.5 GUIDING QUESTIONS

This thesis aims to answer the following questions, which are grouped in two main topics:

1. Improving our understanding of jet-medium interactions, particularly during the initial stages
 - a) How can the jet quenching parameter \hat{q} be obtained in QCD kinetic theory for a general, possibly anisotropic, distribution function $f(\mathbf{p})$?
 - b) What is the time evolution of the jet quenching parameter $\hat{q}(\tau)$ during the hydrodynamization process in heavy-ion collisions and is its numerical value close to the large values reported during the Glasma stage?
 - c) Do the jet quenching parameter or its directional values exhibit universal dynamics? Does it follow a hydrodynamic attractor?
 - d) How different is the collision kernel $C(\mathbf{q}_\perp)$ from its thermal and small- x counterparts during the bottom-up evolution from its thermal counterpart? Can we identify specific features from the anisotropic plasma background?
2. Improving our understanding of QCD equilibration
 - a) What is the impact of typically employed simplified screening prescriptions in QCD kinetic theory simulations, both on the jet quenching parameter and the time evolution itself?
 - b) Do late-time attractors beyond the hydrodynamic attractors exist? For which observables are they relevant?
 - c) How do the splitting rates obtained from the nonequilibrium anisotropic collision kernel $C(\mathbf{q}_\perp)$ compare to those employed in QCD kinetic theory simulations using an isotropic approximation?

1.6 OUTLINE

This thesis is organized as follows. Chapter 3 starts with a discussion on how an energetic parton loses energy in a quark-gluon plasma, and how different energy loss formalisms depend on the collision kernel $C(\mathbf{q}_\perp)$. The following Chapter 3.6.6 contains an introduction to QCD kinetic theory, discusses all the relevant ingredients, and how one might, in principle, derive it from QCD itself. It also discusses how QCD thermalizes in isotropic and expanding systems and how the QCD kinetic theory simulations employed in this thesis are performed.

Chapter 4.4 addresses Questions 1a, 1b and the parts of Question 2a regarding \hat{q} . It first discusses how the jet quenching parameter \hat{q} can be obtained in QCD kinetic theory. Then \hat{q} is calculated using a scaled thermal distribution and an effectively two-dimensional distribution as toy models to model features of the bottom-up equilibration process. Chapter 4.4 concludes with obtaining the jet quenching parameter \hat{q} during the hydrodynamization process between the Glasma and hydrodynamic stage.

The following Chapter 6 addresses Questions 1c and 2b. There, it is shown that the ratio of the jet quenching parameters cannot be well described using the typical hydrodynamic attractor time scale. Instead, the new concept of *limiting attractors* is introduced.

Question 2a is addressed in Chapter 6.4.8, where the screening prescription is discussed in more detail, in particular its gauge invariance. Additionally, numerical studies using different screening prescriptions are performed, both in isotropic and expanding systems. In this chapter, also the effects of different screening prescriptions in the background evolution on the jet quenching parameter \hat{q} are studied.

Finally, Chapter 8 is concerned with Questions 1d and 2c. First, the collision kernel is obtained during the hydrodynamization process in heavy-ion collision. Then, its Fourier transformed quantity, the dipole cross section, is computed and used as input to calculate the splitting rates using a novel method employed here for the first time.

A summary and conclusion are provided in Chapter A.

In Appendix A.6.2, aspects of QCD and nonequilibrium quantum field theories are discussed. Appendix C discusses numerical details on performing QCD kinetic theory simulations. Appendix C.2.2 describes the limits of the jet quenching parameter \hat{q} for large jet energies or large transverse momentum cutoffs. In Appendix E, numerical details on solving the anisotropic AMY rate equations are given. Finally, Appendix F provides an overview of additional plots and results of QCD kinetic theory simulations of the hydrodynamization process. Appendix F discusses notational differences between this thesis and the publications this thesis is based on.

1.7 CONVENTIONS

During this thesis, we will adopt the usual convention of setting the fundamental constants $c = \hbar = 1$, which simplifies our expressions and allows measuring every dimensionful quantity in units of energy. Throughout this thesis, we will employ the mostly-plus metric convention for the Minkowski metric $\eta_{\mu\nu}$, i.e.,

$$\eta_{\mu\nu} = \begin{pmatrix} -1 & 0 & 0 & 0 \\ 0 & 1 & 0 & 0 \\ 0 & 0 & 1 & 0 \\ 0 & 0 & 0 & 1 \end{pmatrix}, \quad (1.5)$$

such that the scalar product of two vectors $P^\mu = (P^0, \mathbf{p})$ and $K^\mu = (K^0, \mathbf{k})$ is $P \cdot K = -P^0 K^0 + \mathbf{p} \cdot \mathbf{k}$. Four-vectors in Minkowski space are denoted by uppercase letters, e.g., P . Lowercase boldfaced letters, e.g., \mathbf{p} , denote three-dimensional (or sometimes also two-dimensional) Euclidean vectors, whose magnitude is given by lowercase non-bold symbols, i.e., $p = |\mathbf{p}|$. For instance, a light-like $P^2 = 0$ vector can be represented as $P^\mu = (p, \mathbf{p})$.

2

JET ENERGY LOSS

In heavy-ion collisions, highly energetic particles are created, move through the quark-gluon plasma and cascade into a series of lower energetic particles, which then hadronize and are measured as jets in the detectors. Measuring their modification in the presence of a medium may yield insights into the nonequilibrium properties of QCD. However, a first principle calculation of this process is difficult. From a perturbative point of view, the dominant process for energy loss is inelastic gluon emission, where an energetic quark or gluon emits another gluon, as depicted in Fig. 2.1. Therefore, jet energy loss is typically modeled as a sequence of single gluon emissions, neglecting the interference of two subsequent emissions for simplicity. In this chapter, we discuss how the rate of a jet particle emitting a single gluon can be calculated. Although a *jet* is experimentally only well-defined through jet clustering algorithms, we will often refer to the single energetic particle we are considering as a *jet*.

2.1 HOW DOES AN ENERGETIC GLUON LOSE ENERGY IN A MEDIUM

In a vacuum, a $1 \rightarrow 2$ splitting process is kinematically forbidden. In a medium, however, the quark in Fig. 2.1 can receive elastic momentum kicks (as depicted by the gluon exchange lines) and be brought slightly off-shell, which opens the phase space for a splitting process. Describing such a single-splitting process is surprisingly complicated. To illustrate the physical picture, we will start by making simple estimates for the relevant processes, which can be found, e.g., in the review [158].

In the simplest case, the rate for gluon emission is proportional to the rate of receiving a momentum kick Γ_{el} . This can be estimated using Eq. (1.4), $\hat{q} = \frac{d\langle p_\perp^2 \rangle}{dt}$. Integrating this, we obtain that during a time interval Δt , a jet acquires the transverse momentum $\Delta p_\perp^2 \sim m^2 \sim \hat{q}\Delta t$, where m is a typical momentum transfer usually taken to be of the order of the screening mass. The rate $\Gamma_{\text{el}} \sim 1/\Delta t$ is then

$$\Gamma_{\text{el}} \sim \frac{\hat{q}}{m^2}. \quad (2.1)$$

Assuming the emission process is triggered by these elastic collision, we obtain the *Bethe-Heitler* rate

$$\frac{d\Gamma^{\text{BH}}}{dz} \sim \alpha_s P_{g \rightarrow g}(z) \frac{\hat{q}}{m^2}, \quad (2.2)$$

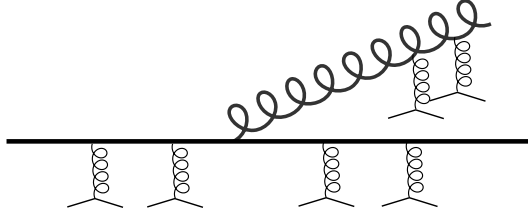


Figure 2.1: Inelastic gluon emission: A parton receives momentum kicks while traveling through the quark-gluon plasma and emits a gluon.

where the splitting function is given by

$$P_{g \rightarrow g}(z) = C_A \frac{1 + z^4 + (1 - z)^4}{z(1 - z)}, \quad z \ll 1 \quad P_{g \rightarrow g}^{\text{soft}}(z) \approx \frac{2C_A}{z}, \quad (2.3)$$

where z is the energy fraction of the emitted gluon, which we approximated for the case of soft gluon emissions $z \ll 1$. The constant $C_A = N_c$ is a group constant, see Appendix A.1 and Eq. (A.7). The Bethe-Heitler rate is only relevant if the formation time of the splitting process t^{form} is much smaller than the rate at which the elastic collisions occur that trigger the splitting process, i.e., $t^{\text{form}} \ll 1/\Gamma_{\text{el}}$. To begin with, one may easily estimate the formation time by considering the time it takes for the wave packet of the emitted gluon with size $\Delta x_\perp \sim 1/k_\perp$ not to overlap with the mother gluon [159]. Taking the transverse velocity to be $v_\perp = k_\perp/k$, we obtain $t^{\text{form}} \sim \Delta x_\perp/v_\perp = k/k_\perp^2$, where we can then use the definition of the jet quenching parameter \hat{q} from Eq. (1.4) to arrive at

$$t^{\text{form}} \sim \sqrt{\frac{\omega}{\hat{q}}}, \quad (2.4)$$

where $\omega = k$ is the energy of the emitted gluon (and, in general, the smallest energy of all participating partons). Thus, the Bethe-Heitler rate is valid for emitted energies

$$\omega \ll \frac{m^4}{\hat{q}}. \quad (2.5)$$

If this condition is not met, the individual emissions would overlap and one needs to take quantum mechanical interference effects into account. This is known as LPM suppression (first considered for QED in Refs. [160, 161], and obtained for QCD in [83, 85–87]). The rate can then be estimated similarly as in Eq. (2.2), but using the formation time (2.4),

$$\frac{d\Gamma^{\text{LPM}}}{dz} \sim \alpha_s P_{g \rightarrow g}^{\text{soft}}(z) \sqrt{\frac{\hat{q}}{\omega}}. \quad (2.6)$$

For its treatment in QCD, slightly different formalisms have been developed by different authors.¹

¹ Ref. [96] provides a convenient overview of how the different conventions and formalisms are related.

2.2 AMY RATE EQUATIONS

In the limit of an infinite and time-independent medium, the rates for (nearly collinear) gluon emission or quark-antiquark creation were obtained by Arnold, Moore, and Yaffe [19, 94], and are given by²

$$\gamma_{qg}^q(p; p', k) = \gamma_{\bar{q}g}^{\bar{q}}(p; p', k) = \frac{p'^2 + p^2}{p'^2 p^2 k^3} \mathcal{F}_q^{\hat{n}}(p, p', k), \quad (2.7)$$

$$\gamma_{q\bar{q}}^g(p; p', k) = \frac{k^2 + p'^2}{p'^3 p^3 k^3} \mathcal{F}_q^{\hat{n}}(k, -p', p), \quad (2.8)$$

$$\gamma_{gg}^g(p; p', k) = \frac{p'^4 + p^4 + k^4}{p'^3 p^3 k^3} \mathcal{F}_g^{\hat{n}}(p, p', k), \quad (2.9)$$

where

$$\mathcal{F}_s^{\hat{n}}(p, p', k) = \frac{d_s C_s \alpha_s}{2(2\pi)^3} \int \frac{d^2 \mathbf{h}}{(2\pi)^2} 2\mathbf{h} \cdot \text{Re} \mathbf{F}_s^{\hat{n}}(\mathbf{h}; p', p, k), \quad (2.10)$$

where C_s is the quadratic Casimir group constant corresponding to species s , given by Eq. (A.7). Furthermore, \mathbf{F} is the solution to the integral equation

$$\begin{aligned} 2\mathbf{h} = i\delta E(\mathbf{h}; p', p, k) \mathbf{F}_s^{\hat{n}}(\mathbf{h}; p', p, k) + \int \frac{d^4 Q}{(2\pi)^4} 2\pi \delta(v_{\hat{n}} \cdot Q) v_{\hat{n}}^\mu v_{\hat{n}}^\nu g^2 \langle\langle A_\mu(Q) [A_\nu(Q)]^* \rangle\rangle \\ \times \left\{ (C_s - \frac{C_A}{2}) [\mathbf{F}_s^{\hat{n}}(\mathbf{h}; p', p, k) - \mathbf{F}_s^{\hat{n}}(\mathbf{h} - k\mathbf{q}_\perp; p', p, k)] \right. \\ \left. + \frac{C_A}{2} [\mathbf{F}_s^{\hat{n}}(\mathbf{h}; p', p, k) - \mathbf{F}_s^{\hat{n}}(\mathbf{h} + p'\mathbf{q}_\perp; p', p, k)] \right. \\ \left. + \frac{C_A}{2} [\mathbf{F}_s^{\hat{n}}(\mathbf{h}; p', p, k) - \mathbf{F}_s^{\hat{n}}(\mathbf{h} - p\mathbf{q}_\perp; p', p, k)] \right\}. \end{aligned} \quad (2.11)$$

The vector \mathbf{h} is a two-dimensional vector in the plane transverse to the direction of the splitting particles, \hat{n} . The double brackets $\langle\langle A_\mu(Q) [A_\nu(Q)]^* \rangle\rangle$ denote the mean square fluctuations of the background gauge fields and is given by the (Fourier transformed) Wightman correlator (A.32a). The energy difference δE is given by

$$\delta E(\mathbf{h}; p', p, k) = \frac{m_{\text{eff},g}^2}{2k} + \frac{m_{\text{eff},s}^2}{2p} - \frac{m_{\text{eff},s}^2}{2p'} + \frac{\mathbf{h}^2}{2pkp'}, \quad (2.12)$$

and can be obtained by taking the particle momenta in Fig. 2.1 to be

$$(P')^\mu = (E_{\mathbf{p}'}, p', p_\perp + k_\perp, 0), \quad K^\mu = (E_{\mathbf{k}}, p, k_\perp, 0), \quad P^\mu = (E_{\mathbf{p}}, p, p_\perp, 0) \quad (2.13)$$

for a splitting $P' \rightarrow P + K$. Enforcing momentum conservation and expanding the energy for large $p' = p + k$, $E_{\mathbf{p}} = \sqrt{p^2 + p_\perp^2 + m_{\text{eff},s}^2} \approx p + \frac{m_{\text{eff},s}^2 + p_\perp^2}{2p}$, which leads to Eq. (2.12) when defining $\mathbf{h} = z\mathbf{k}_\perp - (1-z)\mathbf{p}_\perp$, where $z = p/p'$. The effective masses

² With a slightly different convention of $\frac{d\Gamma}{dz} = \frac{(2\pi)^3}{v_g |\mathbf{p}|} \gamma(p; zp, (1-z)p)$.

encode medium-dependent corrections to the dispersion relation of the particles and are given explicitly in Eqs. (3.11) and (3.12) in Section 3.6.6.

The four-dimensional integral can be split into one part along the splitting and temporal direction, and another part containing the transverse integral (along \mathbf{q}_\perp),

$$2\mathbf{h} = i\delta E(\mathbf{h}; p', p, k) \mathbf{F}_s^{\hat{n}}(\mathbf{h}; p', p, k) + \int \frac{d^2\mathbf{q}_\perp}{(2\pi)^2} \bar{C}(\mathbf{q}_\perp) \times \left\{ \begin{aligned} & \left(C_s - \frac{C_A}{2} \right) [\mathbf{F}^{\hat{n}}(\mathbf{h}; p', p, k) - \mathbf{F}_s^{\hat{n}}(\mathbf{h} - k\mathbf{q}_\perp; p', p, k)] \\ & + \frac{C_A}{2} [\mathbf{F}_s^{\hat{n}}(\mathbf{h}; p', p, k) - \mathbf{F}_s^{\hat{n}}(\mathbf{h} + p'\mathbf{q}_\perp; p', p, k)] \\ & + \frac{C_A}{2} [\mathbf{F}_s^{\hat{n}}(\mathbf{h}; p', p, k) - \mathbf{F}_s^{\hat{n}}(\mathbf{h} - p\mathbf{q}_\perp; p', p, k)] \end{aligned} \right\}, \quad (2.14)$$

where the function

$$\bar{C}(\mathbf{q}_\perp) = C(\mathbf{q}_\perp)/C_R = g^2 \int \frac{dQ^0 dQ^\parallel}{(2\pi)^2} 2\pi \delta(v_{\hat{n}} \cdot Q) v_{\hat{n}}^\mu v_{\hat{n}}^\nu \langle\langle A_\mu(Q) [A_\nu(Q)]^* \rangle\rangle \quad (2.15)$$

is the collision kernel $C(\mathbf{q}_\perp)$ stripped of its color factor C_R and encodes the broadening of hard particles during the splitting process. It can be represented as a Wightman correlator of the gluon field generated by the hard particles moving through the plasma. In an isotropic plasma, it can be evaluated analytically (see Appendix A.5.4).

This integral equation (2.11) is typically solved by going to impact parameter space, where the before-mentioned dipole cross section or potential $C(\mathbf{x})$ naturally appears (see Eq. (1.2)),

$$\bar{C}(\mathbf{x}) = \int \frac{d^2\mathbf{q}_\perp}{(2\pi)^2} (1 - e^{i\mathbf{x} \cdot \mathbf{q}_\perp}) \bar{C}(\mathbf{q}_\perp). \quad (2.16)$$

We will discuss in Chapter 8 (and Appendix E) how to obtain the splitting rate γ numerically for an anisotropic collision kernel $C(\mathbf{q}_\perp)$. If the incoming particle is highly energetic, only the small- $|\mathbf{x}|$ behavior of this dipole cross section $C(\mathbf{x})$ is important, and the rate can be obtained by an expansion in logarithms [101, 121].

These rate equations are used to study jet quenching in the MARTINI framework [141], and will be a fundamental ingredient for the effective kinetic description of QCD [19], which we will introduce and discuss in the next Chapter 3.6.6.

2.3 MEDIUM-INDUCED RADIATION SPECTRUM IN A FINITE MEDIUM

2.3.1 Energy spectrum

In a medium with finite length and also time varying properties, the spectrum is usually written in a seemingly different form (see, e.g., [84, 96, 97]),

$$\omega \frac{dI}{d\omega} = \frac{\alpha_s z P_{s \rightarrow g}(z)}{[z(1-z)E]^2} \text{Re} \int_0^\infty dt_1 \int_{t_1}^\infty dt_2 \partial_{\mathbf{x}} \cdot \partial_{\mathbf{y}} \{ \mathcal{K}(\mathbf{y}, t_2; \mathbf{x}, t_1) - \mathcal{K}_{\text{vac}}(\mathbf{y}, t_2; \mathbf{x}, t_1) \}, \quad (2.17)$$

where \mathcal{K} is the Green's function for a two-dimensional Schrödinger equation

$$i\partial_t \psi(\mathbf{x}, t) = (\delta E(\mathbf{p}_x) - i\Gamma_3(\mathbf{x}, t)) \psi(\mathbf{x}, t), \quad (2.18)$$

with initial condition $\mathcal{K}(\mathbf{x}, t; \mathbf{y}, 0) = \delta^{(2)}(\mathbf{x} - \mathbf{y})$. That this spectrum (2.17) is related to the rates obtained in the previous section can be seen, e.g., that in the integral equation (2.11) the energy difference δE from Eq. (2.12) appears as well. The potential Γ_3 is also reminiscent of the terms in the integral equation,

$$\Gamma_3(\mathbf{x}, t) = \frac{C_A}{2} \bar{C}(\mathbf{x}, t) + \left(C_s - \frac{C_A}{2} \right) \bar{C}(z\mathbf{x}, t) + \frac{C_A}{2} \bar{C}((1-z)\mathbf{x}, t), \quad (2.19)$$

where the function $\bar{C}(\mathbf{x}, t)$, as in Eq. (2.16), is related to the collision kernel $\bar{C}(\mathbf{q}_\perp, t)$. For highly-energetic partons, we have seen before in the qualitative discussion that the LPM regime is that of relevance. There, the results depended crucially on the jet quenching parameter \hat{q} , which determines the small distance behavior (see Eq. (1.3)) of this dipole cross section $C(\mathbf{b}, t)$, which we will discuss in more detail in Section 7.2.1.

2.3.2 Medium-induced radiation spectrum differential in transverse momentum

One may also, instead of just giving the energy spectrum of emitted gluons, consider explicitly gluons with different transverse momenta, i.e., become differential in k_\perp . Doing that for a general gluon energy fraction z becomes rather convoluted (see, e.g., Ref. [162]), and we will stick to the case of soft emissions $z \ll 1$ here. In that case, the spectrum can be written as (see, e.g., [92])

$$\frac{dI}{d\omega d^2\mathbf{k}} = \frac{\bar{\alpha}}{2\pi\omega^3} \text{Re} \int_{t_0}^{\infty} dt_2 \int_{t_0}^{t_2} dt_1 \int_{\mathbf{x}} e^{-i\mathbf{k}\cdot\mathbf{x}} \mathcal{P}(\mathbf{x}, \infty; t_2) \partial_{\mathbf{x}} \cdot \partial_{\mathbf{y}} \mathcal{K}(\mathbf{x}, t_2; \mathbf{y}, t_1)_{\mathbf{y}=0} - \frac{8\bar{\alpha}\pi}{\mathbf{k}^2\omega}. \quad (2.20)$$

The functions \mathcal{P} and \mathcal{K} describe the broadening of the emitted gluon and the splitting process, respectively. Again, the medium enters these quantities via the dipole cross section $C(\mathbf{x}, t)$,

$$\partial_t \mathcal{P}(\mathbf{x}, t; t_1) = -C(\mathbf{x}, t) \mathcal{P}(\mathbf{x}, t; t_1), \quad (2.21)$$

$$\left(i\partial_t - \frac{\partial_{\mathbf{x}}^2}{2\omega} + iC(\mathbf{x}, t) \right) \mathcal{K}(\mathbf{x}, t; \mathbf{y}, t_1) = i\delta^{(2)}(\mathbf{x} - \mathbf{y}) \delta(t_1 - t). \quad (2.22)$$

Indeed, the equation for the Green's function \mathcal{K} here can be obtained by taking the $z \ll 1$ limit of the previous section and is the same function that appears in Eq. (2.17). As discussed before, for a highly energetic jet, the small- $|\mathbf{x}|$ behavior of the dipole cross section is most important and can be expressed (to a first approximation) as

$$C(\mathbf{x}, t) = \frac{1}{4} \hat{q}(t) \mathbf{x}^2 + \dots, \quad (2.23)$$

where the parameter \hat{q} is the jet quenching parameter from Eq. (1.3) and (1.4). Because this parameter characterizes the small distance behavior of the dipole

cross section, it is an important ingredient for jet energy loss and jet quenching calculations. This parameter will also be the central object of Chapter 4.4.

This quadratic approximation is also known as the *harmonic approximation* or the *harmonic oscillator approximation*, because in the approximation (2.23), the two-dimensional Schrödinger equation (2.18) (and Eq. (2.22)) reduces to that of a (time-dependent) harmonic oscillator. This allows for an analytic solution. More physically motivated, this approximation is also referred to as the *multiple soft scattering approximation*, because the jet quenching parameter \hat{q} describes the momentum broadening due to many (soft) scatterings with the medium (see Eq. (1.4)).

We will further discuss this small distance behavior in more detail in Section 7.2.1.

3

QCD KINETIC THEORY

In this chapter, we discuss the assumptions and equations of the effective kinetic theory description of QCD. We discuss how medium effects enter and how they are typically approximated. In Section 3.4.5, we discuss how a kinetic description can be derived from the underlying quantum field theory, and derive the expression for the elastic scattering rate. We discuss how QCD kinetic theory has been used to study QCD equilibration in Section 3.5.1. Finally, we conclude this chapter in Section 4 by discussing and giving more details on how to perform numerical simulations of QCD kinetic theory.

3.1 VALIDITY OF QCD KINETIC THEORY

At sufficiently weak coupling (which, in physical terms for QCD, means sufficiently high energies), QCD admits an effective kinetic description, first formulated by Arnold, Moore, and Yaffe [19]. Generally, a kinetic description is valid when the mean free path between collisions (or interactions) is much larger than the duration of a scattering/collision process, which is treated as instantaneous. Additionally, the quantum mechanical wave packets corresponding to the particles must be well describable by classical particles, meaning that the De Broglie wavelength must be much smaller than the mean free path.

In the weak-coupling picture, this is the case: The extent of typical excitations with momenta $P \sim T$ in a thermal system is $\sim 1/T$, while the mean free path is $1/(g^2 T)$ for small-angle scatterings and $1/(g^4 T)$ for large angle scatterings. Since the formation time for a gluon emission $1/(g^2 T)$ is of similar order as the mean free path between small-angle scatterings, it is required to take the quantum mechanical interference between different splitting processes into account, leading to the LPM rate (2.6) with mean free path¹ $1/(g^4 T)$.

While the estimates in the previous paragraph were given for a plasma in thermal equilibrium, the kinetic description is also valid out of equilibrium, given that certain conditions are fulfilled [19]. We assume that all particle masses are negligible with respect to thermal (or effective) masses $\sim gT$, which should again be much smaller than the momenta of “relevant” physical excitations, constituting a *scale separation* between the “relevant” excitations and medium-dependent corrections to dispersive relations or to the inverse Debye screening length. Further required assumptions are that the distribution functions $f_s(t, \mathbf{p}, \mathbf{x})$ do not vary significantly

¹ This can be seen by using the simple estimate $\hat{q} \sim g^4 T^3$ (see later Chapter 4.4) in the LPM rate $d\Gamma^{\text{LPM}}/dz \sim g^2 \sqrt{\hat{q}/\omega}$ from Eq. (2.6).

over spacetime regions of the formation time t^{form} of near-collinear processes (see Eq. (2.4)) for the relevant excitations. Furthermore, the distribution functions should not vary significantly with $\mathcal{O}(m_{\text{eff},s}) \sim gT$ changes in momentum, and the distribution function should not be non-perturbatively large, $f_s \ll 1/\alpha_s$.

3.2 THE EQUATIONS OF QCD KINETIC THEORY

The Boltzmann equations for the effective kinetic theory description of QCD have been formulated in Ref. [19], where all leading-order relevant scattering processes are taken into account. While next-to-leading order (NLO) corrections have also been obtained [20], this thesis focuses on the leading order description.

In a kinetic description, the fundamental quantity is the distribution function

$$f_s(t, \mathbf{p}, \mathbf{x}) = \frac{(2\pi)^3}{\nu_s} \frac{dN_s}{d^3\mathbf{p} d^3\mathbf{x}}, \quad (3.1)$$

describing the number of particles N_s of species s per phase-space volume. It is averaged over all ν_s spin and color states ($\nu_g = 2d_A = 2(N_c^2 - 1)$ for gluons and $\nu_q = 2d_F = 2N_c$ for quarks/antiquarks). Equivalently, we may view the distribution function $f_s(t, \mathbf{p}, \mathbf{x})$ as the distribution function for a single species of a particular color and spin state, which is identical for all ν_s degrees of freedom.

The distribution functions obey the coupled Boltzmann equations

$$\left(\frac{\partial}{\partial t} + \mathbf{v} \cdot \nabla \right) f_s(t, \mathbf{p}, \mathbf{x}) = -\mathcal{C}_s^{1 \leftrightarrow 2}[f_a(t, \mathbf{p}, \mathbf{x})] - \mathcal{C}_s^{2 \leftrightarrow 1}[f_a(t, \mathbf{p}, \mathbf{x})], \quad (3.2)$$

which describe how they change due to elastic ($\mathcal{C}^{2 \leftrightarrow 2}$) and inelastic ($\mathcal{C}^{1 \leftrightarrow 2}$) collisions. The collision terms are local in space \mathbf{x} and time t ; therefore, their explicit space-time dependence will be frequently omitted.

The inelastic collision term $\mathcal{C}^{1 \leftrightarrow 2}$ describes strict collinear splitting (where all momenta are proportional to a unit vector $\hat{\mathbf{n}} = \hat{\mathbf{p}} = \mathbf{p}/p$), and is given by

$$\begin{aligned} \mathcal{C}_a^{1 \leftrightarrow 2}[f_i(\mathbf{p})] &= \frac{(2\pi)^3}{2p^2\nu_a} \sum_{bc} \int_0^\infty dp' dk' \delta(p - p' - k') \gamma_{bc}^a(p; p', k') \\ &\quad \times \left\{ f_a(\mathbf{p}) (1 \pm f_b(p' \hat{\mathbf{p}})) (1 \pm f_c(k' \hat{\mathbf{p}})) - f_b(p' \hat{\mathbf{p}}) f_c(k' \hat{\mathbf{p}}) (1 \pm f_a(\mathbf{p})) \right\} \\ &+ \frac{(2\pi)^3}{p^2\nu_a} \sum_{bc} \int_0^\infty dp' dk \delta(p + k - p') \gamma_{ab}^c(p'; p, k) \\ &\quad \times \left\{ f_a(\mathbf{p}) f_b(k \hat{\mathbf{p}}) (1 \pm f_c(p' \hat{\mathbf{p}})) - f_c(p' \hat{\mathbf{p}}) (1 \pm f_a(k \hat{\mathbf{p}})) (1 \pm f_b(\mathbf{p})) \right\}. \end{aligned} \quad (3.3)$$

The upper signs are to be used for gluons (bosons) and the lower signs for quarks (fermions),

$$(1 \pm f_a(\mathbf{p})) = \begin{cases} 1 + f_a(\mathbf{p}), & \text{for gluons, i.e., } a = g, \\ 1 - f_a(\mathbf{p}), & \text{for quarks, i.e., } a = q, \bar{q} \end{cases}, \quad (3.4)$$

representing Bose enhancement and Fermi blocking, respectively. The effective splitting/joining rates $\gamma_{bc}^a(p; p', k)$ depend on the unit vector $\hat{\mathbf{n}}$ and interpolate

between the Bethe-Heitler and LPM regime. They were already discussed in the last Chapter 2.1, but are, for completeness, reiterated here. They are given by

$$\gamma_{qg}^q(p; p', k) = \gamma_{\bar{q}g}^{\bar{q}}(p; p', k) = \frac{p'^2 + p^2}{p'^2 p^2 k^3} \mathcal{F}_q^{\hat{n}}(p, p', k), \quad (3.5a)$$

$$\gamma_{q\bar{q}}^g(p; p', k) = \frac{k^2 + p'^2}{p'^3 p^3 k^3} \mathcal{F}_q^{\hat{n}}(k, -p', p), \quad (3.5b)$$

$$\gamma_{gg}^g(p; p', k) = \frac{p'^4 + p^4 + k^4}{p'^3 p^3 k^3} \mathcal{F}_g^{\hat{n}}(p, p', k), \quad (3.5c)$$

where

$$\mathcal{F}_s^{\hat{n}}(p, p', k) = \frac{d_s C_s \alpha_s}{2(2\pi)^3} \int \frac{d^2 \mathbf{h}}{(2\pi)^2} 2\mathbf{h} \cdot \text{Re} \mathbf{F}_s^{\hat{n}}(\mathbf{h}; p', p, k), \quad (3.6)$$

and \mathbf{F} is the solution to the integral equation

$$\begin{aligned} 2\mathbf{h} = i\delta E(\mathbf{h}; p', p, k) \mathbf{F}_s^{\hat{n}}(\mathbf{h}; p', p, k) + \int \frac{d^2 \mathbf{q}_\perp}{(2\pi)^2} \bar{C}(\mathbf{q}_\perp) \\ \times \left\{ \left(C_s - \frac{C_A}{2} \right) [\mathbf{F}^{\hat{n}}(\mathbf{h}; p', p, k) - \mathbf{F}_s^{\hat{n}}(\mathbf{h} - k\mathbf{q}_\perp; p', p, k)] \right. \\ \left. + \frac{C_A}{2} [\mathbf{F}_s^{\hat{n}}(\mathbf{h}; p', p, k) - \mathbf{F}_s^{\hat{n}}(\mathbf{h} + p'\mathbf{q}_\perp; p', p, k)] \right. \\ \left. + \frac{C_A}{2} [\mathbf{F}_s^{\hat{n}}(\mathbf{h}; p', p, k) - \mathbf{F}_s^{\hat{n}}(\mathbf{h} - p\mathbf{q}_\perp; p', p, k)] \right\}. \end{aligned} \quad (3.7)$$

The vector \mathbf{h} is a two-dimensional vector in the plane transverse to the direction of the splitting particles, $\hat{\mathbf{n}}$. The energy difference δE is given by

$$\delta E(\mathbf{h}; p', p, k) = \frac{m_{\text{eff},g}^2}{2k} + \frac{m_{\text{eff},s}^2}{2p} - \frac{m_{\text{eff},s}^2}{2p'} + \frac{\mathbf{h}^2}{2p k p'}. \quad (3.8)$$

The function $\bar{C}(\mathbf{q}_\perp) = C(\mathbf{q}_\perp)/C_R$ is the collision kernel stripped of its color factor and encodes the broadening of hard particles during the splitting process. It can be represented as a Wightman correlator (see Eqs. (2.15), and Eq. (A.15) in Appendix A.6.2 for its definition) of the gluon field generated by the hard particles moving through the plasma. With an isotropic screening approximation, it can be written as the difference of the retarded transverse and longitudinal hard thermal loop propagators evaluated at $\omega = q_\parallel = 0$ (see Appendix A.5.4),

$$\bar{C}(\mathbf{q}_\perp) = g^2 T_* \left(\frac{1}{q_\perp^2} - \frac{1}{q_\perp^2 + m_D^2} \right), \quad (3.9)$$

with the infrared temperature T_* given by

$$T_* = \frac{\sum_s \nu_s \frac{g^2 C_s}{d_A} \int \frac{d^3 \mathbf{p}}{(2\pi)^3} f(\mathbf{p}) (1 \pm f(\mathbf{p}))}{m_D^2} \quad (3.10)$$

and with the nonequilibrium Debye mass

$$m_D^2 = 2m_{\text{eff},g}^2 = \sum_s 4\nu_s \frac{g^2 C_s}{d_A} \int \frac{d^3 p}{(2\pi)^3 2|\mathbf{p}|} f_s(\mathbf{p}). \quad (3.11)$$

The effective quark mass of flavor s is given by

$$m_{\text{eff},s}^2 = 2g^2 C_F \int \frac{d^3 p}{(2\pi)^3 2|\mathbf{p}|} [2f_g(\mathbf{p}) + f_s(\mathbf{p}) + f_{\bar{s}}(\mathbf{p})]. \quad (3.12)$$

In equilibrium, they are given by

$$T_* = T, \quad m_D^2 = g^2 T^2 \left(\frac{N_c}{3} + \frac{n_f}{6} \right), \quad m_{\text{eff},s}^2 = \frac{C_F g^2}{4}. \quad (3.13)$$

The splitting rates γ_{bc}^a are symmetric under the exchange of the outgoing particles

$$\gamma_{bc}^a(p; p', k) = \gamma_{cb}^a(p; k, p'). \quad (3.14)$$

The elastic collision term $\mathcal{C}^{2\leftrightarrow 2}$ is given by

$$\begin{aligned} \mathcal{C}_a^{2\leftrightarrow 2}[f_i(\mathbf{p})] &= \frac{1}{4|\mathbf{p}|\nu_a} \sum_{bcd} \int_{\mathbf{k}\mathbf{p}'\mathbf{k}'} \left| \mathcal{M}_{cd}^{ab}(\mathbf{p}, \mathbf{k}; \mathbf{p}', \mathbf{k}') \right|^2 (2\pi)^4 \delta^4(P + K - P' - K') \\ &\times \left\{ f_a(\mathbf{p}) f_b(\mathbf{k}) [1 \pm f_c(\mathbf{p}')] [1 \pm f_d(\mathbf{k}')] - f_c(\mathbf{p}') f_d(\mathbf{k}') [1 \pm f_a(\mathbf{p})] [1 \pm f_b(\mathbf{k})] \right\}. \end{aligned} \quad (3.15)$$

Again, the upper signs are to be used for gluons and the lower signs for quarks, as stated in Eq. (3.4). The Lorentz-invariant integration measure is defined as

$$\int_{\mathbf{k}} := \int \frac{d^3 \mathbf{k}}{(2\pi)^3 2k}. \quad (3.16)$$

At leading-order, the required matrix elements are listed in Table 3.1, where s, t , and u are the usual Lorentz invariant Mandelstam variables, which are given in terms of the incoming (P, K) and outgoing (P', K') momenta,

$$s = -(P + K)^2, \quad t = -(P' - P)^2, \quad u = -(K' - P)^2. \quad (3.17)$$

Recall that we use the mostly plus metric convention here, see Eq. (1.5). The Mandelstam variables satisfy the usual relation (for massless particles)

$$s + t + u = 0. \quad (3.18)$$

The matrix elements for the elastic collision term obey the symmetries

$$\left| \mathcal{M}_{cd}^{ab}(\mathbf{p}, \mathbf{k}; \mathbf{p}', \mathbf{k}') \right|^2 = \left| \mathcal{M}_{dc}^{ab}(\mathbf{p}, \mathbf{k}; \mathbf{k}', \mathbf{p}') \right|^2 = \left| \mathcal{M}_{cd}^{ba}(\mathbf{k}, \mathbf{p}; \mathbf{p}', \mathbf{k}') \right|^2 = \left| \mathcal{M}_{ab}^{cd}(\mathbf{p}', \mathbf{k}'; \mathbf{p}, \mathbf{k}) \right|^2, \quad (3.19)$$

corresponding to switching the outgoing particles ($c \leftrightarrow d$), the incoming particles ($a \leftrightarrow b$), or the incoming with the outgoing particles ($ab \leftrightarrow cd$).

In thermal equilibrium, both elastic and inelastic collision terms identically vanish due to the detailed balance condition. This can be seen easily by including the thermal distribution functions

$$f_{\pm}(k; T) = \frac{1}{\exp(k/T) \mp 1} \quad (3.20)$$

in the collision terms (3.3) and (3.15). The upper sign f_+ denotes the Bose-Einstein distribution (relevant for gluons) and f_- the Fermi-Dirac distribution (relevant for quarks and antiquarks). Note that this label in f_{\pm} is chosen such that the statistical factors in (3.4) become $(1 \pm f_{\pm}(p))$.

$ab \leftrightarrow cd$	$ \mathcal{M}_{cd}^{ab} ^2/g^4$
$q_1 q_2 \leftrightarrow q_1 q_2,$	
$q_1 \bar{q}_2 \leftrightarrow q_1 \bar{q}_2,$	
$\bar{q}_1 q_2 \leftrightarrow \bar{q}_1 q_2,$	$8 \frac{d_F^2 C_F^2}{d_A} \left(\frac{s^2+u^2}{\underline{t}^2} \right)$
$\bar{q}_1 \bar{q}_2 \leftrightarrow \bar{q}_1 \bar{q}_2$	
$q_1 q_1 \leftrightarrow q_1 q_1,$	
$\bar{q}_1 \bar{q}_1 \leftrightarrow \bar{q}_1 \bar{q}_1$	$8 \frac{d_F^2 C_F^2}{d_A} \left(\frac{s^2+u^2}{\underline{t}^2} + \frac{s^2+t^2}{\underline{u}^2} \right) + 16 d_F C_F \left(C_F - \frac{C_A}{2} \right) \frac{s^2}{tu}$
$q_1 \bar{q}_1 \leftrightarrow q_1 \bar{q}_1$	$8 \frac{d_F^2 C_F^2}{d_A} \left(\frac{s^2+u^2}{\underline{t}^2} + \frac{t^2+u^2}{s^2} \right) + 16 d_F C_F \left(C_F - \frac{C_A}{2} \right) \frac{u^2}{st}$
$q_1 \bar{q}_1 \leftrightarrow q_2 \bar{q}_2$	$8 \frac{d_F^2 C_F^2}{d_A} \left(\frac{t^2+u^2}{s^2} \right)$
$q_1 \bar{q}_1 \leftrightarrow gg$	$8 d_F C_F^2 \left(\frac{u}{\underline{t}} + \frac{t}{\underline{u}} \right) - 8 d_F C_F C_A \left(\frac{t^2+u^2}{s^2} \right)$
$\bar{q}_1 g \leftrightarrow \bar{q}_1 g$	$-8 d_F C_F^2 \left(\frac{u}{s} + \frac{s}{\underline{u}} \right) + 8 d_F C_F C_A \left(\frac{s^2+u^2}{\underline{t}^2} \right)$
$gg \leftrightarrow gg$	$16 d_A C_A^2 \left(3 - \frac{su}{\underline{t}^2} - \frac{st}{\underline{u}^2} - \frac{tu}{s^2} \right)$

Table 3.1: Matrix elements for the elastic collision term (3.15) from [19]. Singly-underlined denominators indicate infrared-sensitive contributions from soft-gluon exchange, doubly-underlined denominators from soft-fermion exchange. The constants d_F , C_F , d_A , and C_A are given in Eq. (A.7).

3.3 MEDIUM EFFECTS: SCREENING OF SOFT MODES

3.3.1 Where screening is needed

In the inelastic collision term, medium effects enter via the collision kernel $\bar{C}(\mathbf{q}_\perp)$, opening up the phase space for the effective $1 \rightarrow 2$ splitting and $2 \rightarrow 1$ merging processes.

For the elastic $2 \leftrightarrow 2$ scattering processes² entering the elastic collision term (3.15), one needs to calculate the $2 \rightarrow 2$ scattering matrix elements up to the needed order in perturbation theory, in our case up to leading order. However, it is a well-known fact in thermal field theory that for a thermal medium, a naïve expansion in loops is not sufficient, i.e., for instance, the leading order expressions need input from an arbitrarily high number of loops. This happens when an internal propagator becomes soft, in which case it has to be resummed using the hard thermal loop effective theory [163–165], which has been applied to non-thermal media as well [36, 37, 166, 167].

The most straightforward way to compute the scattering matrix elements with medium effects included is to reevaluate the matrix elements and replace all internal propagators with resummed hard thermal loop (HTL) propagators.³ This is rather cumbersome,⁴ and Arnold, Moore, and Yaffe [19] propose a different, leading-order equivalent, way to achieve the same effect. One simply needs to replace the underlined terms in Table 3.1 by

$$\underline{\frac{(s-u)^2}{t^2}} \rightarrow |G_{\mu\nu}(P-P') (P+P')^\mu (K+K')^\nu|^2, \quad (3.21a)$$

$$\underline{\frac{u}{t}} \rightarrow \frac{4\text{Re}[(P \cdot Q)(K \cdot Q)^*] + sQ \cdot Q^*}{|Q \cdot Q|^2}, \quad (3.21b)$$

where the first line is needed for soft-gluon exchanges and the second line is for soft-quark exchanges. Here, $G_{\mu\nu}(Q)$ denotes the retarded gluon propagator, and Q is defined as $Q^\mu = P^\mu - P'^\mu - \Pi_{\text{Ret}}^\mu(P - P')$. We will discuss why the retarded propagator needs to be used in more detail in Section 3.4.5. Note that when using the vacuum propagator

$$G_{\mu\nu}^0(Q) = \frac{\eta^{\mu\nu}}{Q^2} \quad (3.22)$$

in Eq. (3.21a), the right-hand side reduces to the left-hand side, i.e., for no medium modifications, we recover the vacuum case. We discuss the motivation for this replacement and its validity in more detail in the following.

In this thesis, we mainly consider gluons, and in particular, we will only need the prescription for soft-gluon exchange (3.21a). This can be motivated as follows:

² This subsection follows the discussion in Ref. [4].

³ Throughout this thesis, we will keep using the phrase *hard thermal loops* even for systems out of equilibrium, where other authors have used *hard loops* instead.

⁴ For instance, even for the vacuum case, where the gluon propagator is given by Eq. (3.22) instead of the more complicated HTL propagator (A.41), Peskin and Schroeder note that the cross section for “gluon-gluon scattering [...] is rather tedious to evaluate” [168].

First, note that using relation (B.35) between the Mandelstam variables, we may rewrite the gluon-gluon matrix element from Table 3.1 as

$$\frac{|\mathcal{M}|^2}{4\lambda^2 d_A} = 9 + \frac{(t-s)^2}{\underline{u}^2} + \frac{(s-u)^2}{\underline{t}^2} + \frac{(u-t)^2}{s^2}. \quad (3.23)$$

Using the symmetry of exchanging u and t (corresponding to the exchange of the external particles with momenta \mathbf{p}' and \mathbf{k}'), we may rewrite this to

$$\frac{|\mathcal{M}|^2}{4\lambda^2 d_A} = 9 + 2 \frac{(s-u)^2}{\underline{t}^2} + \frac{(u-t)^2}{s^2}. \quad (3.24)$$

At tree level, which is relevant for the leading-order matrix elements in Table 3.1, only one internal propagator G appears. Medium corrections to its free form G_0 are conventionally encoded in the self-energy (see Appendix A.3), and the full propagator can be schematically written (when $G_0^{-1} = Q^2$) as

$$G(Q) = \frac{1}{Q^2 + \Pi(Q)}. \quad (3.25)$$

Thus, the self-energy introduces an effective mass m_{eff} . In a (thermal) medium, this self-energy is proportional to the screening mass scale $\Pi \sim m_D^2 = \mathcal{O}(g^2 T^2)$ (see Eq. (3.11)). Therefore, at leading order, medium effects are only relevant for soft momenta $Q \sim \mathcal{O}(gT)$.

Using the Mandelstam variables (3.17), it is easy to see that internal soft momenta correspond to the case⁵ $|t| = |Q^2| \ll s$, where $Q^\mu = (\omega, \mathbf{q}) = P'^\mu - P^\mu$. This implies that both $\omega, q \ll p, k$ (see Appendix B.7). Therefore, the small t behavior is the region of interest for medium modifications, i.e., the region where

$$0 < -t \ll s \approx -u. \quad (3.26)$$

At leading order, the QCD $2 \leftrightarrow 2$ scattering matrix elements are spin-independent for soft momentum exchange (we show that explicitly in Appendix B for elastic quark-quark and gluon-gluon scattering). Therefore, medium effects can be included as in a theory with fictitious scalar ‘quarks’, which can be regarded as a generalization of scalar QED. For quark scattering in this fictitious scalar QCD, the vertex factor is given by $-igt^a(P+K)^\nu$, where P and K are the momenta of the in- and outgoing quark, g is the coupling constant and t^a is a basis element of the $\mathfrak{su}(N_c)$ Lie algebra. There are no spinor factors for external legs, and thus the squared amplitude (without color and coupling factors) is given by

$$|\mathcal{M}|^2 \propto |(P+P')^\mu(K+K')^\nu G_{\mu\nu}(Q)|^2, \quad (3.27)$$

which precisely corresponds to the screening prescription (3.21a) (with color factors reinstated such that for no screening the vacuum case is reproduced). In Appendix B, it is demonstrated that this simple argument using scalar QCD indeed reproduces the leading order correct prescription for quark and gluon scattering with soft-gluon exchange.

⁵ For the small u region, one may always use the symmetry $t \leftrightarrow u$ to rewrite the matrix element (3.24) such that only the small t behavior needs to be regulated.

3.3.2 Debye-like screening

Equation (3.21a) is typically implemented in QCD kinetic theory implementations [21–26, 169, 170] in a very simple approximation. Instead of using the (full) hard thermal loop (HTL) propagator (Eq. (A.41) in Appendix A.6.2), one uses a simple (isotropic) Debye-like screened propagator [169],

$$G_{\mu\nu} = \frac{\eta_{\mu\nu}}{Q^2} \frac{q^2}{q^2 + \xi_g^2 m_D^2}, \quad (3.28)$$

which at the level of the matrix elements corresponds to replacing

$$\frac{(s-u)^2}{t^2} \rightarrow \frac{(s-u)^2}{t^2} \frac{q^4}{(q^2 + \xi_g^2 m_D^2)^2}. \quad (3.29)$$

The constant $\xi_g = e^{5/6}/\sqrt{8}$ is chosen to approximate the HTL propagator in isotropic systems [169], or—as we will see in Chapters 4.4 and 6.4.8—for longitudinal momentum broadening. For the soft-fermion diagrams, a similar prescription with a different constant ξ_q is used in the literature.

In Ref. [169], the value of ξ_g is obtained by writing the elastic collision term for an isotropic distribution function as

$$\begin{aligned} C^{2 \leftrightarrow 2} &= \frac{1}{2^9 \pi^5 v} \int_0^\infty dk \int_0^{2\pi} d\phi_{qp} \\ &\times \int_{-p}^k d\omega \{f(p)f(k)(1+f(p+\omega))(1+f(k-\omega)) - f(p+\omega)f(k-\omega)(1+f(p))(1+f(k))\} \\ &\times \int_{|\omega|}^{\min(2k-\omega, 2p+\omega)} dq \int_0^{2\pi} d\phi_{qk} \frac{|\mathcal{M}|^2}{p^2}. \end{aligned} \quad (3.30)$$

Since screening effects are only important for soft internal momenta, $q, \omega \ll k, p$, we may expand the distribution functions for small ω . The first nonvanishing term is quadratic in ω since the matrix element is even. Therefore, we can fix the constant ξ_g by requiring [169] that in this limit

$$\int_{-\infty}^{\infty} d\omega \omega^2 \int_{|\omega|}^{\infty} dq \int_0^{2\pi} d\phi \left(|\mathcal{M}_{\text{HTL}}|^2 - |\mathcal{M}_{\text{Debye1}}|^2 \right) = 0. \quad (3.31)$$

This isotropic screening prescription neglects the effect of plasma instabilities which would otherwise be present in anisotropic systems [34–38, 171]. However, numerical evidence indicates that these instabilities do not play a dominant role at the time scales of interest for kinetic theory simulations [42, 43] and when a quasiparticle picture has become applicable [172–174].

In Chapter 4.4, we will see that this simple screening prescription does not accurately describe both the longitudinal and transverse broadening of partons and in Chapter 6.4.8, we will compare kinetic theory simulations using this simple Debye-like screened matrix element to simulations where the HTL matrix element is used.

3.4 HOW KINETIC THEORY EMERGES FROM QUANTUM FIELD THEORY

Before going on to discuss QCD thermalization and how to perform QCD kinetic theory simulations, let us discuss how the Boltzmann equation and, in particular, the collision terms can be obtained from the underlying quantum field theory.

This procedure, in principle, is well understood [175, 176], but several complications arise when considering QCD. First, QCD is a gauge theory and one has to deal with the redundancies that come from the gauge symmetry. Secondly, as discussed before, $1 \rightarrow 2$ particle splittings (see Chapter 3) occur at a similar rate as elastic collisions, and thus need to be included in a consistent kinetic description. We will not consider these complications here in detail, and consider the more easily accessible case of a scalar theory.

We will mainly follow the presentation laid out in Ref. [177] (similar presentations with slightly different notation and conventions can be found, e.g., in Refs. [175, 176, 178–181]) and do not attempt to provide a very rigorous derivation here. This section should be seen as motivating, which physical approximations are needed to derive kinetic equations and, in particular, motivate why the internal propagators in the matrix elements of the elastic collision terms are retarded ones. For this chapter, we will need some of the formalism of nonequilibrium quantum field theory briefly reviewed in Appendix A.6.2.

A typical technique to derive kinetic theory is to start from the Kadanoff-Baym equations, perform a Wigner transform to phase space and then a gradient expansion, keeping only the lowest-order terms in spatial gradients. Additionally, one performs the quasiparticle approximation, and the Kadanoff-Baym ansatz [175, 178], where one identifies the Wightman functions with the phase-space distribution function and the spectral function. The quasiparticle approximation (taking the width of the spectral function to be zero, effectively replacing it with a delta function) means physically approximating the lifetime of the (quasi-)particles to be infinite between collisions, which is needed for any kinetic description to be valid. This implies that the particles are stable between collisions and can only change their momentum state (without the inclusion of force terms in the Boltzmann equation) or decay due to collisions encoded in the collision terms.

3.4.1 Kadanoff-Baym equations

Let us start by discussing the Kadanoff-Baym evolution equations for the propagator, and how these equations arise from the underlying quantum field theory. For scalar field theory, let us start with the Lagrangian

$$\mathcal{L}(X) - j(X)\phi(X) = -\frac{1}{2}\partial_\mu\phi(X)\partial^\mu\phi(X) - \frac{m^2}{2}\phi^2(X) - V(\phi(X)) - j(X)\phi(X), \quad (3.32)$$

where we have included an external source term with the source $j(X)$. One may derive the equations of motion for the full propagator by first considering the equations of motion (using $\partial^2 = \partial_\mu\partial^\mu$)

$$-m^2\phi(X) + \partial^2\phi(X) = \frac{\partial V}{\partial\phi} + j(X), \quad (3.33)$$

and taking the ensemble average $\langle \dots \rangle$ (e.g., by using the path integral formalism, see Eq. (A.10) in Appendix A.6.2). One then obtains

$$(\partial^2 - m^2)(-iG(X, Y)) + \int d^4Z (-i\Pi(X, Z))(-iG(Z, Y)) = \delta^{(4)}(X - Y), \quad (3.34)$$

where the full propagator $G(x, y)$ and self-energy $\Pi(x, y)$ can be defined as the functional derivatives

$$-iG(X, Y) = \frac{\delta\langle\phi(X)\rangle}{\delta j(Y)}, \quad i\Pi(X, Y) = \frac{\delta}{\delta\langle\phi(Y)\rangle} \left\langle \frac{dV}{d\phi}(X) \right\rangle. \quad (3.35)$$

Eq. (3.34) has the nice physical interpretation that the difference between the full and free propagator is the self-energy Π (see Eq. (A.27) in Appendix A.6.2).

Eq. (3.34) can also be obtained on the Schwinger-Keldysh contour (see Appendix A.2), and it is useful to decompose the full (time-ordered) propagator into the Wightman functions $G^<$ and $G^>$ (see Appendix A.2) and perform a similar decomposition of the self-energy (see Eqs. (A.32c) and (A.29)),

$$G(X, Y) = \Theta(X^0 - Y^0)G^>(X, Y) + \Theta(Y^0 - X^0)G^<(X, Y), \quad (3.36)$$

$$\Pi(X, Y) = -i\Pi^\delta(X)\delta^{(4)}(X - Y) + \Theta(X^0 - Y^0)\Pi^>(X, Y) + \Theta(Y^0 - X^0)\Pi^<(X, Y). \quad (3.37)$$

Inserting this decomposition into (3.34) and neglecting⁶ terms depending on the initial time t_0 , we obtain the Kadanoff-Baym equations

$$(\partial_X^2 - m^2 - \Pi^\delta(X))G^>(X, Y) = i \int_{-\infty}^{\infty} d^4Z (\Pi^R(X, Z)G^>(Z, Y) + \Pi^>(X, Z)G^A(Z, Y)), \quad (3.38a)$$

$$(\partial_X^2 - m^2 - \Pi^\delta(X))G^<(X, Y) = i \int_{-\infty}^{\infty} d^4Z (\Pi^R(X, Z)G^<(Z, Y) + \Pi^<(X, Z)G^A(Z, Y)), \quad (3.38b)$$

$$(\partial_Y^2 - m^2 - \Pi^\delta(X))G^>(X, Y) = i \int_{-\infty}^{\infty} d^4Z (G^>(X, Z)\Pi^A(Z, Y) + G^R(X, Z)\Pi^>(Z, Y)), \quad (3.38c)$$

$$(\partial_Y^2 - m^2 - \Pi^\delta(X))G^<(X, Y) = i \int_{-\infty}^{\infty} d^4Z (G^<(X, Z)\Pi^A(Z, Y) + G^R(X, Z)\Pi^<(Z, Y)). \quad (3.38d)$$

These equations are exact, but only useful if we know the exact form of the self-energies. In practice, truncating the self-energy at some point constitutes an approximation here.

3.4.2 Wigner transform

The next step is to perform a Wigner transform

$$f(X, Y) \mapsto \tilde{f}(\bar{X}, P), \quad (3.39)$$

⁶ This is justified for initial times in the remote past [175, 177].

which consists of a coordinate transformation to relative and central coordinates,

$$S^\mu = X^\mu - Y^\mu, \quad \bar{X}^\mu = \frac{X^\mu + Y^\mu}{2}, \quad (3.40)$$

and then performing a Fourier transform with respect to the relative coordinate S ,

$$\tilde{f}(k, \bar{X}) = \int d^4S e^{-IK \cdot S} f(X(S, \bar{X}), Y(S, \bar{X})). \quad (3.41)$$

Taking the difference of Eqs. (3.38a) and (3.38c) leads to expressions

$$\partial_X^2 - \partial_Y^2 = 2\partial_S \cdot \partial_{\bar{X}}, \quad \Pi^\delta(X) - \Pi^\delta(Y) = -(S \cdot \partial_{\bar{X}})\Pi^\delta(\bar{X}). \quad (3.42)$$

Importantly, the Wigner transform of a general convolution such as those on the right-hand side of Eqs. (3.38) is [181]

$$\begin{aligned} \int d^4Z A(X, Z)B(Z, Y) &\mapsto e^{\frac{i}{2}(\partial_X^A \cdot \partial_P^B - \partial_P^A \cdot \partial_X^B)} \tilde{A}(\bar{X}, P) \tilde{B}(\bar{X}, P) \\ &= \tilde{A}(\bar{X}, P) \tilde{B}(\bar{X}, P) + \frac{i}{2} \{ \tilde{A}(\bar{X}, P), \tilde{B}(\bar{X}, P) \}_{\text{PB}} + \dots, \end{aligned} \quad (3.43)$$

where $\{A, B\}_{\text{PB}} = \partial_P A \cdot \partial_{\bar{X}} B - \partial_{\bar{X}} A \cdot \partial_P B$ denotes the Poisson bracket. The Boltzmann equation is obtained by next expanding in gradients of $\partial_{\bar{X}}$. Using identities from Appendix A.4, we obtain

$$\begin{aligned} &\left(-2K^\mu + \frac{\partial \text{Re}\tilde{\Pi}(K, \bar{X})}{\partial K_\mu} \right) \frac{\partial \tilde{G}^>(K, \bar{X})}{\partial \bar{X}^\mu} - \frac{\partial \text{Re}\tilde{\Pi}(K, \bar{X})}{\partial \bar{X}_\mu} \frac{\partial \tilde{G}^>(K, \bar{X})}{\partial K^\mu} \\ &- \{ \tilde{\Pi}^>(K, \bar{X}), \text{Re}\tilde{G}^R(K, \bar{X}) \}_{\text{PB}} = -(\tilde{G}^>(K, \bar{X})\tilde{\Pi}^<(K, \bar{X}) - \tilde{\Pi}^>(K, \bar{X})\tilde{G}^<(K, \bar{X})), \end{aligned} \quad (3.44)$$

where we have defined $\text{Re}\tilde{\Pi}(K, \bar{X}) = \Pi^\delta(\bar{X}) + \text{Re}\tilde{\Pi}^R(K, \bar{X})$.

3.4.3 Quasiparticle approximation

Using the quasiparticle approximation,

$$\tilde{\rho}(K, \bar{X}) = 2\pi \text{sign}(K^0) \delta(-K^2 - M^2 - \text{Re}\tilde{\Pi}(K, \bar{X})) g(K) = 2\pi \text{sign}(K^0) \delta(K_0^2 - E_{\mathbf{k}}^2) g(K), \quad (3.45)$$

we enforce the particles to be stable between collisions, which was one of the requirements for kinetic theory listed in the beginning. With this approximation, one may also neglect the Poisson bracket in Eq. (3.44) [177]. We have included here an additional function $g(Q)$, which is unity, $g(Q) \equiv 1$, in our case of scalar particles, but for gluons reads $g(Q) = -\eta_{\mu\nu} \delta_{ab}$ and for fermions $g(Q) = \mathcal{Q} + m$.

The distribution function is introduced via the Kadanoff-Baym ansatz [175, 178],

$$\tilde{G}^<(K, \bar{X}) = \tilde{\rho}(K, \bar{X}) \tilde{N}(K, \bar{X}), \quad \tilde{G}^>(K, \bar{X}) = \tilde{\rho}(K, \bar{X}) [1 + \tilde{N}(K, \bar{X})], \quad (3.46)$$

which is true in thermal equilibrium when inserting the Bose-Einstein distribution (3.20) [177], and is used as the definition of the distribution function out of equilibrium. Together with the quasiparticle approximation, the off-shell distribution

function $\tilde{N}(K, \bar{X})$ can be brought on-shell, using $\tilde{N}(K, \bar{X}) = -(1 + \tilde{N}(-K, \bar{X}))$ from Eqs. (A.37) and (A.38)),

$$\tilde{G}^<(K, \bar{X}) = 2\pi\delta(K_0^2 - E_{\mathbf{k}}^2(\bar{X})) (\Theta(K^0)f(\mathbf{k}, \bar{X}) + \Theta(-K^0)(1 + f(-\mathbf{k}, \bar{X}))), \quad (3.47a)$$

$$\tilde{G}^>(K, \bar{X}) = 2\pi\delta(K_0^2 - E_{\mathbf{k}}^2(\bar{X})) (\Theta(K^0)(1 + f(\mathbf{k}, \bar{X})) + \Theta(-K^0)f(-\mathbf{k}, \bar{X})), \quad (3.47b)$$

with the on-shell distribution function

$$f(\mathbf{k}, \bar{X}) = \tilde{N}(K^0 = E_{\mathbf{k}}, \mathbf{k}, \bar{X}). \quad (3.48)$$

The splitting in Eq. (3.47) is done to enforce the K^0 component in (3.48) to be always positive.

We can then integrate Eq. (3.44) over (positive) K^0 to bring the distribution function on-shell and arrive at

$$\begin{aligned} & \left(\partial_{\bar{t}} + \frac{\mathbf{k}}{E_{\mathbf{k}}(\bar{X})} \cdot \partial_{\bar{x}} - \partial_{\bar{x}} E_{\mathbf{k}}(\bar{X}) \cdot \partial_{\mathbf{k}} \right) f(\mathbf{k}, \bar{X}) \\ &= -\frac{1}{2E_{\mathbf{k}}(\bar{X})} ((1 + f(\mathbf{k}, \bar{X})) \Pi_E^<(\mathbf{k}, \bar{X}) - \Pi_E^>(\mathbf{k}, \bar{X}) f(\mathbf{k}, \bar{X})), \end{aligned} \quad (3.49)$$

which has the correct structure to compare with the Boltzmann equation (3.2). Note that $\mathbf{v} = \mathbf{k}/E_{\mathbf{k}}$. Here, we can identify the gain and loss term, where the loss term is given by $\Pi_E^>(\mathbf{k}, \bar{X})$ and multiplied by the distribution function $f(\mathbf{k}, \bar{X})$. Here, the E in $\Pi_E^>(\mathbf{k}, \bar{X})$ defines the on-shell self-energy, i.e.,

$$\Pi_E^>(\mathbf{k}, \bar{X}) = \tilde{\Pi}^>(K^0 = E_{\mathbf{k}}, \mathbf{k}, \bar{X}). \quad (3.50)$$

To recapitulate, the only approximations to arrive at this equation were the gradient expansion and the quasiparticle approximation, together with setting the initial time t_0 in the remote past. Using this, we were able to derive a Boltzmann equation for the distribution function $f(\mathbf{k}, \bar{X})$. The next step is to evaluate the self-energies $\Pi^>$ and $\Pi^<$ in terms of the distribution function $f(\mathbf{k}, \bar{X})$, i.e., to write it in terms of degrees of freedom for which we again may use the quasiparticle approximation.

3.4.4 Decay rate

Let us focus here on the decay rate (or the loss term) given by $\Pi_E^>$. The gain term can be obtained similarly by replacing $>\leftrightarrow<$.

Cutting rule for the self-energy

For the self-energy $\tilde{\Pi}^<$, there exists a convenient *cutting rule* (see [182, 183]),

$$\begin{aligned} \tilde{\Pi}^>(K) &= \sum_n \frac{1}{n!} \left(\prod_{j=1}^n \int \frac{d^4 Q_j}{(2\pi)^4} \right) (2\pi)^4 \delta^4(Q_1 + \dots + Q_n - K) \\ &\quad \times \mathcal{M}_{ar...r}(P; Q_1, \dots, Q_n) \mathcal{M}_{ar...r}(-P; -Q_1, \dots, -Q_n) \\ &\quad \times \tilde{G}^>(Q_1) \dots \tilde{G}^>(Q_n) \end{aligned} \quad (3.51)$$

The diagram shows a ladder network with two nodes, each represented by a hatched circle. A horizontal line labeled K connects the two nodes. n arrows, labeled Q_1, Q_2, \dots, Q_n , point from the left node to the right node. Dashed lines and arrows indicate a continuation of the network structure.

where $\mathcal{M}_{ar...r}$ are *fully retarded amplitudes*, i.e. they represent a matrix element with exactly one a -index in the r/a basis (see Appendix A.2). The sum runs over all the propagators $\tilde{G}^>(Q_1) \dots$ that are inserted between the two diagrams, or equivalently, over all the lines that are *cut* and then replaced by $\tilde{G}^>(Q_1) \dots$. For particles with spin or color, the additional indices are summed over (e.g., consider an index in the amplitude $\mathcal{M}_{ar...r}$ to belong to one momentum Q_i ; then the propagator with Q_i carries the same index and connects it to the corresponding index in the conjugate amplitude $\mathcal{M}_{ar...r}^*$).

Self-energy for pure gluons

Let us now consider⁷ the gluon self-energy in a purely gluonic system, which appears in the loss term in the Boltzmann equation (3.49), and use the cutting rule to obtain it. For that, let us consider a specific term appearing in the self-energy for pure gluons, the term where three internal lines are cut according to the cutting rule (3.51),

$$\delta_{ah} \eta^{\sigma\epsilon} \Pi_{\sigma\epsilon}^{> ah}(P) \ni \frac{1}{6} \int \frac{d^4 Q_1 d^4 Q_2 d^4 Q_3}{(2\pi)^{12}} \times \tilde{G}_{\alpha\mu}^{> gd}(Q_1) \tilde{G}_{\beta\nu}^{> eb}(Q_2) \tilde{G}_{\gamma\rho}^{> fc}(Q_3) (2\pi)^4 \delta^4(Q_1 + Q_2 + Q_3 - P) \quad (3.53)$$

$$\times \left(\begin{array}{c} \text{Diagram 1: } \sigma, a \sim P \text{ (input)} \rightarrow \text{Hatched Circle} \text{ (intermediate)} \rightarrow \rho, c \text{ (output)} \\ \text{with momenta } Q_1, Q_2, Q_3 \text{ and labels } \nu, b \text{ and } \mu, d. \end{array} \right) \left(\begin{array}{c} \text{Diagram 2: } \epsilon, h \sim P \text{ (input)} \rightarrow \text{Hatched Circle} \text{ (intermediate)} \rightarrow \gamma, f \text{ (output)} \\ \text{with momenta } Q_1, Q_2, Q_3 \text{ and labels } \beta, e \text{ and } \alpha, g. \end{array} \right)^* .$$

⁷ A similar discussion was included in my diploma thesis [184].

The arrows denote (retarded) propagators in the r/a basis (see Appendix A.2).

Let us bring this expression into a more convenient form. With the Kadanoff-Baym ansatz (3.46), and the quasiparticle approximation (3.45) with $g(Q) = -\eta_{\mu\nu}\delta_{ab}$ for gluons, the Wightman functions $\tilde{G}^>$ can be written using (3.47b) as

$$\tilde{G}_{\mu\nu}^{> ab}(Q) = -2\pi\eta_{\mu\nu}\delta^{ab}\frac{1}{2E_{\mathbf{q}}}[\delta(Q^0 - E_{\mathbf{q}})(1 + f(\mathbf{q})) + \delta(Q^0 + E_{\mathbf{q}})f(-\mathbf{q})]. \quad (3.54)$$

Due to rotational symmetry, $E_{\mathbf{q}} = E_{-\mathbf{q}}$. Inserting this for the gluonic propagators in (3.53), we can write the two diagrams as the squared amplitude, where we take $|\mathcal{M}|^2$ to be summed over all initial and final polarizations and colors.

$$|\mathcal{M}|^2 = \eta_{\alpha\mu}\eta_{\beta\nu}\eta_{\gamma\rho}\eta_{\sigma\epsilon}\delta_{ah}\delta_{gd}\delta_{eb}\delta_{fc} \times \left(\begin{array}{c} \text{Diagram 1: } \sigma, a \sim P \rightarrow \text{shaded loop} \rightarrow \rho, c \\ \text{Diagram 2: } \epsilon, h \sim P \rightarrow \text{shaded loop} \rightarrow \gamma, f \end{array} \right)^* = \left| \begin{array}{c} \text{Diagram 1: } \sigma, a \sim P \rightarrow \text{shaded loop} \rightarrow \rho, c \\ \text{Diagram 2: } \epsilon, h \sim P \rightarrow \text{shaded loop} \rightarrow \gamma, f \end{array} \right|^2, \quad (3.55)$$

with the corresponding legs contracted and summed over all colors (and polarizations).

The Q^0 integrals in (3.53) can now be performed, where for every $\tilde{D}^>$ the delta function removes the Q^0 integral and yields two terms according to (3.54),

$$\begin{aligned} & \frac{1}{6} \int \frac{d^3\mathbf{q}_1 d^3\mathbf{q}_2 d^3\mathbf{q}_3}{(2\pi)^9 2E_{\mathbf{q}_1} 2E_{\mathbf{q}_2} 2E_{\mathbf{q}_3}} (2\pi)^4 \delta^3(\mathbf{q}_1 + \mathbf{q}_2 + \mathbf{q}_3 - P) |\mathcal{M}|^2 \\ & \times \left\{ \delta(E_{\mathbf{q}_1} + E_{\mathbf{q}_2} + E_{\mathbf{q}_3} - E_p) \left[(1 + f_{\mathbf{q}_1})(1 + f_{\mathbf{q}_2})(1 + f_{\mathbf{q}_3}) \right] \right. \\ & + \delta(-E_{\mathbf{q}_1} + E_{\mathbf{q}_2} + E_{\mathbf{q}_3} - E_p) \left[f_{-\mathbf{q}_1}(1 + f_{\mathbf{q}_2})(1 + f_{\mathbf{q}_3}) \right] \\ & + \text{similar with } \mathbf{q}_1 \leftrightarrow \mathbf{q}_2, \quad \mathbf{q}_1 \leftrightarrow \mathbf{q}_3 \\ & + \delta(-E_{\mathbf{q}_1} - E_{\mathbf{q}_2} + E_{\mathbf{q}_3} - E_p) \left[f_{-\mathbf{q}_1} f_{-\mathbf{q}_2} (1 + f_{\mathbf{q}_3}) \right] \\ & + \text{similar with } \mathbf{q}_2 \leftrightarrow \mathbf{q}_3, \quad \mathbf{q}_1 \leftrightarrow \mathbf{q}_3 \\ & \left. \delta(-E_{\mathbf{q}_1} - E_{\mathbf{q}_2} - E_{\mathbf{q}_3} - E_p) \left[f_{-\mathbf{q}_1} f_{-\mathbf{q}_2} f_{-\mathbf{q}_3} \right] \right\} \end{aligned} \quad (3.56)$$

$$\begin{aligned} & = \frac{1}{6} \int \frac{d^3\mathbf{q}_1 d^3\mathbf{q}_2 d^3\mathbf{q}_3}{(2\pi)^9 2E_{\mathbf{q}_1} 2E_{\mathbf{q}_2} 2E_{\mathbf{q}_3}} (2\pi)^4 |\mathcal{M}|^2 \\ & \times \left\{ \delta^4(Q_1 + Q_2 + Q_3 - P) \Big|_{(Q_i)^0 = E_{\mathbf{q}_i}} \left[(1 + f_{\mathbf{q}_1})(1 + f_{\mathbf{q}_2})(1 + f_{\mathbf{q}_3}) \right] \right. \\ & + \delta^4(-Q_1 + Q_2 + Q_3 - P) \Big|_{(Q_i)^0 = E_{\mathbf{q}_i}} \left[f_{\mathbf{q}_1}(1 + f_{\mathbf{q}_2})(1 + f_{\mathbf{q}_3}) \right] \\ & + \text{similar with } \mathbf{q}_1 \leftrightarrow \mathbf{q}_2, \quad \mathbf{q}_1 \leftrightarrow \mathbf{q}_3 \\ & + \delta^4(-Q_1 - Q_2 + Q_3 - P) \Big|_{(Q_i)^0 = E_{\mathbf{q}_i}} \left[f_{\mathbf{q}_1} f_{\mathbf{q}_2} (1 + f_{\mathbf{q}_3}) \right] \\ & + \text{similar with } \mathbf{q}_2 \leftrightarrow \mathbf{q}_3, \quad \mathbf{q}_1 \leftrightarrow \mathbf{q}_3 \\ & \left. \delta^4(-Q_1 - Q_2 - Q_3 - P) \Big|_{(Q_i)^0 = E_{\mathbf{q}_i}} \left[f_{\mathbf{q}_1} f_{\mathbf{q}_2} f_{\mathbf{q}_3} \right] \right\}. \end{aligned} \quad (3.57)$$

For particles with an (effective) mass, energy-momentum conservation can only be fulfilled for the second delta function.

We thus obtain

$$\begin{aligned} \delta_{ah} \eta^{\sigma\epsilon} \Pi_{\sigma\epsilon}^> (P) & \stackrel{3\text{ lines}}{=} \frac{1}{2} \int \frac{d^3\mathbf{q}_1 d^3\mathbf{q}_2 d^3\mathbf{q}_3}{(2\pi)^9 2E_{\mathbf{q}_1} 2E_{\mathbf{q}_2} 2E_{\mathbf{q}_3}} (2\pi)^4 |\mathcal{M}|^2 \\ & \times \delta^4(-Q_1 + Q_2 + Q_3 - P) \Big|_{(Q_i)^0 = E_{\mathbf{q}_i}} \left[f_{\mathbf{q}_1}(1 + f_{\mathbf{q}_2})(1 + f_{\mathbf{q}_3}) \right]. \end{aligned} \quad (3.58)$$

From the self-energy $\Pi^>$, we can now easily obtain the decay rate of an excitation with momentum P using the Boltzmann equation (3.49) with the normalization $1/(2E_p)$. Taking the trace over all colors and spins in Eq. (3.53) leads to the sum of all ν_g excitations. Additionally, we only considered three cut propagators, which corresponds to elastic processes (2 particles going in, 2 particles going out). Thus, the elastic decay or scattering rate of a particle with momentum P is

$$\begin{aligned} \Gamma_{\text{el}} & = \frac{1}{4p\nu_a} \sum_{bcd} \int_{\mathbf{k}\mathbf{p}'\mathbf{k}'} (2\pi)^4 \delta^4(P + K - P' - K') \\ & \times \left| \mathcal{M}_{cd}^{ab}(\mathbf{p}, \mathbf{k}; \mathbf{p}', \mathbf{k}') \right|^2 f_b(\mathbf{k}) [1 \pm f_d(\mathbf{k}')] [1 \pm f_c(\mathbf{p}')]. \end{aligned} \quad (3.59)$$

Here, we have used $E_p = |\mathbf{p}| = p$, and generalized this equation to include also quarks. Eq. (3.59) describes the decay rate or scattering rate of a particle of species

a with momentum \mathbf{p} due to elastic collisions $p + k \rightarrow p' + k'$. The sum is over all possible scattering processes including particles b, c and d .

We will use this equation (3.59) in the next Chapter 4.4 as a starting point to obtain the jet quenching parameter \hat{q} .

3.4.5 Relation to the Boltzmann equation

Comparing with the elastic collision kernel in QCD kinetic theory, we recognize that Eq. (3.59) constitutes exactly the contribution to the elastic collision kernel Eq. (3.15) from the decay rate. The gain term can be computed in a similar way.

For the inelastic collision kernel (3.3), evaluating the self-energy using the techniques from the previous sections is more complicated because one has to take into account the physics of LPM suppression. However, using the radiation rate γ from Section 2.2 as an effective vertex, we can use the cutting rule (3.51) with two internal cut lines to arrive at (3.3), similar to the steps taken here.

3.5 WHAT WE KNOW ABOUT QCD EQUILIBRATION

As mentioned in the introduction, understanding and simulating how an equilibrated quark-gluon plasma is formed in heavy-ion collisions is an active research area. While for the very earliest times after the collision, classical statistical simulations need to be performed [13], we will focus here on studies and considerations using QCD kinetic theory, which can describe how an over-occupied system (possibly taken from an earlier classical statistical simulation) equilibrates. While analytic and parametric estimates exist [38, 159, 185, 186], numerical studies have been performed using QCD kinetic theory in isotropic systems [21, 22, 187], and also including quarks and nonzero chemical potential [23–26]. A review on QCD thermalization can be found, e.g., in [13, 158].

3.5.1 Thermalization of isotropic systems

For initially over-occupied systems (right panel of Fig. 3.1), where $f \gg 1$, but still $f \ll 1/\alpha_s$ for kinetic theory to be applicable, the initial energy is carried by a large number of soft particles. There, the initial evolution quickly falls on top of a scaling solution, which is referred to as a *non-thermal fixed point*,

$$f(t, p) = (Qt)^\alpha f_S \left((Qt)^\beta \frac{p}{Q} \right). \quad (3.60)$$

Conservation laws relate the exponents α and β . For instance, energy conservation

$$\varepsilon(t) = \int \frac{d^3 p}{(2\pi)^3} p f(\mathbf{p}) = \text{const}, \quad (3.61)$$

implies the relation

$$\alpha = 4\beta. \quad (3.62)$$

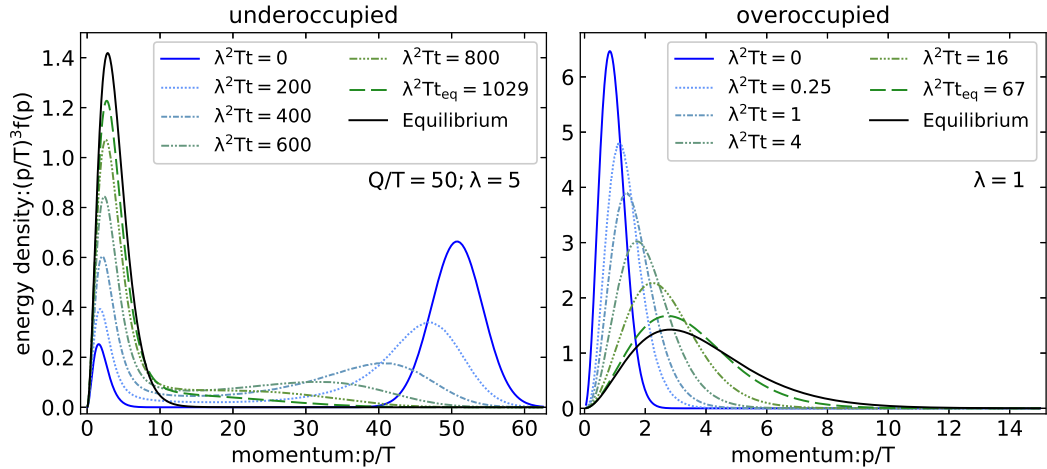


Figure 3.1: Thermalization of isotropic nonabelian plasmas at NLO for an under-occupied (left) and over-occupied (right) initial condition. Figure from [187].

With a more rigorous analysis considering how the Boltzmann equation behaves at the scaling solution, one obtains further $\alpha = -4/7$, $\beta = -1/7$.

This self-similar evolution breaks down once the condition $f \gg 1$ is no longer satisfied. The thermalization time can be easily obtained by noting that we start with an initial energy density $\epsilon \sim Q^4/\alpha_s$, which leads to a final temperature $T \sim Q\alpha_s^{-1/4} \gg Q$. The self-similar evolution ends, once the hard scale in the distribution function $Q(Qt)^{-\beta} \sim T$, which leads to

$$t_{\text{therm.}} \sim \frac{1}{\alpha_s^2 T}. \quad (3.63)$$

In this regime, classical statistical simulations and kinetic theory simulations are both valid and detailed analysis between both approaches has shown their equivalence [169].

For initially under-occupied systems (left panel of Fig. 3.1), the total energy is concentrated at a small number $f_0 \ll 1$ of very hard particles of momentum Q , such that $T \ll Q$. These hard particles emit soft gluons which form a soft thermal bath. After such a bath has formed, the remaining hard particles of momentum Q thermalize by democratic splitting $Q \rightarrow Q/2 + Q/2$. The formation time t^{form} of such a splitting is given by Eq. (2.4), $t^{\text{form}} \sim \sqrt{\omega/\hat{q}}$. Since this scales with the energy of the emitted gluon $\omega \sim Q$, the formation time is long and the splitting takes place in the LPM regime. Taking the LPM rate from Eq. (2.6), the number of emitted gluons above a frequency ω can be estimated to be (see also [98])

$$\Delta N(\omega) = \int_{\omega} d\omega' \int_0^t dt' \frac{d\Gamma}{d\omega'} \sim \alpha_s t \sqrt{\frac{\hat{q}}{\omega}}. \quad (3.64)$$

If we assume that the system thermalizes once the first democratic splitting with $\omega \approx Q/2$ has occurred, we can define the thermalization time when the number of emitted gluons is of order unity, i.e., we consider $\Delta N(Q) \sim 1$ and take $t \sim t_{\text{therm.}}$. We then obtain

$$t_{\text{therm.}} \sim \frac{1}{\alpha_s} \sqrt{\frac{Q}{\hat{q}}}. \quad (3.65)$$

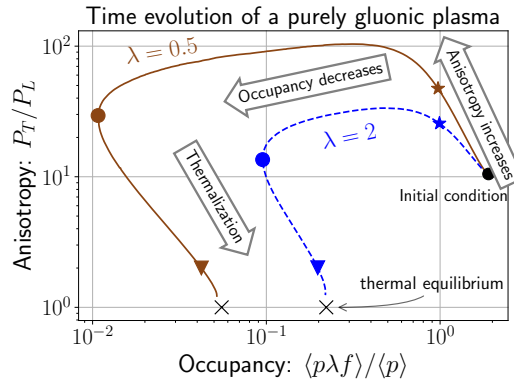


Figure 3.2: Time evolution of a gluonic plasma undergoing Bjorken expansion with an over-occupied initial condition (black dot) in the anisotropy-occupancy plane. The three stages of bottom-up thermalization are denoted by arrows.

Assuming⁸ $\hat{q} \sim \alpha_s^2 T^3$, we obtain

$$t_{\text{therm.}} \sim \frac{1}{\alpha_s^2 T} \sqrt{\frac{Q}{T}}, \quad (3.66)$$

3.5.2 Thermalization of expanding systems

In expanding and, thus, anisotropic systems, the appearance of plasma instabilities [34–37, 133, 188–196] complicates the picture (see also the review [39]), but it has been observed in classical simulations that they do not play a significant role at least at the early times where these simulations are valid [42, 43]. We will, therefore, not consider the effect of these plasma instabilities here.

How expanding systems thermalize has been worked out by Baier, Mueller, Schiff, and Son about 25 years ago [185]. Starting from an overoccupied initial condition $f \sim 1/\lambda$ which should be obtained from classical statistical simulations of the earlier dynamics, quasiparticles and a kinetic description become applicable at a time scale of around $\tau \sim 1/Q_s$. At this time, the (hard) gluons have momenta of order Q_s . While the system is dominated by rapid expansion, the interaction of the hard particles leads to the emission of soft gluons.

When the occupancy drops below $1/\lambda$ (star marker in Fig. 3.2), the plasma becomes under-occupied and a classical description is no longer applicable. While the anisotropy stays roughly constant, a soft bath is built by further branching, which thermalizes first. A significant amount of the total energy is still carried by the remaining small number of hard gluons, which, in the third stage, lose energy through multiple hard branchings, until equilibrium is reached at a time that is parametrically given by

$$\tau_{\text{BMSS}} = \alpha_s^{-13/5} / Q_s. \quad (3.67)$$

⁸ We will obtain a more precise expression for the jet quenching parameter \hat{q} in Chapter 4.4. For now, as a simple estimate, we may take $\hat{q} = \int d^2 \mathbf{q}_\perp q_\perp^2 d\Gamma_{\text{el}} / d^2 \mathbf{q}_\perp$, which for dimensional reasons is proportional to T^3 and we obtain a factor α_s^2 from the matrix elements for the scattering rate (3.59) from Table 3.1.

A simple estimate for this thermalization time can be given following Ref. [21] by noticing that the physical picture for thermalization is as in the under-occupied isotropic case and taking the energy density to be as in a simple free streaming expansion

$$\varepsilon(\tau) \sim \frac{Q_s^3}{\alpha_s \tau}, \quad T(\tau) \sim \left(\frac{Q_s^3}{\alpha_s \tau} \right)^{1/4}. \quad (3.68)$$

Combining this with Eq. (3.66), we obtain

$$\tau_{\text{therm}} = \frac{1}{\alpha_s^2 T(\tau_{\text{therm}})} \sqrt{\frac{Q_s}{T(\tau_{\text{therm}})}} = \alpha_s^{-13/5} / Q_s. \quad (3.69)$$

The physical picture of bottom-up thermalization is quite robust and is also seen in simulations solving the Boltzmann equation (3.2) in diffusion approximation [197–199].

3.6 PERFORMING QCD KINETIC THEORY SIMULATIONS

This thesis relies heavily on QCD kinetic theory simulations. In this section, all concepts needed for performing these numerical simulations are introduced. The code used for the publications [1–3] is publicly available [170]. We will discuss how the Boltzmann equation (3.2) is solved, what initial conditions are used, how observables are calculated, and conclude with discussing discretization effects.

3.6.1 Symmetries of the distribution function

Throughout the thesis, we will consider the distribution function to be a function of only three parameters: $f(t, \mathbf{p}, \mathbf{x}) = f(\tau, p, \cos \theta_p)$, i.e., the proper time τ , the magnitude of the momentum p , and its angle to the beam axis θ_p , which we motivate now.

1. First, we assume that the system is *boost invariant* [200], i.e., the distribution function only depends on the rapidity difference $\tilde{f}(\tau, p, y - \eta)$ for momenta P and spacetime X ,

$$P_\mu = p(\cosh y, \hat{\mathbf{v}}_\perp, \sinh y) = (p, \mathbf{p}_\perp, p_z), \quad (3.70a)$$

$$X_\mu = (\tau \cosh \eta, \mathbf{x}_\perp, \tau \sinh \eta) = (t, \mathbf{x}_\perp, z). \quad (3.70b)$$

A boost with rapidity η' would shift $y \rightarrow y + \eta'$, $\eta \rightarrow \eta + \eta'$, thus leaving the distribution function f invariant. It is then enough to consider the system at $z = \eta = 0$.

2. Further, we assume *homogeneity in the transverse plane*, i.e., the distribution function does not depend on \mathbf{x}_\perp . This is justified for large and homogeneous colliding nuclei.
3. Additionally, we assume rotational symmetry around the beam axis, i.e., in the transverse plane,

$$f(k, \cos \theta_k, \phi_k + \alpha) = f(k, \cos \theta_k, \phi_k), \quad \forall \alpha \in [0, 2\pi), \quad (3.71)$$

which is justified by assuming that the initial particle production is isotropic, with only the longitudinal expansion singling out one preferred direction.

4. Mirror symmetry around $z = 0$ in symmetric collisions,

$$f(k, \cos \theta_k, \phi_k) = f(k, -\cos \theta_k, \phi_k). \quad (3.72)$$

With all these assumptions, at $z = \eta = 0$, the distribution function can be written as

$$f(t, \mathbf{p}) = f(\tau, p, p_z) = f(\tau, p, \cos \theta_p). \quad (3.73)$$

Mathematically, we employ here a sloppy notation using the same symbol f for $f(\tau, p, p_z) = f(\tau, p, \cos \theta_p)$. Additionally, the time argument will be sometimes suppressed.

At nonzero z or spacetime rapidity η , the distribution function can be obtained from $f(\tau, p, \cos \theta_p)$ by using (3.70), $\tilde{f}(\tau, p, y) = f(\tau, p, \tanh y)$ and by boost-invariance,

$$\tilde{f}(\tau, p, y - \eta) = f(\tau, p, \tanh(y - \eta)). \quad (3.74)$$

Using these symmetries, the spatial derivative in the Boltzmann equation (3.2) can be rewritten (at $\eta = z = 0$) to [200]

$$\mathbf{v} \cdot \nabla_x f(\tau, \mathbf{p}, z) = -\frac{p_z}{\tau} \frac{\partial}{\partial p_z} f(\tau, p, p_z), \quad (3.75)$$

and represents the effective longitudinal Bjorken expansion. Besides that, we will sometimes also consider isotropic distribution functions $f(p)$ without Bjorken expansion, for which $\mathbf{v} \cdot \nabla_x f(\tau, \mathbf{p}, z) = 0$.

3.6.2 Boltzmann equation and initial condition

With the approximations mentioned in the previous section, the Boltzmann equation (3.2) for a purely gluonic system is then given by

$$\left(\frac{\partial}{\partial \tau} - \frac{p_z}{\tau} \frac{\partial}{\partial p_z} \right) f(\tau, \mathbf{p}) = -\mathcal{C}^{1 \leftrightarrow 2}[f(\tau, \mathbf{p})] - \mathcal{C}^{2 \leftrightarrow 2}[f(\tau, \mathbf{p})], \quad (3.76)$$

with the collision kernels $\mathcal{C}^{1 \leftrightarrow 2}$ and $\mathcal{C}^{2 \leftrightarrow 2}$ containing inelastic and elastic collisions described in more detail in Section 3.3.1. For the spatial derivative, we have already inserted the boost-invariant expansion term (3.75), which is not present for the isotropic nonexpanding simulations also performed in this thesis. If present, this expansion term accounts for the effective longitudinal Bjorken expansion of the system.

As an initial condition, ideally, we would take at some time, e.g., $\tau_0 = 1/Q_s$ [185], the full lattice configuration obtained in a classical statistical simulation of the Glasma, extract a gluon distribution function (perhaps using the methods discussed in Section 3.4.5, or as, e.g., done in Refs. [64, 201, 202]) and use this as input for our kinetic theory simulation. While performing this matching seems feasible in principle, for this thesis, we follow the approach and initial conditions

ξ_0	A
2	0.96789
4	2.05335
10	5.24171

Table 3.2: Parameter choices for the initial condition (3.77) for different anisotropy parameters ξ_0 that leave the initial energy density constant.

from Ref. [22], where a parameterization of the JIMWLK evolved (2+1D) Glasma result from Ref. [203] is used,

$$f(p_\perp, p_z, \tau=1/Q_s) = \frac{2A(\xi_0)\langle p_T \rangle}{\lambda p_\xi} \exp\left(-\frac{2p_\xi^2}{3\langle p_T \rangle^2}\right), \quad (3.77)$$

with $p_\xi = \sqrt{p_\perp^2 + (\xi_0 p_z)^2}$ and $\langle p_T \rangle = 1.8Q_s$. Different parameter choices for the initial anisotropy parameter ξ_0 and the normalization constant A are given in Table 3.2, which are chosen to keep the initial energy density constant for varying anisotropies. Here, the p_z dependence is obtained by “de”-squeezing the transverse momentum $p_\perp \rightarrow \sqrt{p_\perp^2 + \xi^2 p_z^2}$. Recall that the 't Hooft coupling λ is defined via

$$\lambda = g^2 N_c = 4\pi N_c \alpha_s. \quad (3.78)$$

To give results in physical units, one has to choose a value for the saturation momentum Q_s . For most of this thesis, we will not choose any particular value and discuss the results in units of Q_s . However, in Section 4.3.2 (which is based on Ref. [1]), we will attempt to make a comparison to the value of the jet quenching parameter \hat{q} during the Glasma stage, for which we need to choose a value of Q_s . There, the saturation momentum Q_s is chosen to reproduce the energy density of the Glasma in Ref. [153] at initial time $Q_s \tau = 1$ at the coupling $\lambda = 10$, which leads to $Q_s = 1.4$ GeV. Remarkably, the same value is also obtained in Ref. [204], where it was found that precisely this value is needed for the EKT setup to be consistent with the later hydrodynamic evolution. We will discuss this matching in more detail in Section 4.2. Additionally, one could also proceed as in Ref. [157], where coupling and saturation momentum Q_s are related via the one-loop beta function of QCD,

$$\alpha_s(Q_s) = \frac{\lambda(Q_s)}{4\pi N_c} = \frac{1}{\frac{33-3n_f}{12\pi} \ln \frac{Q_s^2}{\Lambda_{\text{QCD}}^2}}, \quad (3.79)$$

to obtain for $n_f = 0$ and $Q_s = 1.4$ GeV approximately $\lambda \approx 11$ for $\Lambda_{\text{QCD}} = 200$ MeV, thus leading to a value in the same ballpark. It should be emphasized, however, that this matching is meant to serve as an estimate for which value of Q_s to choose, and is needed to provide numerical values in physical units.

3.6.3 Observables and Landau matching

We define the expectation value of an observable $O(\mathbf{p}, t)$ for a given distribution function $f(\mathbf{p}, t)$ via

$$\langle O(t) \rangle = \frac{\nu_g}{n(t)} \int \frac{d^3 \mathbf{p}}{(2\pi)^3} O(\mathbf{p}, t) f(\mathbf{p}, t), \quad (3.80)$$

which is normalized by the particle number density

$$n(t) = \nu_g \int \frac{d^3 \mathbf{p}}{(2\pi)^3} f(\mathbf{p}, t), \quad (3.81)$$

such that $\langle 1 \rangle = 1$.

An important class of such observables are the components of the energy-momentum tensor,

$$T^{\mu\nu} = \nu_g \int \frac{d^3 \mathbf{p}}{(2\pi)^3} \frac{p^\mu p^\nu}{|\mathbf{p}|} f(\mathbf{p}), \quad (3.82)$$

whose diagonal entries correspond to the energy density $\varepsilon = T^{00} = n \langle p \rangle$,

$$\varepsilon = \nu_g \int \frac{d^3 \mathbf{p}}{(2\pi)^3} |\mathbf{p}| f(\mathbf{p}), \quad (3.83)$$

transverse pressure $P_T = T^{xx} = T^{yy}$ and longitudinal pressure $P_L = T^{zz}$. Since QCD kinetic theory is conformal, $T^{\mu\nu}$ must be traceless, which leads to $\varepsilon = 2P_T + P_L$. For an isotropic system, $P_L = P_T = \varepsilon/3$.

We will frequently compare the nonequilibrium system (described by the distribution function $f(\mathbf{p}, t)$) to a corresponding thermal system. This comparison is not unique. While a thermal system is uniquely identified by its temperature, for a nonthermal system, temperature cannot be uniquely identified. A common way to do that is to use the Landau matching prescription, where the energy density ε is used to define an effective temperature T_ε as the temperature of the thermal system which has the same energy density as the nonthermal system,

$$T_\varepsilon(t) = \left(\frac{30 \varepsilon(t)}{\nu_g \pi^2} \right)^{1/4}. \quad (3.84)$$

Matching other quantities is also possible, and the best matching prescription may depend on the observable. For instance, in Ref. [7], several matchings were considered for the *heavy-quark diffusion coefficient* κ , and Landau matching (3.84) provided the best results.

3.6.4 Time markers and time scales

As discussed above, for plasmas undergoing Bjorken expansion, thermalization occurs in several stages according to the bottom-up picture. To better identify the different stages in the results and plots, we introduce time markers that should roughly correspond to the boundaries between the different stages, which we

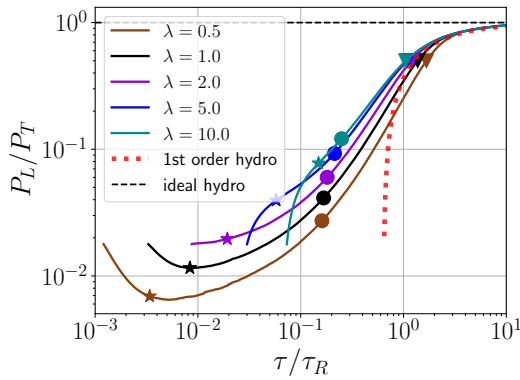


Figure 3.3: Pressure ratio in QCD kinetic theory simulations with Debye-like screened matrix elements. The first-order hydrodynamic expression (3.86) is shown as a red dotted curve and the ideal hydro expectation (unity) as a constant line.

can best see in Fig. 3.2. The star and circle markers are related to the occupancy $\langle pf \rangle / \langle p \rangle$, with the star placed where it first drops below $1/\lambda$ and the circle placed at its minimum value. Finally, the triangle marker is placed when the pressure ratio $P_T/P_L = 2$, and corresponds to a system that has almost isotropized.

We will frequently rescale the time in units of the bottom-up thermalization estimate (3.67),

$$\tau_{\text{BMSS}} = \alpha_s^{-13/5} / Q_s = \left(\frac{\lambda}{4\pi N_c} \right)^{-13/5} / Q_s. \quad (3.85a)$$

Additionally, we will also frequently use the relaxation time,

$$\tau_R(\tau) = \frac{4\pi\eta/s}{T_\epsilon(\tau)}, \quad (3.85b)$$

which depends on the shear viscosity η over entropy density s , and the effective temperature T_ϵ defined in Eq. (3.84). It is the only time scale that appears in first-order hydrodynamics. For instance, there the pressure ratio [46] is given by

$$\frac{P_L}{P_T} = 1 - \frac{2}{\pi} \frac{\tau}{\tau_R}. \quad (3.86)$$

Note that the dimensionless ratio η/s depends on the coupling λ . It has been calculated from perturbative QCD [205, 206], but in practice, for using it in QCD kinetic theory simulations, it is extracted numerically [23, 27, 28, 56]. We will discuss how this ratio can be extracted in more detail in Chapter 6.4.8.

In Fig. 3.3, we show the pressure ratio obtained from QCD kinetic theory simulations at various couplings and how it approaches the first order hydrodynamic result (3.86). Additionally, we also show the ideal hydrodynamic estimate, where $P_L = P_T = \epsilon/3$. This shows that QCD kinetic theory approaches hydrodynamics at late times. In fact, kinetic theory is more general than hydrodynamics, and the hydrodynamic equations of motion can be obtained from kinetic theory [207, 208].

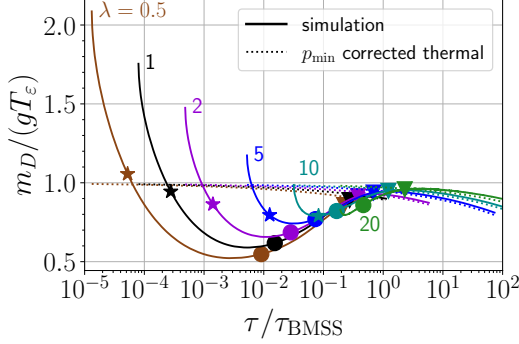


Figure 3.4: Debye mass over its thermal value gT_e during kinetic theory simulations of expanding systems for different couplings. As a dotted line, we show the p_{\min} corrected Debye mass from Eq. (3.87).

3.6.5 Extrapolating EKT to large couplings

Although QCD kinetic theory is only valid at weak couplings, it is often extrapolated to larger values of the coupling, where no first-principle fully dynamical simulation of QCD is possible. There, using the Boltzmann equations and QCD kinetic theory should be viewed as a (mathematically well-defined) model for QCD equilibration. Its study using these larger couplings may nevertheless provide useful phenomenological insights into QCD equilibration and hydrodynamization in heavy-ion collisions. Since the Debye mass m_D is proportional to the coupling, the naïve extrapolation $\lambda \rightarrow \infty$ leads to $m_D \rightarrow \infty$, and thus the screened t -channel small-angle-scattering terms in the matrix element (6.20a) vanish and only the s -channel and constant parts remain. Therefore, at sufficiently large couplings, differences in the screening prescription should become less important, albeit in a regime outside of any theoretical control.

3.6.6 Numerical details and discretization artifacts

The implementation used in this thesis is based on Refs. [21, 22, 169] and is publicly available [170]. The distribution function $f(\tau, \mathbf{p})$ is stored on a finite momentum grid, with $p_{\min} \leq p \leq p_{\max}$. The collision kernels, which consist of several integrals, are evaluated using Monte Carlo methods. The numerical algorithm is constructed in such a way that energy and momentum are exactly conserved. More details on the discretization and on how the collision kernels are evaluated can be found in Appendix C.

Let us now focus on one aspect which is independent of the precise discretization and evaluation of the collision kernels, which is having a nonzero p_{\min} and finite p_{\max} . This will have the effect that any observable (3.80) will have discretization

artifacts. For instance, even for a thermal distribution, the Debye mass m_D obtained from Eq. (3.11) for a nonzero p_{\min} is given by [7]

$$m_D^2(p_{\min}) = \frac{8\lambda}{(2\pi)^2} \int_{p_{\min}}^{\infty} dp p f_+(p) = \frac{2\lambda T \left(T \text{Li}_2 \left(e^{-\frac{p_{\min}}{T}} \right) - p_{\min} \log \left(1 - e^{-p_{\min}/T} \right) \right)}{\pi^2}. \quad (3.87)$$

Moreover, if we simulate an expanding system, all characteristic timescales will decrease; thus, discretization effects, and in particular $p_{\min} > 0$ effects, will have increased importance over time. This is demonstrated in Fig. 3.4, where the Debye mass obtained from Eq. (3.11) over its thermal value gT_c is plotted. At late times, the ratio deviates significantly from unity. The dotted lines are the p_{\min} corrected expression for the Debye mass (3.87), and agree very well with the results from the nonequilibrium simulation. This demonstrates that finite p_{\min} effects are the leading discretization effect for the Debye mass.

In Appendix C, we discuss in more detail the precise discretization used and how the collision terms are evaluated, including the coordinate system used for the integration in the elastic collision term.

4

MOMENTUM BROADENING OF JETS

The most straightforward aspect of jet-medium interactions to study is jet momentum broadening, in particular, characterized by the jet quenching parameter \hat{q} from Eq. (1.4). The physical picture is that of a highly energetic parton (e.g., a quark for a quark-jet) moving through the quark-gluon plasma and receiving (random) momentum kicks from the plasma constituents. This parameter is not only interesting on its own but is also used as input to calculate jet energy loss by medium-induced gluon emission in the harmonic approximation (see Eq. (1.3)). In this chapter, we address how the jet quenching parameter \hat{q} can be obtained in a nonequilibrium plasma of quarks and gluons. Results are presented for thermal equilibrium and simple (toy) models (scaled thermal distributions and effectively two-dimensional distributions). Finally, we conclude this chapter with the extraction of \hat{q} using QCD kinetic theory simulations of the initial stages in heavy-ion collisions and compare the extracted values with numerical simulations of the previous Glasma stage.

This chapter is based on Refs. [1, 2].

4.1 OBTAINING THE JET QUENCHING PARAMETER IN QCD KINETIC THEORY

4.1.1 *Relation of jet quenching parameter and scattering rate*

Let us consider an energetic parton with a large but finite momentum \mathbf{p} , which should be much larger than all other relevant momentum scales in the plasma. This plasma of quarks and gluons will be far from equilibrium during the initial stages in heavy-ion collisions, so we generalize the definition (1.4) to account for momentum broadening in different directions,

$$\hat{q}^{ij}(p) = \int d^3\mathbf{q} q^i q^j \frac{d\Gamma_{el}}{d^3\mathbf{q}}, \quad (4.1)$$

and, in particular, have also included the possibility of longitudinal momentum broadening, i.e., broadening along the direction of the propagation of the jet.

For the total transverse momentum broadening coefficient \hat{q} , we need to sum over the directions perpendicular to the jet direction. If we consider the jet to be moving in the x -direction, we obtain the usual jet quenching parameter

$$\hat{q} = \hat{q}^{yy} + \hat{q}^{zz}, \quad (4.2)$$

which measures the average transverse momentum transfer squared to the jet parton per unit time. Additionally, we can also consider longitudinal momentum broadening, i.e., momentum broadening in the direction of the jet,

$$\hat{q}_L = \hat{q}^{xx}. \quad (4.3)$$

Let us recall the expression for the elastic scattering rate, Eq. (3.59), which was derived in Section 3.4.4,

$$\begin{aligned} \Gamma_{\text{el}} = \frac{1}{4p\nu_a} \sum_{bcd} \int_{\mathbf{k}\mathbf{p}'\mathbf{k}'} (2\pi)^4 \delta^4(P + K - P' - K') \\ \times \left| \mathcal{M}_{cd}^{ab}(\mathbf{p}, \mathbf{k}; \mathbf{p}', \mathbf{k}') \right|^2 f_b(\mathbf{k}) [1 \pm f_d(\mathbf{k}')] [1 \pm f_c(\mathbf{p}')], \end{aligned} \quad (4.4)$$

and which we need as input for \hat{q} using Eq. (4.1). The sum is over all possible scattering processes. It describes the rate of a particle of species a with momentum \mathbf{p} being scattered out of its momentum state due to elastic collisions $p + k \rightarrow p' + k'$. The expression is completely symmetric under the exchange of the outgoing particles $\mathbf{p}' \leftrightarrow \mathbf{k}'$ and $c \leftrightarrow d$, as it should be. However, including $q^i q^j$ as in Eq. (4.1) breaks this symmetry. Effectively, we need to choose with respect to which outgoing particle we measure the transferred momentum. We choose here to define the harder outgoing particle to be the jet particle and label it c with momentum \mathbf{p}' , which is consistent with other studies, e.g., [20, 101, 102, 118]. In particular, this definition arises naturally if one thinks of \hat{q} as a diffusion coefficient (with small momentum transfer), and amounts to defining

$$\mathbf{q} = \mathbf{p}' - \mathbf{p}. \quad (4.5)$$

With this choice, we may relabel our momenta such that $p' > k'$, which leads to an additional factor of 2.¹ This will lead to more matrix elements than those from Table 3.1, since processes with the external outgoing particles switched are treated symmetrically there. For instance, $qg \leftrightarrow gq$ and $qg \leftrightarrow qg$ have the same matrix element in Ref. [19] while we need to explicitly distinguish them here. We will discuss this new complication in more detail and list the required matrix elements explicitly in Table 4.1 in Section 4.1.3.

We then arrive at

$$\begin{aligned} \hat{q}^{ij} = \frac{1}{2p\nu_a} \sum_{bcd} \int_{\substack{\mathbf{k}\mathbf{p}'\mathbf{k}' \\ p' > k'}} q^i q^j (2\pi)^4 \delta^4(P + K - P' - K') \\ \times \left| \mathcal{M}_{cd}^{ab}(\mathbf{p}, \mathbf{k}; \mathbf{p}', \mathbf{k}') \right|^2 f_b(\mathbf{k}) [1 \pm f_d(\mathbf{k}')] [1 \pm f_c(\mathbf{p}')]. \end{aligned} \quad (4.6)$$

Due to the requirement that $p' > k'$, if the jet energy p is large enough, we may set $f(\mathbf{p}') \rightarrow 0$.

¹ We use the identity

$$\int_{\mathbf{k}'\mathbf{p}'} g(k', p') = 2 \int_{\mathbf{k}'\mathbf{p}'} g(k', p') \Theta(p' - k'),$$

for symmetric functions $g(p', k') = g(k', p')$.

To simplify this integral, it is convenient to rewrite the integral measures in (4.6) to

$$\begin{aligned}\hat{q}^{ij} = & \frac{1}{2p\nu_a} \sum_{bcd} \int \frac{d^4K d^4P' d^4K'}{(2\pi)^5} q_\perp^i q_\perp^j \delta^{(4)}(P + K - P' - K') \left| \mathcal{M}_{cd}^{ab}(\mathbf{p}, \mathbf{k}; \mathbf{p}', \mathbf{k}') \right|^2 \\ & \times \delta(K^2) \delta(P'^2) \delta(K'^2) \Theta(K^0) \Theta(P'^0) \Theta(K'^0) f^b(\mathbf{k}) \left[1 \pm f^d(\mathbf{k}') \right] \Theta(p' - k').\end{aligned}\quad (4.7)$$

Using the delta function, we eliminate the K' integral. For convenience, we will keep writing K' or \mathbf{k}' as a short notation for $P + K - P'$ or $\mathbf{p} + \mathbf{k} - \mathbf{p}'$, respectively. Similarly to Ref. [206], and in accordance with our discussion on how to introduce \mathbf{q} (see Eq. (4.5)), we define $Q^\mu = (\omega, \mathbf{q})^\mu$ as

$$\begin{aligned}Q = P' - P & \Leftrightarrow \mathbf{q} = \mathbf{p}' - \mathbf{p} = \mathbf{k} - \mathbf{k}', \\ \omega = p' - p & = k - k'.\end{aligned}\quad (4.8)$$

Note that unlike the external momenta P, K, P' and K' , the transfer momentum Q is not necessarily light-like, i.e., $Q^2 = \mathbf{q}^2 - \omega^2 \geq 0$. Then we have $d^4K d^4P' = d^4K d^4Q$ and thus

$$\begin{aligned}\hat{q}^{ij} = & \frac{1}{2p\nu_a} \sum_{bcd} \int \frac{d^4K d^4Q}{(2\pi)^5} q^i q^j \left| \mathcal{M}_{cd}^{ab}(\mathbf{p}, \mathbf{k}; \mathbf{p}', \mathbf{k}') \right|^2 f^b(\mathbf{k}) \left[1 \pm f^d(\mathbf{k}') \right] \\ & \times \Theta(p' - k') \Theta(K^0) \Theta(P^0 + \omega) \Theta(K^0 - \omega) \delta(K^2) \delta((P + Q)^2) \delta((K - Q)^2).\end{aligned}\quad (4.9)$$

Using $P^2 = K^2 = 0$, $P \cdot Q = -p\omega + pq \cos \theta_{qp}$ and $K \cdot Q = -k\omega + kq \cos \theta_{qk}$, where θ_{qp} is the angle between \mathbf{p} and \mathbf{q} (and θ_{qk} between \mathbf{k} and \mathbf{q}), we can rewrite the last two delta functions as

$$\begin{aligned}\delta((P + Q)^2) \delta((K - Q)^2) & \\ = & \frac{1}{4pkq^2} \delta\left(\cos \theta_{qp} - \frac{\omega}{q} - \frac{\omega^2 - q^2}{2pq}\right) \delta\left(\cos \theta_{qk} - \frac{\omega}{q} + \frac{\omega^2 - q^2}{2kq}\right).\end{aligned}\quad (4.10)$$

This fixes the angles between \mathbf{q} and \mathbf{k} , and between \mathbf{q} and \mathbf{p} . Additionally, the integration region is restricted to

$$|\omega| < q, \quad p > \frac{q - \omega}{2}, \quad k > \frac{q + \omega}{2}. \quad (4.11)$$

Subsequently performing the K^0 integral yields

$$\begin{aligned}\hat{q}^{ij} = & \frac{1}{16p^2\nu_a} \sum_{bcd} \int \frac{d^3\mathbf{k} d^3\mathbf{q} d\omega}{(2\pi)^5 q^2 k^2} q^i q^j \left| \mathcal{M}_{cd}^{ab}(\mathbf{p}, \mathbf{k}; \mathbf{p}', \mathbf{k}') \right|^2 f^b(\mathbf{k}) \left[1 \pm f^d(\mathbf{k} - \mathbf{q}) \right] \\ & \times \Theta(p' - k') \Theta\left(p - \frac{q - \omega}{2}\right) \Theta\left(k - \frac{q + \omega}{2}\right) \Theta(q - |\omega|) \\ & \times \delta\left(\cos \theta_{qp} - \frac{\omega}{q} - \frac{\omega^2 - q^2}{2pq}\right) \delta\left(\cos \theta_{qk} - \frac{\omega}{q} + \frac{\omega^2 - q^2}{2kq}\right).\end{aligned}\quad (4.12)$$

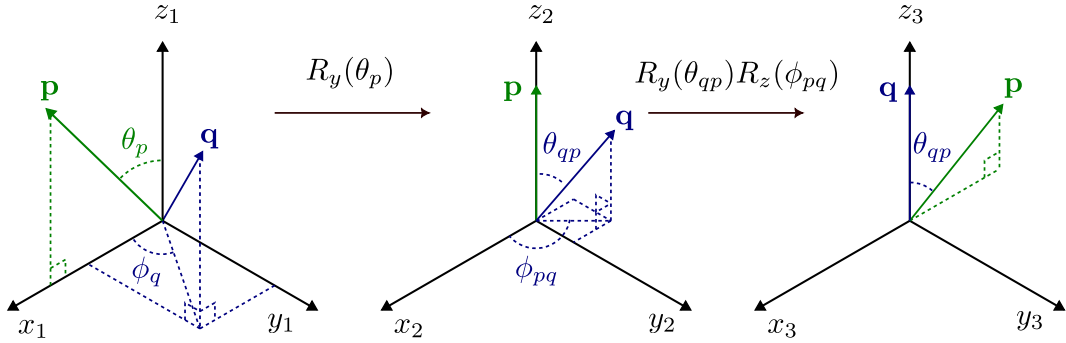


Figure 4.1: The integration frames. (Left:) ‘Lab frame’. The jet momentum \mathbf{p} lies in the $x - z$ plane. (Center:) ‘ p -frame’, obtained by rotating the ‘lab frame’ around the y -axis, such that \mathbf{p} points in the z direction. (Right:) ‘ q -frame’. Here, \mathbf{q} points in the z direction and \mathbf{p} lies in the $x - z$ plane. Figure from [2].

4.1.2 Coordinate systems

We will now discuss how the integration variables and coordinate systems are chosen to perform this integral. We use a different choice here than when evaluating the elastic collision term in the kinetic theory simulations (see Appendix B.3). In particular, since $f(\mathbf{p})$ is stored on a grid in a specific coordinate system (let us call it *lab frame*), we need to establish how the vectors \mathbf{k} and \mathbf{k}' in the lab frame depend on the integration variables. In the *lab frame*, we denote the vectors with lower index 1,

$$\mathbf{p}_1 = p(\sin \theta_p, 0, \cos \theta_p), \quad (4.13a)$$

$$\mathbf{q}_1 = q(\sin \theta_q \cos \phi_q, \sin \theta_q \sin \phi_q, \cos \theta_q), \quad (4.13b)$$

$$\mathbf{k}_1 = k(\sin \theta_k \cos \phi_k, \sin \theta_k \sin \phi_k, \cos \theta_k). \quad (4.13c)$$

In accordance with the discussion in Section 3.6.1, we assume azimuthal symmetry around the z -axis, so we can always rotate this frame such that \mathbf{p} lies in the $x - z$ plane (effectively having the jet go into the x direction). For choosing the integration frames, we follow Ref. [206] and use the jet momentum \mathbf{p} as a distinct direction. In this second frame (*p-frame*), denoted by a subscript 2, in which \mathbf{p} points in the z direction and that is obtained via a rotation of the *lab frame* around the y -axis (see Fig. 4.1),

$$\mathbf{p}_2 = p(0, 0, 1), \quad (4.14a)$$

$$\mathbf{q}_2 = q(\sin \theta_{qp} \cos \phi_{pq}, \sin \theta_{qp} \sin \phi_{pq}, \cos \theta_{qp}), \quad (4.14b)$$

$$\mathbf{k}_2 = k(\sin \theta_{pk} \cos \phi_{pk}, \sin \theta_{pk} \sin \phi_{pk}, \cos \theta_{pk}). \quad (4.14c)$$

Here, we perform the integral over \mathbf{q} .

The \mathbf{k} integral is then performed in a third frame, in which \mathbf{q} points in the z direction and \mathbf{p} lies in the $x - z$ plane. We call this the *q-frame* and denote it by a subscript 3:

$$\mathbf{p}_3 = p(\sin \theta_{qp}, 0, \cos \theta_{qp}), \quad (4.15a)$$

$$\mathbf{q}_3 = q(0, 0, 1), \quad (4.15b)$$

$$\mathbf{k}_3 = k(\sin \theta_{qk} \cos \phi_{qk}, \sin \theta_{qk} \sin \phi_{qk}, \cos \theta_{qk}). \quad (4.15c)$$

The components of the vectors transform between the frames according to the matrix relations

$$\mathbf{v}_2 = A \mathbf{v}_1, \quad A = R_y(\theta_p), \quad (4.16a)$$

$$\mathbf{v}_3 = B \mathbf{v}_2, \quad B = R_y(\theta_{qp}) R_z(\phi_{pq}), \quad (4.16b)$$

where $R_y(\alpha)$ and $R_z(\alpha)$ denote the matrices corresponding to a rotation with angle α around the y - and z -axis, respectively. The transformation matrices read

$$A = \begin{pmatrix} \cos \theta_p & 0 & -\sin \theta_p \\ 0 & 1 & 0 \\ \sin \theta_p & 0 & \cos \theta_p \end{pmatrix}, \quad (4.17a)$$

$$B = \begin{pmatrix} \cos \theta_{qp} \cos \phi_{pq} & \cos \theta_{qp} \sin \phi_{pq} & -\sin \theta_{qp} \\ -\sin \phi_{pq} & \cos \phi_{pq} & 0 \\ \cos \phi_{pq} \sin \theta_{qp} & \sin \theta_{qp} \sin \phi_{pq} & \cos \theta_{qp} \end{pmatrix}. \quad (4.17b)$$

For the calculation of \hat{q}^{ij} we use the components q_\perp^i of \mathbf{q} in the p -frame,

$$q^1 = (\mathbf{q}_2)^1 = q \sin \theta_{qp} \cos \phi_{pq}, \quad (4.18a)$$

$$q^2 = (\mathbf{q}_2)^2 = q \sin \theta_{qp} \sin \phi_{pq}, \quad (4.18b)$$

$$q^3 = (\mathbf{q}_2)^3 = q \cos \theta_{qp}. \quad (4.18c)$$

In this way, the components 1 and 2 are perpendicular to \mathbf{p} and quantify the momentum broadening transverse to the jet.

Having taken the Dirac delta functions in Eq. (4.6) into account, we choose ϕ_{pq} , ϕ_{qk} , k , ω , and q as independent integration variables. Therefore, we need to express all other quantities in terms of them. All other angles are then fixed. For example, the on-shell conditions $|\mathbf{k}'|^2 = |\mathbf{k} - \mathbf{q}|^2 = (k - \omega)^2$ and $|\mathbf{k}' + \mathbf{q}|^2 = (k' + \omega)^2$ lead to

$$\cos \theta_{qk} = \frac{\omega}{q} - \frac{\omega^2 - q^2}{2kq}, \quad (4.19a)$$

$$\cos \theta_{qp} = \frac{\omega}{q} + \frac{\omega^2 - q^2}{2pq}, \quad (4.19b)$$

$$\cos \theta_{k'q} = \frac{\omega}{q} + \frac{\omega^2 - q^2}{2k'q}. \quad (4.19c)$$

Next, we discuss how to express the angles θ_k and $\theta_{k'}$ in terms of the integration variables needed for evaluating the distribution functions $f(\mathbf{k})$ and $f(\mathbf{k}')$ in (4.6) in the lab frame. From Eqs. (4.16a) and (4.16b), we obtain $\mathbf{k}_1 = A^T B^T \mathbf{k}_3$. From $(\mathbf{k}_1)_z$ we can read off

$$\cos \theta_k = \sin \phi_{qk} \sin \phi_{pq} \sin \theta_{qk} \sin \theta_p \quad (4.20a)$$

$$- \cos \phi_{qk} \sin \theta_{qk} (\cos \phi_{pq} \cos \theta_{qp} \sin \theta_p + \cos \theta_p \sin \theta_{qp}) \\ + \cos \theta_{qk} (\cos \theta_p \cos \theta_{qp} - \cos \phi_{pq} \sin \theta_p \sin \theta_{qp}),$$

and a similar expression holds for $\cos \theta_{k'}$,

$$\cos \theta_{k'} = \sin \phi_{qk} \sin \phi_{pq} \sin \theta_{qk'} \sin \theta_p \quad (4.20b)$$

$$- \cos \phi_{qk} \sin \theta_{qk'} (\cos \phi_{pq} \cos \theta_{qp} \sin \theta_p + \cos \theta_p \sin \theta_{qp}) \\ + \cos \theta_{qk'} (\cos \theta_p \cos \theta_{qp} - \cos \phi_{pq} \sin \theta_p \sin \theta_{qp}).$$

The azimuthal angle is $\phi_{qk'} = \phi_{qk}$ because $\mathbf{k}' = \mathbf{k} - \mathbf{q}$ and \mathbf{q} points in the z direction in the q -frame.

4.1.3 Formula for the jet quenching parameter for finite jet energy

We are now ready to give the formula for the components of \hat{q} ,

$$\begin{aligned} \hat{q}^{ij} &= \frac{1}{2^9 \pi^5 \nu_a} \sum_{bcd} \int_0^{2\pi} d\phi_{pq} \int_0^{2\pi} d\phi_{qk} \int_0^\infty dq \int_{\max(-q, q-2p, \frac{q-2p}{3})}^q d\omega \int_{\frac{q+\omega}{2}}^{p+2\omega} dk \\ &\times q^i q^j \frac{|\mathcal{M}_{cd}^{ab}|^2}{p^2} f_b(\mathbf{k}) (1 \pm f_d(\mathbf{k}')). \end{aligned} \quad (4.21)$$

Recall that $\nu_a = 2d_R$, where d_R is the dimension of the representation of the jet particle. The upper sign in Eq. (4.21) is to be used when the d particle is a boson (gluon), and the lower sign if it is a fermion (quark), see Eq. (3.4). The components q^i of Eq. (4.21) in the p -frame read

$$q^1 = q \sin \theta_{qp} \cos \phi_{pq}, \quad (4.22a)$$

$$q^2 = q \sin \theta_{qp} \sin \phi_{pq}, \quad (4.22b)$$

$$q^3 = q \cos \theta_{qp}. \quad (4.22c)$$

Although we started with the collision term (3.15) with the same matrix elements, our choice $p' > k'$ breaks the symmetry of exchanging the outgoing particles, $(abcd) \leftrightarrow (abdc)$ (see (3.19)). This implies that we have to distinguish between, for example, ' $q_1 g \leftrightarrow q_1 g'$ ' and ' $q_1 g \leftrightarrow g q_1'$ ', and thus require more matrix elements. Recall that they are conveniently given in terms of the Lorentz-invariant Mandelstam variables s , t , and u (see Eq. (3.17)), which are defined with respect to the momenta corresponding to the particles with labels a, b, c, d ,

$$s = -(P + K)^2, \quad t = -(P' - P)^2, \quad u = -(K' - P)^2. \quad (4.23)$$

The additional matrix elements resulting from the reduced symmetry can be obtained from Table 3.1 by relabeling $p' \leftrightarrow k'$ and $c \leftrightarrow d$, effectively switching

$$s \rightarrow s, \quad t \rightarrow u, \quad u \rightarrow t. \quad (4.24)$$

These resulting matrix elements are still symmetric under $(abcd) \leftrightarrow (badc)$ and are listed in Tab. 4.1. In the underlined terms, medium effects have to be included, as we will discuss in Section 4.1.5.

The Mandelstam variables are given explicitly by

$$t = \omega^2 - q^2, \quad (4.25)$$

$$s = -\frac{t}{2q^2} \left((p + p')(k + k') + q^2 - \sqrt{(4pp' + t)(4k'k + t)} \cos \phi_{qk} \right), \quad (4.26)$$

$$u = \frac{t}{2q^2} \left((p + p')(k + k') - q^2 - \sqrt{(4pp' + t)(4k'k + t)} \cos \phi_{qk} \right), \quad (4.27)$$

with $p' = p + \omega$ and $k' = k - \omega$. The expressions for s and u as in Eqs. (4.26) and (4.27) can also be found in [206] and are similar to those used in the elastic collision

$ab \leftrightarrow cd$	$ \mathcal{M}_{cd}^{ab} ^2 / g^4$
$q_1 q_2 \leftrightarrow q_1 q_2,$	
$q_1 \bar{q}_2 \leftrightarrow q_1 \bar{q}_2,$	
$\bar{q}_1 q_2 \leftrightarrow \bar{q}_1 q_2,$	$8 \frac{d_F^2 C_F^2}{d_A} \left(\frac{s^2+u^2}{\underline{t}^2} \right)$
$\bar{q}_1 \bar{q}_2 \leftrightarrow \bar{q}_1 \bar{q}_2$	
$q_1 q_2 \leftrightarrow q_2 q_1,$	
$q_1 \bar{q}_2 \leftrightarrow \bar{q}_2 q_1,$	$8 \frac{d_F^2 C_F^2}{d_A} \left(\frac{s^2+t^2}{u^2} \right)$
$\bar{q}_1 q_2 \leftrightarrow q_2 \bar{q}_1,$	
$\bar{q}_1 \bar{q}_2 \leftrightarrow \bar{q}_2 \bar{q}_1$	
$q_1 q_1 \leftrightarrow q_1 q_1,$	$8 \frac{d_F^2 C_F^2}{d_A} \left(\frac{s^2+u^2}{\underline{t}^2} + \frac{s^2+t^2}{u^2} \right) + 16 d_F C_F \left(C_F - \frac{C_A}{2} \right) \frac{s^2}{tu}$
$\bar{q}_1 \bar{q}_1 \leftrightarrow \bar{q}_1 \bar{q}_1$	
$q_1 \bar{q}_1 \leftrightarrow q_1 \bar{q}_1$	$8 \frac{d_F^2 C_F^2}{d_A} \left(\frac{s^2+u^2}{\underline{t}^2} + \frac{t^2+u^2}{s^2} \right) + 16 d_F C_F \left(C_F - \frac{C_A}{2} \right) \frac{u^2}{st}$
$q_1 \bar{q}_1 \leftrightarrow \bar{q}_1 q_1$	$8 \frac{d_F^2 C_F^2}{d_A} \left(\frac{s^2+t^2}{u^2} + \frac{u^2+t^2}{s^2} \right) + 16 d_F C_F \left(C_F - \frac{C_A}{2} \right) \frac{t^2}{su}$
$q_1 \bar{q}_1 \leftrightarrow q_2 \bar{q}_2,$	$8 \frac{d_F^2 C_F^2}{d_A} \left(\frac{t^2+u^2}{s^2} \right)$
$q_1 \bar{q}_1 \leftrightarrow \bar{q}_2 q_2$	
$q_1 \bar{q}_1 \leftrightarrow gg$	$8 d_F C_F^2 \left(\frac{u}{\underline{t}} + \frac{t}{u} \right) - 8 d_F C_F C_A \left(\frac{t^2+u^2}{s^2} \right)$
$q_1 g \leftrightarrow q_1 g,$	
$\bar{q}_1 g \leftrightarrow \bar{q}_1 g$	$-8 d_F C_F^2 \left(\frac{u}{s} + \frac{s}{u} \right) + 8 d_F C_F C_A \left(\frac{s^2+u^2}{\underline{t}^2} \right)$
$q_1 g \leftrightarrow g q_1,$	$-8 d_F C_F^2 \left(\frac{t}{s} + \frac{s}{\underline{t}} \right) + 8 d_F C_F C_A \left(\frac{s^2+t^2}{u^2} \right)$
$\bar{q}_1 g \leftrightarrow g \bar{q}_1$	
$gg \leftrightarrow gg$	$16 d_A C_A^2 \left(3 - \frac{su}{\underline{t}^2} - \frac{st}{u^2} - \frac{tu}{s^2} \right)$

Table 4.1: Matrix elements for the jet quenching parameter \hat{q} , obtained from the matrix elements from Table 3.1 by breaking the symmetry of exchanging outgoing particles. They are obtained by replacing $c \leftrightarrow d$ and $t \leftrightarrow u$. Singly-underlined denominators indicate infrared-sensitive contributions from soft gluon exchange and double-underlined denominators from soft fermion exchange. The group constants are given in Eq. (A.7). Table taken from [2].

terms, Eqs. (B.15) and (B.16) (they only differ in the argument of the cosine). Note that we defined the components \hat{q}^{ij} with respect to the jet direction. If the jet moves perpendicular to the beam-axis z in the x -direction as in Fig. 1.2, then $\cos \theta_p = 0$, and $\hat{q}^{yy} = \hat{q}^{22}$ is the momentum broadening in the y direction and $\hat{q}^{zz} = \hat{q}^{11}$ is the momentum broadening in the beam direction, which sum to the usual $\hat{q} = \hat{q}^{11} + \hat{q}^{22}$. Longitudinal momentum broadening can be obtained from $\hat{q}_L = \hat{q}^{33}$. If we replace $\hat{q}^i \hat{q}^j$ by ω in (4.21), we obtain elastic (collisional) energy loss.

4.1.4 Symmetries of \hat{q}^{ij}

Let us now discuss the symmetries of the matrix \hat{q}^{ij} . For a *spherically* symmetric distribution function $f(\mathbf{k}) = f(|\mathbf{k}|)$, it is easy to see that

$$\hat{q}^{12} = \hat{q}^{13} = \hat{q}^{23} = 0, \quad \hat{q}^{11} = \hat{q}^{22}. \quad (4.28)$$

For a phase space density that is *azimuthally* symmetric around the z -axis (beam direction), i.e., $f(k, \cos \theta_k)$, we also find that

$$\hat{q}^{12} = \hat{q}^{23} = 0. \quad (4.29)$$

For a jet moving in the x or beam direction, we additionally find

$$\hat{q}^{13} = 0, \quad \text{if } \cos \theta_p = 0 \text{ or } \cos \theta_p = 1. \quad (4.30)$$

The fact that $\hat{q}^{12} = \hat{q}^{23} = 0$ can be seen by rewriting the angular integrals $\int_0^{2\pi} d\phi_{pq} \int_0^{2\pi} d\phi_{qk} g(\phi_{pq}, \phi_{qk}) = \int_{-\pi}^{\pi} d\phi_{pq} \int_{-\pi}^{\pi} d\phi_{qk} g(\phi_{pq}, \phi_{qk})$ and then splitting the ϕ_{pq} integral into the integral from $(-\pi, 0)$ and $(0, \pi)$ to arrive at

$$\int_0^{2\pi} d\phi_{pq} \int_0^{2\pi} d\phi_{qk} g(\phi_{pq}, \phi_{qk}) = \int_0^{\pi} d\phi_{pq} \int_{-\pi}^{\pi} d\phi_{qk} [g(-\phi_{pq}, -\phi_{qk}) + g(\phi_{pq}, \phi_{qk})]$$

The angles θ_k and $\theta_{k'}$ depend on the angles ϕ_{qk} and ϕ_{pq} , but are not changed by simultaneously replacing $\phi_{qk} \rightarrow -\phi_{qk}$ and $\phi_{pq} \rightarrow -\phi_{pq}$. In the matrix element, ϕ_{qk} appears in s and u in the cosine argument, which is an even function. The only change happens in $q_2 \rightarrow -q_2$ in (4.22b), which results in $\hat{q}^{12} = \hat{q}^{23} = 0$.

To show that $\hat{q}^{13} = 0$ for $v_p = 0$, we consider the phase shift $\phi_{pq} \rightarrow \phi_{pq} + \pi$ which, for $\cos \theta_p = 0$, changes $\cos \theta_k \rightarrow -\cos \theta_k$. In our assumption (3.72), the distribution function is symmetric around the $z = 0$ plane, thus $f(k, -\cos \theta_k) = f(k, \cos \theta_k)$ and thus this only results in $q^1 \rightarrow -q^1$. Thus we obtain $\hat{q}^{13} = 0$.

4.1.5 Medium screening effects

In Section 3.3.2, we have already discussed how medium effects enter the kinetic theory description of QCD by effectively screening soft-momentum transfer in the matrix elements.

Similarly, also for the jet quenching parameter \hat{q} screening becomes important when the Mandelstam variable t becomes small $s \gg t \sim \mathcal{O}(m_D^2)$. This concerns the underlined terms with inverse powers of t in the matrix elements listed in Tab. 4.1. Because we enforced $p' > k'$, we could only have $|u| \ll s$ when $k \gg p$, which is

highly suppressed by the fact that we are choosing p to be hard and k to be a medium particle. Thus, unlike for the elastic collision term (3.15), we only need to implement screening effects in terms with t in the denominator.

Similar as in Section 3.3.2, we include medium modifications by replacing the singly underlined terms in the matrix elements in Tab. 4.1 by

$$M_0 = \frac{(s-u)^2}{t^2} \rightarrow |G_R(P-P')_{\mu\nu}(P+P')^{\mu}(K+K')^{\nu}|^2 \equiv M_{\text{screen}}, \quad (4.31)$$

where G_R denotes the retarded gluon propagator in the HTL approximation. Recall that the retarded propagator is needed because we started from the decay rate (3.59), which includes the fully retarded amplitudes via the cutting rule (3.51), thus the internal lines must be retarded propagators.

Furthermore, we will employ two different approximations, neglecting plasma instabilities as in the elastic collision kernel: First, we will use the isotropic hard thermal loop resummed gluon propagator, which we will refer to as *isoHTL* screening. In a second step, we further approximate and use the simple Debye-like screening prescription already introduced before (see 3.3.2), but we will find that a different screening parameter ξ_g^{\perp} is needed to account for the correct treatment of transverse momentum broadening.

In any case, the singly underlined terms in Tab. 4.1 can be rewritten in terms of the unscreened (vacuum) expression M_0 using Eq.(3.18),

$$\frac{s^2+u^2}{t^2} = \frac{1}{2} + \frac{1}{2}M_0, \quad \frac{su}{t^2} = \frac{1}{4} - \frac{1}{4}M_0. \quad (4.32)$$

Using the full isotropic HTL propagator (see Appendix A.5.2 for details), the screened matrix element reads explicitly

$$\mathcal{M}_{\text{HTL}} = \frac{c_1^2}{A^2+B^2} + \frac{c_2^2}{C^2+D^2} - \frac{2c_1c_2(AC+BD)}{(A^2+B^2)(C^2+D^2)}, \quad (4.33)$$

where A, B, C, D are obtained from the real and imaginary parts of the retarded HTL self-energies and are explicitly given by

$$A = q^2 + m_D^2 \left(1 + \frac{\omega}{2q} \ln \frac{q-\omega}{q+\omega} \right), \quad B = -\frac{m_D^2 \omega}{2q} \pi, \quad (4.34a)$$

$$C = q^2 - \omega^2 + \frac{m_D^2}{2} \left(\frac{\omega^2}{q^2} + \left(\frac{\omega^2}{q^2} - 1 \right) \frac{\omega}{2q} \ln \frac{q-\omega}{q+\omega} \right), \quad D = \frac{\pi m_D^2 \omega}{4q} \left(1 - \frac{\omega^2}{q^2} \right), \quad (4.34b)$$

and

$$c_1 = (2p+\omega)(2k-\omega), \quad c_2 = 4pk \sin \theta_{qp} \sin \theta_{qk} \cos \phi_{qk}. \quad (4.35a)$$

Note that for isotropic distributions, the last term in Eq. (4.33) can be dropped since it is proportional to $\cos \phi_{qk}$ and will thus vanish in the angular integral needed for \hat{q} .

The doubly underlined terms in Tab. 4.1 correspond to soft fermionic exchange. Here, we do not need to consider them explicitly because, as we will discuss in Section 4.1.6, they are subleading in $1/p$.

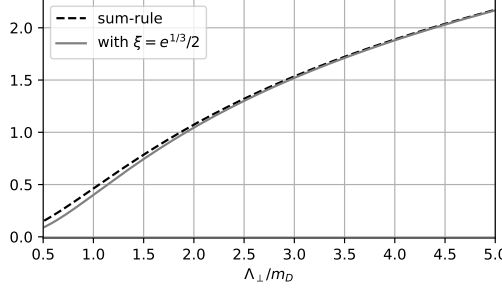


Figure 4.2: Shown are the HTL sum rule result on the left-hand side of Eq. (4.38) as a dashed curve and the values from the approximated expression on its right-hand side with the parameter ξ given by (4.39) as a continuous line. The plot shows that for $\Lambda_\perp \gtrsim 4m_D$ the screening approximation of the full HTL matrix element provides accurate results. Figure taken from [2].

Next, we will consider the Debye-like screening prescription already mentioned in Section 3.3.2,

$$\mathcal{M}_{\text{HTL}} \rightarrow M_\xi = \frac{(s-u)^2}{t^2} \frac{q^4}{(q^2 + (\xi_g^\perp)^2 m_D^2)^2}. \quad (4.36)$$

As explained in Section 3.3.2, this replacement can be justified when we are not directly interested in the matrix element but in the (weighted) integral over it, as in computations of \hat{q} or $\mathcal{C}^{2\leftrightarrow 2}$. The Debye-like screened matrix element M_ξ agrees with \mathcal{M}_{HTL} at large q , but behaves differently in the small q region. It includes a constant ξ_g^\perp that is fixed such that the integral over the Debye-like screened matrix element matches the result of the full isotropic HTL matrix element. For transverse momentum broadening, this integral needs to be taken in the high energy limit $p \rightarrow \infty$, be weighted with q_\perp^2 and integrated over $d^2 q_\perp$ to obtain \hat{q} . Thus, similarly as fixing ξ_g in the elastic collision kernel using Eq. (3.31), we fix ξ_g^\perp by requiring that

$$\int_0^\infty d q_\perp q_\perp^3 \int_{-\infty}^\infty \frac{d\omega}{\sqrt{q_\perp^2 + \omega^2}} \int_0^{2\pi} d\phi_{qk} (\mathcal{M}_{\text{HTL}} - M_\xi) = 0. \quad (4.37)$$

This matching is different than in the case needed for the time evolution (see Section 3.3.2), where one is matching the longitudinal momentum transfer rather than the transverse one (replace $q_\perp^3 \rightarrow \omega^2 q_\perp$ in (4.37)), which leads to a different value $\xi_g \neq \xi_g^\perp$.

In the case considered here, we take both matrix elements in the limit $p \rightarrow \infty$, and additionally consider the soft limit $\omega \ll k$, $q_\perp \ll k$. We then first integrate over ω . For \mathcal{M}_{HTL} this can, in the soft limit, be done analytically using a sum rule [100], which is discussed in more detail in Appendix A.5.4. Then, the q_\perp integral is performed up to a cutoff Λ_\perp to obtain the following condition

$$\begin{aligned} & \frac{2}{3} \ln \left(1 + \frac{\Lambda_\perp^2}{m_D^2} \right) \\ &= 4 \ln \frac{\Lambda_\perp}{2 \xi_g^\perp m_D} - \frac{\Lambda_\perp^2}{(\xi_g^\perp m_D)^2} - \frac{(\Lambda_\perp^4 + 2\Lambda_\perp^2(\xi_g^\perp m_D)^2 + 4(\xi_g^\perp m_D)^4) \ln \frac{\Lambda_\perp}{\xi_g^\perp m_D + \sqrt{\Lambda_\perp^2 + (\xi_g^\perp m_D)^2}}}{(\xi_g^\perp m_D)^3 \sqrt{\Lambda_\perp^2 + (\xi_g^\perp m_D)^2}} \end{aligned} \quad (4.38)$$

where the left-hand side stems from \mathcal{M}_{HTL} . Expanding both sides of the equation for large cutoff $\Lambda_\perp \gg \xi m_D$ leads to

$$\xi_g^\perp = \frac{e^{1/3}}{2} = 0.6978 \dots \quad (4.39)$$

In Fig. 4.2 we demonstrate the agreement of both sides of Eq. (4.38) as a function of the cutoff Λ_\perp . For large momentum cutoffs $\Lambda_\perp \gtrsim 4m_D$, the approximation seems to work very well. We note that the value ξ_g^\perp in Eq. (4.39) entering the matrix element in \hat{q} is slightly different from the one typically used obtained in section 3.3.2 for the elastic collision kernel $\mathcal{C}^{2\leftrightarrow 2}$, ξ_g .

This approximation will be investigated in Section 4.2.2 numerically by comparison with the HTL-screened results. There, it is found that the largest differences occur for a small cutoff Λ_\perp or a large coupling λ . For physically motivated values $\lambda = 10$ and $\Lambda_\perp = T$, the screening prescriptions differ by 30%, showing that the choice of the screening prescription can be important for the evaluation of the jet quenching parameter \hat{q} .

4.1.6 Towards the limit $p \rightarrow \infty$: NLO terms in $1/p$

In the derivation of \hat{q} , we have considered the jet momentum p to be much larger than all other momentum scales of the plasma. However, in the strict limit $p \rightarrow \infty$ the momentum diffusion coefficient \hat{q} exhibits a logarithmic divergence, unless the exchanged momentum is limited by a cutoff. We will first, in this subsection, discuss the limit of p being large, but not infinite. Then, in Section 4.1.7, we will introduce a cutoff on q_\perp and take $p \rightarrow \infty$. In the limit of large p , only the terms su/t^2 and $(s^2 + u^2)/t^2$ in the matrix elements (Tab. 4.1) are $\sim p^2$ and thus contribute.

For example, let us consider the screened gluonic matrix element,

$$\frac{|\mathcal{M}_{gg}^{gg}|^2}{p^2} = 16d_A C_A^2 \frac{\left(2k - \omega - \sqrt{(2k - \omega)^2 - q^2} \cos \phi_{qk}\right)^2}{(q^2 + (\xi_g^\perp)^2 m_D^2)^2} \left(1 + \frac{\omega}{p} + \mathcal{O}\left(\frac{1}{p^2}\right)\right). \quad (4.40)$$

Here, k is a medium momentum scale (the collision integral is proportional to $f(\mathbf{k})$) and we can thus assume that $k \ll p$ even if formally k is integrated up to infinity. Naïvely, one might assume that $\frac{\omega}{p} = \mathcal{O}\left(\frac{1}{p}\right)$. However, p appears in the boundaries of ω , ($p > (q - \omega)/2$, see (4.11)), and, therefore, we need to carefully consider the term ω/p . For positive ω we obtain $\omega < k \ll p$, such that it indeed becomes negligible. However, for negative ω ,

$$\left|\frac{\omega}{p}\right| = \frac{-\omega}{p} < \frac{p - k}{2p} = \frac{1}{2} - \frac{k}{2p}, \quad (4.41)$$

which does not vanish for $p \rightarrow \infty$. A more careful calculation (carried out explicitly in Appendix C.2.2) shows that the leading large p contribution in Eq. (4.40) diverges logarithmically $\sim \ln p$, whereas the $\mathcal{O}(\omega/p)$ contribution becomes constant in p . Thus, indeed, the leading behavior is obtained by considering the $p \gg \omega$ term(s) in the matrix element.

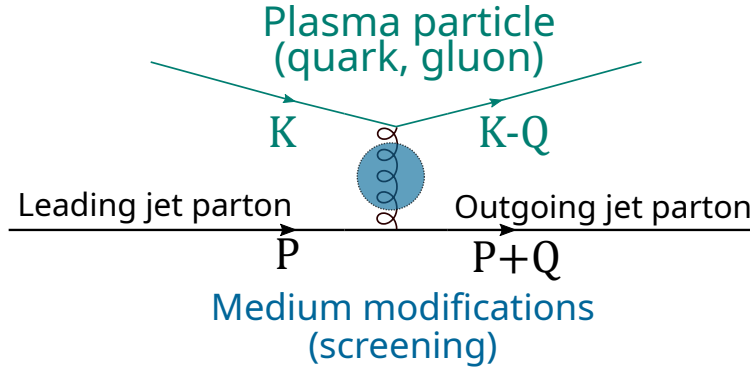


Figure 4.3: Feynman diagram for a t -channel gluon exchange process that dominates the matrix element for the jet quenching parameter \hat{q} in the high-energy limit $p \rightarrow \infty$. In the internal gluon propagator, medium effects should be included as explained in Section 4.1.5. Figure reused from [2].

To summarize, for large jet energies $E_{\text{jet}} = p$, the jet quenching parameter is given by

$$\hat{q}(p \gg T_\epsilon) \simeq a_p \ln p + b_p, \quad (4.42)$$

where b_p is a (yet undetermined) coefficient depending on the precise form of the integrand. Here, T_ϵ is the characteristic momentum scale of plasma particles, e.g., the temperature in thermal equilibrium. The coefficient a_p for isotropic distributions is derived explicitly in Appendix C.2.2 as

$$a_p/C_R = \frac{C_A g^4}{4\pi^3} \int_0^\infty dk k^2 f_g(k) + \sum_f \frac{g^4}{8\pi^3} \int_0^\infty dk k^2 f_f(k), \quad (4.43)$$

where f_g is the gluon distribution function and the subscript f in f_f labels different quark species.

4.1.7 Limit $p \rightarrow \infty$ with a momentum cutoff

We now introduce a cutoff Λ_\perp to restrict the maximum amount of transverse momentum transfer in the scattering,

$$q_\perp^2 = q^2 - \omega^2 < \Lambda_\perp^2. \quad (4.44)$$

It is now possible to directly take the limit $p \rightarrow \infty$ in the matrix element without any potential divergences (as is shown in Appendix C.2.2), which considerably simplifies the calculation. In this limit, there is also a reduced number of matrix elements, which are given explicitly in Tab. 4.2. Only t -channel gluon exchange diagrams contribute, as depicted in Fig. 4.3. Apart from that, a few changes need to be made to the formula of \hat{q} presented in Section 4.1.3. In Eq. (4.21), we need

$ab \leftrightarrow cd$	$\lim_{p \rightarrow \infty} \mathcal{M}_{cd}^{ab} ^2 / (p^2 g^4)$
$q_1 q_i \leftrightarrow q_1 q_i,$ $\bar{q}_1 q_i \leftrightarrow \bar{q}_1 q_i,$ $q_1 \bar{q}_i \leftrightarrow q_1 \bar{q}_i,$ $\bar{q}_1 \bar{q}_i \leftrightarrow \bar{q}_1 \bar{q}_i$	$4 \frac{d_F^2 C_F^2}{d_A} \tilde{M}_{\text{screen}}$
$q_1 g \leftrightarrow q_1 g,$ $\bar{q}_1 g \leftrightarrow \bar{q}_1 g$	$4 d_F C_F C_A \tilde{M}_{\text{screen}}$
$g g \leftrightarrow g g$	$4 d_A C_A^2 \tilde{M}_{\text{screen}}$

Table 4.2: The matrix elements for \hat{q} as in Tab. 4.1 in the limit $p \rightarrow \infty$. Here $\tilde{M}_{\text{screen}} = \lim_{p \rightarrow \infty} M_{\text{screen}} / p^2$ denotes the appropriate screening terms \tilde{M}_{HTL} or \tilde{M}_{ξ} as explained in Section 4.1.5 and Appendix A.5.2, and quark flavors are labeled by the index i . Table taken from [2].

to change the integration limits to account for the transverse momentum cutoff condition (4.44),

$$\begin{aligned} \hat{q}^{ij} = & \frac{1}{2^9 \pi^5 \nu_a} \sum_{bcd} \int_0^{2\pi} d\phi_{pq} \int_0^{2\pi} d\phi_{qk} \\ & \times \left(\int_0^{\Lambda_1} dq \int_{-q}^q d\omega + \int_{\Lambda_1}^{\infty} dq \left[\int_{-q}^{-\sqrt{q^2 - \Lambda_1^2}} d\omega + \int_{\sqrt{q^2 - \Lambda_1^2}}^q d\omega \right] \right) \quad (4.45) \\ & \times \int_{\frac{q+\omega}{2}}^{\infty} dk q^i q^j \lim_{p \rightarrow \infty} \frac{|\mathcal{M}_{cd}^{ab}|^2}{p^2} f_b(\mathbf{k}) (1 \pm f_d(\mathbf{k}')) . \end{aligned}$$

As before, the upper and lower signs in the term $(1 \pm f_d)$ denote bosonic particles (gluons) and fermionic particles (quarks), respectively, see Eq. (3.4).

In this limit, one needs to replace (4.19b) by $\cos \theta_{qp} = \omega/q$ (see Appendix D) and the few nonvanishing matrix elements for $\lim_{p \rightarrow \infty} \frac{|\mathcal{M}|^2}{p^2}$ are tabulated in Tab. 4.2. In that limit, we do not need the explicit expressions (4.26) and (4.27) for s, u in terms of our phase space integration variables. From the matrix elements in Tab. 4.2 and (4.21), one naturally finds Casimir scaling

$$\frac{\hat{q}^{\text{gluon}}}{C_A} = \frac{\hat{q}^{\text{quark}}}{C_F}, \quad (4.46)$$

i.e., the jet quenching parameter for a quark and gluon jet are equivalent up to color factors.

The screened matrix element $\tilde{M}_{\text{screen}}$ in Tab. 4.2 is implemented as detailed in Section 4.1.5. In the $p \rightarrow \infty$ limit, the isotropic HTL matrix element from Eq. (4.33) becomes

$$\tilde{M}_{\text{HTL}} = \frac{\tilde{c}_1^2}{A^2 + B^2} - \frac{\tilde{c}_2^2}{C^2 + D^2} + \frac{2\tilde{c}_1\tilde{c}_2(AC + BD)}{(A^2 + B^2)(C^2 + D^2)}, \quad (4.47)$$

with the parameters A , B , C , and D given by (4.34) and

$$\tilde{c}_1 = \lim_{p \rightarrow \infty} \frac{c_1}{p} = 2(2k - \omega), \quad (4.48a)$$

$$\tilde{c}_2 = \lim_{p \rightarrow \infty} \frac{c_2}{p} = 4k \sin \theta_{qp} \sin \theta_{qk} \cos \phi_{qk}. \quad (4.48b)$$

Again, for isotropic systems, we do not need to include the last term in (4.47), since it vanishes in the angular integral when calculating \hat{q}^{ij} .

For the *Debye-like* screening approximation, we obtain (c.f. (4.36))

$$\tilde{M}_\xi = 4 \frac{(2k - \omega - \sqrt{(2k - \omega)^2 - q^2} \cos \phi_{qk})^2}{(q^2 + (\xi_g^\perp)^2 m_D^2)^2}, \quad (4.49)$$

with $\xi_g^\perp = e^{1/3}/2$ as before.

4.1.8 Limiting behavior for large cutoff

The jet quenching parameter \hat{q} exhibits a logarithmic behavior when the cutoff Λ_\perp exceeds the typical hard momenta T_ϵ of the plasma constituents.

$$\hat{q}(\Lambda_\perp \gg T_\epsilon) \simeq a_{\Lambda_\perp} \ln \Lambda_\perp + b_{\Lambda_\perp}, \quad (4.50)$$

with (see Appendix C.2.2)

$$a_{\Lambda_\perp}/C_R = \frac{g^4}{\pi} \int \frac{d^3 k}{(2\pi)^3} \left(N_c f_g(\mathbf{k}) + \frac{1}{2} \sum_f f_f(\mathbf{k}) \right). \quad (4.51)$$

For isotropic distributions, it reads

$$a_{\Lambda_\perp}/C_R \simeq \frac{C_A g^4}{2\pi^3} \int_0^\infty dk k^2 f_g(k) + \sum_f \frac{g^4}{4\pi^3} \int_0^\infty dk k^2 f_f(k). \quad (4.52)$$

This is the same logarithmic behavior as in Eq. (4.43), keeping in mind that now the phase space is limited by Λ_\perp^2 rather than p , and thus $\ln p$ gets replaced by $2 \ln \Lambda_\perp$.

For thermal equilibrium, this yields

$$\hat{q}^{\text{therm}}(\Lambda_\perp \gg T) \simeq \frac{C_R}{\pi^3} g^4 \zeta(3) T^3 \left(N_c + \frac{3}{4} n_f \right) \ln \Lambda_\perp + \text{const}, \quad (4.53)$$

which is Eq. (C.39) in Appendix C.2.2 and agrees with Ref. [101], as we will later discuss around Eq. (4.77a).

4.1.9 Interpreting the momentum cutoff

A peculiar feature of the jet quenching parameter \hat{q} is its dependence on a transverse momentum cutoff Λ_\perp . Let us discuss here briefly where this dependence comes from and how to interpret this cutoff in physical terms.

In a kinetic picture, the reason for the cutoff is taking the jet momentum $p \rightarrow \infty$. In this case, the jet particle can inject an unrestricted amount of transverse momentum

into the collision, which leads to a logarithmic divergence. It has to be regulated by introducing a cutoff Λ_\perp , which restricts transverse momentum transfer $q_\perp < \Lambda_\perp$. Practically all analytic calculations that rely on quasiparticles or hard-thermal loop frameworks, but even with different interaction potentials, need to employ this cutoff.

A simple way of setting the cutoff is to use the relation between the coefficient a_{Λ_\perp} for large cutoff Λ_\perp and the coefficient a_p for large (finite) jet energy p (see Eqs. (4.43) and (4.52)). Requiring that the dynamics of jet quenching calculated with a cutoff in the $p \rightarrow \infty$ approximation has the same leading logarithmic behavior as a kinematically more accurate one with a finite p , we should choose the cutoff such that

$$\Lambda_\perp^{\text{kin}} \sim \sqrt{pT}, \quad (4.54)$$

where p is the energy of the jet parton and T is an additional dimensionful scale (e.g., the temperature in equilibrium). This kinematic cutoff $\Lambda_\perp^{\text{kin}}$ is widely used in the literature (see, e.g., [114, 115, 118, 120, 149, 209–211]).

While this is a straightforward result of our definition for \hat{q} in Eq. (1.4), it should be kept in mind that this parameter only encodes the momentum diffusion due to elastic $2 \leftrightarrow 2$ scattering processes, and competing inelastic effects like splittings or gluon emissions are neglected. For radiative energy loss calculations, one can restrict the cutoff by considering the rate of momentum exchange processes and comparing it with the ‘life-time’ of the leading parton under consideration. During an LPM splitting process (see also the discussion in section 2.1), this corresponds to the *formation time* t^{form} , Eq. (2.4). Therefore, we are interested in the accumulated transverse momentum until a splitting occurs. To calculate radiative energy loss of the leading parton in the harmonic approximation, the jet quenching parameter \hat{q} naturally appears in the expansion of the interaction potential in position space, Eq. (2.23). In this approximation, it is sufficient to use a momentum cutoff Λ_\perp of the order of the typical total momentum transfer Q_\perp during the formation time [96]. By definition, it is given by $Q_\perp^2 \sim \hat{q}t^{\text{form}}$, where for a small medium with length $L < t^{\text{form}}$ one should replace t^{form} by L . The formation time of the splitting $p \rightarrow p_1 + p_2$ can be estimated as $(t^{\text{form}})^2 \sim E_i/\hat{q}$, with E_i being the energy of the emitted gluon, see Eq. (2.4). It has been argued [101, 121] that energy loss is dominated by processes in which both daughters share a similar energy fraction $p_1 \sim p_2 \sim p$, which enables us to use the leading-parton energy in the formation time estimate. With the parametric relation $\hat{q} \sim g^4 T^3$, we obtain for a large medium $L > t^{\text{form}}$ the expression

$$\Lambda_\perp^{\text{LPM}} \sim g (pT^3)^{1/4}. \quad (4.55)$$

In order to present our results in a form that can be applied to different pictures of energy loss, we generally give our results as functions of Λ_\perp . In section 4.3.2, we will use these cutoffs as a model to study the jet quenching parameter during the initial stages in heavy-ion collisions.

In Chapter 7.2.1, we will discuss how to obtain the small distance behavior of the dipole cross section $C(|x|)$ in more detail, in particular without the need for a cutoff.

4.2 ANALYTICAL RESULTS FOR THE JET QUENCHING PARAMETER IN SPECIAL CASES

Let us now calculate the jet quenching parameter \hat{q} for some special cases. In Section 4.2.1, we first review the derivation of \hat{q} for quark-gluon plasmas in thermal equilibrium [100, 101] and compare the results with numerical evaluations of Eq. (4.45). Additionally, an interpolation formula is provided that reproduces the numerically obtained values of the quenching parameter in thermal equilibrium \hat{q}^{therm} for different couplings and momentum cutoffs.

In Section 4.2.2, we then consider toy models for the bottom-up thermalization process in heavy-ion collisions (see Section 3.5.2). First, an effectively two-dimensional distribution is studied to model the large momentum-space anisotropy encountered in the initial stages in heavy-ion collisions and then the thermal results of Section 4.2.1 are generalized to a scaled thermal distribution to model over- and under-occupied systems that are typically encountered in the bottom-up thermalization picture.

We also study the different contributions to \hat{q} that are linear or quadratic in the distribution function by splitting the jet quenching parameter \hat{q} into its individual components,

$$\hat{q} = \hat{q}_f + \hat{q}_{ff}. \quad (4.56)$$

Similarly as in Ref. [212], we refer to \hat{q}_f as the *classical* and \hat{q}_{ff} as the *Bose-enhanced* part of \hat{q} .²

4.2.1 Thermal distribution

The equilibrium form of the particle distributions is given by Eq. (3.20),

$$f_{\pm}(k; T) = \frac{1}{\exp(k/T) \mp 1}, \quad (4.57)$$

where T is the plasma temperature. The upper signs f_+ denote the Bose-Einstein distribution and f_- is the Fermi-Dirac distribution.

In thermal equilibrium, \hat{q} has already been calculated for the limiting cases of small and large cutoffs Λ_{\perp} in [101, 102], which is briefly summarized here. In Section 4.2.2, we will generalize this derivation to the case of a scaled thermal distribution, which is obtained by rescaling a thermal distribution.

For evaluating \hat{q} , we work in the $p \rightarrow \infty$ limit with a transverse momentum cutoff Λ_{\perp} , as discussed in Section 4.1.7. Since the distribution function is spherically symmetric, one has $\hat{q}^{11} = \hat{q}^{22}$ and we can restrict the discussion to the sum $\hat{q} = \hat{q}^{11} + \hat{q}^{22}$. Our starting point is Eq. (4.45), where we integrate over the modulus of $\mathbf{q} = (\mathbf{q}_{\perp}, q^3)$. For $p \rightarrow \infty$, we obtain $q^3 = \omega$ and thus

$$q^2 = q_{\perp}^2 + \omega^2. \quad (4.58)$$

² This Bose-enhanced term can also be considered to be a *classical field* contribution because it is dominant in highly occupied systems $f \gg 1$ that can be studied numerically using classical-statistical simulations. This can be seen in the limit of $\lambda \rightarrow 0$ with λf held constant, in which only \hat{q}_{ff} survives.

It will be useful to change the integration variables from (q, ϕ_{pq}, ω) to (q^1, q^2, ω) , which yields a factor q from the Jacobian,

$$\int_0^{2\pi} d\phi_{pq} \int_0^\infty dq \int_{-q}^q d\omega \Theta(\Lambda_\perp^2 + \omega^2 - q^2) = \int_{q_\perp < \Lambda_\perp} d^2 \mathbf{q}_\perp \int_{-\infty}^\infty \frac{d\omega}{\sqrt{q_\perp^2 + \omega^2}}. \quad (4.59)$$

In the limit $p \rightarrow \infty$, the matrix elements in Tab. 4.2 do not allow for identity-changing processes, which means that the leading parton a and the outgoing parton c are of the same type, $a = c$, and similarly $b = d$. Therefore, we can scale out the Casimir factor of the jet C_R , and the prefactors in front of $\tilde{M}_{\text{screen}}$ in Tab. 4.2 neatly combine with $1/\nu_a$ for the degrees of freedom of the jet particle to

$$\Xi_+ = 2N_c, \quad (4.60a)$$

$$\Xi_- = 4n_f \frac{d_F C_F}{d_A} = 2n_f, \quad (4.60b)$$

for scattering off a gluon and off a quark/anti-quark, respectively, which leads to Casimir scaling (see also Eq. (4.46)).

There are two limiting cases in which an analytic result for \hat{q} can be obtained: for small and large momentum cutoffs. We discuss both cases in the following.

Small momentum cutoff

For small momentum cutoffs $\Lambda_\perp \ll T$, the expression for \hat{q} in Eq. (4.45) with (4.59) and the prefactors (4.60) becomes

$$\hat{q}(\Lambda_\perp) = C_R \sum_{\pm} \Xi_{\pm} \frac{g^4}{2^9 \pi^5} \int_0^\infty dk f_{\pm}(k) (1 \pm f_{\pm}(k)) \int_0^{\Lambda_\perp} d^2 \mathbf{q}_\perp q_\perp^2 \int_0^{2\pi} d\phi_{qk} \int_{-\infty}^\infty \frac{d\omega \tilde{M}_{\text{HTL}}}{\sqrt{q_\perp^2 + \omega^2}}. \quad (4.61)$$

We have extended the lower boundary³ of the k -integral to 0 and approximated $f(k - \omega) \approx f(k)$. This is appropriate because large values of ω are suppressed by the matrix element \tilde{M}_{HTL} , as can be seen from Eq. (4.40).

The last two integrals can be evaluated analytically using a sum rule [100] as discussed in Appendix A.5.4,

$$\hat{q}(\Lambda_\perp) = \frac{C_R g^4}{(2\pi)^3} 2 \int_{q_\perp < \Lambda_\perp} \frac{d^2 \mathbf{q}_\perp}{2\pi} q_\perp^2 \frac{1}{q_\perp^2 (q_\perp^2 + m_D^2)} \sum_{\pm} \Xi_{\pm} \int_0^\infty dk k^2 f_{\pm}(k) (1 \pm f_{\pm}(k)). \quad (4.62)$$

Note that until now we have only assumed spherical symmetry, but have not used a specific form for the distribution function $f(k)$. The thermal form of \hat{q} for a small cutoff is then obtained by performing the integrals over the distribution function,

$$\int_0^\infty dk k^2 f_{\pm}(k) = 2T^3 \zeta_{\pm}(3), \quad (4.63a)$$

$$\int_0^\infty dk k^2 (f_{\pm}(k))^2 = \pm 2T^3 (\zeta_{\pm}(2) - \zeta_{\pm}(3)), \quad (4.63b)$$

³ The largest error of this approximation comes from the f_+^2 term. It can be estimated by $\int_0^{\frac{q+\omega}{2}} k^2 f_+^2 < \frac{q+\omega}{2} \lim_{k \rightarrow 0} (k^2 f_+^2)$, where the k^2 factor stems from \tilde{M}_{HTL} and we approximated the integral by the maximum value of the integrand at $k = 0$. This yields the error estimate $\frac{T^2(q+\omega)}{2}$, which for $q_\perp < \Lambda_\perp \ll T$ is much smaller than the leading-order contribution $\int_0^\infty k^2 f_+^2 = 2T^3 (\zeta(2) - \zeta(3))$ (see Eq. (4.63)) for $q, \omega \ll T$.

where $\zeta_+(s) = \zeta(s)$ is the Riemann Zeta function and $\zeta_-(s) = (1 - 2^{1-s})\zeta(s)$ denotes its fermionic counterpart as in Ref. [101]. Using $\zeta(2) = \pi^2/6$, we obtain

$$\hat{q}(\Lambda_\perp) = \int_{q_\perp < \Lambda_\perp} d^2\mathbf{q}_\perp q_\perp^2 \frac{g^2 C_R T}{(2\pi)^2} \frac{m_D^2}{q_\perp^2(q_\perp^2 + m_D^2)}, \quad (4.64)$$

from which we can read off the elastic scattering rate $\frac{d\Gamma_{\text{el}}}{d^2q_\perp}$. This leads us to the thermal form of \hat{q} for a small cutoff,⁴

$$\hat{q}^{\text{therm}}(\Lambda_\perp \ll T) = \frac{g^2}{4\pi} C_R T m_D^2 \ln \left(1 + \frac{\Lambda_\perp^2}{m_D^2} \right). \quad (4.65)$$

For a thermal system, the terms containing $\zeta_\pm(3)$ cancel for the total \hat{q} , but are important if one considers the *Bose-enhanced* part separately, as in (4.56). Splitting off the *Bose-enhanced* term as in (4.56), we obtain

$$\hat{q}_f^{\text{therm}}(\Lambda_\perp \ll T) = \zeta(3) (12N_c + 9n_f) C_L, \quad (4.66a)$$

$$\hat{q}_{ff}^{\text{therm}}(\Lambda_\perp \ll T) = [2N_c(\pi^2 - 6\zeta(3)) + n_f(\pi^2 - 9\zeta(3))] C_L, \quad (4.66b)$$

with $C_L = \frac{g^4 T^3 C_R}{24\pi^3} \ln \left(1 + \frac{\Lambda_\perp^2}{m_D^2} \right)$ and the thermal Debye mass given by Eq. (3.13).

Large momentum cutoff

For large momentum cutoffs, the jet quenching parameter has been calculated in Ref. [101] for a thermal system. To later generalize this to a scaled thermal distribution, we briefly review the derivation here. It relies on constructing an interpolating formula for the elastic scattering rate

$$\frac{C(q_\perp)}{(2\pi)^2} = \frac{d\Gamma_{\text{el}}}{d^2q_\perp} \simeq C_R \frac{g^4 T^3 F(q_\perp/T)}{q_\perp^2(q_\perp^2 + m_D^2)}, \quad (4.67)$$

where the function $F(q_\perp/T)$ interpolates between the known limits of this quantity (we will discuss both limits later in Chapter 8, see Eq. (7.23)) and can be calculated in the approximation $q \gg m_D$. It is then split into gluonic (I_+) and fermionic (I_-) contributions,⁵

$$F(q_\perp/T) = \frac{1}{\pi^2} (\Xi_+ I_+(q_\perp/T) + \Xi_- I_-(q_\perp/T)). \quad (4.68)$$

Following the notation in Ref. [101], we write these contributions to the collision kernel in the limit $p \rightarrow \infty$ and $q_\perp \gg m_D$ as

$$I_\pm \left(\frac{q_\perp}{T} \right) = \frac{\pi^2}{T^3} \int \frac{dq_z}{2\pi} \int \frac{d^3\mathbf{k}}{(2\pi)^3} 2\pi\delta(q_z + |\mathbf{k} - \mathbf{q}| - k) \frac{(k - k_z)^2}{k|\mathbf{k} - \mathbf{q}|} f_\pm(\mathbf{k}) [1 \pm f_\pm(\mathbf{k} - \mathbf{q})]. \quad (4.69)$$

This formula follows directly from the t-channel matrix element in Tab. 4.1, i.e., su/t^2 , with $t^2 = q_\perp^4$ being scaled out in (4.67) and $s \simeq -u = 2p(k - k_z)$.

⁴ This form is actually valid in general for any isotropic distribution $f(k)$ with the replacement of $T \rightarrow T_*$ (see Eq. (3.10)) and the more generally evaluated Debye mass m_D as in Eq. (3.11).

⁵ In principle, we could take Eq. (4.61) instead and relax the assumption of small momentum transfer, i.e., keep $f_\pm(k)(1 \pm f_\pm(k - \omega))$. However, the strategy employed in Ref. [101] (scaling out this factor $F(q_\perp/T)$ in (4.67)) allows us to evaluate the expression analytically in the large q_\perp limit, where the matrix element does not need to be screened, and we can use the simpler form su/t^2 instead.

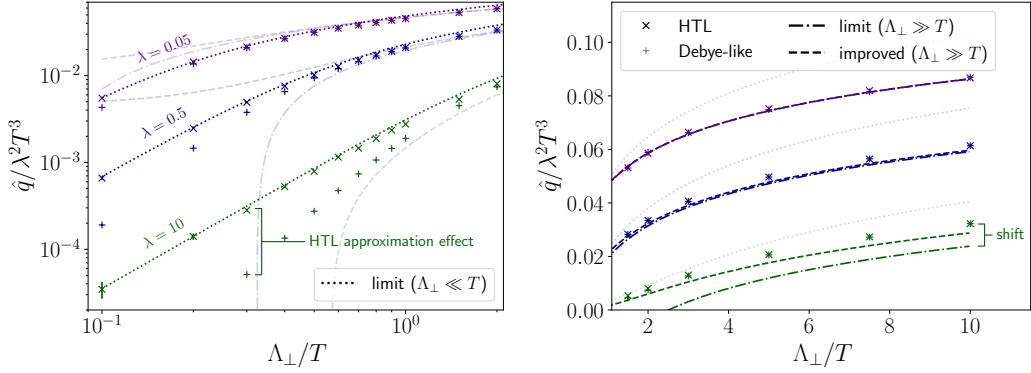


Figure 4.4: The coefficient \hat{q} for a quark jet in thermal equilibrium for different 't Hooft couplings $\lambda = g^2 N_c$ and transverse momentum cutoffs Λ_\perp , with (left:) small $\Lambda_\perp \lesssim T$ (logarithmically scaled axis), and (right:) large $\Lambda_\perp \gtrsim T$. The dotted curve labeled 'limit ($\Lambda_\perp \ll T$)' shows the analytical limiting expression of (4.65), the dash-dotted curve 'limit ($\Lambda_\perp \gg T$)' illustrates (4.77a), and 'improved ($\Lambda_\perp \gg T$)' denotes (4.78a). The small '+'-symbols show the numerical results with the Debye-like screened matrix element (4.49), whereas the '×'-symbols show the results with the full HTL matrix element (4.47). The curves that are not valid in the respective limit are displayed with lighter color but are still shown because (4.65) is often also used at large Λ_\perp as an approximation. Figures adapted from [2].

As in (4.56) we can identify the contributions coming from the f and f^2 parts via

$$I_\pm(q_\perp/T) = I_\pm^f + I_\pm^{ff}(q_\perp/T), \quad (4.70)$$

where I_\pm^f will turn out to be a constant. To evaluate them, the thermal functions are written as

$$f_\pm(p) = \sum_{m=1}^{\infty} (\pm 1)^{m-1} e^{-mp/T}. \quad (4.71)$$

This can then be inserted into Eq. (4.69) to rewrite the equation as a double sum,

$$I_\pm^f\left(\frac{q_\perp}{T}\right) = \sum_{m=1}^{\infty} (\pm 1)^{m-1} I_{m0}(q_\perp/T), \quad (4.72)$$

$$I_\pm^{ff}\left(\frac{q_\perp}{T}\right) = \sum_{m=1}^{\infty} \sum_{n=1}^{\infty} (\pm 1)^{m+n-1} I_{mn}(q_\perp/T), \quad (4.73)$$

with

$$I_{mn}\left(\frac{q_\perp}{T}\right) = \frac{\pi^2}{T^3} \int \frac{dq_z}{2\pi} \int \frac{d^3\mathbf{k}}{(2\pi)^3} 2\pi\delta(q_z + |\mathbf{k} - \mathbf{q}| - k) \frac{(k - k_z)^2}{k|\mathbf{k} - \mathbf{q}|} e^{-mk/T} e^{-n|\mathbf{k} - \mathbf{q}|/T}. \quad (4.74)$$

In [101], I_\pm was split in a similar way isolating the $n = 0$ term $I_\pm(\infty)$, which is exactly the constant $I_\pm^f = I_\pm(\infty) = \zeta_\pm(3)$. This is a consequence of the fact that for large momentum transfer only the f part contributes, as discussed in Section 4.1.8. In Ref. [101], the integrals in (4.74) are evaluated analytically,

$$I_{mn}\left(\frac{q_\perp}{T}\right) = \frac{mn}{2(m+n)^3} \left(\frac{q_\perp}{T}\right)^3 K_2\left(\frac{q_\perp}{T} \sqrt{mn}\right), \quad (4.75)$$

where $K_\nu(z)$ is the modified Bessel function of the second kind. With that, we can write the collision kernel in thermal equilibrium as the infinite double sum

$$C(q_\perp) = \frac{2C_R g^4 T^3}{q_\perp^2 (q_\perp^2 + m_D^2) \pi^2} \frac{q_\perp^2}{T^2} \sum_{m=1}^{\infty} \sum_{n=0}^{\infty} (N_c + n_f (-1)^{m+n-1}) \frac{mn}{2(m+n)^3} K_2\left(\frac{q_\perp}{T} \sqrt{mn}\right). \quad (4.76)$$

Performing the remaining integrals over \mathbf{q}_\perp as in Ref. [101] leads to the following expression for the jet quenching parameter \hat{q} for large cutoffs $\Lambda_\perp \gg T$,

$$\hat{q}^{\text{therm}}(\Lambda_\perp \gg T) = C_R \frac{g^4 T^3}{\pi^2} \sum_{\pm} \Xi_{\pm} \mathcal{I}_{\pm}(\Lambda_\perp), \quad (4.77a)$$

$$\mathcal{I}_{\pm}(\Lambda_\perp) = \frac{\zeta_{\pm}(3)}{2\pi} \ln\left(\frac{\Lambda_\perp}{m_D}\right) + \Delta \mathcal{I}_{\pm}, \quad (4.77b)$$

$$\Delta \mathcal{I}_{\pm} = \frac{\zeta_{\pm}(2) - \zeta_{\pm}(3)}{2\pi} \left[\ln\left(\frac{T}{m_D}\right) + \frac{1}{2} - \gamma_E + \ln 2 \right] - \frac{\sigma_{\pm}}{2\pi}, \quad (4.77c)$$

$$\sigma_+ = 0.386043817389949, \quad (4.77d)$$

$$\sigma_- = 0.011216764589789, \quad (4.77e)$$

where γ_E is the Euler-Mascheroni constant, and $\sigma_{\pm} = \sum_{k=1}^{\infty} \frac{(\pm 1)^{k-1}}{k^3} \ln[(k-1)!]$.

This formula (4.77), as opposed to the one for small cutoffs (4.65), has the (unphysical) feature that the logarithm $\ln T/m_D$ becomes negative for $m_D \geq T$. Of course, in perturbation theory at weak couplings, one has $m_D \sim gT \ll T$. However, to get an analytical expression that is well-behaved also for larger couplings, we add a constant to the argument of the logarithm, which still preserves the leading order accuracy at weak coupling. To be explicit, we replace $2 \ln x \rightarrow \ln(1 + x^2)$ in both logarithms, and we will denote the resulting ‘improved’ analytic expressions for \hat{q} by \hat{q}_{im} . Although the replacement does not change the result at leading order, we will see that this choice of regularization significantly improves the agreement with numerical evaluations of (4.21), as we will discuss in the next subsection. Moreover, the Bose-enhanced part \hat{q}_{ff} of (4.56) is solely due to $\Delta \mathcal{I}_{\pm}$ in (4.77b). With these replacements in the logarithm, the contribution \hat{q}_{f} has the same form as for small momentum cutoffs (4.66a), $\hat{q}_{\text{f}}(\Lambda_\perp \ll T) = \hat{q}_{\text{f}}(\Lambda_\perp \gg T)$.

With this procedure, the improved version of Eq. (4.77a) becomes

$$\hat{q}_{\text{im}}^{\text{therm}}(\Lambda_\perp \gg T) = \hat{q}_{\text{f}}^{\text{therm}}(\Lambda_\perp \ll T) + \hat{q}_{\text{ff,im}}^{\text{therm}} \quad (4.78a)$$

with

$$\hat{q}_{\text{ff,im}}^{\text{therm}} = C_R g^4 T^3 \sum_{\pm} \Xi_{\pm} \left\{ \frac{\zeta_{\pm}(2) - \zeta_{\pm}(3)}{4\pi^3} \left[\ln\left(1 + \frac{T^2}{m_D^2}\right) + 1 - 2\gamma_E + 2\ln 2 \right] - \frac{\sigma_{\pm}}{2\pi^3} \right\}. \quad (4.78b)$$

Comparison with numerical results

Let us now compare the analytical small and large cutoff limits of \hat{q} given by (4.65) and (4.77a) or the improved version (4.78a) to a numerical evaluation of \hat{q} using (4.45). For simplicity we consider a purely gluonic plasma, i.e., $n_f = 0$. In particular, we want to study how well these analytic formulae describe the full

numerical evaluation of the \hat{q} integral, although being only valid for asymptotic regions of the cutoff Λ_\perp . We also want to compare the expressions using the full HTL screened matrix element (isoHTL) (4.47) with the simpler Debye-like screened matrix element (4.49) and study the impact of different screening approximations on the jet quenching parameter \hat{q} .

Fig. 4.4 shows \hat{q} for various momentum cutoffs Λ_\perp and different 't Hooft couplings $\lambda = g^2 N_c$. The prefactor $\lambda^2 T^3$ is scaled out in the plots, leaving a nontrivial coupling dependence that enters via the Debye mass m_D in the logarithms originating from the matrix element. The curves show the analytic expressions for small cutoffs (dotted, Eq. (4.65)), large cutoffs (dash-dotted, Eq. (4.77a)) and the improved large-cutoff version (dashed, (4.78a)), while the numerical evaluation of \hat{q} is depicted by crosses for the HTL matrix elements (4.47) and plus signs for the Debye-like screened ones (4.49). In the left panel of Fig. 4.4, we observe that the small-cutoff form of \hat{q} accurately agrees with the numerical evaluation using the full HTL matrix element in the corresponding region $\Lambda_\perp \ll T$, even for $\Lambda_\perp \rightarrow 0$. Note that the frequently employed form of \hat{q} in this limit with the approximation $\ln\left(1 + \frac{\Lambda_\perp^2}{m_D^2}\right) \rightarrow 2 \ln \frac{\Lambda_\perp}{m_D}$ (not shown in the figure) would become negative at too small cutoffs $\Lambda_\perp \sim m_D$, and is, thus, not well behaved in the limit $\Lambda_\perp \rightarrow 0$.

In the region $\Lambda_\perp \gg T$ (right panel of Fig. 4.4), we observe that for small couplings $\lambda \sim 0.05$ both analytic large-cutoff expressions agree very well with the numerical values. However, they start to differ when increasing the coupling $\lambda \gtrsim 0.5$. This is denoted as 'shift' in Fig. 4.4. We find that the values from the improved formula (4.78a) are closer to the numerical values than from the original formula (4.77a), i.e., the shift is smaller. However, for large couplings $\lambda \sim 10$, the improved analytic expression still seems to underestimate \hat{q} , with the difference being a constant. This is because the leading logarithmic behavior stems from the large q_\perp behavior of the collision kernel (see Section 4.1.8 and Appendix C.2.2), whereas for the constant, one requires the exact form of the collision kernel for all q_\perp (in particular also for $q_\perp \approx T$), where the form (4.76) and approximations used in evaluating the q_\perp integral over it [101] are only valid for small couplings.

Turning now to a comparison of the matrix elements, we observe in Fig. 4.4 that for small values of the coupling $\lambda \sim 0.05$ (left panel) as well as for large cutoffs $\Lambda_\perp \gg T$ (right panel), the results with the Debye-like screening approximation (4.49) agree well with the full HTL matrix element (4.47). However, they start deviating with growing coupling at small cutoffs $\Lambda_\perp \lesssim T$ (left panel). To guide the eye, for $\Lambda_\perp = 0.3T$ this difference is denoted as 'HTL approximation effect'. For $\Lambda_\perp = T$ and $\lambda = 10$ the deviation between the approximated and the HTL matrix elements is of the order of 30%.

Interpolation formula for \hat{q} in thermal equilibrium

We have now verified that the analytic expressions (4.65) and (4.77a) describe \hat{q} only in certain limits and Eq. (4.77a) only holds for small couplings $\lambda \lesssim 0.5$. For phenomenological calculations, a general simple formula (or parametrization) for \hat{q} in thermal equilibrium may be useful without the need to perform the high-dimensional integral (4.21) numerically for the required value of the coupling λ and transverse momentum cutoff Λ_\perp . Thus, we construct an interpolation formula

λ	\tilde{b}	\tilde{d}	\tilde{e}
0.5	0.0011944 ± 0.0000020	4.114 ± 0.013	-0.76919 ± 0.00058
1.0	0.0037772 ± 0.0000062	2.4910 ± 0.0029	-0.24707 ± 0.00041
1.5	0.007379 ± 0.000013	2.0956 ± 0.0018	0.03349 ± 0.00032
2.0	0.011905 ± 0.000021	1.9636 ± 0.0014	0.20498 ± 0.00029
2.5	0.017295 ± 0.000031	1.8987 ± 0.0012	0.32796 ± 0.00028
3.0	0.023563 ± 0.000042	1.8653 ± 0.0010	0.42226 ± 0.00026
3.5	0.030716 ± 0.000054	1.84570 ± 0.00096	0.49864 ± 0.00025
4.0	0.038770 ± 0.000067	1.83331 ± 0.00088	0.56271 ± 0.00024
4.5	0.047761 ± 0.000082	1.82484 ± 0.00080	0.61789 ± 0.00023
5.0	0.057714 ± 0.000099	1.81902 ± 0.00075	0.66626 ± 0.00022
5.5	0.06864 ± 0.00012	1.81444 ± 0.00071	0.70960 ± 0.00021
6.0	0.08061 ± 0.00014	1.81130 ± 0.00069	0.74868 ± 0.00020
6.5	0.09362 ± 0.00015	1.80845 ± 0.00067	0.78441 ± 0.00020
7.0	0.10772 ± 0.00017	1.80584 ± 0.00066	0.81733 ± 0.00020
7.5	0.12296 ± 0.00020	1.80380 ± 0.00065	0.84781 ± 0.00019
8.0	0.13933 ± 0.00022	1.80168 ± 0.00064	0.87635 ± 0.00019
8.5	0.15687 ± 0.00024	1.80026 ± 0.00064	0.90313 ± 0.00019
9.0	0.17562 ± 0.00026	1.79871 ± 0.00064	0.92836 ± 0.00019
9.5	0.19569 ± 0.00029	1.79776 ± 0.00063	0.95195 ± 0.00019
10.0	0.21701 ± 0.00031	1.79691 ± 0.00063	0.97442 ± 0.00019
10.5	0.23960 ± 0.00034	1.79628 ± 0.00063	0.99579 ± 0.00019
11.0	0.26361 ± 0.00036	1.79589 ± 0.00063	1.01605 ± 0.00019
11.5	0.28894 ± 0.00039	1.79532 ± 0.00063	1.03544 ± 0.00019
12.0	0.31570 ± 0.00042	1.79489 ± 0.00063	1.05399 ± 0.00019
12.5	0.34386 ± 0.00045	1.79432 ± 0.00062	1.07188 ± 0.00019
13.0	0.37349 ± 0.00048	1.79405 ± 0.00062	1.08902 ± 0.00019
13.5	0.40461 ± 0.00052	1.79343 ± 0.00062	1.10557 ± 0.00019
14.0	0.43722 ± 0.00054	1.79316 ± 0.00062	1.12149 ± 0.00019
14.5	0.47134 ± 0.00058	1.79241 ± 0.00062	1.13694 ± 0.00019
15.0	0.50704 ± 0.00061	1.79162 ± 0.00061	1.15192 ± 0.00019
15.5	0.54431 ± 0.00066	1.79053 ± 0.00061	1.16651 ± 0.00019
16.0	0.58324 ± 0.00070	1.78988 ± 0.00060	1.18054 ± 0.00020
16.5	0.62381 ± 0.00074	1.78933 ± 0.00060	1.19420 ± 0.00019
17.0	0.66613 ± 0.00078	1.78922 ± 0.00060	1.20734 ± 0.00019
17.5	0.71013 ± 0.00081	1.78864 ± 0.00059	1.22017 ± 0.00019
18.0	0.75590 ± 0.00085	1.78805 ± 0.00059	1.23280 ± 0.00019
18.5	0.80337 ± 0.00090	1.78734 ± 0.00058	1.24516 ± 0.00019
19.0	0.85257 ± 0.00094	1.78699 ± 0.00058	1.25721 ± 0.00019
19.5	0.90367 ± 0.00099	1.78674 ± 0.00058	1.26879 ± 0.00019
20.0	0.9565 ± 0.0010	1.78563 ± 0.00058	1.28029 ± 0.00019

Table 4.3: Fitted coefficients for the interpolation formula for \hat{q} in Eq. (4.81). The values were obtained by numerically integrating (4.45) and the HTL-screened matrix element (4.47), then numerically fitting the coefficient \tilde{b} in the region $\Lambda_\perp \gg T$, and finally fitting \tilde{d} and \tilde{e} in the range $0.1T < \Lambda_\perp < 15T$. Table from [2].

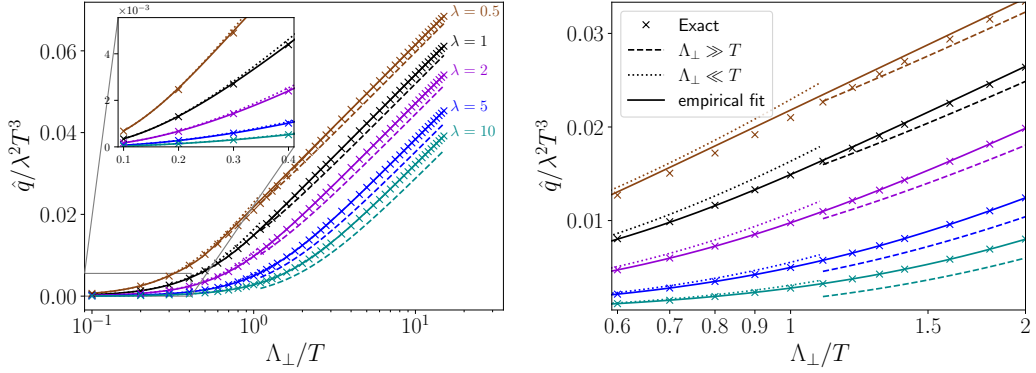


Figure 4.5: (Left:) The interpolation formula (4.81) for the jet quenching parameter \hat{q} with the fitted coefficients listed in Tab. 4.3 is shown as continuous lines for different couplings λ (color-coded). The numerical evaluation of Eq. (4.45) is shown as crosses, the limiting expressions for soft (4.65) and hard cutoffs (4.77a) as dotted and dashed curves. The inset shows the behavior at small momentum cutoffs. (Right:) Focus on the interpolation region $\Lambda_\perp \sim T$. For $\lambda \geq 1$ we see very good agreement with the numerical results. Plots adapted from [2].

that reproduces the analytical results in the limits $\Lambda_\perp \ll T$ and for $\Lambda_\perp \gg T$ and agrees with our numerical evaluation.

From (4.65) and (4.77a) we know the behavior of \hat{q} for small $\Lambda_\perp \ll T$ and large cutoffs $\Lambda_\perp \gg T$. As discussed before, (4.77a) differs from the numerical evaluation of \hat{q} by a constant shift for larger values of the coupling $\lambda \gtrsim 0.5$. Our strategy is to find an empirical fit function that smoothly interpolates in between,

$$\frac{\hat{q}^{\text{emp}}}{C_R T^3} = \begin{cases} \tilde{c} \ln(1 + \Lambda_\perp^2/m_D^2), & \text{for } \Lambda_\perp \ll T \\ \tilde{a} \ln(\Lambda_\perp/m_D) + \tilde{b}, & \text{for } \Lambda_\perp \gg T. \end{cases} \quad (4.79)$$

The switching between those two cases will be done using a hyperbole tangent that smears out a step function with width parameter \tilde{d} ,

$$\Theta_{\tilde{d}}(x) = \frac{1 + \tanh(\tilde{d}x)}{2}, \quad (4.80)$$

which approaches the usual step function for $\tilde{d} \rightarrow \infty$.

This leads to the following form for the fit formula

$$\frac{\hat{q}^{\text{emp}}}{C_R T^3} = \tilde{c} \ln\left(1 + \frac{\Lambda_\perp^2}{m_D^2}\right) \Theta_{\tilde{d}}\left(\tilde{e} - \ln \frac{\Lambda_\perp}{T}\right) + \left(\tilde{a} \ln \frac{\Lambda_\perp}{m_D} + \tilde{b}\right) \Theta_{\tilde{d}}\left(\ln \frac{\Lambda_\perp}{T} - \tilde{e}\right). \quad (4.81)$$

For the coefficients \tilde{c} and \tilde{a} , we use the prefactors of (4.65) and (4.77a), which have the following values for a gluonic plasma:

$$\tilde{c} = \frac{\lambda^2}{12\pi N_c}, \quad \tilde{a} = \frac{\lambda^2 \zeta(3)}{\pi^3 N_c}. \quad (4.82)$$

This leaves only three fit parameters: The constant \tilde{b} encodes the linear shift in the large Λ_\perp/T region, while \tilde{d} and \tilde{e} describe the width and position of the switching between the two limiting cases in (4.79). First, the coefficient \tilde{b} is obtained, such

that it correctly reproduces $\hat{q} \simeq \tilde{a} \ln \Lambda_\perp/m_D + \tilde{b}$ in the large Λ_\perp/T region. Then, the coefficients \tilde{d} and \tilde{e} are determined by fitting them to the numerical data.

The results for the remaining fit parameters in Eq. (4.81) are listed in Tab. 4.3 for the couplings $\lambda = 0.5 - 20$. The resulting \hat{q} are shown in Fig. 4.5 as continuous lines. For comparison, the numerically obtained values are included as crosses, and the limiting expressions for hard and soft cutoffs, Eqs. (4.77a) and (4.65), respectively, as dashed and dotted lines. Consistently with the construction of the fit formula, its values are seen to agree well with the numerically evaluated \hat{q} in the left panel of Fig. 4.5 and in the inset showing the small cutoff behavior at $\Lambda_\perp \ll T$. The right panel of Fig. 4.5 shows the interpolation region $\Lambda_\perp \sim T$. We find a very good agreement with the numerics for $\lambda \geq 1$, while for smaller couplings $\lambda \lesssim 0.5$ deviations grow in this region. Note that the fit formula provides a smooth interpolating expression for \hat{q} with improved accuracy in this region as compared to the previous limiting forms.

Thus, the expression (4.81) together with the coefficients in Tab. 4.3 can be used to obtain \hat{q} in thermal equilibrium for any transverse momentum cutoff Λ_\perp and the listed couplings λ in the weak coupling limit at leading-order.

4.2.2 Toy models for bottom-up thermalization

As toy models for the bottom-up thermalization process that we discussed in Section 3.5.2, we consider first an effectively two-dimensional distribution in Section 4.2.2. Then, \hat{q} is computed analytically in Section 4.2.2 using an isotropic scaled thermal distribution, which models key features of the over- and under-occupied bottom-up stages.

Effectively two-dimensional distribution

As a toy model for the large anisotropies encountered at early times in the bottom-up thermalization scenario, we consider an effectively two-dimensional system and calculate the jet quenching parameter \hat{q} for that system. For that, we consider a distribution function with vanishing k_z momentum,

$$f(\mathbf{k}) = B(k_x, k_y) \delta(k_z/Q), \quad (4.83)$$

where B is (for the moment) an arbitrary function of k_x and k_y , and Q is an energy scale. Due to its vanishing momentum in beam direction $k_z = 0$, such a state is similar in spirit to the Glasma, where the jet quenching parameter has also been studied [152, 153, 155–157].

First, let us focus on the *Bose-enhanced* part \hat{q}_{ff} in kinetic theory. This agrees with \hat{q} in a classical-statistical framework since there is no \hat{q}_{f} contribution in the classical field limit. By inserting the two-dimensional distribution (4.83) into the \hat{q} integral (4.21), we immediately find

$$\hat{q}_{\text{ff}}^{zz} = 0, \quad (4.84)$$

due to its proportionality to $\int (q^z)^2 \delta(k_z) \delta(k'_z)$. Note that this is true regardless of the precise form of the matrix element or screening prescription. Thus, a purely

two-dimensional momentum distribution remains two-dimensional in the classical field limit of kinetic theory.

Let us now consider a special case of (4.83) for which we may obtain an analytic expression for the jet quenching parameter, where all particles have a specific momentum \tilde{k} ,

$$f(\mathbf{k}) = A \delta\left(\frac{k_x^2 + k_y^2 - \tilde{k}^2}{Q^2}\right) \delta(k_z/Q). \quad (4.85)$$

First, note that we do not need to enforce a momentum cutoff $q_\perp < \Lambda_\perp$, because \hat{q}_{ff}^{yy} is finite even for $p \rightarrow \infty$. Hence, we consider here the case where the transverse momentum cutoff Λ_\perp is sufficiently large, at least $\Lambda_\perp > 2\tilde{k}$, as we will see below.

For \hat{q}_{ff}^{yy} we start with Eq. (4.12) and insert the special two-dimensional distribution $f(\mathbf{k})$ from (4.85), obtaining

$$\begin{aligned} \hat{q}_{ff}^{yy} = & \frac{A^2 Q^6}{16 p^2 \nu} \int \frac{d^3 \mathbf{k} d^3 \mathbf{q} d\omega}{(2\pi)^5 q^2 k^2} q^y q^y |\mathcal{M}(\mathbf{p}, \mathbf{k}; \mathbf{p}', \mathbf{k}')|^2 \\ & \times \delta\left(\cos \theta_{qp} - \frac{\omega}{q} - \frac{\omega^2 - q^2}{2pq}\right) \delta\left(\cos \theta_{qk} - \frac{\omega}{q} + \frac{\omega^2 - q^2}{2kq}\right) \\ & \times \theta(p' - k') \theta\left(p - \frac{q - \omega}{2}\right) \Theta\left(k - \frac{q + \omega}{2}\right) \Theta(q - |\omega|) \\ & \times \delta(k_z) \delta(q_z) \delta(k^2 - \tilde{k}^2) \delta((\mathbf{k} - \mathbf{q})^2 - \tilde{k}^2). \end{aligned} \quad (4.86)$$

We first integrate out k_z and q_z . Additionally, for $p \rightarrow \infty$ we may drop the theta functions containing p and p' . We then rewrite the delta functions as $\delta((\mathbf{k} - \mathbf{q})^2 - \tilde{k}^2) = \delta(\omega^2 - 2\omega\tilde{k}) = \frac{1}{2\tilde{k}}(\delta(\omega) + \delta(\omega - 2\tilde{k}))$, allowing us to integrate over ω . The $\delta(\omega - 2k)$ term vanishes because then the third step function becomes $\Theta(-q/2) = 0$. Integrating over ω then enforces $\omega = 0$. Finally, in the large- p limit, the first delta function can be simplified to $\delta(\cos \theta_{qp}) = q\delta(q_x)$, allowing us to perform the q_x integral as well. We then arrive at

$$\begin{aligned} \hat{q}_{ff}^{yy} = & \frac{A^2 Q^6}{16 p^2 \nu} \int \frac{dk_x dk_y dq_y}{(2\pi)^5 q_y k^2} (q_y)^2 |\mathcal{M}(\mathbf{p}, \mathbf{k}; \mathbf{p}', \mathbf{k}')|^2 \\ & \times \delta\left(\cos \theta_{qk} - \frac{|q_y|}{2\tilde{k}}\right) \Theta\left(\tilde{k} - \frac{|q_y|}{2}\right) \frac{1}{4\tilde{k}^2} \delta(k - \tilde{k}), \end{aligned} \quad (4.87)$$

where we have used $\delta(k^2 - \tilde{k}^2) = \frac{1}{2\tilde{k}}\delta(k - \tilde{k})$. Effectively, \mathbf{q} is parallel to the y -axis and \mathbf{k} lies in the $x - y$ plane with length \tilde{k} and $k_y = |q_y|/2$. For the matrix element we need $q = |q_y|$, $k = \tilde{k}$ and ϕ_{qk} , which is the polar angle of \mathbf{k} in a frame, in which \mathbf{q} points in the z direction and \mathbf{p} lies in the $x - z$ plane, see Section 4.1.2. In our case, \mathbf{q} is orthogonal to \mathbf{p} , thus we perform the \mathbf{k} integration in a frame, in which $\mathbf{q} = q \mathbf{e}_{z^3}$, $\mathbf{p} = -p \mathbf{e}_{x^3}$. Since \mathbf{k} must lie in the $\mathbf{p} - \mathbf{q}$ plane, we obtain

$$\phi_{qk} \in \{0, \pi\}. \quad (4.88)$$

We get a factor 2 from the symmetry $q_y \leftrightarrow -q_y$ and insert the gluonic matrix element from Tab. 4.2 with the Debye-like screening approximation (4.49), and sum over

the possible values of $\cos \phi_{qk}$, 1 and -1. Thus we obtain, for a momentum cutoff $\Lambda_\perp > 2\tilde{k}$,

$$\begin{aligned}\hat{q}_{\text{ff}}^{yy} &= \frac{d_A C_A^2 A^2 g^4 Q^6}{2^6 \pi^5 \nu \tilde{k}^3} \int_0^{2\tilde{k}} dq q \frac{\left(2\tilde{k} - \sqrt{4\tilde{k}^2 - q^2}\right)^2 + \left(2\tilde{k} + \sqrt{4\tilde{k}^2 - q^2}\right)^2}{(q^2 + \xi^2 m_D^2)^2} \\ &= \frac{d_A C_A^2 A^2 g^4 Q^6}{(2\pi)^5 \nu \tilde{k}^3} \int_0^{2\tilde{k}} dq q \frac{8\tilde{k}^2 - q^2}{(q^2 + \xi^2 m_D^2)^2}.\end{aligned}\quad (4.89)$$

The integral over q can be performed analytically, which yields

$$\hat{q}_{\text{ff}}^{yy} = \frac{d_A C_A^2 A^2 g^4}{2^7 \pi^5 d_R \tilde{k}^3} Q^6 \left\{ 4\tilde{k}^2 \left(\frac{2}{\xi^2 m_D^2} - \frac{1}{4\tilde{k}^2 + \xi^2 m_D^2} \right) + \ln \frac{\xi^2 m_D^2}{4\tilde{k}^2 + \xi^2 m_D^2} \right\}, \quad (4.90)$$

where $m_D^2 = A \frac{g^2 Q^3}{\pi^2 \tilde{k}}$ according to Eq. (3.11).

Indeed, in Section 4.3.2 we will observe that in the over-occupied and anisotropic earliest stage of bottom-up thermalization one has $\hat{q}^{zz} < \hat{q}^{yy}$ and that this is due to $\hat{q}_{\text{ff}}^{zz} < \hat{q}_{\text{ff}}^{yy}$, which is consistent with the simple toy model presented here.

Scaled thermal distribution

Let us now study another aspect encountered during bottom-up thermalization: over and under-occupied systems. For simplicity, we use an isotropic toy model and consider a scaled thermal distribution, i.e., we scale the amplitude of the thermal distribution (4.57) with N_\pm . Here N_+ denotes the scaling parameter of the Bose-Einstein distribution and N_- the scaling parameter of the Fermi-Dirac distribution,

$$f_\pm(k; T) = \frac{N_\pm}{\exp(k/T) \mp 1}. \quad (4.91)$$

This allows us to easily generalize the results obtained in Section 4.2.1 for the jet quenching parameter \hat{q} in a thermal medium. We start with \hat{q} given by Eq. (4.62). Splitting the f and ff contributions and using the integrals (4.63) over thermal distributions, we obtain for small cutoff

$$\begin{aligned}\hat{q}(\Lambda_\perp \ll T, N_\pm) &= \frac{g^4 T^3 C_R}{24 \pi^3} \ln \left(1 + \frac{\Lambda_\perp^2}{m_D^2} \right) \\ &\times \left(\pi^2 (2N_c(N_+)^2 + n_f(N_-)^2) + \zeta(3) [9n_f N_-(1 - N_-) - 12N_c N_+(N_+ - 1)] \right),\end{aligned}\quad (4.92)$$

which generalizes the equilibrium ($N_\pm = 1$) result in Eq. (4.65). Similarly, we can generalize the large cutoff formula (4.77a) to

$$\hat{q}(\Lambda_\perp \gg T, N_\pm) = C_R \frac{g^4 T^3}{\pi^2} \sum_\pm \Xi_\pm \mathcal{I}_\pm(\Lambda_\perp, N_\pm), \quad (4.93a)$$

$$\mathcal{I}_\pm(\Lambda_\perp, N_\pm) = \frac{N_\pm \zeta_\pm(3)}{2\pi} \ln \left(\frac{\Lambda_\perp}{m_D} \right) + (N_\pm)^2 \Delta \mathcal{I}_\pm, \quad (4.93b)$$

with $\Delta \mathcal{I}_\pm$ given by Eq. (4.77c), which entirely determines \hat{q}_{ff} ,

$$\hat{q}_{\text{ff}}(\Lambda_\perp \gg T, N_\pm) = C_R \frac{g^4 T^3}{\pi^2} \sum_\pm (N_\pm)^2 \Xi_\pm \Delta \mathcal{I}_\pm. \quad (4.93c)$$

Furthermore, similarly to our discussion for the thermal result in Section 4.2.1, by replacing $2\ln(\Lambda_\perp/m_D) \rightarrow \ln(1 + (\Lambda_\perp/m_D)^2)$ in (4.93b), we obtain an ‘improved’ formula valid for large cutoffs that is finite even at small Λ_\perp and generalizes Eq. (4.78a). Then we can again split off the Bose-enhanced contribution as in (4.56), $\hat{q} = \hat{q}_f + \hat{q}_{ff}$. We note that $\hat{q}_f(\Lambda_\perp)$ has the same form for small and large cutoffs,

$$\hat{q}_f(\Lambda_\perp, N_\pm) = \zeta(3) (12N_+N_c + 9n_fN_-) C_L(\Lambda_\perp), \quad (4.94a)$$

with, as before, $C_L(\Lambda_\perp) = \frac{g^4 T^3 C_R}{24\pi^3} \ln\left(1 + \frac{\Lambda_\perp^2}{m_D^2}\right)$. Again, the Bose-enhanced terms differ

$$\hat{q}_{ff}(\Lambda_\perp \ll T, N_\pm) = \left[2N_c(N_+)^2(\pi^2 - 6\zeta(3)) + n_f(N_-)^2(\pi^2 - 9\zeta(3)) \right] C_L(\Lambda_\perp), \quad (4.94b)$$

$$\begin{aligned} \hat{q}_{ff,im}(\Lambda_\perp \gg T, N_\pm) &= C_R g^4 T^3 \sum_{\pm} \Xi_{\pm}(N_\pm)^2 \\ &\times \left\{ \frac{\zeta_{\pm}(2) - \zeta_{\pm}(3)}{4\pi^3} \left[\ln\left(1 + \frac{T^2}{m_D^2}\right) + 1 - 2\gamma_E + 2\ln 2 \right] - \frac{\sigma_{\pm}}{2\pi^3} \right\}. \end{aligned} \quad (4.94c)$$

The Debye mass entering these expressions for the scaled thermal distributions is given by (see Eq. (3.11))

$$m_D^2 = \frac{g^2 T^2}{3} \left(N_+ N_c + \frac{N_- n_f}{2} \right). \quad (4.95)$$

Thus, m_D scales with $\sqrt{\lambda N_\pm}$. The occupation of fermions N_- cannot become large due to Pauli blocking. For large gluon occupancies N_+ , this may pose a problem for the validity of perturbation theory that requires $m_D \ll T$ and that our arguments and the derivations in [101] are based on. We can estimate the breakdown scale by requiring $m_D \ll T$, which leads to

$$N_+ \ll \frac{1}{N_c} \left(\frac{3}{g^2} - \frac{N_- n_f}{2} \right). \quad (4.96)$$

This is, of course, in line with the usual limitations of perturbation theory, which breaks down at nonperturbatively large occupation numbers $f \gtrsim 1/g^2$.

Let us now compare these expressions with a numerical evaluation of \hat{q} using Eq. (4.45). For a purely gluonic system, the individual contributions \hat{q}_f/λ and \hat{q}_{ff} (from Eqs. (4.94)) depend only on the product λN_+ , and not on the coupling λ and occupation N_+ individually.⁶

$$\hat{q}(\Lambda_\perp, N_+, \lambda) = \lambda \left(\frac{\hat{q}_f}{\lambda} \right) (\Lambda_\perp, \lambda N_+) + \hat{q}_{ff}(\Lambda_\perp, \lambda N_+). \quad (4.97)$$

These contributions are plotted in Fig. 4.6 for small (left) and large (right) cutoffs $\Lambda_\perp = 0.2T$ and $10T$, respectively, divided by the prefactor

$$\hat{q}_f \sim \lambda(\lambda N_+) T^3, \quad \hat{q}_{ff} \sim (\lambda N_+)^2 T^3. \quad (4.98)$$

⁶ The Debye mass entering the matrix element depends only on the product λN_+ (see Eq. (3.11)). The quantum part \hat{q}_f comes naturally with a factor N_+ from the single distribution function and a factor λ^2 from the matrix element, and thus \hat{q}_f/λ is only a function of the product λN_+ . The classical wave contribution \hat{q}_{ff} comes naturally with a prefactor $\lambda^2 N_+^2$.

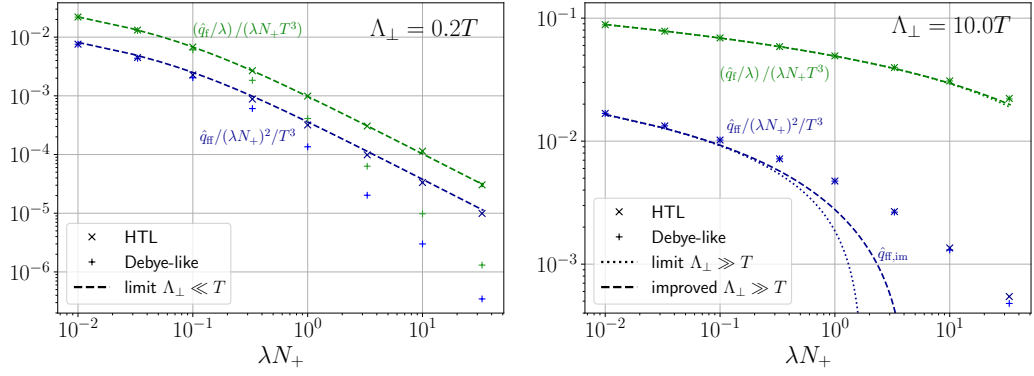


Figure 4.6: The individual components \hat{q}_f (green) and \hat{q}_{ff} (blue) as defined in (4.56) and rescaled according to their parametric estimates in (4.98) as functions of their only argument λN_+ for $\Lambda_\perp/T = 0.2$ (left) and $\Lambda_\perp/T = 10$ (right). The isoHTL screened results are shown with 'x'-symbols, and the Debye-like screened results are shown as '+'-symbols. The left panel shows the small-cutoff form (4.94b) for \hat{q}_{ff} and Eq. (4.94a) for \hat{q}_f labeled as " $\Lambda_\perp \ll T$ ". The right panel depicts both large-cutoff expressions (4.94a) for \hat{q}_f and (4.93c) for \hat{q}_{ff} labeled "limit $\Lambda_\perp \gg T$ " and its improved version (4.94c) labeled as "improved $\Lambda_\perp \gg T$ ". Figures adapted from [2].

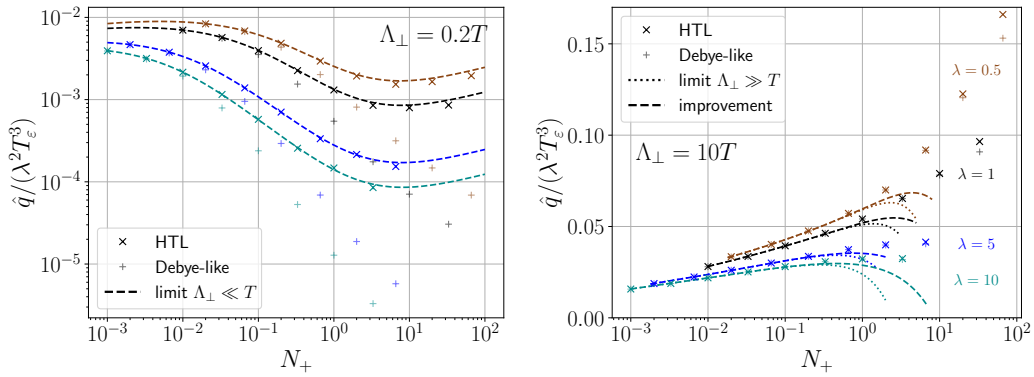


Figure 4.7: The jet quenching parameter \hat{q} for a scaled thermal distribution (4.91) as a function of N_+ for different couplings λ for cutoff $\Lambda_\perp/T = 0.2$ (left) and $\Lambda_\perp/T = 10$ (right). As in Fig. 4.6, the isoHTL results are shown with x-symbols, and Debye-like screened results as + symbols. In the left panel, the small-cutoff form (4.92) is labeled as " $\Lambda_\perp \ll T$ ". The right panel shows both the large-cutoff expression Eq. (4.93a) labeled as "limit $\Lambda_\perp \gg T$ " and the improved version obtained by summing Eqs. (4.94a) and (4.94c) labeled as "improvement". Figures adapted from [2].

We observe that their values deviate significantly from the simple estimates in Eq. (4.98). This is a consequence of screening effects and the scaling of the Debye mass. In particular, one finds for sufficiently small cutoffs $\Lambda_\perp \lesssim m_D, T$ and large occupancies that

$$\frac{\hat{q}_f}{\lambda^2 N_+ T^3} \sim \frac{\hat{q}_{ff}}{\lambda^2 N_+^2 T^3} \sim \frac{\Lambda_\perp^2}{m_D^2} \sim (\lambda N_+)^{-1}, \quad (4.99)$$

which is visible in the left panel of Fig. 4.6 for sufficiently large λN_+ . Note that for a sufficiently large $\lambda N_+ \gg 1$ the effective kinetic theory description used here ceases to be valid. Similarly to the equilibrium case discussed in Section 4.2.1 and particularly in Fig. 4.4, the expression for small cutoffs (4.92) nicely agrees with the numerical values in the small-cutoff asymptotic region, plotted in the left panel of Fig. 4.6. In the right panel, for large cutoffs, we observe that the analytic form for \hat{q}_f in Eq. (4.94a) remains a very good description coinciding with the numerical values, whereas the analytic estimate for \hat{q}_{ff} in Eq. (4.93c) (and its improvement Eq. (4.94c)) ceases to describe the data for nonperturbatively large occupancies $\lambda N_+ \gtrsim 1$. This is expected from the condition (4.96), and we see sizable deviations already at $\lambda N_+ \gtrsim 0.1$.

The full HTL screening and the Debye-like screening (4.49) nicely agree with each other at large cutoffs for the whole λN_+ range despite the aforementioned limitations concerning \hat{q}_{ff} . On the other hand, for small cutoffs (left panel), the Debye-like screening approximation shows large deviations from the full HTL screening, albeit in the large λN_+ region which should be taken with caution, as discussed above. The resemblance to the thermal case here is, of course, no coincidence since by setting $N_+ = 1$, we recover the thermal results.

Recombining the contributions from \hat{q}_f and \hat{q}_{ff} , we show \hat{q} in Fig. 4.7 for the couplings $\lambda = 0.5, 1, 2, 5$ and 10 as functions of the occupancy N_+ , for the small cutoff $\Lambda_\perp/T = 0.2$ in the left panel and the large cutoff $\Lambda_\perp/T = 10$ in the right panel. The values are shown scaled by the effective temperature T_ε that represents the temperature of a thermal system with the same energy density, Eq. (3.84),

$$T_\varepsilon = (N_+)^{1/4} T. \quad (4.100)$$

For comparison, also the analytic expectations are shown for small (4.92) and large cutoffs (4.93) as well as its improved expression (4.94). Similarly as for \hat{q}_f and \hat{q}_{ff} , we observe for \hat{q} in Fig. 4.7 that the small-cutoff expression agrees well with our (HTL-)screened data points while the large-cutoff expressions describe the data points until $N_+ \lesssim 1/\lambda$. Moreover, the improved formula for large cutoffs increases the validity of the analytic result only to slightly larger occupancy N_+ . This plot emphasizes the importance of screening effects that prevent the naïve scaling with N_+ or N_+^2 . We, therefore, should be cautious when using such analytic expressions to describe over-occupied systems with typical occupancies $N_+ \sim 1/\lambda$. Instead, transport coefficients in such systems can be studied using classical-statistical lattice simulations [152, 153, 157, 213]. In particular, it has been shown [213] that nonperturbative corrections can be substantial.

Interestingly, as visible in Fig. 4.7, increasing the occupancy N_+ does not appear to drastically increase the value of the jet quenching parameter \hat{q} . In particular, for small cutoff $\Lambda_\perp/T = 0.2$ visible in the left panel, we observe that the scaled \hat{q} in fact

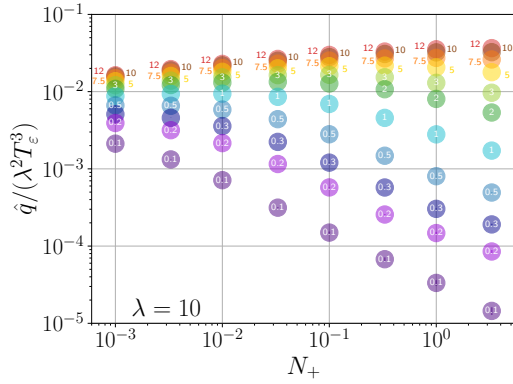


Figure 4.8: Jet quenching parameter \hat{q} for a scaled Bose-Einstein distribution (4.91) as a function of its amplitude N_+ for different momentum cutoffs Λ_\perp (numbers in circle markers) and coupling $\lambda = 10$. Figure from [2].

decreases with increasing occupancy. Even for large cutoffs (right panel), increasing the occupancy by several orders of magnitude only leads to a slight increase in the jet quenching parameter. This behavior is due to a combination of two effects. The first effect is that the increasing occupation number also increases the Debye mass m_D . Thus, a detailed understanding of screening effects is particularly important for a quantitative analysis of \hat{q} . The second effect comes from dividing the value of \hat{q} by the third power of the effective temperature $T_\varepsilon \sim N_+^{1/4}$, which increases with the occupancy when the hard momentum scale T is kept fixed.

Fig. 4.8 provides an overview of the numerical values of \hat{q} for the phenomenologically relevant coupling $\lambda = 10$ in heavy-ion collisions. Different values of the cutoff Λ_\perp are color-coded and written in the circle markers in the figure. We observe the same behavior at small and large cutoffs that we have found in Fig. 4.7. This involves a fast (power-law) decrease with growing occupancy N_+ at small cutoffs as $\hat{q}/(\lambda^2 T_\varepsilon^3) \sim N_+^{-3/4}$, and a slow growth at high cutoffs. We additionally see how \hat{q} interpolates smoothly between these two behaviors at small and large cutoffs. From a physical point of view, this confirms the observation that for small cutoffs, jet quenching in an over-occupied (isotropic) system similar to a scaled thermal distribution may be strongly suppressed. However, as stated below Eq. (4.99), these parameters may lie beyond the range of applicability of the original integral formula for \hat{q} , Eq. (4.21).

4.3 OBTAINING \hat{q} BETWEEN GLASMA AND HYDRODYNAMICS

Finally, let us consider the jet quenching parameter \hat{q} during a numerical simulation of the bottom-up thermalization process in heavy-ion collisions. This subsection is based on [1].

As already briefly discussed in the introduction, this is motivated by the large values of \hat{q} reported during the Glasma stage [152–157], while other studies require it to be negligible at these earliest times [76]. Importantly, different jet quenching studies treat the earliest stages before hydrodynamics becomes applicable differ-

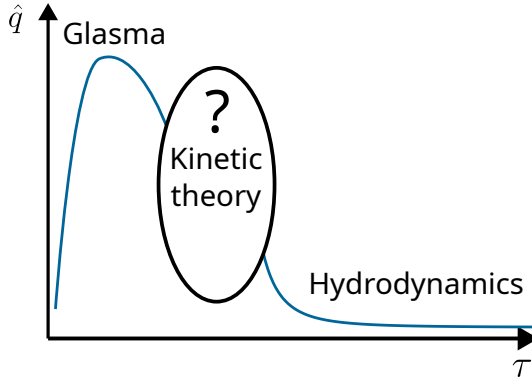


Figure 4.9: Sketch of the evolution of the jet quenching parameter \hat{q} during the initial stages in heavy-ion collisions, depicting the goal of this section: To obtain the jet quenching parameter between the Glasma and hydrodynamic stage. Figure from [1].

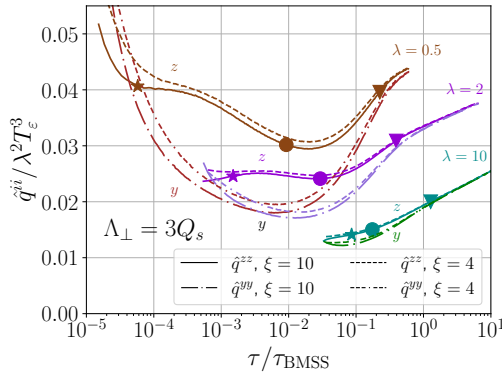


Figure 4.10: Jet quenching parameter in y and z directions rescaled by $\lambda^2 T_\varepsilon^3$ for momentum cutoff $\Lambda_\perp = 3Q_s$ for an expanding system for different couplings and initial conditions (solid: $\xi = 10$, dashed: $\xi = 4$). Figure adapted from [1].

ently [76, 147, 148, 151] with partly different conclusions, showing the need for a better theoretical understanding of jet quenching during the initial stages.

The goal of this section is to obtain the jet quenching parameter \hat{q} between the Glasma and hydrodynamic stage, as sketched in Fig. 4.9. To do that, the Boltzmann equation (3.76)

$$-\frac{\partial f_{\mathbf{p}}}{\partial \tau} + \frac{p_z}{\tau} \frac{\partial f_{\mathbf{p}}}{\partial p_z} = \mathcal{C}^{1 \leftrightarrow 2}[f_{\mathbf{p}}] + \mathcal{C}^{2 \leftrightarrow 2}[f_{\mathbf{p}}] \quad (4.101)$$

is solved to numerically obtain the distribution function $f(\mathbf{p}, t)$ throughout the pre-equilibrium evolution, which is used as input for calculating the jet quenching parameter via Eq. (4.45). The distribution function is initialized with the initial conditions described in Section 3.6.2 with anisotropy parameters $\xi_0 \in \{4, 10\}$. In the elastic collision kernel, soft-gluon exchanges are regulated using the Debye-like screening prescription as discussed in Section 3.3.2.

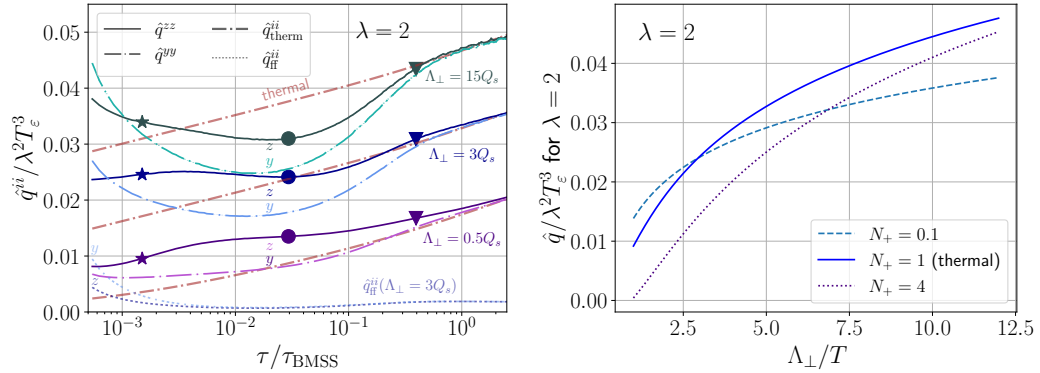


Figure 4.11: (Left): Evolution of \hat{q}^{zz} and \hat{q}^{yy} for a quark jet during bottom-up thermalization for $\lambda = 2$ and different cutoffs Λ_\perp . The Bose enhanced contributions \hat{q}_{ff}^{ii} for $\Lambda_\perp = 3Q_s$ are added as dotted curves of the same color, visible at the bottom of the figure. For comparison, thermal curves for the same $T_\epsilon(\tau)$ are shown as brown dash-dotted lines. Figure adapted from [1]. (Right): Jet quenching parameter for a scaled thermal distribution with different scaling coefficients N_+ as a function of the transverse momentum cutoff Λ_\perp . Figure from [2].

4.3.1 Results for a fixed momentum cutoff Λ_\perp

We start by discussing the resulting jet quenching parameter \hat{q} at fixed transverse momentum cutoffs Λ_\perp and later generalize this to more realistic models of evolving (time-dependent) momentum cutoffs. As discussed in Section 4.1.4, the mixed components $\hat{q}^{yz} = \hat{q}^{zy} = 0$ vanish due to symmetry arguments, so we need to focus here only on the diagonal components $\hat{q}^{zz}(\tau)$ and $\hat{q}^{yy}(\tau)$. They are plotted in Fig. 4.10 for a cutoff $\Lambda_\perp = 3Q_s$ for different couplings and initial anisotropy parameters $\xi_0 = 10$ (solid lines) and $\xi_0 = 4$ (dashed lines). For these anisotropy parameters, we find little sensitivity regarding varying the initial conditions, less than 15% for the considered parameters, and observe qualitatively similar behavior for different couplings.

To further study the evolution of \hat{q}^{ii} , Fig. 4.11 shows their values for different cutoffs Λ_\perp for anisotropy parameter $\xi_0 = 10$ and coupling $\lambda = 2$. Qualitatively similar effects can also be found for other couplings, and $\lambda = 2$ is chosen for illustrative purposes. The estimates for an energy-density matched (see Eq. (3.84)) thermal system $\hat{q}_{\text{therm}}^{ii} = \frac{1}{2} \hat{q}_{\text{therm}}$ are also shown as dash-dotted lines and are obtained by evaluating Eq. (4.45) with a thermal distribution. For that, the empirical formula (4.81) from Section 4.2.1 is used with the p_{\min} corrected Debye mass (3.87) to account for discretization artifacts. The contribution from the Bose-enhanced \hat{q}_{ff} term is shown separately as dotted lines. We observe that in general, the order of magnitude of \hat{q}^{ii} follows the energy-density matched thermal values. During the earliest stage of bottom-up thermalization, which is characterized by overoccupation and extreme anisotropy and consists of the time before the star markers, the results of \hat{q} are above the energy-density matched thermal ones.

In the next stage, and in particular, when minimum occupancy is reached (marked by the circles), the values for large cutoffs Λ_\perp undershoot the thermal ones, while those for a small cutoff overshoot them. This behavior can be understood by

considering the scaled thermal distribution studied in the previous section 4.2.2. The analytic expression for \hat{q} for a scaled thermal distribution, Eq. (4.93), is shown for different occupancies in the right panel of Fig. 4.11. Similarly, as in the left panel, when increasing the cutoff Λ_\perp , the thermal \hat{q} first underpredicts the actual under-occupied \hat{q} , and this ordering reverses when the cutoff is increased. This simple toy model for an under-occupied distribution, thus, provides an intuitive explanation of the ordering of the thermal and nonthermal curves during the under-occupied regime in the bottom-up evolution.

Finally, approaching thermal equilibrium (signaled by the triangle markers), the values of \hat{q}^{ii} also approach the thermal expectation. An interested reader might wonder why the thermal values seem to grow over time. This is because we consider $\hat{q}(\tau)$ at a fixed transverse momentum cutoff Λ_\perp , but due to Bjorken expansion, all scales in the plasma continuously decrease. Thus, effectively, the cutoff increases and the rise observed in the jet quenching parameter comes from this increase.

For almost the entire evolution we find that momentum broadening in the beam direction is larger than transverse to it, $\hat{q}^{zz} > \hat{q}^{yy}$. This seems to be typical for anisotropic systems with occupancies up to order unity, as has been found for transport coefficients in the context of kinetic theory [131, 132]. It should be emphasized that in our formulation, this ordering is a result of the anisotropic under-occupied distribution and, thus, does not stem from the matrix element for which an isotropic HTL screening prescription is used. It leads to a sizable difference in the total momentum broadening in different directions. Moreover, a low momentum cutoff can be associated with the momentum broadening of the plasma constituents themselves. Thus the larger broadening in the z direction for smaller Λ_\perp is consistent with the isotropization dynamics in the bottom-up scenario. Remarkably, jet quenching studies in the Glasma [152, 153, 157] have revealed a similar ordering $\hat{q}^{zz} > \hat{q}^{yy}$ as we find for most of the evolution of \hat{q} in our kinetic simulations, although for a different reason. There the enhancement of \hat{q}^{zz} seems to stem primarily from a slight asymmetry between the chromo-magnetic and -electric fields in the underlying classical-statistical description of the Glasma.

Interestingly, we find that for large cutoffs the ordering is reversed at early times before the star marker, leading to $\hat{q}^{zz} < \hat{q}^{yy}$. This mainly stems from the Bose enhancement of the over-occupied plasma phase at the beginning of the evolution. To see this, consider the Bose-enhancement part \hat{q}_{ff} of \hat{q} shown in Fig. 4.10 separately for the y and z directions. Note that \hat{q}_{ff} is finite in the limit $\Lambda_\perp \rightarrow \infty$, and the value at $\Lambda_\perp = 3Q_s$ that is plotted is already close to that limit. While for the non-Bose enhanced term \hat{q}_f , the anisotropy $p_z \ll p_\perp$ leads to $\hat{q}_f^{zz} > \hat{q}_f^{yy}$, for the Bose-enhanced term the effect is the opposite, $\hat{q}_{ff}^{zz} < \hat{q}_{ff}^{yy}$. This ordering can be understood from studying the extremely anisotropic effectively two-dimensional distribution in Section 4.2.2. There, we found that in the limit of extreme anisotropy (no particles moving in the z direction), $\hat{q}_{ff}^{zz} = 0$, which explains the ordering $\hat{q}_{ff}^{zz} < \hat{q}_{ff}^{yy}$ shown in Fig. 4.11.

Finally, as in the previous sections, let us compare differently screened matrix elements for the evaluation of the jet quenching parameter \hat{q} . In Fig. 4.12, we show the components \hat{q}^{ii} for both the isoHTL screened matrix element ((4.47), solid lines) and the Debye-like screened matrix element ((4.49), dotted lines). We find that

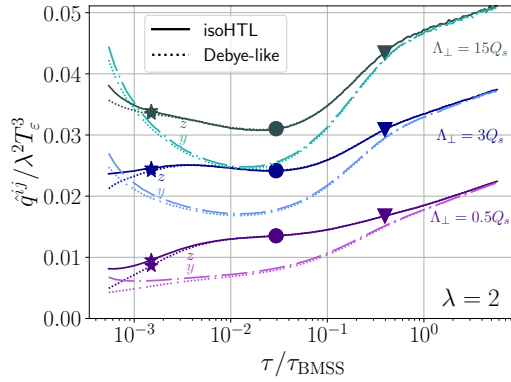


Figure 4.12: Components of the jet quenching parameter \hat{q}^{ii} for differently screened matrix elements. Solid lines: isoHTL screening, dotted lines: Debye-like screening. Figure adapted from Ref. [1].

these two screening prescriptions only slightly differ at early times and for smaller cutoffs (as expected).

Note, however, that in the matrix element in the elastic collision term of the Boltzmann equation, always the Debye-like screened matrix element is used. We will study the effects of using the isoHTL screening for the time evolution in Chapter 6.4.8.

4.3.2 Results for realistic cutoff dependence

Kinematic and LPM cutoff

Until now, we have studied the jet quenching parameter \hat{q} using a fixed cutoff Λ_\perp . This is unphysical since during the plasma expansion all characteristic energy scales decrease. To account for this, we choose cutoff models that depend on the jet energy E_{jet} and effective plasma temperature T_ϵ , introduced and motivated in Section 4.1.9,

$$\Lambda_\perp^{\text{LPM}}(E_{\text{jet}}, T_\epsilon) = \zeta^{\text{LPM}} g \times (E_{\text{jet}} T_\epsilon^3)^{1/4}, \quad (4.102a)$$

$$\Lambda_\perp^{\text{kin}}(E_{\text{jet}}, T_\epsilon) = \zeta^{\text{kin}} g \times (E_{\text{jet}} T_\epsilon)^{1/2}. \quad (4.102b)$$

Recall that the first cutoff model $\Lambda_\perp^{\text{LPM}}$ is a rough estimate of the accumulated transverse momentum during the formation time of a gluon emission during the LPM regime. Variants of the kinematic cutoff model $\Lambda_\perp^{\text{kin}}$ have been widely used in the literature (see, e.g., [114, 115, 118, 120, 149, 209–211]) and take into account that the plasma particles the jet scatters off have momentum $k \sim T$. These arguments only provide parametric estimates, so we have included a (so far unknown) proportionality constant $\zeta^{\text{...}}$, which will be determined by requiring that \hat{q} reproduces some reference value. It should be emphasized here that \hat{q} is regarded as a medium property relevant for a jet with an appropriate fixed energy E_{jet} and we do not study the actual evolution of a jet.

We do not expect any substantial differences between these two cutoff models (4.102) since the dependence of \hat{q} on the cutoff is only logarithmic for large Λ_\perp ,

$$\hat{q}^{ii}(\Lambda_\perp \gg T_e) \simeq a_{\Lambda_\perp}^i \ln \frac{\Lambda_\perp}{Q_s} + b_{\Lambda_\perp}^i. \quad (4.103)$$

In practice, we fit the coefficients $a_{\Lambda_\perp}^i$ and $b_{\Lambda_\perp}^i$ to the large cutoff behavior of the numerically obtained values for \hat{q} . Although, as discussed in Section C.2.2, the coefficients $a_{\Lambda_\perp}^i$ should be the same for different directions, we employ here a more general parametrization, allowing for differences in different directions. The resulting coefficients $a_{\Lambda_\perp}^y$ and $a_{\Lambda_\perp}^z$ differ only slightly. The numerical values of $a_{\Lambda_\perp}^i/Q_s^3$ and $b_{\Lambda_\perp}^i/Q_s^3$ as functions of $Q_s \tau$ for $\lambda = 0.5, 1, 2, 5$ and 10 for the initial conditions in Eq. (3.77) are publicly available in [214].

Matching the Glasma: Problems and strategy employed here

One of our goals is to make contact with the large \hat{q} values reported in the Glasma [152, 153, 155, 157], and to assess whether these large values reported there are plausible from a kinetic theory perspective. To achieve that, ideally, we would take at some time, e.g., $\tau_0 = 1/Q_s$, the full configuration obtained in a classical statistical simulation of the Glasma, extract a gluon distribution function (as, e.g., done in Ref. [201, 202]) and use this as input for our kinetic theory simulation. Performing this matching seems feasible in principle but is very complicated in practice, particularly because the Glasma simulations that are used to obtain values for the jet quenching parameter \hat{q} in Refs. [153, 157] employ a boost-invariant approximation (they are effectively 2+1D simulations). From that, we cannot immediately obtain any information about the p_z dependence of the gluon distribution function $f(\mathbf{p}, \tau_0)$, which, physically, broadens due to plasma instabilities [35, 215, 216].

As discussed in Section 3.6.2, as a first step, a parameterization of the JIMWLK evolved (2+1D) Glasma result from Ref. [203] is used, which we also use as initial condition (3.77), similar to what is done in Ref. [22]. There, the p_z dependence is then obtained by “de-”squeezing the transverse momentum $p_\perp \rightarrow \sqrt{p_\perp^2 + \xi_0^2 p_z^2}$. To make a meaningful comparison to the Glasma results, the value of Q_s is chosen such that the energy density of the Glasma in Ref. [153] is reproduced at the initial time $Q_s \tau = 1$ for coupling $\lambda = 10$. We allow for a different value of Q_s^{Glasma} in Glasma simulations that might not correspond to the value of Q_s we use due to different definitions and conventions. For the Glasma simulation in Ref. [153], $Q_s^{\text{Glasma}} = 2 \text{ GeV}$ and $m/(g^2 \mu) = 0.1$ with 50 color sheets have been used, where $g^2 \mu$ and Q_s^{Glasma} are related as in Ref. [217]. Performing the matching of the energy density at $Q_s \tau = 1$ (which is an implicit equation requiring as input the energy density $\varepsilon^{\text{Glasma}}(\tau)$ from Ref. [153]) yields a value of $Q_s = 1.4 \text{ GeV}$. Remarkably, this is the same value as obtained in Ref. [204], where it was found that precisely this value is needed for the EKT setup to be consistent with the later hydrodynamic evolution. This shows the consistency of both approaches.

To summarize, the matching is performed both in the form of the distribution function (parameterized and squeezed [22]) and the energy density.

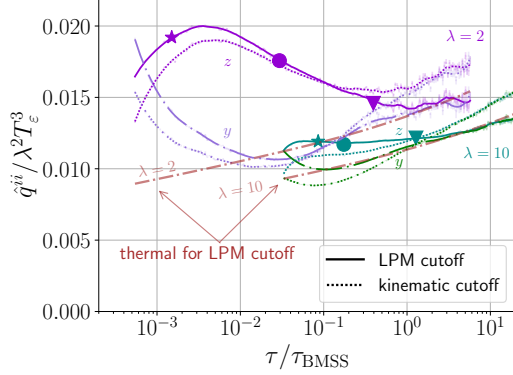


Figure 4.13: Evolution of \hat{q}^{yy} and \hat{q}^{zz} for the cutoff models in (4.102a) (solid) and (4.102b) (dashed) with jet energy $E_{\text{jet}} = 100 \text{ GeV}$, $Q_s = 1.4 \text{ GeV}$ and T_ϵ extracted from the plasma simulation for $\xi = 10$. The curves were smoothed using a Savitzky-Golay filter, while the original curves with estimated error bars are shown transparently beneath. Thermal curves for the LPM cutoff model are included for comparison. Figure adapted from [1].

Numerical results

We fix the values of the parameters ζ^{\dots} in Eq. (4.102) at the triangle marker close to thermal equilibrium. At this time, where the temperature is $T_\epsilon = 0.21 Q_s = 295 \text{ MeV}$ for a realistic coupling $\lambda = 10$. More concretely, we require the jet quenching parameter \hat{q} to match the median value for \hat{q}_{therm} in the LBT parametrization of Ref. [115] by the JETSCAPE collaboration in order to be close to a traditional numerical estimate for a thermal distribution. For $E_{\text{jet}} = 100 \text{ GeV}$, one finds the numerical values $\zeta^{\text{LPM}} = 0.70$ and $\zeta^{\text{kin}} = 0.16$, whereas for $E_{\text{jet}} = 20 \text{ GeV}$ the values $\zeta^{\text{LPM}} = 1.14$ and $\zeta^{\text{kin}} = 0.40$ are obtained. We will discuss different matching conditions in the next subsection, which, importantly, do not significantly change the results.

Fig. 4.13 shows the resulting \hat{q}^{yy} and \hat{q}^{zz} for the anisotropy parameter $\xi_0 = 10$ and jet energy $E_{\text{jet}} = 100 \text{ GeV}$. Both cutoff parametrizations of Eq. (4.102) are shown for different values of the coupling λ (color-coded). We find that the evolution of \hat{q}^{yy} is similar as for fixed cutoffs, with $\hat{q}^{yy} > \hat{q}^{zz}$ for most of the nonequilibrium evolution except for a short period of reversed ordering at the beginning for $\lambda = 2$. In particular, longitudinal momentum broadening is more efficient than expected from a thermal system, as indicated by the dashed thermal line for comparison, which we only show for the LPM cutoff (4.102a). As anticipated, both cutoff models lead to similar results, with the LPM cutoff yielding systematically larger values than the kinematic cutoff model during the pre-hydrodynamic evolution. For $\lambda = 10$ they differ by less than 20%, while the variation of initial anisotropies has a much smaller impact, as we have seen in Fig. 4.10.

This relatively mild sensitivity to the initial parameters and cutoff models enables us to obtain results for \hat{q} throughout the pre-equilibrium stages, effectively extrapolating backward from a fit to a phenomenological extraction by the JETSCAPE collaboration at the triangle time marker close to equilibrium. The results of this procedure are shown in Fig. 4.14 for jet energies $E_{\text{jet}} = 20 \text{ GeV}$ and 100 GeV . Varia-

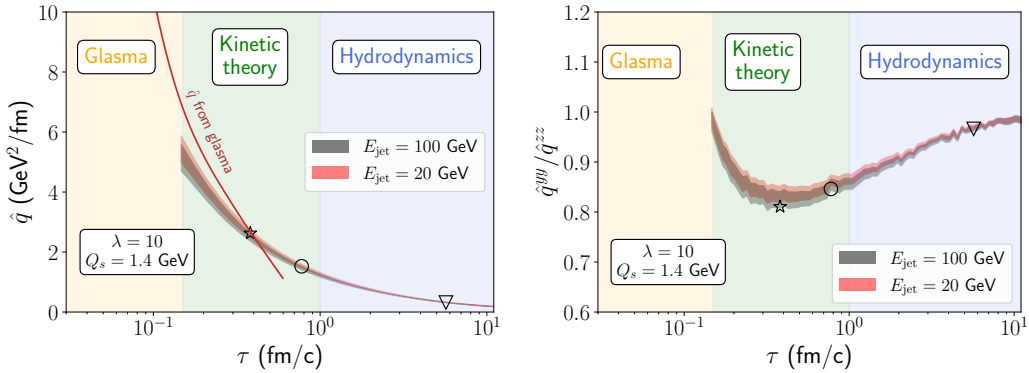


Figure 4.14: Jet quenching parameter \hat{q} during the initial stages in heavy-ion collisions. Different regions with different effective descriptions are color-coded. (Left): Jet quenching parameter for different jet energies and varying cutoff models (bands) and comparison to the Glasma results from [153]. (Right): Anisotropy ratio $\hat{q}^{yy}/\hat{q}^{zz}$ during the initial stages. Figures reused from Ref. [1].

tions in cutoff models and initial conditions are represented in the bands. With the procedure described above to fix the cutoff, we find that the bands for different jet energies almost overlap.

Additionally, the numerical results of the Glasma calculation of Ref. [153] are also included in Fig. 4.14. We observe that at $\tau \sim 0.2 \text{ fm}/c$, the jet quenching parameter $\hat{q} \approx 4 - 5 \text{ GeV}^2/\text{fm}$, which is comparable (but not identical) to the values during the Glasma regime at this time. It should be noted that we do not precisely match the Glasma distribution function at our initialization time, and this matching should be regarded as a crude estimate. In particular, a similar matching procedure employed in Ref. [7] by the same authors leads to a much worse matching for a closely related transport parameter, the *heavy-quark diffusion coefficient* κ . This shows that the matching procedure here is perhaps too crude for a quantitative matching of the transport coefficients. However, this does not change the message of Ref. [1] that the seemingly large values of \hat{q} during the Glasma phase are plausible from a kinetic theory perspective.

Finally, the right panel shows the ratio of the jet broadening coefficients $\hat{q}^{yy}/\hat{q}^{zz}$ for these times, showing a suppression of up to 20% between the Glasma and the hydrodynamic regimes.

Note that the boundary between kinetic theory and hydrodynamics in Fig. 4.14 is—somewhat arbitrarily—chosen to be $\tau = 1 \text{ fm}/c$ to give an estimate of where typical hydrodynamic evolution is expected to be valid. The actual numerical values shown in the plots are all obtained using kinetic theory, as discussed in Section 4, and it should be noted that at late times QCD kinetic theory simulations are indistinguishable from hydrodynamics (see Fig. 3.3).

Matching different cutoffs

A perhaps unsatisfying aspect of the previous discussion is that in order to present numerical results, we were required to fix the proportionality constants introduced in (4.102) to reproduce a reference value of the jet quenching parameter \hat{q} . For that, we chose to use the JETSCAPE result [15] obtained from Bayesian inference,

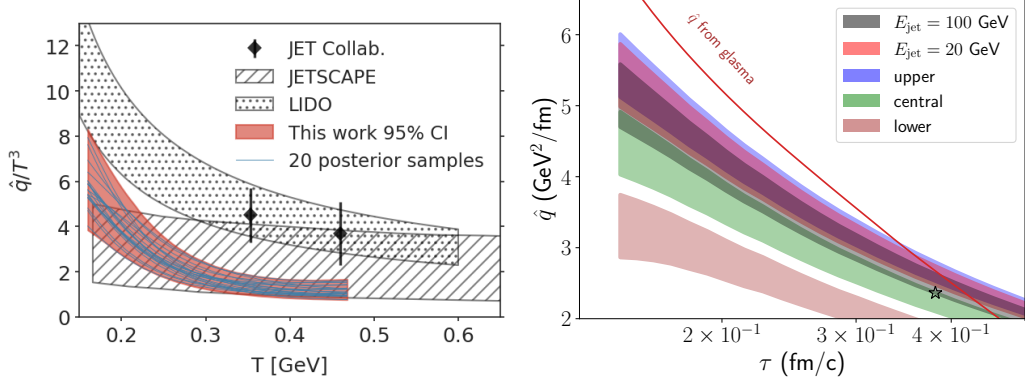


Figure 4.15: (Left): Temperature dependence of \hat{q} resulting from an information field based Bayesian inference. Figure from [116]. (Right): Early-time behavior of \hat{q} (jet energy 50 GeV) for different cutoff matchings from Ref. [116], as explained in the text. Figure from [1].

because a convenient and simple parameterization is provided there. However, it is an interesting question to which extent the results would change had we chosen to fix the cutoff in a different way. Here, we explore matching to the values from Ref. [116] for comparison, which are depicted in the left panel of Fig. 4.15. At the matching temperature $T_\epsilon = 295 \text{ MeV}$, their curves are consistent with the LBT model employed in the previous matching but exhibit a larger spread. To quantify the uncertainty in the extraction, we choose upper ($\hat{q} = 2.5T^3$), central ($\hat{q} = 2T^3$), and lower ($\hat{q} = 1.5T^3$) parts of the error band in the left panel of Fig. 4.15. While these values are independent of the jet energy, we choose $E_{\text{jet}} = 50 \text{ GeV}$ for Eqs. (4.102) to make a concrete comparison. The results (for the early times) are shown in the right panel of Fig. 4.15, where we observe that the upper and central values are compatible with the JETSCAPE parametrization and also consistent with the Glasma values, whereas the lower bound yields slightly smaller values.

4.4 CONCLUDING REMARKS

In this chapter, we studied how the jet quenching parameter \hat{q} can be obtained within QCD kinetic theory, both for finite jet energy and for the limit of an infinite jet energy with a transverse momentum cutoff Λ_\perp . We generalized earlier analytic calculations of this parameter to toy models relevant to the bottom-up thermalization process in heavy-ion collisions. In particular, we considered a scaled thermal distribution to model an under-occupied stage, and an effectively two-dimensional distribution, modeling the initial large anisotropy in heavy-ion collisions. Comparing with numerical results, we found that different screening prescriptions lead to different results for small couplings or cutoffs. In particular, we investigated HTL and Debye-like screening in the matrix element needed for the evaluation of \hat{q} . Furthermore, we found that the previous analytic expressions, which are derived in the weakly coupled limit, do not accurately describe the jet quenching parameter when extrapolated to larger values of the coupling, for which we provided a convenient parameterization.

Finally, we went on to study the jet quenching parameter \hat{q} during the Glasma and hydrodynamic phase at the early stages in heavy-ion collisions. We find that the numerical results for the jet quenching parameter \hat{q} follow roughly Landau-matched thermal estimates while exhibiting a sizable anisotropy $\hat{q}^{zz} > \hat{q}^{yy}$ for most of the pre-equilibrium evolution. This emphasizes the importance of going beyond approximating \hat{q} with its equilibrium value, which seems to systematically underestimate \hat{q} and is isotropic by construction.

The results of \hat{q} during the kinetic regime could be used in the future to extend current frameworks that employ a hydrodynamic medium evolution to extract \hat{q} from experimental data [114–116]. Although based on scattering processes with on-shell partons, the extracted values for \hat{q} can also enter jet evolution models in order to include medium effects during the initial large virtuality phase [151].

The anisotropy $\hat{q}^{zz} > \hat{q}^{yy}$ remains during most of the pre-hydrodynamic evolution including the Glasma and kinetic stages, and, thus, may leave imprints on experimental observables. In particular, it has been pointed out that such anisotropies in the jet quenching parameter lead to jet hadron polarization [218], and may be probed experimentally by studying spin-polarized and azimuthal jet observables [219].

In Chapter 8, we will consider the collision kernel $C(\mathbf{q}_\perp)$, which can be thought of as a generalization of the jet quenching parameter, during the initial stages in heavy-ion collisions.

5

LIMITING ATTRACTORS IN HEAVY-ION COLLISIONS

As discussed in the introduction, it has been found that the time evolution of the nonequilibrium QCD plasma generated in heavy-ion collision quickly follows a universal curve, the hydrodynamic attractor. This was first seen in the context of hydrodynamics, where the pressure anisotropy for various different initial conditions quickly collapses on the universal hydrodynamic attractor curve. Moreover, it has been found that a similar attractor exists for kinetic theory simulations at different couplings, when the time is rescaled with the relaxation time τ_R from Eq. (3.85b), $\tau_R = 4\pi\eta/s/T$ [27, 56]. However, as discussed in Section 3.5.2, there is another time scale involved when studying the bottom-up equilibration in heavy-ion collisions from kinetic theory. There, the equilibration time scales parametrically as $\tau_{\text{BMSS}} \sim \alpha_s^{-13/5}$. In this chapter, we discuss the relevance of these different time scales for the pressure ratio, jet quenching parameter and the *heavy-quark diffusion coefficient*, which is a related quantity describing the momentum diffusion of heavy-quarks in the quark-gluon plasma.

This chapter is based on Ref. [3].

5.1 TIME SCALES AND INITIAL CONDITIONS

In Section 3.5.2, we discussed how, in a weak-coupling picture, the out-of-equilibrium plasma created in heavy-ion collisions reaches equilibrium according to the bottom-up hydrodynamization picture [185]. Within this picture, the time scale for thermalization is given by the parametric estimate τ_{BMSS} from Eq. (3.67) (restated below), while first-order hydrodynamics is governed by the time scale τ_R , which is related to the shear viscosity over entropy ratio η/s (see Eq. (3.85b)),

$$\tau_{\text{BMSS}}(\lambda) = \alpha_s^{-13/5}/Q_s, \quad \tau_R(\lambda, \tau) = \frac{4\pi\eta/s(\lambda)}{T_\varepsilon(\tau)}. \quad (5.1)$$

Recall the relation for the coupling constant $\alpha_s = \lambda/(4\pi N_c)$. The numerical values of¹ $\eta/s(\lambda)$ can be obtained by using a functional basis [206] or by the late-time behavior of the pressure ratio (e.g., in [28]). We will discuss how to extract η/s in more detail in Chapter 6.4.8. For now, the values from Ref. [56] are used (given for

¹ In this thesis, only the ratio of the shear viscosity over entropy density η/s is considered, and this ratio depends on the coupling λ .

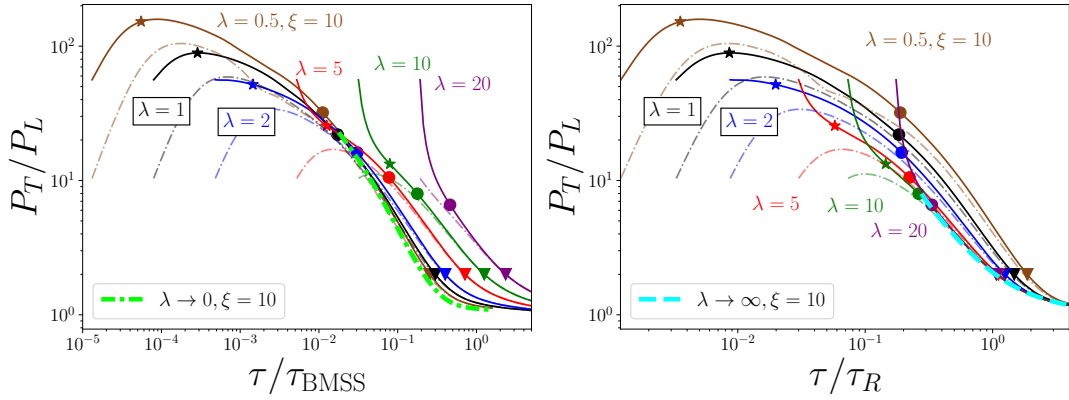


Figure 5.1: Pressure ratio as functions of τ/τ_{BMSS} (left) and τ/τ_R (right). The extrapolations to vanishing and infinite coupling (the limiting attractors) are performed for each value of τ as demonstrated in Fig. 5.2, and are denoted as thick dashed lines. Figures from Ref. [3].

$1 \leq \lambda \leq 10$). For $\lambda = 0.5$ and $\lambda = 20$, the values used here have been extracted² using the methods described in Chapter 6.4.8,

$$\frac{\eta}{s}(\lambda=0.5) = 80, \quad \frac{\eta}{s}(\lambda=20) = 0.22. \quad (5.2)$$

The equilibration process is simulated using QCD kinetic theory, as already employed in the previous Chapter 4.4. More details on the exact setup are detailed in Section 4. For that, the Boltzmann equation (3.76)

$$\left(\frac{\partial}{\partial \tau} - \frac{p_z}{\tau} \frac{\partial}{\partial p_z} \right) f(\tau, \mathbf{p}) = -\mathcal{C}^{1 \leftrightarrow 2}[f(\tau, \mathbf{p})] - \mathcal{C}^{2 \leftrightarrow 2}[f(\tau, \mathbf{p})], \quad (5.3)$$

is numerically solved to obtain the time evolution of the gluon distribution function $f(\mathbf{p}, \tau)$. Only gluons are considered, which are the dominant degrees of freedom for equilibration and hydrodynamization. As initial conditions, we employ Eq. (3.77), with $\xi_0 \in \{4, 10\}$. In the plots, also the time markers introduced in Section 3.6.4 are added: The star marker is placed when the occupancy drops below unity, the circle marker at minimum occupancy and the triangle marker at the time where the pressure ratio $P_L/P_T = 0.5$.

5.2 LIMITING ATTRACTORS IN THE PRESSURE RATIO

First, let us consider the pressure ratio P_T/P_L , obtained from the diagonal components of the energy-momentum tensor $T^{\mu\nu}$ from Eq. (3.82). Figure 5.1 shows the pressure ratio in units of both time scales: in the left panel as a function of τ/τ_{BMSS} and in the right panel as a function of τ/τ_R . We observe that for each coupling, the curves from different initial conditions with $\xi_0 = 4$ and 10 approach each other. This collapse of curves for various different initial conditions for a single coupling has already been extensively studied in the literature [58, 63, 64]. In the context of

² The values used here slightly differ from the values extracted in Section 6.4.4. This is because the current chapter is based on Ref. [3], which appeared earlier than Ref. [4], upon which Chapter 6.4.8 is based, where $\eta/s(\lambda = 0.5) \approx 77$ and $\eta/s(\lambda = 20) \approx 0.2$ is found using a more rigorous analysis.

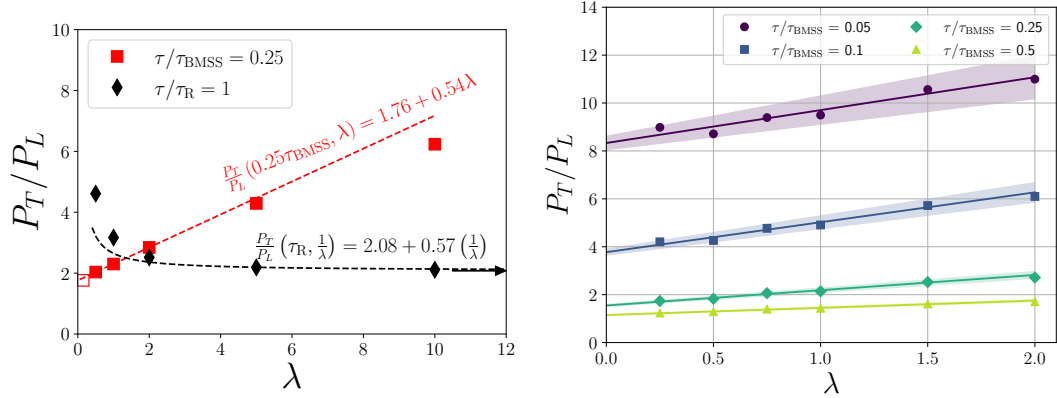


Figure 5.2: (Left): Pressure ratio at a fixed time as a function of the coupling λ in the units of both time scales. We also show the fits and their parametrizations, which are used to extrapolate to vanishing coupling (empty square) or infinite coupling (black arrow). Figure taken from [3]. (Right): Extrapolation procedure for the bottom-up limiting attractor for different times. Additional data points for $\lambda \in \{0.25, 0.75, 1.5\}$.

this chapter, it will be more interesting to compare simulations at different values of the coupling.

Let us start our discussion with the pressure ratio in the right panel of Fig. 5.1, where the time is rescaled with the relaxation time τ_R . For sufficiently large values of the coupling (consider $\lambda \geq 5$), the curves become indistinguishable after $\tau/\tau_R \gtrsim 0.3$. This serves as motivation to define a *limiting attractor* for large couplings, which can be obtained by extrapolating $\lambda \rightarrow \infty$ linearly in $1/\lambda$, i.e.,

$$\frac{P_T}{P_L}(\tau/\tau_R) = a(\tau/\tau_R) + b(\tau/\tau_R) \frac{1}{\lambda}, \quad (5.4)$$

where a and b are functions of the rescaled time τ/τ_R . We define the value of the limiting large coupling (hydrodynamic) attractor as the value of the coefficient $a(\tau/\tau_R)$, which is shown as a light-blue dashed line in Fig. 5.1. How quickly this hydrodynamic limiting attractor is approached, depends on the value of the coupling. For large values $\lambda \geq 5$, the approach occurs already close to the circle markers. In contrast, for weaker couplings $\lambda \leq 2$, we find that the hydrodynamic limiting attractor is approached at a significantly later time, even after the triangle marker.

In contrast to this, we show the pressure ratio plotted as a function of the time variable rescaled with the bottom-up time scale τ_{BMSS} in the left panel of Fig. 5.1. There, we observe a rather opposite picture, where the curves corresponding to smaller couplings seem to approach each other, even when the system is still far from equilibrium. Similarly as in the extrapolation to infinite coupling (5.4), we define a limiting weak-coupling *bottom-up* attractor obtained by extrapolating to vanishing coupling,

$$\frac{P_T}{P_L}(\tau/\tau_{\text{BMSS}}) = a(\tau/\tau_{\text{BMSS}}) + b(\tau/\tau_{\text{BMSS}}) \times \lambda, \quad (5.5)$$

with two different functions a and b of the rescaled time τ/τ_{BMSS} . Similarly, as before, the coefficient $a(\tau/\tau_{\text{BMSS}})$ gives the numerical value of the bottom-up limiting attractor and is shown as a green dash-dotted line in the figure.

We explicitly illustrate the extrapolation procedure that constructs the limiting attractors visible in Fig. 5.2. The left panel shows for each coupling λ the corresponding value of the pressure ratio P_T/P_L at a fixed rescaled time $\tau/\tau_{\text{BMSS}} = 0.25$. Performing the linear fit from (5.5) allows extrapolating to the limiting value of P_T/P_L for $\lambda \rightarrow 0$. Similarly, for fixed $\tau/\tau_R = 1$, the Eq. (5.4) leading to the hydrodynamic limiting attractor is shown as a black dashed curve in Fig. 5.2. One might argue that here a linear fit is performed using only a few points. To study the bottom-up limiting attractor in more detail, several additional³ kinetic theory simulations at weak couplings $\lambda \in \{0.25, 0.75, 1.5\}$ were performed, and used to obtain the bottom-up limiting attractor in the right panel of Fig. 5.2. There, we observe that for $\lambda \leq 2$, the values lie approximately on a straight line. The error bar shown in the figure is an estimate of the fit uncertainty from a linear regression procedure.

To summarize, we find that the pressure ratio at weak coupling between the circle and the triangle markers is better described using the bottom-up limiting attractor, while the hydrodynamic limiting attractor provides a better description for strong couplings after the triangle marker. However, it should be noted that at sufficiently late times, even for weak couplings, all curves converge to the hydrodynamic attractor, which is required by the fact that hydrodynamics emerges from kinetic theory close to equilibrium.

5.3 LIMITING ATTRACTORS FOR TRANSPORT COEFFICIENTS OF HARD PROBES

Having identified these limiting attractors in the pressure ratio, we may wonder about other quantities exhibiting similar behavior. In the context of this thesis, it is natural to consider the *jet quenching parameter* \hat{q} , which we have discussed extensively in the previous Chapter 4.4. Additionally, we will also consider the closely related *heavy-quark diffusion coefficient*.

5.3.1 Jet quenching parameter and heavy-quark diffusion coefficient

As discussed thoroughly in the previous Chapter 4.4, the *jet quenching parameter* \hat{q} quantifies the momentum broadening of jets, (see Eq. (1.4)),

$$\hat{q} = \frac{d\langle p_\perp^2 \rangle}{dt}. \quad (5.6)$$

For the derivation in the previous Chapter 4.4, we have taken the idealistic case of a massless jet particle with momentum much larger than all plasma scales. On

³ These additional simulations were performed about two years after those used in Ref. [3]. They use the same initial condition, but the improved adaptive time step employed in Ref. [4] and Chapter 6.4.8, and better discretization parameters. It can be clearly seen that this leads to a slight systematic shift in Fig. 5.2 (right panel) in the form that the newer runs with $\lambda \in \{0.25, 0.75, 1.5\}$ lie slightly above the straight-line fit, whereas the older results lie slightly below. Despite this small bias due to better accuracy, these additional runs further corroborate the results of Ref. [3] presented in the present chapter.

Particle	Momentum	Mass	$\frac{d\langle\Delta p_x^2\rangle}{dt}$	$\frac{d\langle\Delta p_y^2\rangle}{dt}$	$\frac{d\langle\Delta p_z^2\rangle}{dt}$
Jets	$p \rightarrow \infty$ $\hat{\mathbf{p}} = \hat{\mathbf{e}}_x$	$m \rightarrow 0$	$\hat{q}^{xx} = \hat{q}_L$	\hat{q}^{yy}	\hat{q}^{zz}
Heavy quarks	$p \rightarrow 0$	$m \rightarrow \infty$	κ_T	κ_T	κ_z

Table 5.1: Comparison of momentum diffusion coefficients for jets and heavy quarks in an idealized scenario. The top row shows the properties of an idealized jet particle and corresponding transport coefficients \hat{q}^{ii} , while the bottom row lists properties and transport coefficients for a heavy quark.

the other hand, we may also consider the opposite case: a heavy quark. It can be modeled as a particle at rest (in the plasma rest frame) with a mass much larger than all scales in the plasma. This heavy quark will receive momentum kicks from the plasma, which leads to diffusive behavior. Physically, the momentum of the heavy quark can then be modeled by the Langevin equation [220]

$$\frac{dp_i}{dt} = \xi_i(t) - \eta_D p_i, \quad \langle \xi_i(t) \xi_j(t') \rangle = \kappa_i \delta_{ij} \delta(t - t'). \quad (5.7)$$

Here, η_D is a drag coefficient, and $\xi_i(t)$ encodes random momentum kicks. The *heavy quark diffusion coefficient* κ quantifies the mean squared momentum transfer per time,

$$\frac{d\langle(\Delta p)^2\rangle}{dt} = \sum_i \kappa_i \stackrel{\text{rotational symmetry}}{=} 3\kappa. \quad (5.8)$$

In the Langevin equation (5.7), we have allowed for the possibility of having different diffusion coefficients κ_i in different directions in an anisotropic plasma.

We compare the different definitions in these idealized scenarios in Table 5.1. In principle, these coefficients can be thought of as the limits of a more general transport coefficient which depends both on the mass and momentum of the particle.

For the jet quenching parameter, we use Eq. (4.45), which can be written as

$$\hat{q}^{ij} = \frac{1}{4\nu_g} \lim_{p \rightarrow \infty} \int_{\mathbf{k}\mathbf{k}'\mathbf{p}'} \int_{q_\perp < \Lambda_\perp} q_\perp^i q_\perp^j (2\pi)^4 \delta^4(P + K - P' - K') \frac{|\mathcal{M}_{gg}^{gg}|^2}{p} f(\mathbf{k}) (1 + f(\mathbf{k}')). \quad (5.9)$$

In a similar way, the heavy quark momentum diffusion coefficient κ can be obtained via [220]

$$\kappa_i = \frac{1}{2M} \int_{\mathbf{k}\mathbf{k}'\mathbf{p}'} (2\pi)^3 \delta^3(\mathbf{p} + \mathbf{k} - \mathbf{p}' - \mathbf{k}') 2\pi \delta(k' - k) q_i^2 |\mathcal{M}_g|^2 f(\mathbf{k}) (1 + f(\mathbf{k}')). \quad (5.10)$$

Here, M is the mass of the heavy quark and is considered to be much larger than all other relevant scales. Similarly to the jet quenching parameter, \mathbf{p}, \mathbf{p}' are the incoming and outgoing heavy quark momenta, \mathbf{k}, \mathbf{k}' are the incoming and outgoing momenta of the plasma particles. The transferred momentum $q_i^2 \in \{q_z^2, q_T^2 = q_x^2 = q_y^2\}$

distinguishes longitudinal or transverse momentum transfer, and will be used for the longitudinal (κ_z) or transverse (κ_T) diffusion coefficient, respectively. With the convention employed here (and also in Eqs. (5.7) and (5.8)), we obtain $3\kappa = 2\kappa_T + \kappa_z$, and the ratio $\kappa_T/\kappa_z = 1$ for an isotropic system. For the integration measure (3.16), we use $K^0 = M$ for the heavy quark and $k^0 = |\mathbf{k}|$ for plasma particles.

At leading order in the coupling and inverse heavy quark mass, κ is dominated by the t-channel gluon exchange matrix element [220], which we use in an isotropic approximation,

$$|\mathcal{M}_g|^2 = N_c C_R g^4 16 M^2 \frac{k^2 (1 + \cos^2 \theta_{\mathbf{k}\mathbf{k}'})}{(q^2 + m_D^2)^2}. \quad (5.11)$$

More details on the formula and implementation can be found in Ref. [7].

5.3.2 Numerical results

We have identified limiting attractors in the pressure anisotropy ratio in the previous section. Let us now consider anisotropy ratios of transport parameters of hard probes, i.e., consider the ratio of the jet quenching parameter in y and z direction, $\hat{q}^{yy}/\hat{q}^{zz}$, for a large transverse momentum cutoff in Eq. (4.6) and of the transverse and longitudinal heavy-quark diffusion coefficient κ_T/κ_z in Eq. (5.10).

These ratios are presented in Fig. 5.3, with κ_T/κ_z in the left and $\hat{q}^{yy}/\hat{q}^{zz}$ for cutoff $\Lambda_\perp = 5Q_s$ in the right column, both for a wide range of couplings $\lambda = 0.5$ to 20. The top row depicts them as functions of time scaled by the bottom-up time scale τ_{BMSS} . There, we observe a remarkable qualitative similarity in the evolution of both anisotropy ratios. We find that after the circle marker, the curves corresponding to different couplings quickly approach each other, and even the curves for larger couplings seem to approach this universal curve. As before, the extrapolation to zero coupling according to Eq. (5.5) is shown as a light green curve. Note that curves for weaker couplings approach this attractor earlier, and, in particular, at a time when the system is still far from equilibrium.

For possibly later convenience, these bottom-up limiting attractor curves can be fit to the simple form

$$R_{\hat{q},\kappa}(\tau) = 1 + c_1^{\hat{q},\kappa} \ln \left(1 - e^{-c_2^{\hat{q},\kappa} \tau / \tau_{\text{BMSS}}} \right). \quad (5.12)$$

For the jet quenching ratio $R_{\hat{q}}(\tau) \approx \hat{q}^{yy}/\hat{q}^{zz}$, this yields $c_1^{\hat{q}} = 0.12$ and $c_2^{\hat{q}} = 3.45$ while the ratio of the heavy quark diffusion coefficient $R_\kappa(\tau) \approx \kappa_T/\kappa_z$ leads to $c_1^\kappa = 0.093$ and $c_2^\kappa = 1.33$. For both anisotropy ratios, the fits (5.12) are included in the top panels of Fig. 5.3 as dash-dotted lines, labeled “ $\lambda \rightarrow 0$ fit”.

Note that the parametrization in Eq. (5.12) should be taken with caution. While its advantage lies in its simplicity and small number of fit parameters, the approach toward unity may not be captured completely by this simple ad hoc form. In particular, upon closer inspection, we observe that it provides a more accurate description for the bottom-up limiting attractor of the \hat{q} ratio but shows more pronounced deviations for the κ ratio. Moreover, since the functional form can become negative at early times while the \hat{q} and κ anisotropies are always positive in

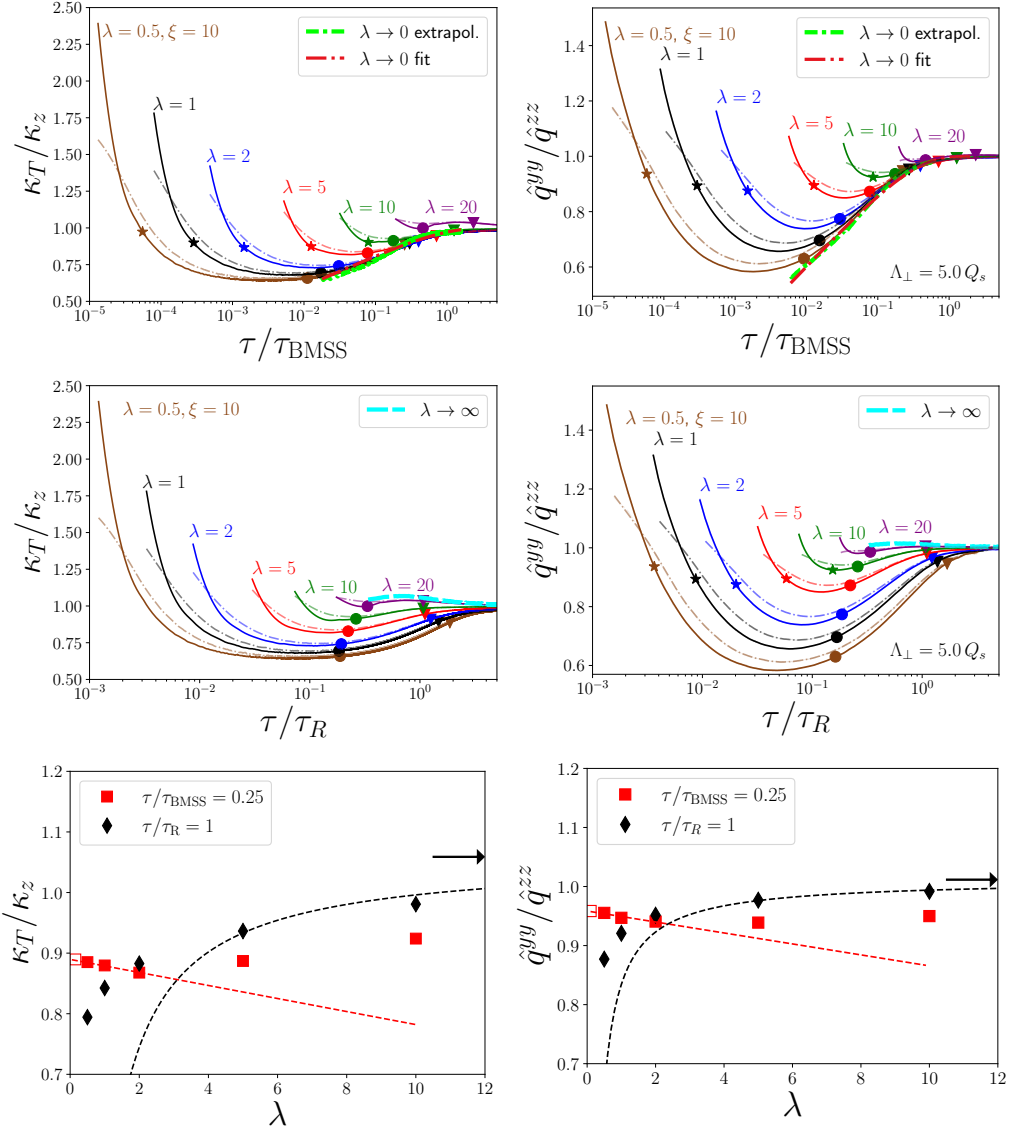


Figure 5.3: Ratios of transverse and longitudinal momentum broadening coefficients of hard probes using different time scalings. Full and dashed lines correspond to anisotropy parameters $\xi_0 = 10$ and $\xi_0 = 4$, respectively. The left column depicts the ratio of the heavy quark diffusion κ_T/κ_z where additionally a Savitzky-Golay filter [221] is applied to the curves to smoothen the data. Similarly, the right column shows the ratio of jet quenching parameters $\hat{q}^{yy}/\hat{q}^{zz}$ for fixed q_\perp cutoff $\Lambda_\perp = 5 Q_s$. In the top row, time is rescaled with τ_{BMSS} , and in the center row with τ_R . The bottom row illustrates the extrapolation procedure to vanishing coupling (empty square) or infinite coupling (black arrow), with the latter performed on the three largest couplings including $\lambda = 20$ not shown in the plots. Plots from Ref. [3].

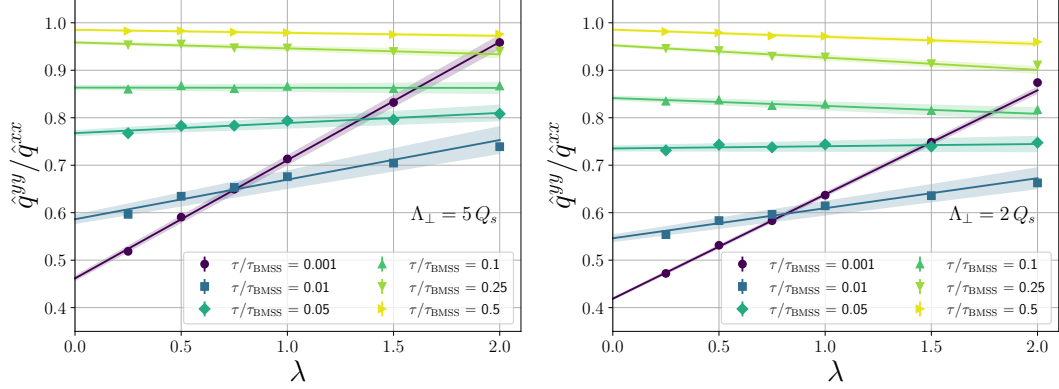


Figure 5.4: Additional examples for extrapolating to the bottom-up limiting attractor for the ratio of the jet quenching parameters $\hat{q}^{yy}/\hat{q}^{zz}$. Shown are values for various rescaled times τ/τ_{BMSS} for different couplings λ , including $\lambda \in \{0.25, 0.75, 1.5\}$. In the different panels, I show different transverse momentum cutoffs Λ_{\perp} .

kinetic theory, we may expect the fits to deviate substantially from the bottom-up limiting attractors at very early times $\tau \ll 0.01 \tau_{\text{BMSS}}$. Irrespective of the exact parametrization, we emphasize that the bottom-up limiting attractors are well-defined at early times.

In contrast, the hydrodynamic limiting attractors for these anisotropy ratios seem to offer less predictive power. This is shown in the central panels of Fig. 5.3 where the ratios are depicted as functions of time scaled with τ_R . As before, the hydrodynamic limiting attractors is obtained by extrapolating to $\lambda \rightarrow \infty$ at fixed τ/τ_R according to Eq. (5.4). The resulting attractors (light blue curves) predict a ratio close to unity long before the system reaches isotropy signaled by the triangle marker. Additionally, the functional form of this attractor is different from the curves for finite couplings and is approached at much later times, even after the triangle marker. Therefore, the bottom-up limiting attractors provide a much more accurate description of these ratio observables for modeling the pre-equilibrium behavior of hard probes.

The bottom panels demonstrate the validity of the fit forms (5.4) and (5.5) at fixed times $\tau/\tau_{\text{BMSS}} = 0.25$ and $\tau/\tau_R = 1$ for the smallest and largest couplings, respectively.

Furthermore, in Fig. 5.4, the extrapolation procedure for the bottom-up limiting attractor is further demonstrated at various different times, including results for a different cutoff $\Lambda_{\perp} = 2Q_s$ as well. For times between $0.001 \leq \tau/\tau_{\text{BMSS}} \leq 0.5$, the values of $\hat{q}^{yy}/\hat{q}^{zz}$ are seen to fall nicely on a straight line, which demonstrates that the extrapolation procedure and the bottom-up limiting attractor is well-defined for these times. Remarkably, the extrapolation seems to work very well even at the very early time $\tau/\tau_{\text{BMSS}} = 0.001$.

5.4 NOTE ON THE TIME SCALES

One might wonder how different the time scales τ_{BMSS} and τ_R in Eq. (5.1) actually are in practice. However, it is not straightforward to compare them since the bottom-

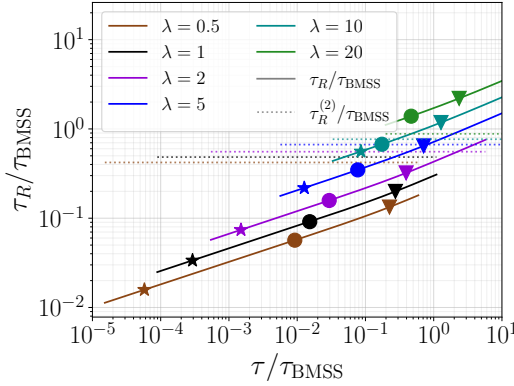


Figure 5.5: Ratio of the two different time scales $\tau_R/\tau_{\text{BMSS}}$ during the simulation for different couplings. Dotted lines show the simple estimate (5.13) for the relaxation time $\tau_R^{(2)}$. Plot adapted from Ref. [3].

up time scale τ_{BMSS} depends only on the coupling λ and is therefore constant in time, while the kinetic relaxation time τ_R also includes the effective (Landau-matched (3.84)) temperature, which decreases throughout the time evolution.

To facilitate comparing these time scales, we may try to express τ_R in terms of the coupling λ . This can be done by utilizing the parametric estimate for the maximum temperature obtained in the bottom-up picture [185], $T_{\text{max}} \sim \alpha_s^{2/5}$ and using the shear viscosity over entropy density [206] $\eta/s \sim \alpha_s^{-2}$ (neglecting the logarithmic dependence). In summary, we would then obtain

$$\tau_R = \frac{4\pi\eta/s}{T} \stackrel{?}{\sim} \alpha_s^{-12/5} = \tau_R^{(2)}, \quad (5.13)$$

which is to be compared with $\tau_{\text{BMSS}} \sim \alpha_s^{-13/5}$. Thus, these time scales seem to be very similar. However, the limiting hydrodynamic attractor seems to work, especially for larger couplings $\lambda \gtrsim 5$, where perturbative estimates such as those used in (5.13) are questionable. Indeed, the values of η/s used when employing the rescaling with the relaxation time (5.1) are extracted from numeric simulations and do not follow the weakly coupling estimate $\eta/s \sim \alpha_s^{-2}$. Thus, Eq. (5.13) does not accurately represent the parametric dependence of τ_R on the coupling λ .

Numerically, it is, of course, straightforward to compare both time scales τ_{BMSS} and τ_R in Eq. (5.1) directly. Their ratio is plotted in Fig. 5.5, with τ_R as solid lines and $\tau_R^{(2)}$ as dotted lines. For small couplings $\lambda \lesssim 2$, the kinetic relaxation time τ_R is much smaller than the bottom-up thermalization estimate τ_{BMSS} for the entire simulation, as visible in Fig. 5.5. In contrast, for larger values of λ , the relaxation time is comparable to and even becomes larger than the bottom-up estimate. In particular, both time scales are approximately identical at the triangle marker ($P_T/P_L = 2$) for $\lambda = 10$. Comparing $\tau_R^{(2)}$ to τ_{BMSS} leads to the same ordering as τ_R , but the timescales are more similar, as is already evident from their definition. However, as discussed before, the time scale $\tau_R^{(2)}$ does not accurately describe the time-varying τ_R in the region of interest (moderate to large couplings).

For weakly coupled systems, the observation that $\tau_{\text{BMSS}} \gg \tau_R$ is consistent with the fact that the bottom-up picture dominates the equilibration process, which

can also be seen by the emergence of the bottom-up limiting attractor for small couplings. It can be understood by the fact that hydrodynamization is dominated by its longest time scale. On the other hand, for larger couplings, we have $\tau_R \gtrsim \tau_{\text{BMSS}}$, which is in line with the hydrodynamic limiting attractor becoming more dominant for larger couplings. This provides a simple explanation for the observed behavior in this chapter.

5.5 CONCLUDING REMARKS

In this chapter, we have focused on the universal features of a set of observables during the bottom-up thermalization process. We have established the concept of limiting attractors, which can be constructed according to Eqs. (5.4) and (5.5) by extrapolating to vanishing or infinite coupling at fixed rescaled times. The bottom-up (weak-coupling) limiting attractor can be obtained using the characteristic bottom-up time scale τ_{BMSS} , while for the hydrodynamic (strong-coupling) limiting attractor the relaxation time τ_R is used.

It should be noted that these two limiting attractors are not contradictory, but should be rather thought of as complementary. For instance, certain observables might be more sensitive to the hydrodynamic limiting attractor (for example the pressure ratio), and others to the bottom-up limiting attractor (for instance the hard probes transport coefficients ratios considered here). Perhaps surprisingly, the often-used hydrodynamic (limiting) attractor seems not to be very useful for the anisotropy ratios of the hard probe transport coefficients considered here, as it predicts only very small deviations from unity while the ratios for finite couplings differ from it both in shape and magnitude.

In this chapter, we consider a purely gluonic system, but the inclusion of quarks would be straightforward. Although qualitative changes to the picture described here would not be expected (because gluons are the dominant degree of freedom during hydrodynamization), it would be important to study whether including quarks enhances or diminishes these limiting attractors.

Furthermore, it would be interesting to perform a broader study to identify other quantities and observables that are sensitive to the bottom-up limiting attractor. This may open the possibility of identifying observables in which both attractors are clearly visible, allowing a detailed study of the interplay of these two limiting attractors.

6

IMPROVING QCD KINETIC THEORY SIMULATIONS

In Chapter 3.6.6, we have introduced and discussed QCD kinetic theory [19], and how medium-effects are included in the Boltzmann equations for the quark and gluon distribution functions $f_s(\mathbf{p}, t)$. These medium effects have been included in a simple way, which we have referred to as *Debye-like screening*. In this chapter, we discuss how to do better; by including the fully resummed hard thermal loop propagator in the matrix elements of the elastic collision term. To quantify the effects of these changes, we will study how the thermalization of QCD is affected by this different screening choice. We will start by considering isotropic systems, and conclude this section with simulations of Bjorken expanding systems now using the full (isotropic) hard-thermal loop matrix element.

This chapter is based on Ref. [4].

6.1 RECAPITULATE: DEBYE-LIKE SCREENING IN QCD KINETIC THEORY

As already discussed in Section 3.3.2, medium-effects are included in QCD kinetic theory in the matrix elements for the elastic collision term using the simple replacement (3.21a),

$$\frac{(s-u)^2}{\underline{t^2}} \rightarrow |G_{\mu\nu}(P-P') (P+P')^\mu (K+K')^\nu|^2, \quad (6.1)$$

where G is the retarded HTL propagator. In the Debye-like screening approximation, this propagator is approximated as (3.28)

$$G_{\mu\nu} = \frac{g_{\mu\nu}}{Q^2} \frac{q^2}{q^2 + \xi_g^2 m_D^2}, \quad (6.2)$$

effectively replacing

$$\frac{(s-u)^2}{t^2} \rightarrow \frac{(s-u)^2}{t^2} \frac{q^4}{(q^2 + \xi_g^2 m_D^2)^2} \quad (6.3)$$

in the underlined terms in Tab. 3.1. Note that, because of the symmetry in exchanging the outgoing particles (exchanging u and t channel), the u channel divergences that would require screening can always be mapped to a t channel divergence and be screened via the replacement in Eq. (6.3).

In this chapter, we will discuss that other replacements, such as replacing su/t^2 , are equally valid and use the full isotropic hard-thermal-loop propagator. We will begin by considering this propagator in a general (isotropic linear) gauge.

6.2 HARD THERMAL LOOP PROPAGATOR

6.2.1 Isotropic HTL gluon propagator in a linear gauge

While the HTL gluon propagator is gauge-dependent, calculating several physical quantities has been shown to be gauge-independent [222–224]. In particular, in an isotropic system, the HTL gluon self-energy can always be written in terms of two functions $\Pi_a(Q)$ and $\Pi_b(Q)$.

In this section, we will discuss the most general form of the gluon propagator with HTL self-energy corrections in a linear gauge that does not break the rotational symmetry in the plasma rest frame. We will show that all gauge-dependent parts of the propagator are proportional to the exchange momentum Q and will vanish when contracted with the external momenta in Eq. (6.1), confirming that the replacement (6.1) is gauge-independent.

The reason for restricting to not breaking the rotational symmetry is that this leaves only two relevant directions for the self-energy: The plasma rest frame, which is defined by the vector $\tilde{n}^\mu = (1, \mathbf{0})$ and momentum of the propagating gluon Q^μ . This will allow for a 4-dimensional basis for the self-energy and propagator, as, e.g., in Ref. [225]. If we included another direction, we would need a higher-dimensional basis, e.g., the one employed in Ref. [226].

In our case, any tensor quantity in this system can be constructed from \tilde{n}^μ , Q^μ , and the metric $g^{\mu\nu}$. For simplicity, we construct our tensor basis with the vector n^μ that is orthogonal to Q^μ ,

$$n_\mu = P_{\mu\nu} \tilde{n}^\nu, \quad P_{\mu\nu} = g_{\mu\nu} - \frac{Q_\mu Q_\nu}{Q^2}. \quad (6.4)$$

In momentum space, we can represent any linear gauge condition [225, 227] $f^\mu A_\mu = 0$ by a general vector $f^\mu(Q)$. If it further does not break rotational invariance (which we assumed), we may decompose f_μ into a part parallel and transverse to Q ,

$$f_\mu = a(Q)Q_\mu + b(Q)n_\mu, \quad (6.5)$$

This general linear gauge includes the Lorenz (covariant) gauge, $f_\mu = Q_\mu$, and the Coulomb gauge, where $f_0 = 0$ and $f_i = q_i$, as well as the temporal axial gauge $f_0 = \Lambda$ and $f_i = 0$, where Λ is a constant scale needed for dimensional reasons. A symmetric basis for the gluon propagator is given by [225]

$$B_{\mu\nu} = \frac{n_\mu n_\nu}{n^2}, \quad C_{\mu\nu} = n_\mu Q_\nu + n_\nu Q_\mu, \quad (6.6a)$$

$$E_{\mu\nu} = \frac{Q_\mu Q_\nu}{Q^2}, \quad A_{\mu\nu} = P_{\mu\nu} - B_{\mu\nu}. \quad (6.6b)$$

The free propagator then reads [225, 227]

$$G_{\mu\nu}^0 = \frac{P_{\mu\nu}}{Q^2} - \frac{1}{f_e Q^2} (f_c C_{\mu\nu} + (f_b + Q^2) E_{\mu\nu}), \quad (6.7)$$

with

$$f_b = \frac{b^2 n^2}{\xi}, \quad f_c = \frac{ab}{\xi}, \quad f_e = \frac{a^2 Q^2}{\xi}, \quad (6.8)$$

where ξ is the gauge-fixing parameter introduced in the Faddeev-Popov procedure [225]. Including the self-energy (see (A.27)), we obtain the dressed propagator,

$$G_{\mu\nu} = \frac{A_{\mu\nu}}{Q^2 + \Pi_a} + \frac{B_{\mu\nu}}{\tilde{b}(Q)} - \frac{f_c + \Pi_c}{\tilde{b}(Q)(f_e + \Pi_e)} C_{\mu\nu} + \frac{Q^2 + \Pi_b + f_b}{\tilde{b}(Q)(f_e + \Pi_e)} E_{\mu\nu}, \quad (6.9)$$

with

$$\tilde{b}(Q) = Q^2 + \Pi_b + f_b - n^2 Q^2 \frac{(f_c + \Pi_c)^2}{f_e + \Pi_e}, \quad (6.10)$$

and where we have similarly decomposed the self-energy in the same tensor basis,

$$\Pi_{\mu\nu} = \Pi_a A_{\mu\nu} + \Pi_b B_{\mu\nu} + \Pi_c C_{\mu\nu} + \Pi_e E_{\mu\nu}. \quad (6.11)$$

The Ward identity forces the HTL self-energy to be transverse, $Q^\mu \Pi_{\mu\nu} = 0$ (see, e.g., [177]). In that case, one finds that $\Pi_c = \Pi_e = 0$, which simplifies $\tilde{b}(Q) = Q^2 + \Pi_b$. All dependence from the gauge choice is now in the parameters f_b , f_c , and f_e , which always appear together with factors of Q_μ . A closer inspection reveals that all terms proportional to Q_μ or Q_ν yield zero when contracted with the external momenta in Eq. (6.1). This follows from

$$Q \cdot (P + P') = (P' - P) \cdot (P + P') = P'^2 - P^2 = 0, \quad (6.12)$$

and similarly with $P \leftrightarrow K$. Therefore, the screening prescription in Eq. (6.1) is gauge invariant for a general linear gauge.

6.2.2 IsoHTL screening

Let us now consider including the full isotropic HTL retarded propagator in Eq. (6.1) for the gluonic matrix element,

$$\frac{|\mathcal{M}_{\text{HTL}}|^2}{16d_A C_A^2 g^4} = \frac{1}{4} \left(9 + \frac{(t-u)^2}{s^2} + 2 |G_{\mu\nu}^{\text{isoHTL}}(P - P')(P + P')^\mu (K + K')^\nu|^2 \right). \quad (6.13)$$

As before, we will refer to this screening prescription as *isoHTL*. Note that, as we have discussed in Section 6.2.1, Eq. (6.13) is gauge invariant. We have already considered a very similar contraction with the external momenta as in Eq. (6.13) for obtaining the isoHTL screened matrix element for the jet quenching parameter in Eq. (4.47). The steps to obtain the isoHTL screened matrix element here are almost identical (see Appendix A.5.3), leading to

$$|G_{\mu\nu}^{\text{isoHTL}}(P - P')(P + P')^\mu (K + K')^\nu|^2 = \frac{c_1^2}{A^2 + B^2} + \frac{c_2^2}{C^2 + D^2} - \frac{2c_1 c_2 (AC + BD)}{(A^2 + B^2)(C^2 + D^2)}, \quad (6.14)$$

with A , B , C , D and c_1 given by Eqs. (4.34) and (4.35), and the only difference being c_2 , which now reads

$$c_2 = 4pk \sin \theta_{qp} \sin \theta_{qk} \cos(\phi_{qk} - \phi_{qp}). \quad (6.15)$$

More details and a more elaborate discussion on the differences to the isoHTL screening for the jet quenching parameter are discussed in Appendix A.5.3.

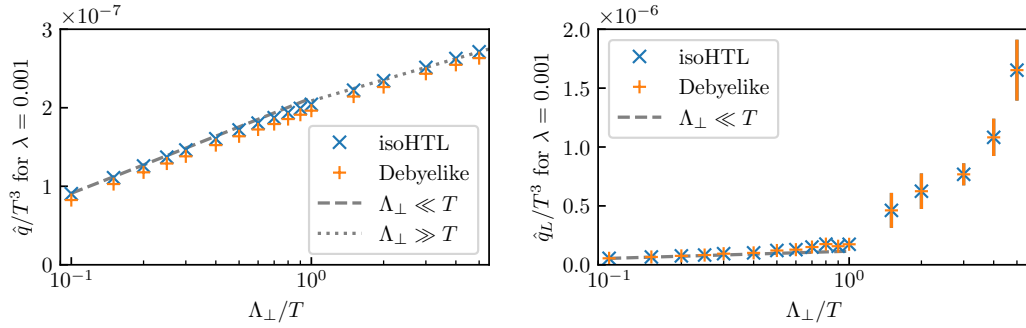


Figure 6.1: Transverse (left) and longitudinal (right) jet quenching parameter in a thermal plasma using both the Debye-like screening prescription with $\xi_g = e^{5/6}/\sqrt{8}$ (usually employed in the elastic collision term) and the isoHTL screened Matrix element. Figure taken from an upcoming publication [228].

6.2.3 Debye-like screening as an approximation to isoHTL

As already briefly discussed in Section 3.3.2, the Debye-like screening prescription (6.3) can be understood as a simple approximation to the full isotropic HTL matrix element (6.14), which we briefly reiterate here. In the original work [169], the screening parameter ξ_g was chosen to reproduce (longitudinal) soft momentum transfer in elastic collisions. This can be seen as follows: For isotropic distributions, mimicking the steps to obtain the jet quenching parameter from Section 4.2, we may write the collision kernel as [169]

$$\begin{aligned} \mathcal{C}^{2 \leftrightarrow 2} = & \frac{1}{2^9 \pi^5 \nu} \int_0^\infty dk \int_0^{2\pi} d\phi_{qp} \\ & \times \int_{-p}^k d\omega \{ f(p)f(k)(1+f(p+\omega))(1+f(k-\omega)) - f(p+\omega)f(k-\omega)(1+f(p))(1+f(k)) \} \\ & \times \int_{|\omega|}^{\min(2k-\omega, 2p+\omega)} dq \int_0^{2\pi} d\phi_{qk} \frac{|\mathcal{M}|^2}{p^2}. \end{aligned} \quad (6.16)$$

Screening effects are only important for soft internal momenta, $q, \omega \ll k, p$. When expanding the distribution functions for small ω , the first nonvanishing term is quadratic in ω since the matrix element is even. One therefore requires that in this limit

$$\int_{-\infty}^\infty d\omega \omega^2 \int_{|\omega|}^\infty dq \int_0^{2\pi} d\phi \left(|\mathcal{M}_{\text{HTL}}|^2 - |\mathcal{M}_{\text{Debye1}}|^2 \right) = 0, \quad (6.17)$$

which fixes the constant $\xi_g = e^{5/6}/\sqrt{8}$ [169].

In Section 4.1.5, we have already seen that using the Debye-like screening prescription for transverse momentum broadening, we obtain a different constant $\xi_g^\perp = e^{1/3}/2$. That is, to match transverse momentum broadening in Section 4.1.5 using (4.37), we needed to include q_\perp^2 in the matching, whereas here we include ω^2 in Eq. (6.17). For a highly energetic jet, we have $q_z = \omega$ from (C.5), and, hence, we match longitudinal broadening here, whereas in Section 4.1.5, we matched transverse momentum broadening. Consequently, the Debye-like screening prescription cannot simultaneously approximate both longitudinal and transverse

momentum diffusion, even in isotropic systems, while the isoHTL prescription can. Therefore, the isoHTL screening prescription is more general and should be used when both processes are important. This is illustrated in Fig. 6.1, where the transverse and longitudinal jet quenching parameter is plotted with both the Debye-like screened matrix element (with screening constant ξ_g) and the isoHTL screened matrix element. Also the analytic limits of \hat{q} from Eqs. (4.65) and (4.77a) are shown, and the corresponding analytic form of \hat{q}_L from Ref. [20] valid for small cutoffs. We observe that only the isoHTL-screened matrix element reproduces the analytic limit in both transverse and longitudinal momentum broadening, whereas the Debye-like screened matrix element can only reproduce one of them. In this case, by choosing ξ_g , the longitudinal broadening is reproduced.

It should be emphasized, again, that both of these screening prescriptions neglect the effect of plasma instabilities, which are generically seen to occur in anisotropic systems [34–38, 131, 133, 171]. However, numerical evidence indicates that these instabilities do not play a dominant role at the time scales of interest for kinetic theory simulations [42, 43] and when a quasiparticle picture becomes applicable [172–174].

6.2.4 Different Debye-like screening prescriptions

As discussed in Section 3.3.2, screening effects need only be included for $|t| \ll s \approx -u$, where the screening prescription screens the divergencies for $t \rightarrow 0$. However, in this limit,

$$I_1 = \frac{(s-u)^2}{4t^2}, \quad I_2 = -\frac{su}{t^2}, \quad I_3 = \frac{s^2}{t^2}, \quad (6.18)$$

are equivalent up to $\mathcal{O}(|t|/s)$, in particular, $I_3/I_1 = 1 + \mathcal{O}(|t|/s)$ and $I_2/I_1 = 1 + \mathcal{O}(t^2/s^2)$.

Instead of screening the first term in (6.18), $(s-u)^2/(4t^2)$, we can also apply the screening prescription (6.3) to any of the other terms in (6.18). The gluonic matrix element can be rewritten in several forms, where these terms appear explicitly,

$$\frac{|\mathcal{M}|^2}{16d_A C_A^2 g^4} = \frac{1}{4} \left(9 + 2 \frac{(s-u)^2}{t^2} + \frac{(t-u)^2}{s^2} \right) \quad (6.19a)$$

$$= 3 - 2 \frac{su}{t^2} - \frac{tu}{s^2} \quad (6.19b)$$

$$= 3 + 2 \frac{s^2}{t^2} + 2 \frac{s}{t} - \frac{tu}{s^2}. \quad (6.19c)$$

These vacuum matrix elements (6.19) are equivalent because of the condition for the Mandelstam variables (3.18), $s + t + u = 0$. To leading-order (or up to $\mathcal{O}(|t|/s)$), the expressions in (6.18) coincide, and we thus have a particular freedom of how to implement the screening. The choice mentioned in Ref. [19] is to implement the screening as in the scalar quark case, Eq. (3.27), which makes the gauge-independence manifest.

In this chapter, we study including the simple Debye-like isotropic screening (3.29) in the different equivalent expressions (6.18) in (6.19), by using the matrix elements,

$$\frac{|\mathcal{M}_{\text{Debye1}}|^2}{16d_A C_A^2 g^4} = \frac{1}{4} \left(9 + 2 \frac{(s-u)^2}{t^2} \frac{q^4}{(q^2 + \xi_g^2 m_D^2)^2} + \frac{(t-u)^2}{s^2} \right), \quad (6.20a)$$

$$\frac{|\mathcal{M}_{\text{Debye2}}|^2}{16d_A C_A^2 g^4} = 3 - 2 \frac{su}{t^2} \frac{q^4}{(q^2 + \xi_g^2 m_D^2)^2} - \frac{tu}{s^2}, \quad (6.20b)$$

$$\frac{|\mathcal{M}_{\text{Debye3}}|^2}{16d_A C_A^2 g^4} = 3 + 2 \left(\frac{s^2}{t^2} + \frac{s}{t} \right) \frac{q^4}{(q^2 + \xi_g^2 m_D^2)^2} - \frac{tu}{s^2}. \quad (6.20c)$$

Because of Eq. (3.18), the second and third matrix elements exactly coincide, $\mathcal{M}_{\text{Debye2}} \equiv \mathcal{M}_{\text{Debye3}}$, and we only need to consider differences between $\mathcal{M}_{\text{Debye1}} \neq \mathcal{M}_{\text{Debye2}}$.

Note that for the region $|t| \ll s$, the agreement of the matrix elements (6.20) is independent of the values of q and m_D . On the other hand, for sufficiently large $q \gg m_D$ and independent of the values of s, t , these matrix elements only differ up to factors of $\mathcal{O}(m_D^2/q^2)$. Since screening effects are only important for these regions of small $q \sim m_D \sim gT$ or small $|t| \ll s$, the matrix elements (6.20) are leading-order equivalent.

6.3 THERMALIZATION OF ISOTROPIC SYSTEMS

We have already discussed how isotropic systems thermalize in Section 6.3. In this section, we will now study how the screening choice modifies QCD thermalization in isotropic systems. For that, numerical simulations using the isoHTL screened matrix element (6.13) are performed and compared with Debye-like screened simulations. In the isotropic case, we consider non-expanding isotropic systems where the longitudinal expansion term in Eq. (3.76) is omitted. Similarly to [21, 187], we start with both an under- and over-occupied initial distribution. The under-occupied simulations are initialized via

$$f(p) = A \exp \left(-(p - Q)^2 / (Q/10)^2 \right), \quad (6.21)$$

with A chosen¹ such that $Q = 50T$, where T is the temperature of the equilibrium system after thermalization. As an initial condition for the over-occupied system, the parametrization of the system's self-similar scaling solution from [169]

$$f(p) = \frac{(Qt)^{-4/7}}{\lambda \tilde{p}} \left(0.22e^{-13.3\tilde{p}} + 2e^{-0.92\tilde{p}^2} \right), \quad (6.22)$$

is used, with $\tilde{p} = (p/Q)(Qt)^{-1/7}$ and initial time $Qt = 0.12$.

The Boltzmann equation (3.76) is solved numerically until equilibrium is reached, using a Debye-like $\mathcal{M}_{\text{Debye1}}$ or isoHTL screened matrix element \mathcal{M}_{HTL} . The system's time evolution can be fully described by the one-dimensional distribution function,

¹ In the simulation, all quantities are given in dimensionless units. There, we first fix $Q = 50$, then adjust A such that the energy density is that of a thermal system with $T = 1$.

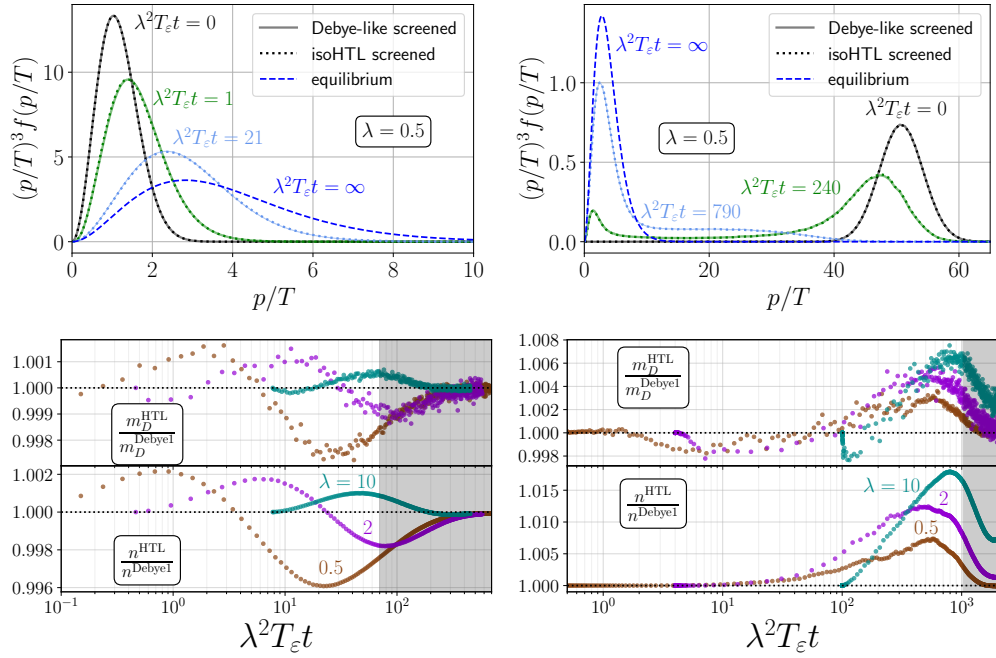


Figure 6.2: Thermalization of an initially over-occupied (left) and under-occupied (right) gluonic plasma. The top row shows the distribution function f scaled with p^3 corresponding to the contribution of f to the energy density. The bottom row shows ratios of observables (Debye mass m_D and particle number n) calculated with isoHTL screening (6.13) over Debye-like screening (variant 1, (6.20a)) as functions of the rescaled time $\lambda^2 T_\varepsilon t$. Figures from [4].

which is depicted in the top row of Fig. 6.2 rescaled with $p^3 f(p, t)$ for initially over- (left) and under-occupied systems (right). We observe that the curves corresponding to the Debye-like (full lines) and isoHTL screening (dotted lines) almost coincide. Hence, for isotropic systems, the Debye-like screening prescription provides a good quantitative approximation of the full HTL matrix element.

Next, as an attempt to better quantify deviations between the different screening prescriptions, we consider a measure for the thermalization time $t_{\text{therm.}}$. We define this time scale implicitly in terms of the effective temperatures following [187]

$$(T_0(t_{\text{therm.}})/T_1(t_{\text{therm.}}))^{\pm 4} = 0.9, \quad (6.23)$$

with + for under- and - for overoccupied systems. The effective temperatures are defined via

$$T_\alpha = \left[\frac{2\pi^2}{\Gamma(\alpha+3)\zeta(\alpha+3)} \int \frac{d^3 p}{(2\pi)^3} p^\alpha f(p) \right]^{1/(\alpha+3)}. \quad (6.24)$$

The first moment $T_1 = T_\varepsilon$ has the physical interpretation of the temperature of a thermal system with the same energy density (Landau matching, see Eq. (3.84)).

$$T_\varepsilon(\tau) = \left(\frac{30\epsilon(\tau)}{\pi^2 \nu_g} \right)^{1/4}. \quad (6.25)$$

Due to energy conservation in non-expanding systems, it is constant throughout the evolution and corresponds to the temperature of the thermal system after

λ	Overoccupied		Underoccupied	
	Debye-like: $\lambda^2 T t_{\text{therm.}}$	isoHTML: $\lambda^2 T t_{\text{therm.}}$	Debye-like: $\lambda^2 T t_{\text{therm.}}$	isoHTML: $\lambda^2 T t_{\text{therm.}}$
0.5	69.7	67.0	1029	1022
2	86.0	84.4	1127	1112
10	93	93	1245	1216

Table 6.1: Thermalization times for initially over- and under-occupied systems. Table adapted from Ref. [4].

equilibration. The other effective temperature, T_0 , is related to the particle number density n , via the relation $T_0 = (\pi^2 n / (\zeta(3) \nu_g))^{1/3}$. The thermalization times are listed in Tab. 6.1. We observe that the full HTL matrix element leads to only slightly smaller thermalization times.

To also quantify differences in the dynamics, in the bottom row of Fig. 6.2, the evolution of the Debye mass (3.11) and number density n are depicted as ratios of a simulation with isoHTML screening over one with Debye-like screening. The gray area indicates when the system is close to equilibrium, i.e., after the thermalization time defined in (6.23). We observe that both the Debye mass and the number density differ only at a sub-percent level between the simulations.

Finally, the excellent agreement for isotropic systems among the screening prescriptions might not come as a big surprise. In fact, as detailed in Section 6.2.3, the Debye-like screening prescription was introduced specifically in the isotropic non-expanding case to approximate (isotropic) HTL screening.

6.4 RESULTS WITH LONGITUDINAL EXPANSION

We now turn to systems undergoing Bjorken expansion, relevant for the initial stages in heavy-ion collisions. For that, we need to include the additional expansion term in the Boltzmann equation (3.76) that was absent for the isotropic case in the previous subsection.

6.4.1 Initial conditions, time markers and time scales

We use the initial conditions discussed in Section 3.6.2 with $\xi_0 = 10$, and the time markers introduced in section 3.6.4. Recall that the star and circle markers are related to the occupancy $\langle pf \rangle / \langle p \rangle$ (star at occupancy $1/\lambda$ and circle at minimum), and the triangle marker is placed when the pressure ratio $P_T / P_L = 2$, indicating that the system has almost isotropized.

We will also use the time scales introduced in Section 3.6.4 and used extensively in Chapter 6, both the relaxation time τ_R and the bottom-up time scale τ_{BMSS} ,

$$\tau_R = \frac{4\pi\eta/s}{T_\epsilon}, \quad \tau_{\text{BMSS}} = \left(\frac{\lambda}{4\pi N_c} \right)^{-13/5} / Q_s. \quad (6.26)$$

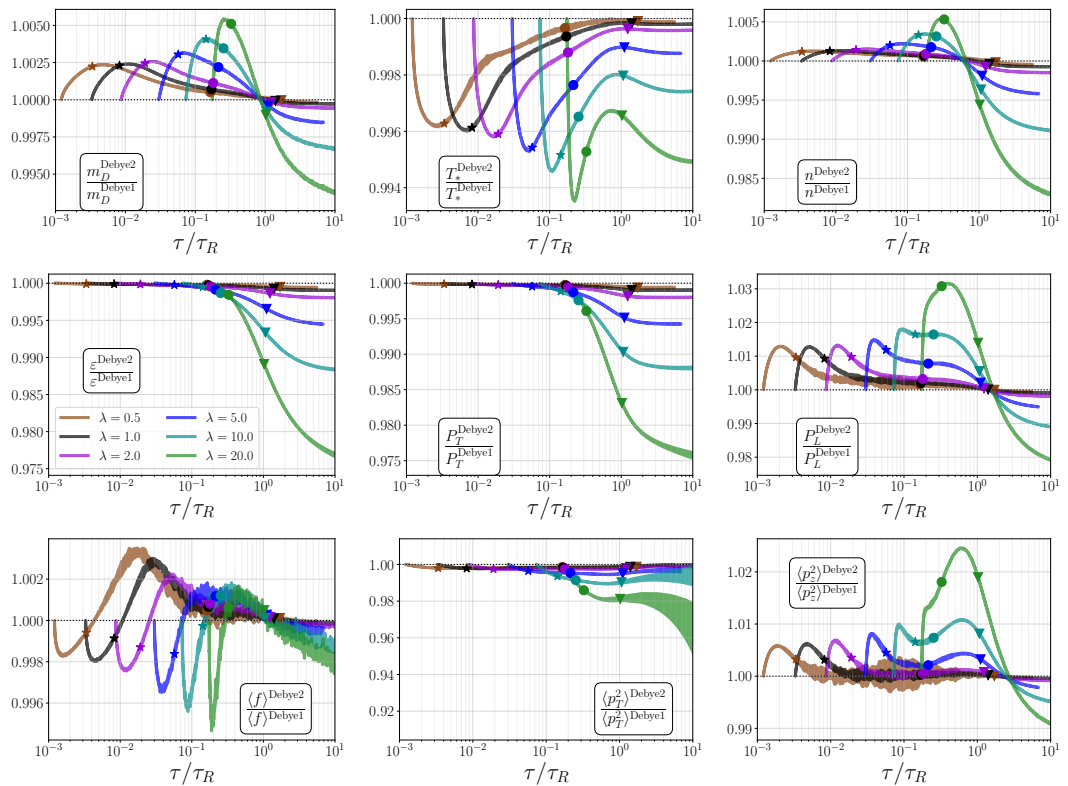


Figure 6.3: Ratios of various observables of simulations with different Debye-like screening prescriptions from Eq. (6.20). The bands denote estimates for the standard error, obtained from statistically averaging over five independent simulations. Plots from Ref. [4].

6.4.2 Comparison of Debye-like screening prescriptions

First, let us consider differences arising from the different variants of implementing the Debye-like screening prescription as written in (6.20). The numerical results for simulations with identical initial conditions but different Debye-like screening prescriptions are presented in Fig. 6.3, where the ratio of various observables is plotted. These observables consist of various moments of the distribution function, such as components of the energy-momentum tensor $T^{\mu\nu}$ from Eq. (3.82), and Debye mass m_D from Eq. (3.11), and the effective infrared temperature T_* given by Eq. (3.10). We observe only very small changes, mostly on a sub-percent level. To verify that these small changes are not caused by random fluctuations or noise from the Monte Carlo evaluation of the collision kernels, several (four to five) simulations with identical parameters but different seeds for the random number generator were performed. The error bands in the figure are estimates of the standard error of the results, see Appendix B.9.

As can be seen in Fig. 6.3, the different Debye-like screening prescriptions differ less for smaller couplings. This is expected because the different screening prescriptions are leading-order equivalent, as we discussed in section 6.2.4. Perhaps surprisingly then, also for larger values of the coupling (even for $\lambda = 20$), the considered observables differ only at a percent level. This is because these matrix elements (6.20) are not only leading-order equivalent but also equivalent in the small angle scattering region where $|t| \ll s$, in accordance with our discussion in Section 6.2.4. In fact, it is well-known that the dynamics is mostly dominated by small-angle scatterings, which is used also as the basis for other QCD studies using the Boltzmann equation in diffusion approximation (BEDA) [66, 73, 74, 197–199, 229]. Indeed, it can be checked that processes with $s \gg |t|$ are dominant for QCD kinetic theory simulations, which is presented in more detail in Appendix Appendix B.8.

6.4.3 Comparison with isoHTL: Pressure ratio

We now turn to the isoHTL screening prescription (6.14). Numerically, employing the isoHTL prescription leads to larger noise and a more unstable numerical evaluation of the differential equation (3.76), and requires an improved step size algorithm which is given in detail in Appendix B.6. We will first discuss the results for the pressure ratio and then move on to other observables.

Fig. 6.4 shows the results for the pressure ratio for different couplings (color-coded) in the left panel, and the ratio between the isoHTL and Debye-like pressure ratio in the right panel. Before discussing these results in more detail, a note about the time scales is in order. As already discussed in Section 3.6.4, curves of the pressure ratio nicely collapse at late times when the time is rescaled with the relaxation time $\tau_R = 4\pi\eta/s/T_\varepsilon$,

$$\frac{P_L}{P_T} = 1 - \frac{2}{\pi} \frac{\tau_R}{\tau}, \quad (6.27)$$

which is shown in the left panel of Fig. 6.4 as a thick red dotted line.

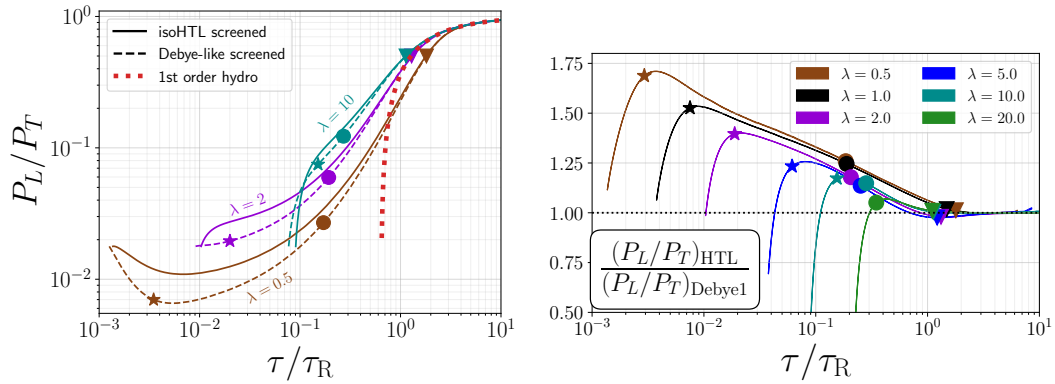


Figure 6.4: Pressure ratio as a function of time for different couplings (colors). In the left panel, the results using the isoHTL-screened matrix element are shown as solid lines, and for the Debye-like screened matrix element as dashed lines. The first-order hydrodynamic estimate is shown as a thick red dotted line. The right panel shows the pressure ratio of the isoHTL-screened simulations normalized to the pressure ratio with Debye-like screening. Time is rescaled with the kinetic relaxation time τ_R . Figures adapted from [4].

Importantly, the shear viscosity η depends on the screening prescription, and for the curves to collapse in Fig. 6.4, one needs to use different values of η/s for different screening prescriptions. We will discuss how to extract this transport parameter in more detail in the next section.

Coming back to the pressure ratio shown in Fig. 6.4, we find that the maximum pressure anisotropy is almost halved by employing the isoHTL screening prescription, i.e., the lowest value of P_L/P_T is larger. While both the isoHTL-screened (solid line) and Debye-like screened curves (dashed line, corresponding to (6.20a)) start at the same value of the pressure ratio by using the same initial condition, the time evolution with the different screening prescriptions shows clear differences: Simulations with Debye-like screening become more anisotropic as compared to isoHTL screening, which is more pronounced at small values of the coupling λ .

This can be understood from the observation that while the Debye-like screening prescription (6.20a) approximates well the longitudinal momentum transfer, it underestimates transverse momentum broadening as encoded in the jet quenching parameter $\hat{\eta}$, see Fig. 6.1. However, transverse momentum broadening is an essential ingredient in the bottom-up equilibration process [185]. The Debye-like screening prescription, therefore, leads to less efficient transverse momentum broadening and to a larger anisotropy.

In contrast, the late-time evolution is less sensitive to the screening prescription if the relaxation time τ_R in Eq. (5.1) is adjusted accordingly. The required parameter η/s is obtained such that the curves follow this late-time first-order hydrodynamic estimate (6.27). We will study the approach to hydrodynamics and thermalization first and then discuss the extraction procedure of η/s together with the numerical results in Section 6.4.4.

Note also that the curves in the right panel of Fig. 6.4 do not start at 1 despite the simulations being initialized with the same initial condition. This is because

due to the different values of η/s for different screening prescriptions, the system is initialized at a different τ/τ_R (as can be seen in the left panel).

6.4.4 Numerical extraction of the specific shear viscosity η/s

As input for the relaxation time τ_R in (5.1), the value of the transport parameter η/s for every coupling and screening prescription is needed. This first-order hydrodynamic parameter quantifies the late-time approach to isotropy. It has been obtained perturbatively in Ref. [205, 206].

General strategy

The general strategy employed here is to compare the late-time evolution of the numerical simulations with a first-order conformal hydrodynamic system, in which the shear viscosity over entropy density η/s is the only medium parameter and uniquely governs the relaxation to isotropy. For a Bjorken expanding system, the pressure ratio is given by Eq. (6.27). However, other ways to extract η/s have been used in the literature. For example, the authors of Ref. [28] fit to the pressure difference

$$\frac{P_T - P_L}{\varepsilon + P} = 2 \left(\frac{\eta/s}{\tau T_e} \right) + 4C_2/3 \left(\frac{\eta/s}{\tau T_e} \right)^2, \quad (6.28)$$

which originates from a second-order hydrodynamic formulation. Here, C_2 is an additional fitting constant, and the (isotropic) pressure P is related to the energy density ε via the conformal relation $P = \varepsilon/3$. Both expressions (6.27) and (6.28) will be used here to obtain the value of η/s for a given coupling λ and screening prescription. While both equations give similar results, they are not identical, and their difference is taken as an estimate of the systematic uncertainty.

Detailed fitting procedure

More concretely, the parameter η/s is extracted by fitting Eq. (6.27) at some late time interval (t_i, t_f) to the pressure anisotropy P_L/P_T of the simulation. There are two main causes of inaccuracy in this procedure: On the one hand, any fixed-order hydrodynamic formula only describes the system's behavior sufficiently close to thermal equilibrium (in the present case: at sufficiently late times). Before that, corrections to the first-order form are expected, which will make the obtained values less reliable when decreasing the initial fit time t_i . On the other hand, the numerical simulations performed here are plagued with discretization artifacts that become worse over time (see Section 3.6.6). Hence, a too large final time t_f may worsen the fit.

Therefore, to obtain the best fit, the start (t_i) and end times (t_f) of the fitting process are varied. The earliest time for t_i is chosen as the time when the pressure anisotropy is $P_L/P_T = 0.5$ (triangle marker). For each (t_i, t_f) pair, the value of η/s and its fit error is recorded. Fig. 6.5 illustrates this procedure for one particular example. The top left panel shows the pressure ratio to which Eq. (6.27) is fitted. The bottom left panel shows the values of η/s obtained for different pairs of initial

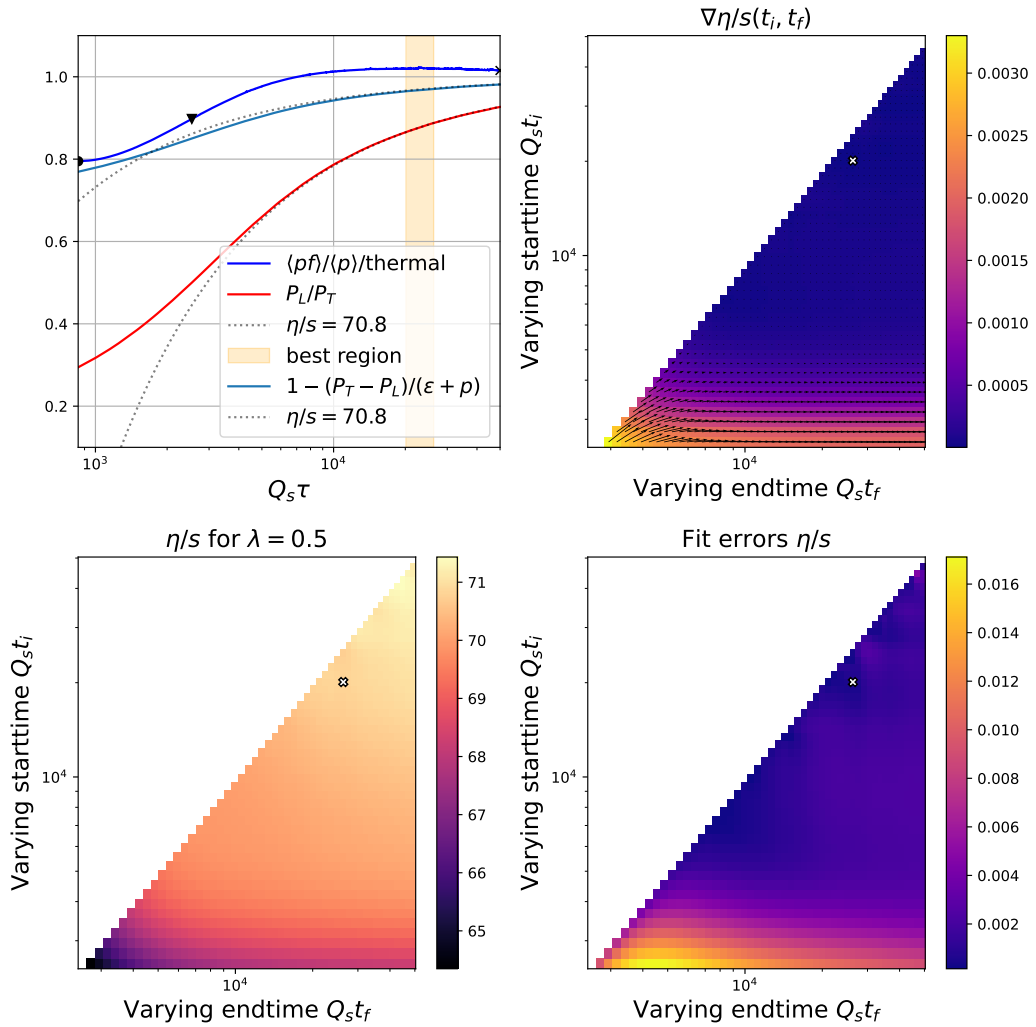


Figure 6.5: One example of how η/s is fitted and its dependence on the start and end of the fit time, for $\lambda = 0.5$ and isoHTML screening. (Top left): Pressure ratio and pressure anisotropy as in (6.27) and (6.28). Shown are also the fits with the best value of η/s . (Bottom left): Fitted values of η/s as a function of the start and end time. (Top right): Gradient of the fitted values of η/s with respect to varying start and end time. (Bottom right): Fit errors from fitting η/s to Eq. (6.27). The cross is the best value obtained as explained in the text.

and final times for the fit, (t_i, t_f) . Calculating also the gradients $\nabla_{t_i, t_f} \eta/s$ (Top right panel) allows extracting the value where the fit-error (bottom right panel) times the gradient is the smallest. This fitting procedure is then performed for several simulations with different random number generator seeds and the results are averaged. From that, the statistical uncertainty is obtained by using a simple error of the mean estimate (see Appendix B.9). The procedure described here is not meant to account for all possible systematic errors. The goal here is to obtain a robust procedure to obtain η/s and investigate whether there are *systematic differences* in the value of η/s for *different screening prescriptions*.

Initial conditions

The shear viscosity over entropy density η/s is a medium parameter and as such, independent of the specific initial condition. For $\lambda \geq 1$, the same initial distribution (3.77) as for all expanding simulations (with $\xi_0 = 10$) is used, for $\lambda = 0.5$ late-time discretization artifacts are reduced by choosing the initialization time $Q_s \tau = 50$ and initial anisotropy $\xi_0 = 2$ with the suitable initial amplitude $A(\xi_0=2) = 0.96789$, see Table 3.2.

Results for η/s

The results of this procedure are summarized in Tab. 6.2, where also the statistical error estimate for the fit procedure is given.

We find that both Debye-like screening prescriptions and both fit formulas (6.27) and (6.28) lead to similar values of η/s which are consistent with earlier numerical extractions [56]. However, the isoHTML values are, in general, about 10% - 20% smaller than those from Debye-like screening. Additionally, they are much closer to the perturbative estimates at next-to-leading-log accuracy [206], which are labeled as “pQCD NLL” and given by

$$\left. \frac{\eta}{s} \right|_{\text{NLL pQCD}} = \frac{34.784}{\lambda^2 \ln [4.789/\sqrt{\lambda}]} \quad (6.29)$$

This formula is based on an expansion in inverse logarithms and is thus only valid at small couplings at next-to-leading logarithmic (NLL) accuracy, and there is good agreement for $\lambda \lesssim 1$ between this formula and the isoHTML values. This may indicate that there are no large systematic biases in the extraction procedure performed here. In general, any such systematic bias would be similar for all screening prescriptions considered in this paper, and thus the decrease of the value of η/s for the isoHTML screening prescription can be seen as a robust statement.

Fig. 6.6 shows the ratio of the extracted values of η/s over the perturbative NLL results from Ref. [206]. As mentioned before, for small couplings $\lambda \lesssim 1$, the values of η/s for the isoHTML matrix element are very close to the pQCD values, whereas the Debye-like screened matrix elements consistently lead to larger values of η/s . At larger couplings, we see increasing discrepancies between the perturbative NLL values and the extracted results. Nevertheless, the isoHTML screening continues to yield consistently smaller values than the Debye-like prescriptions. At such large coupling strengths, we should recall that the inverse log expansion from Ref. [206] breaks down, and also kinetic theory becomes less accurate. However,

λ	Debye1		Debye2		isoHTL		pQCD
	Eq. (6.27)	Eq. (6.28)	Eq. (6.27)	Eq. (6.28)	Eq. (6.27)	Eq. (6.28)	NLL
0.5	76.6(9)	78.2(1)	77.0(2)	78.2(1)	70.6(9)	71(2)	72.7
1.0	23.249(6)	25.0(3)	23.228(6)	25.0(3)	21.55(6)	21.6(7)	22.2
2.0	7.50(4)	7.55(4)	7.49(4)	7.517(10)	6.59(9)	6.3(4)	7.13
5.0	1.7037(5)	1.731(5)	1.6909(4)	1.717(1)	1.44(2)	1.48(3)	1.83
10.0	0.5940(6)	0.60(2)	0.5830(7)	0.55(3)	0.505(2)	0.513(8)	0.838
20.0	0.2120(5)	0.20(1)	0.2027(6)	0.20(1)	0.1759(3)	0.180(2)	1.27

Table 6.2: Extraction of η/s values for various couplings λ using the screening prescriptions Debye1 (6.20a), Debye2 (6.20b), isoHTL (6.13) and the extraction procedures (6.27) and (6.28). The error estimate from our fitting procedure is explained in the text. NLL pQCD denotes the weak coupling perturbative expression (6.29) from [206]. Table adapted from [4].

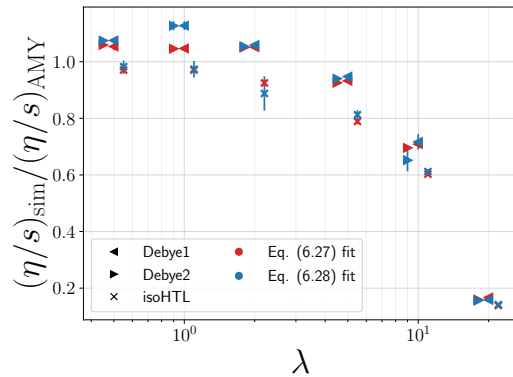


Figure 6.6: Numerically extracted values η/s from Tab. 6.2. The simulation and fit results for the different screening methods and fitting formulas are normalized by the NLL pQCD results stated in the table. For visual ease, the markers are slightly shifted around the value of λ . Adapted from [4].

λ	Debye1, (6.27)	Debye1, (6.28)
0.53	70.49(3)	72.4(8)
2.2	6.39(3)	6.417(4)
11.2	0.5012(8)	0.507(8)

Table 6.3: Extraction of η/s values for different couplings λ and the Debye-like screening (6.20a) for the η/s extraction procedures (6.27) and (6.28). Table from Ref. [4].

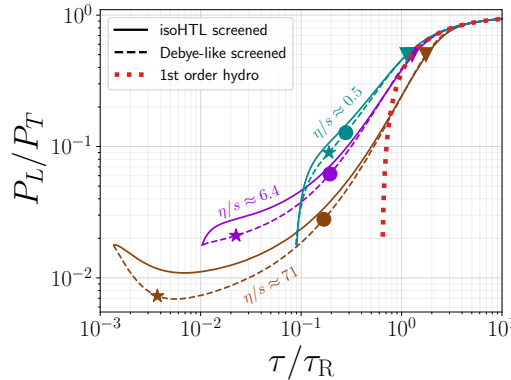


Figure 6.7: Pressure ratio for systems with similar η/s . The values of λ are adjusted between the isoHTL and Debye-like screened simulations to yield a similar value of η/s . Figure from [4].

it is interesting and encouraging to note that both screening prescriptions lead to rather similar values even at large couplings.

6.4.5 Simulations at the same specific shear viscosity η/s

In the previous sections, we have compared the results using Debye-like and isoHTL screening for the same value of the coupling λ . But then we showed that shear viscosity η entering the relaxation time τ_R via Eq. (6.26) depends on the screening prescription. Therefore, one might ask whether the changes in the pressure ratio for different screening prescriptions (shown in Fig. 6.4) are due to the different values of η/s . We will see here that this is not the case. To do that, instead of comparing simulations with the same value of λ , we compare at the same value of η/s .

In particular, the isoHTL screened simulations at couplings $\lambda \in \{0.5, 2, 10\}$ are compared with Debye-like screened simulations with couplings $\lambda \in \{0.53, 2.2, 11.2\}$, which lead to similar values of η/s (see Tab. 6.3). This comparison is illustrated in Fig. 6.7 for the pressure ratio P_L/P_T as a function of the rescaled time τ/τ_R . Again, at late times, the curves coincide and fall on the universal hydrodynamic curve (6.27) as expected from an approach to a hydrodynamical evolution. In contrast, as before, we find that the evolution at early times differs substantially for the different screening prescriptions. The overall behavior is very similar to the comparison between screening prescriptions at the same value of the coupling in Fig. 6.4. Thus, the early-time evolution of the pressure ratio (and similarly of other quantities) is significantly different for the isoHTL screening

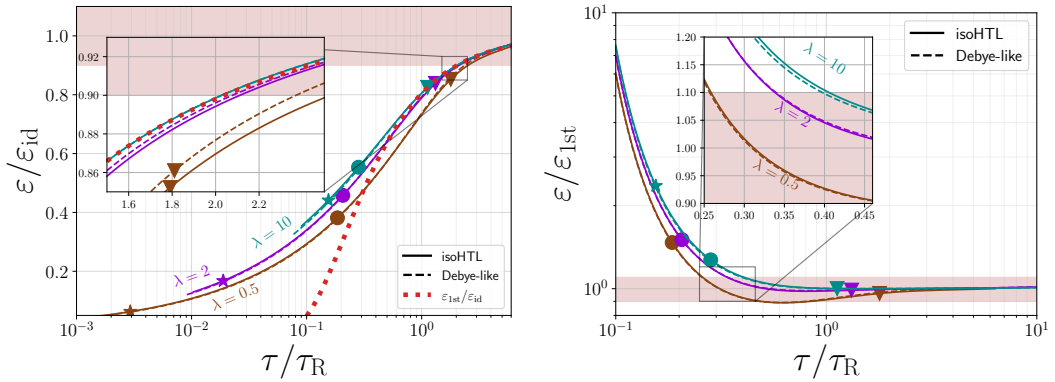


Figure 6.8: Energy density of the nonequilibrium simulation for different couplings λ (color coded) normalized to its ideal (left) and first-order hydrodynamic estimate (right). The results using the isoHTL-screened matrix element are shown as solid lines, for the Debye-like screened matrix element as dashed lines. The top panel also depicts the first-order hydrodynamic estimate as a thick red dotted line. The shaded region indicates a less than 10 % deviation from unity. Figure from Ref. [4].

prescription, both when compared at the same value of the coupling λ or shear viscosity over entropy density η/s .

6.4.6 Thermalization and hydrodynamization time

Next we move on to study how quickly the system thermalizes, and how quickly a hydrodynamic description becomes applicable. In Ref. [24], the thermalization time is defined as the time when the energy density of the nonequilibrium kinetic theory simulation first gets within 10% of the ideal hydrodynamic estimate,

$$\left| 1 - \frac{\varepsilon(\tau_{\text{therm}})}{\varepsilon_{\text{id}}(\tau_{\text{therm}})} \right| = \left| 1 - \frac{T_{\varepsilon}^4(\tau_{\text{therm}})}{T_{\text{id}}^4(\tau_{\text{therm}})} \right| = 0.1. \quad (6.30)$$

Similarly, the hydrodynamization time is defined as the time when the full kinetic theory result gets within 10% of the first-order hydrodynamic estimate,

$$\left| 1 - \frac{\varepsilon(\tau_{\text{hydro}})}{\varepsilon_{\text{1st}}(\tau_{\text{hydro}})} \right| = \left| 1 - \frac{T_{\varepsilon}^4(\tau_{\text{hydro}})}{T_{\text{1st}}^4(\tau_{\text{hydro}})} \right| = 0.1. \quad (6.31)$$

In ideal and first-order hydrodynamics, the temperature evolution is given by

$$T_{\text{id}}(\tau) = \frac{c_1}{\tau^{1/3}}, \quad (6.32)$$

$$\frac{T_{\text{1st}}(\tau)}{T_{\text{id}}(\tau)} = 1 - \frac{1}{6\pi} \frac{\tau_R}{\tau}, \quad (6.33)$$

with a constant c_1 , which has to be fitted at late times from the late-time behavior of the nonequilibrium energy density (or rather the effective temperature T_{ε} from Eq. (3.84)).

The left panel of Fig. 6.8 shows the energy density of the simulation normalized to the energy density of ideal hydrodynamics for different values of the coupling λ .

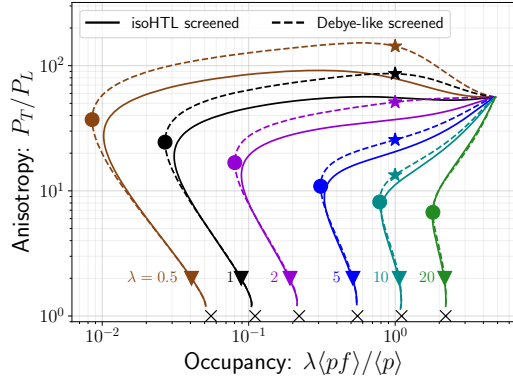


Figure 6.9: Comparison of simulations with isoHTL (solid) and Debye-like (dashed lines) screening prescriptions in the anisotropy (measured by the pressure ratio P_T/P_L) - occupancy (measured by $\lambda\langle pf \rangle / \langle p \rangle$) plane. Figure from [4].

We observe that both the Debye-like screening results (dashed lines, corresponding to Eq. (6.20a)) and the lines associated with simulations using the isotropic HTL matrix element (solid lines, corresponding to Eq. (6.13)) lie almost on top of each other. This is due to the rescaling of time using the relaxation time τ_R , in which the different values for the shear viscosity η/s are already included. In particular, we find that thermalization occurs roughly at the same time, at $\tau_{\text{therm}} \approx 2 \tau_R$ for $\lambda \gtrsim 2$.

The right panel of Fig. 6.8 shows the energy density normalized to the first-order hydrodynamic estimate. Similar to the thermalization case, we find that hydrodynamization occurs roughly at the same time when comparing both screening approximations. The results for different values of the coupling λ differ more than the different screening prescriptions themselves. Hydrodynamization occurs roughly at $\tau_{\text{hydro}} \approx 0.35 \tau_R$.

These results indicate that the impact of changing the screening prescription on the approach to hydrodynamics and to local thermal equilibrium is mainly captured by the values of the coefficient η/s .

6.4.7 Impact of screening prescriptions on early-time dynamics

We have depicted the bottom-up thermalization process [185] already in Fig. 3.2 in Section 3.5.2 (see also Fig. E.1 in Appendix F). We will now discuss how different screening prescriptions impact the curves shown in these figures. Fig. 6.9 depicts the system's time evolution in the occupancy-anisotropy plane, both for Debye-like screened matrix elements (dashed lines) and the isoHTL screening (solid lines). All simulations start with the same initial condition given by Eq. (3.77), shown in the upper-right part of the plot, and then evolve towards thermal equilibrium (black crosses). The isoHTL matrix element leads to a visibly different evolution, especially during the far-from-equilibrium initial stages before minimal anisotropy is reached (circle marker). These differences are seen throughout a wide range of occupation numbers. For instance, for weak couplings, the system reaches a significantly smaller anisotropy in terms of P_T/P_L , as we have seen before in Fig. 6.4. Additionally, the minimal occupancy reached is larger than for Debye-like screening.

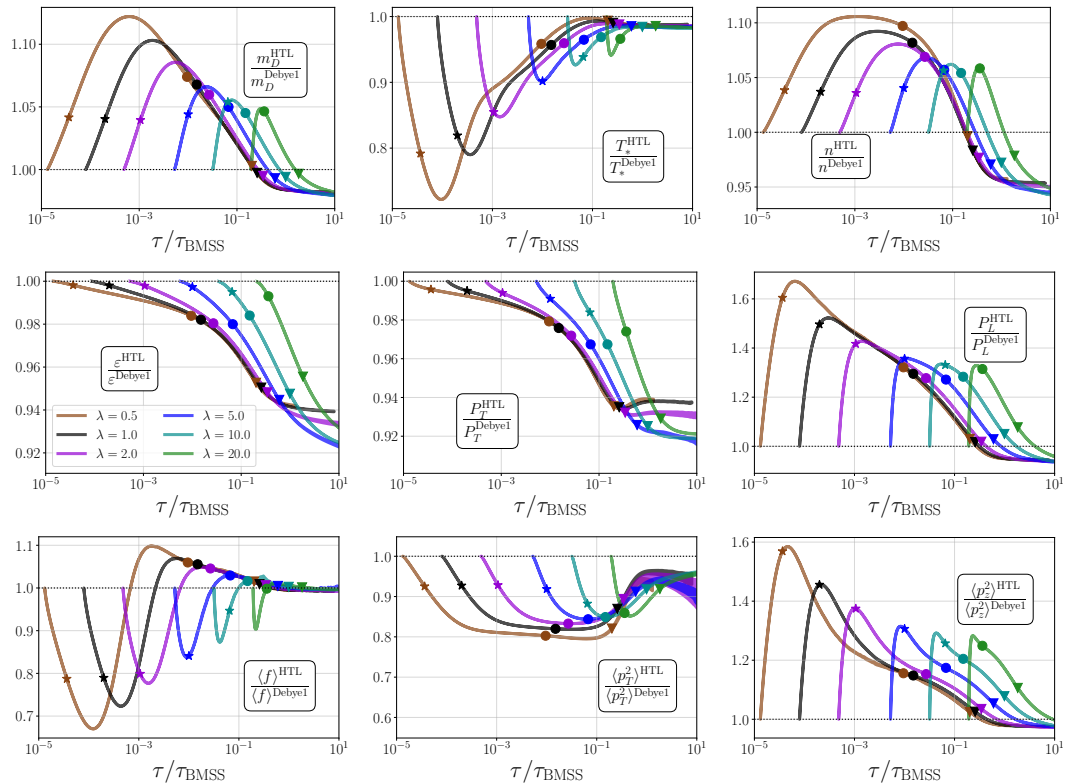


Figure 6.10: Observable ratios obtained from simulations with isoHTL screening normalized by those with the Debye-like screening prescription. Time is rescaled with the bottom-up thermalization time (3.85a). The band corresponds to an error estimate using a statistical average of 5 simulations. Figures from Ref. [4].

Nonetheless, we do not find significant qualitative changes to the bottom-up picture of thermalization [185].

We now move on to study a wide range of different moments of the distribution function, the same moments that were already shown in Fig. 6.3: the Debye mass m_D , effective temperature T_* , particle density n , energy density and pressures ϵ , P_T , P_L , and moments of the distribution function $\langle f \rangle$, $\langle p_T^2 \rangle$ and $\langle p_z^2 \rangle$. Fig. 6.10 shows the ratio of these moments obtained from simulations with the isoHTL screening prescription over the same quantities from a Debye-like screened simulation. Time is rescaled using the bottom-up timescale τ_{BMSS} , because then all ratios start at unity, which is not the case when using the relaxation time τ_R because of the different shear viscosities for the different screening prescriptions, as can be seen, e.g., in Fig. 6.4. Different couplings are indicated with different colors. The bands indicate an estimate of the statistical uncertainty from the Monte Carlo evaluation of the collision terms. They are obtained by performing five simulations for every set of initial conditions with different random number seed and calculating the standard error (see Appendix B.9). We observe that most considered quantities show larger deviations between the screening prescriptions for smaller values of the coupling. This is in line with our expectation that for larger values of the coupling the screening prescriptions differ less, as discussed in Section 3.6.5. Nonetheless, sizable corrections can be found even at large couplings.

For instance, the Debye mass in the isoHTL simulation is enhanced by almost 15% for $\lambda = 0.5$ between the star and circle marker, and by about 5% for $\lambda = 20$. The average occupancy $\langle f \rangle$ is reduced in the isoHTL simulations by over 30% at early times for weak couplings, but even for $\lambda = 20$ we find a reduction of more than 10%. In contrast, the particle density is enhanced by 5 – 10%.

However, the largest deviations concern measures of the bulk anisotropy of the plasma. At late times, the components of the energy-momentum tensor from the isoHTL simulations are about 10% smaller than for the Debye-like screened simulations, which implies a smaller temperature in the subsequent equilibrium plasma. In contrast, the longitudinal pressure increases by more than 60% for $\lambda = 0.5$, and by more than 30% for $\lambda = 10$ and $\lambda = 20$ before eventually also decreasing to values similar to P_T . This effect results from the longitudinal pressure being dominated by particles close to the transverse plane that undergo transverse momentum broadening, i.e., in p_z direction. Since isoHTL leads to a more accurate and more efficient transverse momentum broadening than the simple Debye-like screening prescription (see, e.g., Fig. 4.4), one arrives at the observed higher values of P_L . Similar effects can be seen in the moments of f . Indeed, the anisotropy ratio $\langle p_z^2 \rangle / \langle p_T^2 \rangle$ is also considerably larger for isoHTL simulations than for Debye-like screening. In particular, $\langle p_z^2 \rangle$ overshoots and $\langle p_T^2 \rangle$ is lower in the HTL cases at early times. This significant reduction of anisotropy at early times is, hence, one of the main qualitative differences between these different screening prescriptions.

6.4.8 Evolution of the jet quenching parameter

We have studied the jet quenching parameter with various screening prescriptions already in Chapter 4.4. However, in the previous chapters, the simulations from which $f(\mathbf{p}, \tau)$ was taken as input to calculate the jet quenching parameter were all

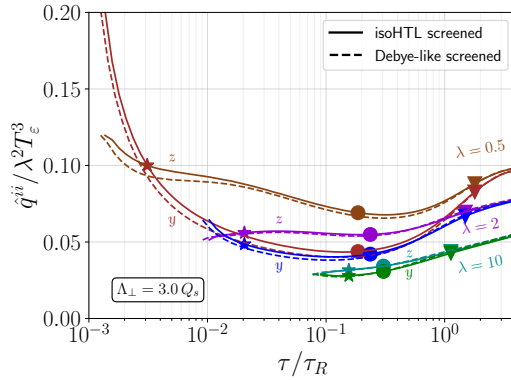


Figure 6.11: Evolution of the jet quenching parameter \hat{q} for couplings $\lambda \in \{0.5, 2, 10\}$. The legend refers to the screening prescriptions used in the time evolution of the plasma background. Figure from [4].

performed using the Debye-like screening prescription in the matrix element. Here, we show that the jet quenching parameter \hat{q} is only mildly influenced by the choice of screening in the medium evolution.

As in the previous chapters, Eq. (4.45) is used to obtain the jet quenching parameter for a fixed transverse momentum cutoff Λ_\perp .

Fig. 6.11 shows the time evolution of the jet quenching parameter along the beam axis \hat{q}^{zz} and in the transverse direction \hat{q}^{yy} for different couplings and screening prescriptions of the plasma. The results are quantitatively close to those presented in the previous chapters, and the curves for isoHTL and Debye-like screened evolutions only mildly differ. Thus, the choice of either Debye-like or isoHTL screening prescription has only a negligible influence on the time evolution and value of the jet quenching parameter \hat{q} .

6.5 CONCLUDING REMARKS

In this chapter, we have discussed results for QCD kinetic theory simulations with the isoHTL screening prescription in the elastic collision term, and compared with simulations using the Debye-like screening prescription. We first reviewed the Debye-like and isoHTL screening prescriptions and discussed, in particular, their gauge invariance. For isotropic systems, we find only minor differences, but for a Bjorken expanding system relevant for the initial nonequilibrium stages in heavy-ion collisions, we find that the maximum anisotropy is drastically reduced when using the isoHTL screening prescription. Changes can also be found in the transport parameter η/s , the shear viscosity over entropy density, which determines the approach to isotropy. Employing the isoHTL screening prescription leads to a reduction of η/s at the same value of the coupling λ , and for small couplings, η/s agrees with the perturbative expression. Finally, we studied whether the jet quenching parameter is influenced by the different screening prescriptions used in the background medium evolution. We find that this is not the case, the value of the jet quenching parameter is almost insensitive to the screening prescription used in the QCD kinetic theory evolution of the background.

 COLLISION KERNEL AND AMY RATES OUT OF EQUILIBRIUM

In Chapter 4.4, we considered the jet quenching parameter \hat{q} , which characterizes the small-distance behavior of the dipole cross section. In this chapter, we go beyond the small distance form and obtain the full dipole cross section, as the Fourier transform of the elastic collision kernel. We will then use this dipole cross section to calculate the gluon emission rates in the AMY formalism. This chapter is based on a paper in preparation [6].

7.1 GOING BEYOND THE JET QUENCHING PARAMETER: ELASTIC COLLISION KERNEL

As discussed in the introduction in Section 2, the jet quenching parameter \hat{q} can be obtained as a moment of the elastic collision kernel (see Eq. (1.4)),

$$\hat{q} = \int \frac{d^2 \mathbf{q}_\perp}{(2\pi)^2} q_\perp^2 C(\mathbf{q}_\perp), \quad (7.1)$$

which is directly related to the elastic scattering rate

$$C(\mathbf{q}_\perp) = (2\pi)^2 \frac{d\Gamma_{\text{el}}}{d^2 \mathbf{q}_\perp}. \quad (7.2)$$

While the jet quenching parameter quantifies the rate of change of transverse momentum squared, $\hat{q} = \frac{d\langle \Delta p_\perp^2 \rangle}{dt}$, the collision kernel $C(\mathbf{q}_\perp)$ encodes the rate for the jet parton to receive a transverse momentum kick with momentum \mathbf{q}_\perp . Additionally, this elastic collision kernel $C(\mathbf{q}_\perp)$ is needed as input to calculate the rate of inelastic gluon emissions (as discussed in Chapter 3), making it an essential quantity that encodes all the relevant medium properties. For solving the AMY rate equations (2.11) relevant for gluon emission, it is convenient to transform to impact parameter space, where the relevant quantity is then the dipole cross section

$$C(\mathbf{x}) = \int \frac{d^2 \mathbf{q}_\perp}{(2\pi)^2} (1 - e^{i\mathbf{x} \cdot \mathbf{q}_\perp}) C(\mathbf{q}_\perp). \quad (7.3)$$

7.1.1 Generalizing the jet quenching parameter to obtain the collision kernel

In Chapter 4.4, we have discussed how to obtain the jet quenching parameter \hat{q} in QCD kinetic theory. The collision kernel can be obtained in a very similar way, which we will briefly discuss here.

We start again with the expression for the elastic scattering rate (3.59),

$$\begin{aligned}\Gamma_{\text{el}} = & \frac{1}{4p\nu_a} \sum_{bcd} \int \frac{d^3\mathbf{k}}{(2\pi)^3 2k} \frac{d^3\mathbf{p}'}{(2\pi)^3 2p'} \frac{d^3\mathbf{k}'}{(2\pi)^3 2k'} |\mathcal{M}_{cd}^{ab}(\mathbf{p}, \mathbf{k}; \mathbf{p}', \mathbf{k}')|^2 \\ & \times (2\pi)^4 \delta^4(P + K - P' - K') f(\mathbf{k})(1 \pm f(\mathbf{k}'))(1 \pm f(\mathbf{p}')),\end{aligned}\quad (7.4)$$

As noted before, the scattering rate (7.4) is symmetric under the exchange of outgoing particles $p' \leftrightarrow k'$ (switching u and t channel), so we can always enforce $p' > k'$, which leads to an additional factor 2. We first integrate over \mathbf{k}' using the delta function and then perform a variable substitution $\mathbf{p}' = \mathbf{p} + \mathbf{q}$. We pull out the integral over \mathbf{q}_\perp and use Eq. (7.2) to arrive at

$$\begin{aligned}C(\mathbf{q}_\perp) = & \frac{1}{2p\nu_a} \sum_{bcd} \int \frac{d^3\mathbf{k}}{(2\pi)^3} \int dq_z \frac{|\mathcal{M}_{cd}^{ab}(\mathbf{p}, \mathbf{k}; \mathbf{p} + \mathbf{q}, \mathbf{k} - \mathbf{q})|^2}{8|\mathbf{k}||\mathbf{k} - \mathbf{q}||\mathbf{p} + \mathbf{q}|} \\ & \times f(\mathbf{k})(1 + f(\mathbf{k} - \mathbf{q}))\delta(p + |\mathbf{k}| - |\mathbf{p} + \mathbf{q}| - |\mathbf{k} - \mathbf{q}|).\end{aligned}\quad (7.5)$$

In the limit $p \rightarrow \infty$, as already was the case for the jet quenching parameter \hat{q} in Section 4.1.7, only the matrix elements in Table 4.2 remain, which can be written in terms of the screened matrix element $\tilde{M}_{\text{screen}}$. For instance, the matrix element for gluon-gluon scattering reduces to

$$\lim_{p \rightarrow \infty} \frac{|\mathcal{M}_{gg}^{gg}|^2}{p^2} = 4d_A C_A^2 |G_R(P - P')_{\mu\nu} (P + P')^\mu (K + K')^\nu|^2,\quad (7.6)$$

and we can use the isotropic retarded hard-thermal loop propagator G_R for the internal soft gluon propagator (isoHTL screening), Eq. (4.47).

The delta function can be rewritten as [205]

$$\delta(q_z - k + k') = \frac{k'}{kq} \delta\left(\cos \theta_{qk} - \frac{q_z}{q} + \frac{t}{2kq}\right) \Theta(k - q_z),\quad (7.7)$$

and only yields a contribution if $k > \frac{q_z + q}{2}$. We then arrive at

$$\begin{aligned}C(\mathbf{q}_\perp) = & \frac{1}{16p\nu_a(2\pi)^3} \sum_{bcd} \int_0^{2\pi} d\phi_{qk} \int_{-\infty}^{\infty} \frac{dq_z}{q} \int_{\frac{q+q_z}{2}}^{\infty} dk \\ & \times \lim_{p \rightarrow \infty} \frac{|\mathcal{M}_{cd}^{ab}(\mathbf{p}, \mathbf{k}; \mathbf{p} + \mathbf{q}, \mathbf{k} - \mathbf{q})|^2}{p^2} f(\mathbf{k})(1 + f(\mathbf{k} - \mathbf{q})).\end{aligned}\quad (7.8)$$

Note that in Chapter 4.4, we have introduced $\omega = p' - p$, which is equivalent to $q_z \equiv \omega$ in the limit $p \rightarrow \infty$. We proceed similarly as in Chapter 4.4, and perform the \mathbf{k} integral in a frame in which \mathbf{q} points in the z direction, and the \mathbf{q} integral is performed in a frame in which \mathbf{p} points in the z direction. In practice for an implementation, we need the angles θ_k and $\theta_{k'}$, which we obtain as in Chapter 4.4 via Eq. (4.20). Note that the collision kernel $C(\mathbf{q}_\perp)$ is a function of the two-dimensional vector \mathbf{q}_\perp in the transverse plane to the jet. Only the component of \mathbf{q} parallel to the jet is integrated over (see also Eq. (2.15)). The remaining two-dimensional vector \mathbf{q}_\perp can be parameterized as

$$\mathbf{q}_\perp = q_\perp \begin{pmatrix} \cos \phi \\ \sin \phi \end{pmatrix} = q_\perp \begin{pmatrix} \cos \phi_{pq} \\ \sin \phi_{pq} \end{pmatrix} = \begin{pmatrix} q_x \\ q_y \end{pmatrix} = \begin{pmatrix} -q_z^{(1)} \\ q_y^{(1)} \end{pmatrix},\quad (7.9)$$

and $q = \sqrt{q_{\perp}^2 + q_z^2}$, all in accordance with Eq. (4.14b) in Section 4.1.2. For a jet moving in the x direction, $\phi_{pq} = 0$ corresponds to momentum broadening along the beam direction, while $\phi_{pq} = \pi/2$ to momentum broadening transverse to the beam direction and to the jet direction.

A note about coordinate systems is in order. The upper index (1) denotes the components in the coordinate system, in which the beam axis defines the z -axis, which is the coordinate system that we called *lab frame* in Section 4.1.2. However, since \mathbf{q}_{\perp} is a two-dimensional vector in the transverse plane to the jet, it is more natural to use a coordinate system, where these two components are labeled q_x and q_y . This is the coordinate system, in which the jet points in the z direction, which we called *p frame* in Section 4.1.2. For our purposes here, it will be more natural to work in this frame, and to label the transverse components $\mathbf{q}_{\perp} = (q_x, q_y)$, as in Eq. (7.9). The spatial coordinate in the transverse plane is $\mathbf{x} = (x, y)$. Furthermore, we will frequently abbreviate the angle of \mathbf{q}_{\perp} in the transverse plane to the jet as $\phi_{pq} = \phi$.

Eq. (7.8) is the final result of this subsection and is the equation that is implemented and evaluated numerically.

7.1.2 Symmetries of the collision kernel

Next, let us discuss the symmetries of the collision kernel $C(\mathbf{q}_{\perp})$, and of the dipole cross section $C(\mathbf{x})$. In momentum space, we can adopt the notation $C(\mathbf{q}_{\perp}) = C(q_x, q_y)$. Since the distribution function $f(\mathbf{k})$ is symmetric around mid-rapidity (mirror-symmetry around the $z = 0$ plane, see Eq. (3.72)), $f(k, \cos \theta_k) = f(k, -\cos \theta_k)$, we obtain $C(q_z^{(1)}, q_y^{(1)}) = C(-q_z^{(1)}, q_y^{(1)})$, and, hence, $C(q_x, q_y) = C(-q_x, q_y)$. Additionally, the distribution function is symmetric under rotations in the transverse plane (see Eq. (3.71)), which implies $C(q_x, q_y) = C(q_x, -q_y)$. Combining this, we obtain

$$C(q_x, q_y) = C(\pm q_x, \pm q_y). \quad (7.10)$$

With that, the Fourier transform (7.3) becomes real,

$$C(x, y) = \int \frac{d^2 \mathbf{q}_{\perp}}{(2\pi)^2} (1 - e^{iq_x x + iq_y y}) C(q_x, q_y) = \int \frac{d^2 \mathbf{q}_{\perp}}{(2\pi)^2} (1 - \cos(\mathbf{q}_{\perp} \cdot \mathbf{x})) C(q_x, q_y) \quad (7.11)$$

From that, we can infer the symmetry properties of the dipole cross section

$$C(x, y) = C(\pm x, \pm y). \quad (7.12)$$

Therefore, we can map all angles $\phi > \pi/2$ into the first quadrant,

$$C(|\mathbf{x}|, \phi) = \begin{cases} C(|\mathbf{x}|, \phi), & 0 < \phi < \pi/2 \\ C(|\mathbf{x}|, \pi - \phi), & \pi/2 < \phi < \pi \\ C(|\mathbf{x}|, \phi - \pi), & \pi < \phi < 3/2\pi \\ C(|\mathbf{x}|, 2\pi - \phi), & 3/2\pi < \phi < 2\pi \end{cases} \quad (7.13)$$

It will be convenient to note here how calculating the coefficients of a Fourier series is simplified under these symmetries. For a function $D(\phi)$ obeying the symmetries (7.13),

$$\begin{aligned} \int_0^{2\pi} d\phi e^{-im\phi} D(\phi) &= \int_0^{\pi/2} d\phi D(\phi) \left(e^{-im\phi} + e^{-im(\pi-\phi)} + e^{-im(\phi-\pi)} + e^{-im(2\pi-\phi)} \right) \\ &= \begin{cases} 0, & m \text{ odd} \\ 4 \int_0^{\pi/2} d\phi \cos m\phi D(\phi), & m \text{ even} \end{cases} \end{aligned} \quad (7.14)$$

7.1.3 Analytic limits: Small and large momentum transfers

Next, we discuss the analytic limits of the collision kernel $C(\mathbf{q}_\perp)$ for small and large momentum transfers. Both limits have implicitly already been discussed before for the jet quenching parameter, but it is insightful to consider these limits here specifically for the collision kernel.

First, we consider large momentum transfer, $|\mathbf{q}_\perp| \rightarrow \infty$, for which it is convenient to start with Eq. (7.5). We consider the case of pure gluons, but including quarks is considered in Appendix C.2.2. For $p \rightarrow \infty$, $|\mathbf{p} + \mathbf{q}| \rightarrow p + q_z$, when $\mathbf{p} = (0, 0, |\mathbf{p}|)$, and then the delta function can be rewritten to constrain q_z ,

$$\delta(k - q_z - |\mathbf{k} - \mathbf{q}|) \rightarrow \frac{q_\perp^2}{2(k - k_z)^2} \delta\left(q_z - \frac{\mathbf{q}_\perp \cdot \mathbf{k}_\perp - q_\perp^2/2}{k - k_z}\right), \quad (7.15)$$

where in the normalization we have already taken the leading term in the limit $q_\perp \rightarrow \infty$. Thus, $q_z \approx -q_\perp^2/(2(k - k_z))$, and $q \rightarrow \infty$. In this limit, screening effects can be neglected in the matrix element, and we may take the vacuum form of the matrix element

$$|\mathcal{M}_{gg}^{gg}|^2 = -16g^4 d_A C_A^2 \frac{su}{t^2} = 16g^4 d_A C_A^2 \frac{4p^2(k - k_z)^2}{q_\perp^4}. \quad (7.16)$$

Inserting this, we obtain

$$C(\mathbf{q}_\perp) = \frac{4d_A C_A^2 g^4}{\nu_g} \frac{1}{q_\perp^4} \int \frac{d^3 \mathbf{k}}{(2\pi)^3} \frac{k - k_z}{k} f(\mathbf{k}). \quad (7.17)$$

Therefore, the broadening kernel is proportional to the number density $J^0 = n = \nu_g \int \frac{d^3 \mathbf{p}}{(2\pi)^3} f(\mathbf{p})$ and the number current in the jet direction $J^z = \nu_g \int \frac{d^3 \mathbf{p}}{(2\pi)^3} f(\mathbf{p}) p_z / |\mathbf{p}|$, which is zero for a distribution that obeys the symmetry condition (3.72). Using that, we obtain

$$\lim_{|\mathbf{q}_\perp| \rightarrow \infty} C(\mathbf{q}_\perp) \rightarrow \frac{g^4 C_R \mathcal{N}}{q_\perp^4}, \quad (7.18)$$

where \mathcal{N} , in the general case also including quarks (see Appendix C.2.2), is given by

$$\mathcal{N} = \int \frac{d^3 \mathbf{k}}{(2\pi)^3} \left(2N_c f_g(\mathbf{k}) + \sum_f f_f(\mathbf{k}) \right). \quad (7.19)$$

Importantly, this does not depend on the angle of \mathbf{q}_\perp for an arbitrary¹ distribution function $f(\mathbf{k})$.

The opposite limit, $|\mathbf{q}_\perp| \rightarrow 0$ is more difficult to take because in this limit screening effects become important. While for isotropic systems, the q_z integral can be performed analytically using a sum rule (see Appendix A.5.4), in the anisotropic case, this is more difficult. Here, it will be enough to demonstrate that the leading behavior is $1/q_\perp^2$. It is not apriori clear that this should be the case since screening effects would naively change the propagators from $1/q^2 \rightarrow 1/(q^2 + \tilde{m}^2)$, where \tilde{m} is some effective screening mass, thus becoming finite at low momenta. Thus, we need to consider the HTL self-energy correction instead and reevaluate the integral more cautiously.

To do that, we start with (7.8), and, following the steps in Appendix A.5.4, we write the matrix element as (without assuming isotropic distributions),

$$\lim_{p \rightarrow \infty} \frac{|\mathcal{M}_{gg}^{gg}|^2}{4d_A C_A^2} = \tilde{c}_1^2 |G_L|^2 + \tilde{c}_2^2 |G_T|^2 - 2\tilde{c}_1\tilde{c}_2 |G_L|^2 |G_T|^2 (AC + BD) \quad (7.20)$$

It is enough to focus on the transverse propagator, (with $x = q_z/q$)

$$|G_T|^2 = -\frac{4q}{q_z m_D^2 \pi (1-x^2)} \frac{\text{Im} \Pi^T(x)}{(q^2 + \text{Re} \Pi^T(x))^2 + (\text{Im} \Pi^T(x))^2}, \quad (7.21)$$

which, when integrated over q_z using the sum rule from Appendix A.5.4 gives

$$\int_{-\infty}^{\infty} \frac{dq_z}{q} |G_T|^2 = -\frac{4}{m_D^2} \left[\frac{1}{q_\perp^2 + \text{Re} \Pi^T(\infty)} - \frac{1}{q_\perp^2 + \text{Re} \Pi^T(0)} \right] = -\frac{4}{m_D^2} \left[\frac{1}{q_\perp^2 + m_D^2/3} - \frac{1}{q_\perp^2} \right]. \quad (7.22)$$

This gives exactly the $1/q_\perp^2$ contribution that we wanted to show and proves that the leading contribution goes like $\sim 1/q_\perp^2$ for small q_\perp , even in an anisotropic system.²

Thus, to summarize, the limiting cases are

$$C(\mathbf{q}_\perp) \rightarrow \begin{cases} \frac{a(\phi)}{q_\perp^2}, & q_\perp \rightarrow 0 \\ \frac{g^2 C_R \mathcal{N}}{q_\perp^4}, & q_\perp \rightarrow \infty \end{cases} \quad (7.23a)$$

where the coefficient $a(\phi)$ may depend on the direction of \mathbf{q}_\perp .

For an isotropic system, the coefficient a for the small q_\perp case can be obtained analytically using exactly the same rule mentioned above. It leads to

$$\lim_{q_\perp \rightarrow 0} C(q_\perp) \rightarrow g^2 C_R T_* \frac{m_D^2}{q_\perp^2 (q_\perp^2 + m_D^2)}, \quad (7.23b)$$

and in equilibrium we have $T_* \rightarrow T$ and the equilibrium form of the Debye mass (3.13).

¹ As long as the assumptions needed for the elastic scattering rate (7.4) are valid.

² A more careful analysis potentially revealing more of the angular information of the coefficient $a(\phi)$ in Eq. (7.23a) may be possible, but since we deal with an isotropic screening prescription, it seems going beyond a simple scaling needed for the extrapolations used here, is not needed and perhaps not useful.

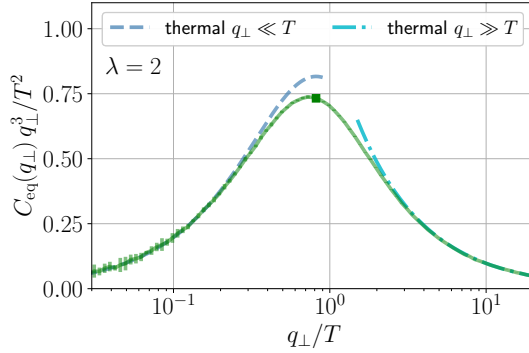


Figure 7.1: Collision kernel $C(q_\perp)$ for a thermal gluonic system multiplied with q_\perp^3 in units of the plasma temperature T for coupling $\lambda = 2$. This is the integrand of the jet quenching parameter \hat{q} . Shown are also the analytic small and large q_\perp limits (7.23), as well as the Debye mass m_D as a square on the curve.

7.1.4 Numerical results

Similar to the jet quenching parameter \hat{q} in Chapter 4.4, Eq. (7.8) is evaluated using Monte Carlo integration. We consider a purely gluonic system with a gluon jet, but in the limit $p \rightarrow \infty$, the collision kernel for a quark jet or parton can be obtained using Casimir scaling (4.46),

$$\frac{C_{\text{gluon}}^{\text{gluon}}(\mathbf{q}_\perp)}{C_A} = \frac{C^{\text{quark}}(\mathbf{q}_\perp)}{C_F}. \quad (7.24)$$

Thermal equilibrium

First, we consider a thermal system, i.e., take $f(\mathbf{k})$ to be the Bose-Einstein distribution $f_+(k)$, Eq. (3.20). The numerical results for the collision kernel multiplied with q_\perp^3 are shown in Fig. 7.1 as a solid green curve. The analytic limits (7.23) are added as dashed and dash-dotted curves. We see that they nicely agree in their respective region of applicability. The collision kernel $C_{\text{eq}}(q_\perp)$ in thermal equilibrium is approximately peaked at the Debye mass, which is indicated by a square on the curve.

We will frequently use the thermal form $C_{\text{eq}}(q_\perp)$ to normalize the nonequilibrium kernel $C(\mathbf{q}_\perp)$, in order to highlight the deviations from the thermal form. For that, always the numerically evaluated $C_{\text{eq}}(q_\perp)$ is used, and computed with the corresponding discretization parameters as in the nonequilibrium case.

Bjorken expanding systems

We now consider gluonic plasmas undergoing Bjorken expansion, motivated by the initial stages in heavy-ion collisions. We take the initial conditions described in more detail in Section 3.6.2 with $\xi_0 = 10$, and use the couplings $\lambda = 2$ and $\lambda = 10$. We use $\lambda = 2$, because for this coupling the qualitative and quantitative features of the bottom-up thermalization (see Chapter 3.5.2) are still clearly visible, and the system is still moderately weakly coupled, and choose $\lambda = 10$ as a more phenomenologically relevant value.

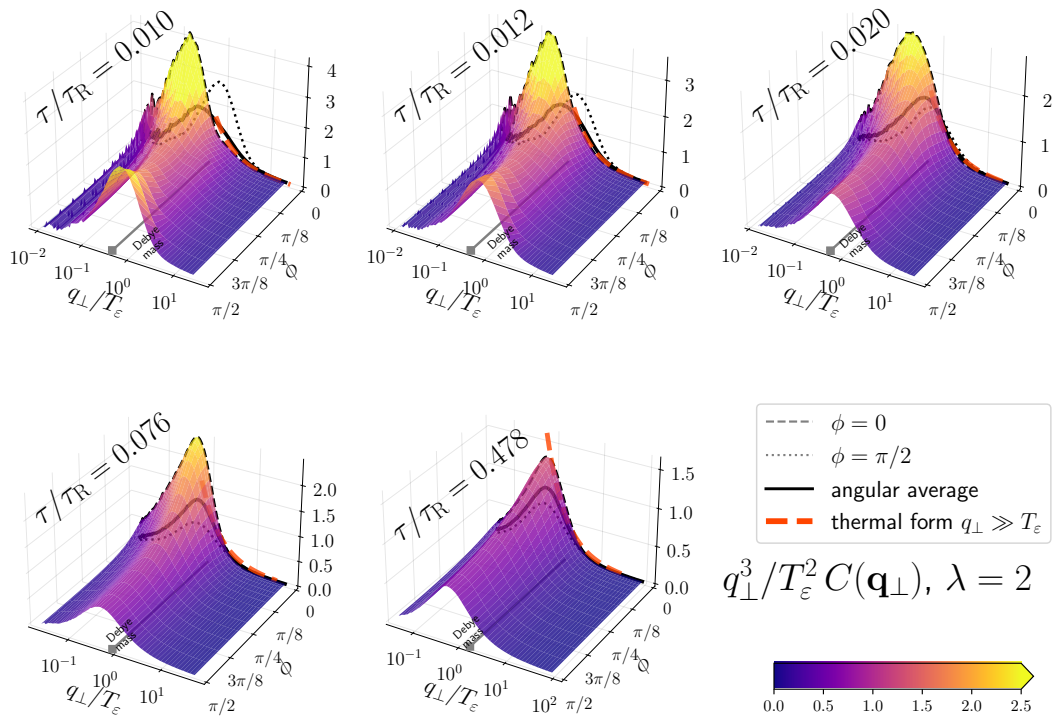


Figure 7.2: Collision kernel $C(\mathbf{q}_\perp)$ of a gluonic plasma undergoing bottom-up thermalization for various times during the evolution for coupling $\lambda = 2$. The back plane shows the projection of the angles $\phi = 0$ and $\phi = \pi/2$, the angular average $\langle C(q_\perp) \rangle_\phi$ and the large q_\perp result (7.23a) in thermal equilibrium with the same energy density.

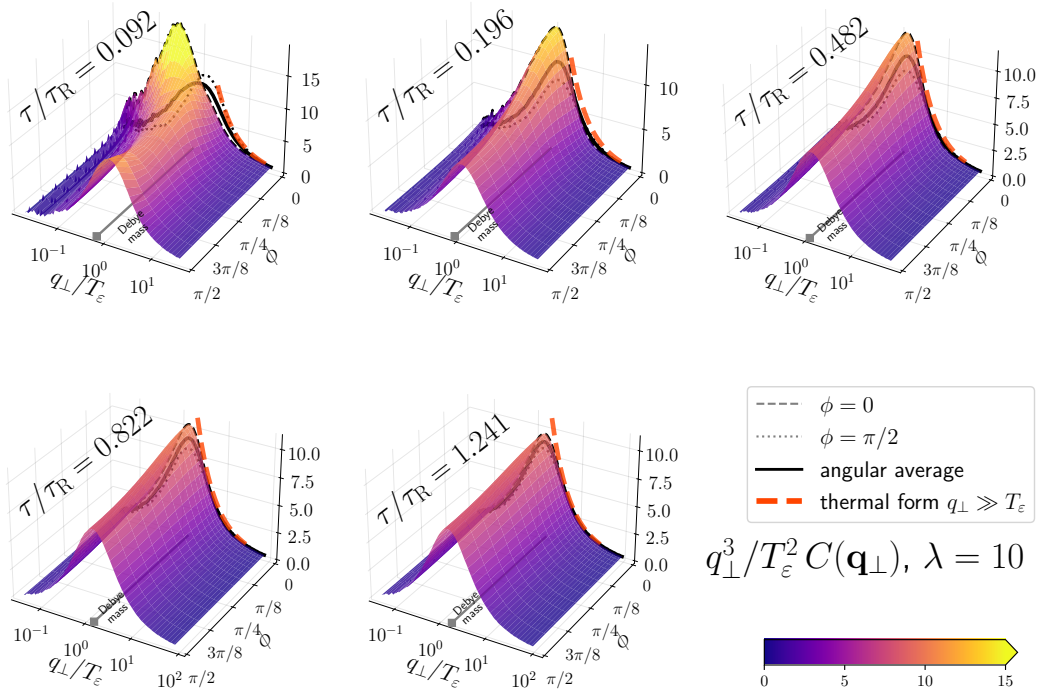


Figure 7.3: Collision kernel $C(\mathbf{q}_\perp)$ of a gluonic plasma undergoing bottom-up thermalization for various times during the evolution for coupling $\lambda = 10$. The back plane shows the projection of the angles $\phi = 0$ and $\phi = \pi/2$, the angular average $\langle C(q_\perp) \rangle_\phi$ and the large q_\perp result (7.23a) in thermal equilibrium with the same energy density.

Figs. 7.2 and 7.3 show the results for the anisotropic collision kernel $C(\mathbf{q}_\perp)$ for various times and the two couplings $\lambda = 2$ (Fig. 7.2) and $\lambda = 10$ (Fig. 7.3). The anisotropic kernel is shown as a surface plot with the height (and color) representing the value of the collision kernel, rescaled with $q_\perp^3/T_\varepsilon^2$, representing the integrand of the jet quenching parameter \hat{q} . Recall that T_ε is an effective temperature of the nonequilibrium system obtained via the Landau matching condition (3.84). The kernel for $\phi = 0$ (broadening along beam axis), $\phi = \pi/2$ (broadening transverse to beam) and the angular averaged collision kernel

$$\langle C(q_\perp) \rangle_\phi = \frac{1}{2\pi} \int_0^{2\pi} d\phi C(q_\perp, \phi) \quad (7.25)$$

are shown as black lines on the back plane, where also the large q_\perp result (7.23a) for a thermal system with temperature T_ε are shown as an orange dashed line. Additionally, the Debye mass is marked with a gray square (and line) on the x -axis (where q_\perp/T_ε is plotted). The time variable is given as a ratio over the relaxation time τ_R (see Eq. (3.85b)).

At late times, the kernel is seen to be isotropic (flat in the ϕ direction), while at early times it is most anisotropic, with a large peak at $\phi = 0$ and a smaller one at $\phi = \pi/2$. The latter is only visible at very early times and is more pronounced for $\lambda = 2$. The peak itself is at the Debye mass for later times and is shifted towards smaller momenta at early times and small angles. Clearly visible is also the noise from the Monte Carlo evaluation of the integral at small momenta and early times, see, e.g., the top left panel in Fig. 7.2.

The angular resolution can be studied in more detail in the top panels of Fig. 7.4. Here, as already shown on the back sides of the three-dimensional plots in Figs. 7.2 and 7.3, both the angular averaged kernel (7.25), and the two angles $\phi = 0$ and $\phi = \pi/2$ are shown for two distinct times. It can be clearly seen that the anisotropy decreases at later times. The box marks the Debye mass. As already mentioned before, for very early times, the nonequilibrium collision kernel is peaked at momenta below the Debye mass, and the peak is shifted even more to lower momenta for smaller angles ϕ . This might suggest that at early times, the effective screening scale is angle-dependent, and considerably lower than the Debye mass at small angles.

This is further corroborated by the central and bottom panels in Fig. 7.4. The central panels show the angular averaged collision kernel for different times. We clearly observe the evolution towards its equilibrium form and its peak shifting from the left towards the Debye mass, which is again indicated by the squares. In the bottom panels, the collision kernel is normalized to its equilibrium form. There, the enhancement of small momentum exchanges for early times is most visible. For instance, for $\lambda = 2$ and $\tau/\tau_R \leq 0.08$, small momentum exchange processes are enhanced by more than a factor 2, which is similar for $\lambda = 10$ and $\tau/\tau_R \leq 0.2$. This indicates that small momentum exchange processes are more likely than in thermal equilibrium and that using a thermal form for the collision kernel drastically underestimates the momentum transfer at small momenta q_\perp . Thus, describing the momentum broadening during the splitting process as a diffusion process in transverse momentum space, as required for the multiple-soft-scattering approximation (see Chapter 3) is a good approximation in this region.

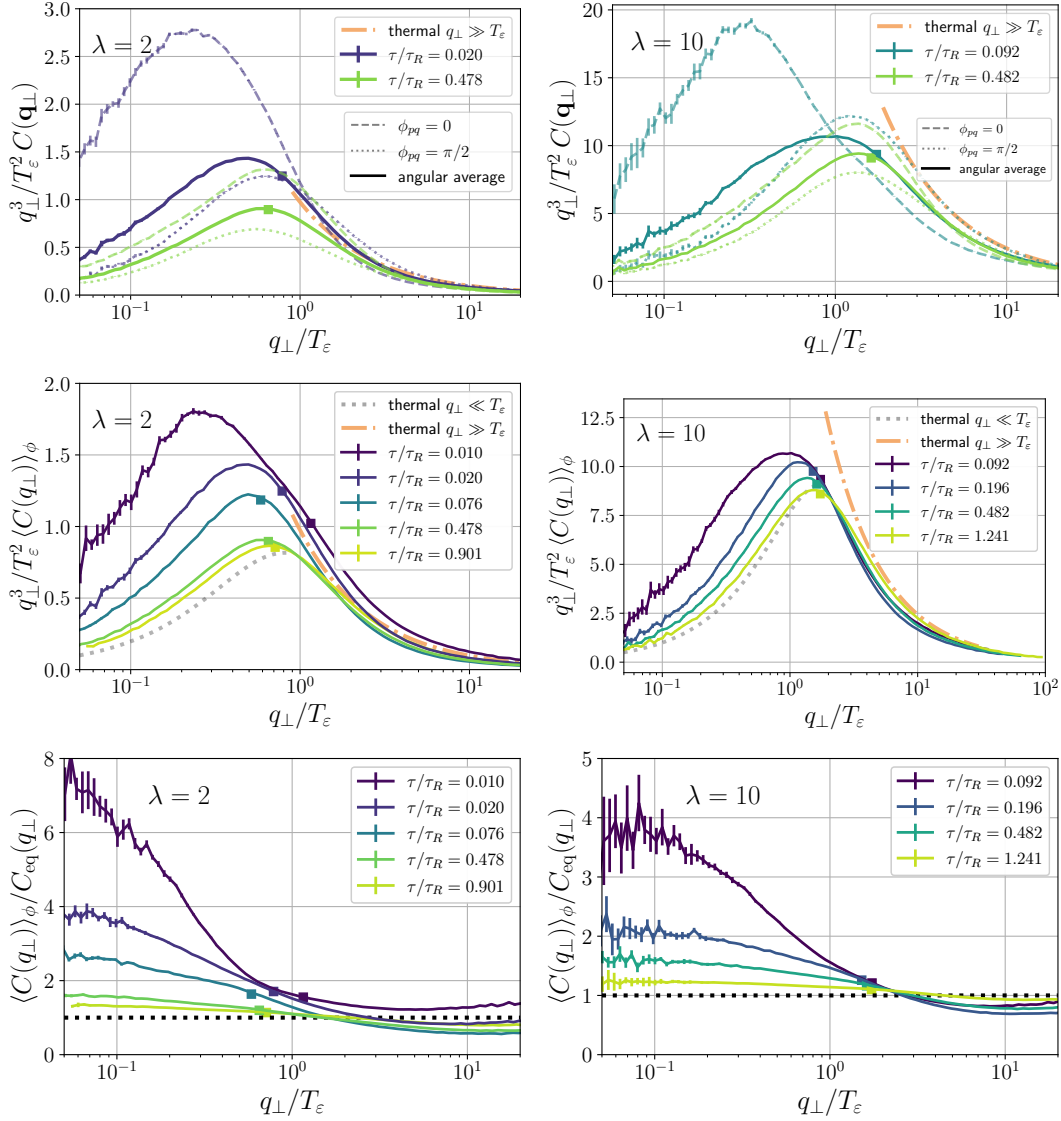


Figure 7.4: Collision kernel $C(\mathbf{q}_\perp)$ for different times as a function of the momentum transfer q_\perp . Runs with coupling $\lambda = 2$ are depicted in the left column and those with $\lambda = 10$ in the right column. The box indicates the Debye mass. (Top): Collision kernel for two angles and angular average at an early and late time. (Center): Angular averaged collision kernel (7.25) for different times (color-coded). Shown are also the limiting analytic expressions for a thermal system (7.23). (Bottom): Angular averaged collision kernel normalized to the thermal one for the Landau-matched temperature T_ε for different times.

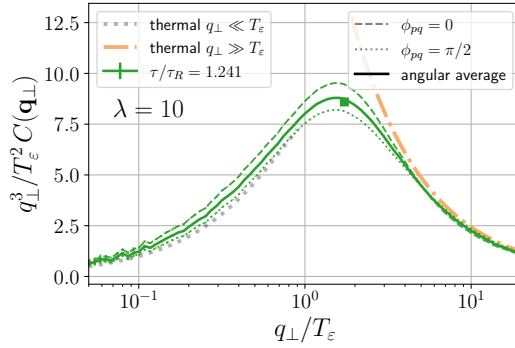


Figure 7.5: Collision kernel for two angles and angular average for $\lambda = 10$, showing the anisotropy present even at a relatively late time.

Since the enhancement gets larger for smaller angles ϕ , scatterings with momentum transfer along the beam axis are more likely. This counteracts the highly anisotropic plasma with small longitudinal momentum extent and contributes to a broadening of the distribution.

At late times, the collision kernel coincides with its equilibrium form, as we can see explicitly in the bottom panel in Fig. 7.4, where at late times the ratio of the nonequilibrium kernel to its equilibrium counterpart is close to unity for all momenta.

Finally, due to the Bjorken expansion, the plasma never fully isotropizes. For instance, the pressure ratio only approaches but never reaches unity (up to numerical uncertainties). In particular, also the collision kernel is expected to remain anisotropic, even at late times. Fig. 7.5 shows the results for the nonequilibrium kernel for $\lambda = 10$, where we observe a clearly visible anisotropy in the kernel even at rather late times $\tau/\tau_R = 1.2$, where a hydrodynamic description starts becoming applicable (see Fig. 3.3). This underlines that understanding which physical effects and observables are sensitive to the anisotropy in the collision kernel (and related jet quenching parameter) is an important step to understanding the nonequilibrium stages in heavy-ion collisions.

7.2 DIPOLE CROSS SECTION

We have already discussed in Section 2.2 that the splitting rate is obtained by transforming the collision kernel to impact parameter space (7.11),

$$C(\mathbf{x}) = \int \frac{d^2 \mathbf{q}_\perp}{(2\pi)^2} (1 - \cos(\mathbf{q}_\perp \cdot \mathbf{x})) C(\mathbf{q}_\perp) \quad (7.26)$$

to obtain the dipole cross section. We will now study the form of this dipole cross section $C(\mathbf{x})$ in expanding systems. The Fourier transform (7.11) is performed numerically. As $C(\mathbf{q}_\perp)$ is obtained on a finite grid $q_\perp^{\min} < q_\perp < q_\perp^{\max}$, smaller and larger values of q_\perp are obtained by extrapolation using the limiting forms (7.23a). In practice, the small q_\perp behavior is fitted to $a_1(\phi)/q_\perp^2$, and the large q_\perp behavior to $a_2(\phi)/q_\perp^4$.

The integral in Eq. (7.26) can be done analytically for the small q_\perp form of the collision kernel for isotropic distributions (7.23b),

$$C(q_\perp) = \frac{C_R g_s^2 m_D^2 T_*}{q_\perp^2 (q_\perp^2 + m_D^2)}, \quad (7.27)$$

which yields (see Appendix A.5.5)

$$C_{\text{iso}}^{\text{appr.}}(|\mathbf{x}|) = \frac{C_R g_s^2 T_*}{2\pi} \left(\gamma_E + K_0(|\mathbf{x}| m_D) + \log \frac{|\mathbf{x}| m_D}{2} \right), \quad (7.28)$$

with T_* and m_D given by Eqs. (3.10) and (3.11). In equilibrium, this then becomes

$$C_{\text{eq}}^{\text{appr.}}(|\mathbf{x}|) = \frac{C_R g_s^2 T}{2\pi} \left(\gamma_E + K_0(|\mathbf{x}| m_D) + \log \frac{|\mathbf{x}| m_D}{2} \right), \quad (7.29)$$

with the equilibrium Debye mass (3.13). This form (7.29) or also the small q_\perp expression (7.27) is also often used in the literature (see, e.g., [97, 124, 125, 169]). For instance, it is used in QCD kinetic theory simulations to calculate the splitting rates γ_{bc}^a as discussed in Section 3.3.1, or also used as a medium model in jet quenching studies. While Eq. (7.29) is convenient because of its simple analytic form, it should be emphasized that it is not the correct form of the dipole cross section in thermal equilibrium. For that, not only the small q_\perp form (7.23b), but the whole possibly numerically evaluated collision kernel needs to be Fourier transformed using Eq. (7.26). Therefore, we label it $C_{\text{eq}}^{\text{appr.}}$, because it constitutes an analytic approximation to the true thermal form of the dipole cross section.

7.2.1 Small distance limit

As explained before, for highly energetic particles (see Chapter 3), the small distance form of the dipole cross section is important. Here, we discuss the analytic limit of the small distance behavior of the dipole cross section and show that it can be expressed using the jet quenching parameter $\hat{q}(\Lambda_\perp)$ with a transverse momentum cutoff.

In an isotropic system (when $C(\mathbf{q}_\perp, t)$ does not depend on the angle ϕ), the angular integral in (7.26) can be done analytically,

$$C(|\mathbf{x}|) = \int_0^\infty \frac{dq_\perp}{2\pi} q_\perp (1 - J_0(|\mathbf{x}| q_\perp)) C(q_\perp). \quad (7.30)$$

First, let us consider the isotropic case of thermal equilibrium. There, to find the small distance $|\mathbf{x}| \ll 1/T$ behavior of the dipole cross section $C(|\mathbf{x}|)$, one might naively expect it to be sufficient to expand the integrand in powers of $|\mathbf{x}|$, $(1 - J_0(|\mathbf{x}| q_\perp)) = \mathbf{x}^2 q_\perp^2 / 4 + \mathcal{O}(\mathbf{x}^4 q_\perp^4)$. However, in this expansion

$$C(|\mathbf{x}|) \sim \mathbf{x}^2 + \mathcal{O}(\mathbf{x}^4), \quad (7.31)$$

the first nonvanishing term for the dipole cross section $C(x)$ is given by the jet quenching parameter \hat{q} ,

$$\hat{q} \sim \int_0^\infty \frac{dq_\perp}{2\pi} q_\perp^3 C(q_\perp) \rightarrow \infty, \quad (7.32)$$

and is divergent (without introducing a UV cutoff), as we have discussed before extensively in Section 4.1.7. Clearly, the problem is the highly oscillatory function $J_0(|\mathbf{x}|q_\perp)$ at large q_\perp . The result could be made finite by introducing again a UV cutoff Λ_\perp , but it is not clear at this stage how this would appear naturally in Eq. (7.30).

And even worse, for the analytically solvable case, (7.29), the small- $|\mathbf{x}|$ behavior is not given by (7.31) but

$$C(|\mathbf{x}| \ll 1/T) = \mathbf{x}^2(a_1 + b_1 \log |\mathbf{x}|) + \dots \quad (7.33)$$

In particular, the logarithmic dependence on $|\mathbf{x}|$ will be important for small- $|\mathbf{x}|$. It is now also clear that the naïve expansion in (7.31) was doomed to fail since it would have never led to a logarithm by just expanding the integrand for small- $|\mathbf{x}|$.

A better way to do it in full generality is to introduce a cutoff Λ_\perp in the integral, and to split the integral in a part below and above the cutoff,

$$C(\mathbf{x}) = \int_{q_\perp < \Lambda_\perp} \frac{d^2 \mathbf{q}_\perp}{(2\pi)^2} (1 - e^{i\mathbf{q}_\perp \cdot \mathbf{x}}) C(\mathbf{q}_\perp) + \int_{\Lambda_\perp}^\infty \frac{dq_\perp}{2\pi} q_\perp C(q_\perp) (1 - J_0(bq_\perp)). \quad (7.34)$$

Here, we have already used that for a general distribution function, the collision kernel becomes isotropic for sufficiently large q_\perp , and is given by (see Eq. (7.23a))

$$C(q_\perp) = \frac{g^4 C_R \mathcal{N}}{q_\perp^4}. \quad (7.35)$$

In the first integral in Eq. (7.34), we can expand the exponential for small \mathbf{x} , which yields exactly the jet quenching parameter \hat{q} with a transverse momentum cutoff Λ_\perp ,

$$\int_{q_\perp < \Lambda_\perp} \frac{d^2 \mathbf{q}_\perp}{(2\pi)^2} (1 - e^{i\mathbf{q}_\perp \cdot \mathbf{x}}) C(\mathbf{q}_\perp) \approx \frac{1}{2} \int_{q_\perp < \Lambda_\perp} \frac{d^2 \mathbf{q}_\perp}{(2\pi)^2} (x^2 q_x^2 + y^2 q_y^2) C(\mathbf{q}_\perp) \quad (7.36)$$

$$= \frac{1}{2} (x^2 \hat{q}^{xx}(\Lambda_\perp) + y^2 \hat{q}^{yy}(\Lambda_\perp)), \quad (7.37)$$

where we have parameterized the vector $\mathbf{x} = (x, y)$. For large enough cutoffs Λ_\perp , we have seen before in Section 4.1.8 (see Eq. (4.50)) that the jet quenching parameter \hat{q} has the simple form

$$\hat{q}^{xx} = a \log \Lambda_\perp / Q_s + b_x, \quad \hat{q}^{yy} = a \log \Lambda_\perp / Q_s + b_y \quad (7.38)$$

The second integral in Eq. (7.34) can be solved analytically for the isotropic large q_\perp form (7.35) (which is also valid for an anisotropic distribution function $f(\mathbf{p})$),

$$\int_{\Lambda_\perp}^\infty \frac{dq_\perp}{2\pi} \frac{C_R g^4 \mathcal{N}}{q_\perp^3} (1 - J_0(|\mathbf{x}|q_\perp)) \quad (7.39)$$

$$= \frac{C_R g^4 \mathcal{N}}{256\pi} \left(\Lambda_\perp^2 \mathbf{x}^4 {}_2F_3 \left(1, 1; 2, 3, 3; -\frac{\Lambda_\perp^2 \mathbf{x}^2}{4} \right) - 32x^2 \left(-1 + \gamma_E + \log \frac{\Lambda_\perp |\mathbf{x}|}{2} \right) \right),$$

$$= -\frac{C_R g^4 \mathcal{N}}{8\pi} \mathbf{x}^2 \left(\gamma_E - 1 + \log \frac{\Lambda_\perp |\mathbf{x}|}{2} \right) + \mathcal{O}(\mathbf{x}^4) \quad (7.40)$$

where ${}_pF_q$ is the generalized hypergeometric function and γ_E is the Euler Mascheroni constant.

Importantly, since the sum of the two integrals in (7.34) cannot depend on Λ_\perp for small $|\mathbf{x}|$, the terms $\log \Lambda_\perp$ must exactly cancel in the sum. In particular, because the large q_\perp form (7.40) is isotropic, so must be the cutoff dependence in Eq. (7.38). This provides another argument for why the coefficient a in (7.38) cannot depend on the direction.

Adding these two expressions, we finally obtain the small $|\mathbf{x}|$ form of the dipole cross section,

$$C(\mathbf{x}, t) \approx \frac{1}{2}(x^2 b_x(t) + y^2 b_y(t)) + \frac{\mathbf{x}^2 \hat{q}_0(t)}{2} \left(1 - \gamma_E - \log \frac{|\mathbf{x}| Q_s}{2} \right), \quad (7.41)$$

where we have redefined $\hat{q}_0(t) = a(t)$, and a , b_x and b_y come from the large cutoff parameterization of the jet quenching parameter (7.38), which leads to

$$\hat{q}_0(t) = a(t) = \frac{g^4 C_R \mathcal{N}(t)}{4\pi}. \quad (7.42)$$

More conventionally (see, e.g., [124]), the small- $|\mathbf{x}|$ form is often written as

$$C(\mathbf{x}, t) \approx \frac{1}{4} \hat{q}_0(t) \mathbf{x}^2 \log \frac{1}{\mathbf{x}^2 \mu_{*0}^2(t)} \quad (7.43)$$

which, for an anisotropic medium, can be generalized to

$$C(\mathbf{x}, t) \approx \frac{1}{4} \hat{q}_0(t) \left(x^2 \log \frac{1}{\mathbf{x}^2 \mu_{*0}^2} + x^2 \log \frac{Q_s^2}{\mu_x^2} + y^2 \log \frac{Q_s^2}{\mu_y^2} \right), \quad (7.44)$$

where we need to identify

$$\mu_i^2 = e^{-\frac{2b_i}{\hat{q}_0}}, \quad \mu_{*0}^2 = \frac{1}{4} e^{2\gamma_E - 2}. \quad \hat{q}_0 = a. \quad (7.45)$$

For the special case of thermal equilibrium (and pure gluons), we can use the result for \hat{q} from Eq. (4.77a) to obtain

$$C_{\text{eq}}(\mathbf{x}) \approx \frac{\mathbf{x}^2}{4} \frac{C_R N_C g^4 T^3}{\pi^3} \quad (7.46)$$

$$\times \left[\zeta(3) \left(1 - \gamma_E + \ln \frac{2}{|\mathbf{x}| m_D} \right) + (\zeta(2) - \zeta(3)) \left\{ \log \frac{T}{m_D} + \frac{1}{2} - \gamma_E + \log 2 \right\} - \frac{\sigma_+}{2\pi} \right] \quad (7.47)$$

from which we may deduce in equilibrium

$$\hat{q}_0 = \frac{C_R N_C g^4 T^3 \zeta(3)}{2\pi^3}, \quad (7.48a)$$

$$\mu_{*0}^2 = \frac{m_D^2}{4} \left(\frac{m_D}{2T} \right)^{2\zeta(2)/\zeta(3)-2} \exp \left[2\gamma_E - 2 - \left(\frac{\zeta(2)}{\zeta(3)} - 1 \right) (1 - 2\gamma_E) + \frac{\sigma_+}{\pi \zeta(3)} \right]. \quad (7.48b)$$

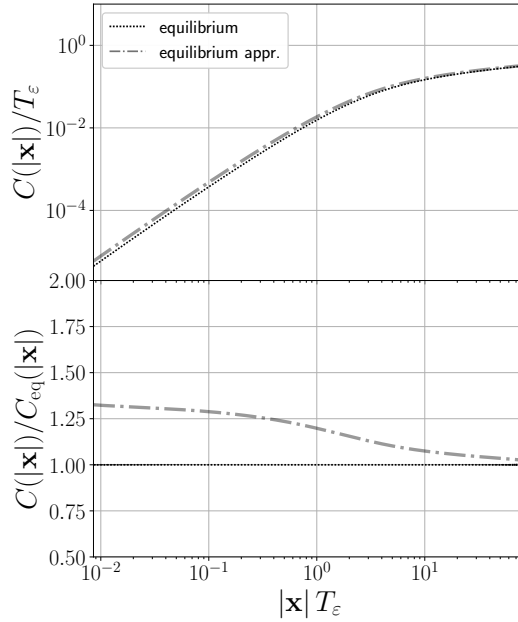


Figure 7.6: Dipole cross section $C(x)$ in thermal equilibrium, compared with an often used analytic approximation (7.29) for $\lambda = 2$.

7.2.2 Numerical results

Let us now move on to discuss the numerical results for the dipole cross section, which we first discuss in thermal equilibrium. Fig. 7.6 compares the thermal form for the dipole cross section $C_{\text{eq}}(|x|)$ with the analytic approximation $C_{\text{eq}}^{\text{appr.}}(|x|)$ from Eq. (7.29). While the upper panel shows both curves on a logarithmic scale, where only little differences are visible, the lower panel depicts their ratio. We find that at small $|x|$, which is the region relevant for highly energetic partons, these two expressions differ by more than 25%, which implies that the small- $|x|$ behavior of $C_{\text{eq}}^{\text{appr.}}$ significantly overestimates the true small- $|x|$ behavior.

Next, we consider the dipole cross section of the expanding plasma for $\lambda = 2$ and two early times in Fig. 7.7. In particular, we consider the times $\tau/\tau_R = 0.01$ (left panels) and $\tau/\tau_R = 0.48$ (right panels). In the upper panels, the dipole cross section is plotted in units of the temperature T_ε ; in the lower panels, it is normalized to its equilibrium form. The two angles $\phi = 0$ and $\phi = \pi/2$, and the angular averaged dipole cross section $\langle C(x) \rangle_\phi$ are shown as solid lines. We compare the full dipole cross section with the small x result (7.41), which is shown as dashed lines, and agrees very well for both times and angles.

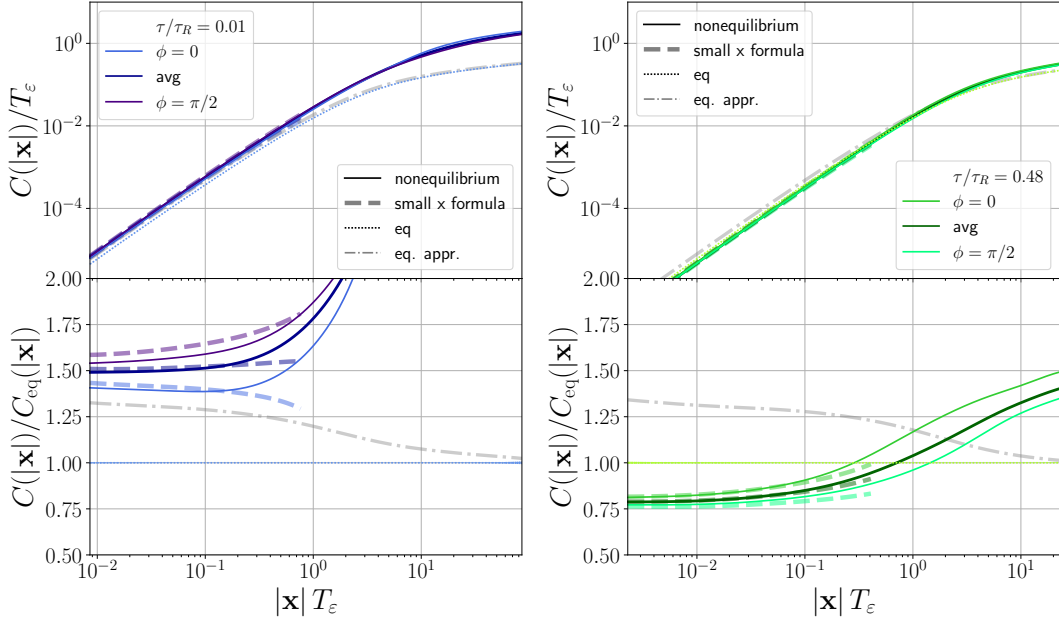


Figure 7.7: Dipole cross section $C(\mathbf{x})$ for two angles and angular average for two distinct times (left and right panels). In the top panels, the dipole cross section itself is shown, in the bottom panels it is normalized to its thermal value. We also show the small- $|\mathbf{x}|$ formula (7.41).

This angular averaged dipole cross section can be obtained from the angular averaged collision kernel, as we show now. For that, consider the angular averaged dipole cross section,

$$\langle C(|\mathbf{x}|) \rangle_\phi = \frac{1}{2\pi} \int_0^{2\pi} d\phi C(|\mathbf{x}|, \phi) = \frac{1}{2\pi} \int_0^{2\pi} d\phi_x \int \frac{d^2 \mathbf{q}_\perp}{(2\pi)^2} (1 - \cos(\mathbf{q}_\perp \cdot \mathbf{x})) C(\mathbf{q}_\perp) \quad (7.49)$$

$$= \frac{1}{2\pi} \int_0^{2\pi} d\phi_x \frac{1}{2\pi} \int_0^{2\pi} d\phi_q \int \frac{dq_\perp q_\perp}{2\pi} (1 - \cos(q_\perp |\mathbf{x}| \cos(\phi_x - \phi_q))) C(q_\perp, \phi_q) \quad (7.50)$$

We can now swap the ϕ_x and ϕ_q integrations and define a new integration variable $\tilde{\phi}_x = \phi_x - \phi_q$, such that

$$\langle C(|\mathbf{x}|) \rangle_\phi = \frac{1}{2\pi} \int_0^{2\pi} d\phi_q \frac{1}{2\pi} \int_{-\phi_q}^{2\pi - \phi_q} d\tilde{\phi}_x \int \frac{dq_\perp q_\perp}{2\pi} (1 - \cos(q_\perp |\mathbf{x}| \cos \tilde{\phi}_x)) C(q_\perp, \phi_q). \quad (7.51)$$

Because we integrate $\tilde{\phi}_x$ over the whole period of the cosine, we may shift it freely, and then have

$$\langle C(|\mathbf{x}|) \rangle_\phi = \frac{1}{2\pi} \int_0^{2\pi} d\tilde{\phi}_x \int \frac{dq_\perp q_\perp}{2\pi} (1 - \cos(q_\perp |\mathbf{x}| \cos \tilde{\phi}_x)) \frac{1}{2\pi} \int_0^{2\pi} d\phi_q C(q_\perp, \phi) \quad (7.52)$$

$$= \int \frac{d^2 \mathbf{q}_\perp}{(2\pi)^2} (1 - \cos(q_\perp |\mathbf{x}| \cos \phi_q)) \langle C(q_\perp) \rangle_\phi, \quad (7.53)$$

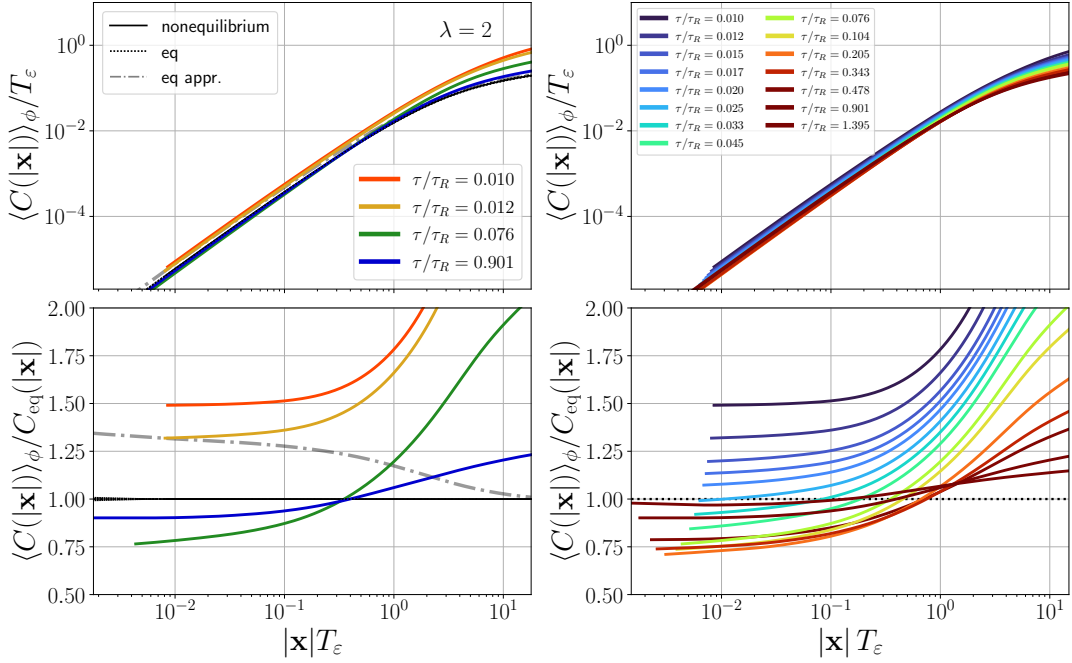


Figure 7.8: Dipole cross section $\langle C(x) \rangle_\phi$ for different times and $\lambda = 2$. In the left panel, four times are chosen to illustrate the general behavior, whereas in the right panel, more times are shown to show the continuous behavior.

which proves that to obtain the angular average of the dipole cross section $\langle C(|x|) \rangle_\phi$, it is enough to use the isotropic already angular averaged collision kernel $\langle C(q_\perp) \rangle_\phi$ (Eq. (7.25)) in the Fourier transform (7.26).

We will now move on to discuss the time evolution of the dipole cross section. The angular averaged dipole cross section $\langle C(x) \rangle_\phi$ is depicted for different times for couplings $\lambda = 2$ in Fig. 7.8 and $\lambda = 10$ in Fig. 7.9. In the top panels, the dipole cross section is normalized by the effective temperature T_ϵ from Eq. (3.84), and in the lower panels by its equilibrium value. In the left panels, four distinct times are shown, whereas the right panels show more times to illustrate the continuous evolution. We observe that the dipole cross section as a function of time behaves qualitatively differently for small and large $|x|$, as compared to its thermal form. For all couplings and times, at large x , the dipole cross section significantly exceeds its equilibrium values and continuously decreases towards equilibrium throughout the time evolution. In contrast, at small $|x|$, which is the relevant region for highly energetic partons (jet quenching), the evolution is not monotonous, and we consider this region in more detail in Fig. 7.10. There, the small- $|x|$ behavior is shown at $|x|T_\epsilon = 0.01$ as a function of time. In particular, for $\lambda = 2$, the dipole cross section is initially about 50% larger than in equilibrium, then quickly drops below its equilibrium value at around $\tau/\tau_R \approx 0.025$, and then approaches its equilibrium value from below. Therefore, for times $\tau/\tau_R \gtrsim 0.025$, gluon radiation and thus jet quenching is suppressed as compared to thermal equilibrium. Naively, in the infinite static medium, the rate/spectrum would go as $\sqrt{\hat{q}}$ (see Eq. (2.6)), and \hat{q} determines the small distance behavior of $\langle C(|x|) \rangle_\phi$. Thus, the suppression in the spectrum is expected to be less dramatic than the suppression of the dipole cross section. The smallest value is at about 0.75 of its thermal value, and we would

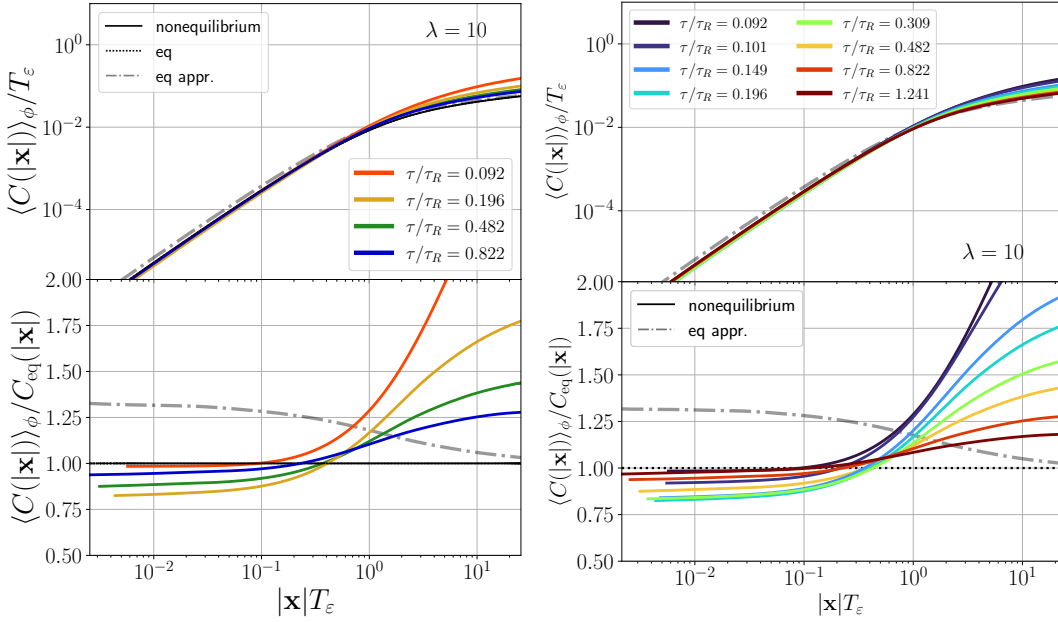


Figure 7.9: Dipole cross section $\langle C(x) \rangle_\phi$ for different times and $\lambda = 10$. In the left panel, four times are chosen to illustrate the general behavior, whereas in the right panel, more times are shown to show the continuous behavior.

therefore expect the suppression to be of $\sqrt{0.75} \approx 0.87$, only of about 10%. This naïve estimate is, of course, very simplistic; in practice, one needs to integrate over the whole splitting process.

An interesting feature of Fig. 7.10 is the angular ordering, i.e. that the dipole cross section for $\phi = 0$ is initially suppressed until the star marker and then enhanced as compared to the $\phi = \pi/2$ cross section. This is similar to the behavior of the jet quenching parameter which was observed in Chapter 4.4.

For $\lambda = 10$, the qualitative behavior, i.e., that the dipole cross section at small $|\mathbf{x}|$ first drops and then rises again as compared to its equilibrium value stays the same, but for the whole evolution, it is below the thermal value, which indicates suppression of jet quenching during the whole evolution. Although this is qualitatively in agreement with findings of phenomenological studies that find jet quenching needs to be suppressed before $\tau = 0.6 \text{ fm}/c$ [76], the effect coming from the rather mild suppression of the dipole cross section at small $|\mathbf{x}|$ is rather too small to explain this. However, this result provides a hint that the nonequilibrium dynamics may influence the collision kernel and dipole cross section and can lead to an effective suppression of jet quenching during the initial stages.

7.3 GLUON RADIATION IN AN ANISOTROPIC MEDIUM

As explained in Chapter 3, the collision kernel is the key input for calculating the rate of inelastic gluon emissions. It is used as the medium input for jet quenching calculations, where one considers a highly energetic parton emitting a gluon. In that case, the dominant contribution comes from the small distance (small- $|\mathbf{x}|$) behavior of the dipole cross section.

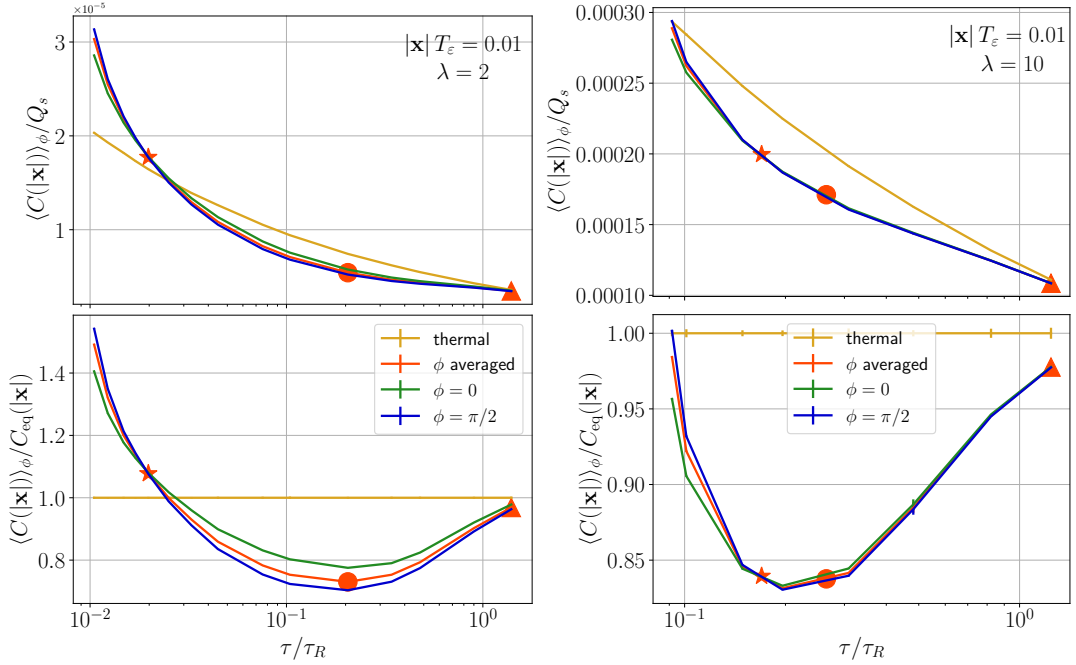


Figure 7.10: Dipole cross section $C(\mathbf{x})$ for a fixed $|\mathbf{x}|T_\varepsilon = 0.01$ as a function of time. Shown is both the angular averaged cross section $\langle C(|\mathbf{x}|) \rangle_\phi$ as a red curve, and the cross section for angles $\phi = 0$ and $\phi = \pi/2$. The upper panels show the cross section normalized to the saturation momentum Q_s , the lower panels to the thermal cross section. Shown are couplings $\lambda = 2$ (left) and $\lambda = 10$ (right).

For less energetic partons, the whole form of the collision kernel becomes important. This is the case needed for calculating the splitting and merging rates γ_{bc}^a included in QCD kinetic theory simulations as discussed in Section 3.3.1. In current QCD kinetic theory implementations (see, e.g., [21–26, 169, 170]) only the approximated thermal dipole cross section (7.28) is used, valid for isotropic systems, effectively taking the analytic Fourier transform (7.11) of the small q_\perp limit (7.23b).

7.3.1 AMY rate equation

In this section, we will consider the full form of the dipole cross section $C(\mathbf{x})$ to calculate the rate in the formalism of Arnold, Moore, and Yaffe. Recall from Section 2.2 that the rate for the process $g \rightarrow gg$ [19, 94] is given by

$$\gamma = \frac{p^4 + p'^4 + k'^4}{p^3 p'^3 k'^3} \frac{d_A \alpha_s}{2(2\pi)^3} \int \frac{d^2 \mathbf{h}}{(2\pi)^2} 2\mathbf{h} \cdot \text{Re} \mathbf{F}, \quad (7.54)$$

where \mathbf{F} is the solution to the integral equation

$$2\mathbf{h} = i\delta E(\mathbf{h})\mathbf{F}(\mathbf{h}) + \frac{1}{2} \int \frac{d^2 \mathbf{q}_\perp}{(2\pi)^2} C(\mathbf{q}_\perp) \times [(3\mathbf{F}(\mathbf{h}) - \mathbf{F}(\mathbf{h} - p\mathbf{q}_\perp) - \mathbf{F}(\mathbf{h} - k\mathbf{q}_\perp) - \mathbf{F}(\mathbf{h} + p'\mathbf{q}_\perp)], \quad (7.55)$$

with $\delta E(\mathbf{h}) = m_D^2/4 \times (1/k + 1/p - 1/p') + h^2/(2pkp')$. The expression for this rate was derived with the assumption of an infinite medium and that the collision kernel

$C(\mathbf{q}_\perp)$ does not significantly change (i.e., is constant) during the formation time ($t^{\text{form}} \sim \sqrt{\omega/\hat{q}}$, see Eq. (2.4)) of a splitting process, but it is valid for all emitted gluon energies. As discussed before, despite these approximations, these rates are used in kinetic theory simulations with the simplified isotropic form (7.23b) of the collision kernel [19, 21–26, 169, 170].

In this thesis, this rate equation is solved numerically for a general collision kernel $C(\mathbf{q}_\perp)$ satisfying the symmetry conditions (7.10) (but it is easy to generalize the method discussed here for a generic kernel). Previously in the literature, numerical evaluations of this rate only considered isotropic collision kernels (or, equivalently, isotropic dipole cross sections) [97, 110, 125–129], or solved the rate equation (7.54) perturbatively around isotropy [230]. To the best of my knowledge, I present here the first method to obtain the rate (7.54) for an anisotropic collision kernel $C(\mathbf{q}_\perp)$.

7.3.2 Solving the AMY rate equation numerically

We follow (and generalize) the method outlined in Ref. [231] and solve Eq. (7.55) in impact parameter space, where the equation reduces to

$$(A - D(z, \mathbf{x}) - B\nabla^2)\mathbf{F}(\mathbf{x}) = -2i\nabla\delta(\mathbf{x}) \quad (7.56)$$

with

$$A = i \frac{m_D^2}{4p} \left(\frac{1}{z} + \frac{1}{1-z} - 1 \right), \quad (7.57)$$

$$B = \frac{i}{2pz(1-z)}, \quad (7.58)$$

$$D(z, \mathbf{x}) = -\frac{1}{2} (C(\mathbf{x}) + C(z\mathbf{x}) + C((1-z)\mathbf{x})), \quad (7.59)$$

and z is the energy fraction of the emitted gluon, i.e., $p \rightarrow zp + (1-z)p$. By going from the original integral equation (7.55) to impact parameter space (7.56), we go from the collision kernel $C(\mathbf{q}_\perp)$ to the dipole cross section $C(\mathbf{x})$, see Appendix E.

In the isotropic case, $\mathbf{F}(\mathbf{x}) \sim xF(|\mathbf{x}|)$, and Eq. (7.56) for small $|\mathbf{x}|$ only has two linearly independent solutions. For the general case, one can decompose the angular information in Fourier modes, and find that there are two linearly independent solutions for every Fourier mode, effectively summing up to infinitely many different independent solutions. The boundary conditions are dictated for small \mathbf{x} by the delta function in Eq. (7.56), and by requiring that $F(\mathbf{x}) \rightarrow 0$ for $|\mathbf{x}| \rightarrow \infty$, as well as that the rate (7.54) is finite.

The rate is solved for 7 and 11 Fourier modes to ensure that the results do not depend on the truncation of the Fourier series. While in the isotropic case, it is enough to solve two independent ordinary differential equations, in the anisotropic case, $n_{\text{fourier}} + 3$ different systems of n_{fourier} coupled ordinary differential equations need to be solved. More details on the numerical method is provided in Appendix E.

For solving the differential equation, the dipole cross section $C(\mathbf{x})$ is needed for possibly arbitrary small and large x . In practice, this is achieved by considering the analytic limits of $C(\mathbf{x})$. We have already extensively discussed the small- $|\mathbf{x}|$ limit in Section 7.2.1, where we found that $C(|\mathbf{x}|) \sim x^2 \log |\mathbf{x}|$. We will now briefly

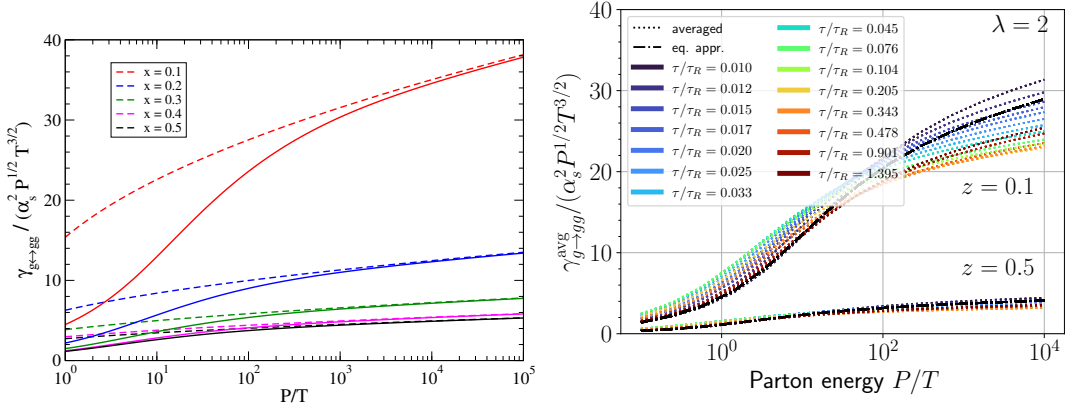


Figure 7.11: Gluon splitting rate γ for various parton energies P . The axes are scaled such that in equilibrium all coupling and temperature dependence cancels. (Left): Plot from Ref. [121] showing the splitting rate in thermal equilibrium for the approximated dipole cross section (7.29) (dashed lines) and its leading-log approximation (solid lines). (Right): Splitting rate as computed for collision kernels at different times for Bjorken expanding system at coupling $\lambda = 2$. Shown are, for simplicity, only the rates obtained from the averaged kernel (dotted lines) and from the approximated dipole cross section (7.29).

also discuss the opposite limit $|\mathbf{x}| \rightarrow \infty$. The Fourier transform (7.3) features a rapidly oscillating function, and the integral is dominated by the region where the exponent is approximately unity, i.e., $q_\perp \sim 1/|\mathbf{x}|$. In the limit $|\mathbf{x}| \rightarrow \infty$, we, therefore, need to consider the $q_\perp \rightarrow 0$ limit of the collision kernel, which we have already worked out in Eq. (7.23a). In this limit, $C(q_\perp) \sim 1/q_\perp^2$, which leads to a logarithmic behavior when performing the integral (7.3).

To summarize, the dipole cross section exhibits the following asymptotic behavior

$$C(|\mathbf{x}|, \phi) \rightarrow \begin{cases} x^2(a_1(\phi) \log |\mathbf{x}| + a_2(\phi)), & |\mathbf{x}| \rightarrow 0 \\ a_3(\phi) \log |\mathbf{x}| + a_4(\phi), & |\mathbf{x}| \rightarrow \infty, \end{cases} \quad (7.60)$$

with angular dependent coefficients $a_i(\phi)$. In the numerical method, Eq. (7.60) is used to extrapolate the numerical results for the dipole cross section to arbitrarily small and large values of $|\mathbf{x}|$.

7.3.3 Numerical results

We now move on to discuss the numerical results for the splitting rate. As in the whole thesis, we consider only gluons, i.e., the process of inelastic gluon radiation $g \rightarrow gg$. First, to validate the numerical approach, we compare the splitting rate obtained from the numerical approach with previously known results for the splitting rate in thermal equilibrium [121], which are shown in the left panel of Fig. 7.11. The axes are scaled in a way to make all curves fall on top of each other in thermal equilibrium for different temperatures T and couplings λ . The dashed lines denote the numerically obtained rate from Ref. [121] using the small q_\perp form of the collision kernel (7.23b), which is equivalent to using the approximated analytic dipole cross section (7.29) in impact parameter space. The dashed lines

represent the next-leading-log solution of Ref. [121] valid at large jet momenta. This corresponds to an expansion in logarithms, and is, thus, similar to the improved opacity expansion [122–124]. Different colors denote different splitting fractions z (labeled in the left plot as x). The right panel shows the results of using the numerical method, applied for angular averaged dipole cross sections $\langle C(|\mathbf{x}|) \rangle_\phi$, and also for the approximated thermal cross section (7.29) as black dash-dotted lines. These latter lines should be compared with the dashed curves in the left panel, and show excellent agreement, validating the numerical method used here. The colored dotted lines correspond to the rates obtained from the dipole cross sections at different times and roughly follow the thermal estimates in magnitude.

We now turn to study the rates obtained from the nonequilibrium kernel in more detail. Fig. 7.12 shows the gluon splitting rate γ obtained from the nonequilibrium dipole cross section $C(\mathbf{x}, \tau)$ at several times for a Bjorken expanding plasma for couplings $\lambda = 2$ (left column) and $\lambda = 10$ (right column). The different times are color-coded, with a consistent color scheme for the same coupling.

In the upper row, the rate for the anisotropic nonequilibrium collision kernel $C(\mathbf{q}_\perp, \tau)$ is plotted over the rate from its angular average $\langle C(q_\perp, \tau) \rangle_\phi$. Remarkably, this ratio is close to unity (less than 2% deviations) for both considered couplings and all considered times. This implies that obtaining the rate for the averaged collision kernel $\langle C(q_\perp) \rangle_\phi$ provides already a very good estimate for the rate obtained from the anisotropic kernel $C(\mathbf{q}_\perp)$. In the latter case, the maximum number of Fourier modes is varied ($n_{\max} = 3$ and $n_{\max} = 5$), where we observe that $n_{\max} = 3$ coincides with $n_{\max} = 5$ for almost the entire parton energy range, and, thus, already provides a very good description. For larger parton energies $P \geq 50T_\varepsilon$, using more Fourier modes leads to numerical problems (e.g., finding the unique linear combination of solutions that satisfies all the boundary conditions). This is seen in the plots by the diverging lines at larger parton energies P . These numerical problems will be discussed in more detail in Appendix E.

Let us now move on to the central panels, where the rate obtained from the nonequilibrium kernel $C(\mathbf{q}_\perp)$ is compared to the Landau-matched thermal rate γ^{eq} . Here, we observe an enhancement of the rate at small parton energies and a suppressed rate at large energies. This suppression aligns with the discussion in the last section regarding the reduction of the small- $|\mathbf{x}|$ behavior of the dipole cross section. However, interpreting the rate at large momenta P is complicated by the fact that an underlying assumption for the rate equation (7.54) is that the collision kernel $C(\mathbf{q}_\perp)$ does not change during the emission process. This is only true for processes with small formation time (2.4),

$$t^{\text{form}} \sim \sqrt{\frac{\omega}{\hat{q}}} = \sqrt{\frac{zP}{\hat{q}}}. \quad (7.61)$$

Let us provide a simple estimate of until which parton energies we may trust the results in Fig. 7.12. For example, consider $\lambda = 2$ (left panels), where in the middle panels, the rate (or rather ratio) seems to be approximately constant between $0.076 < \tau/\tau_R < 0.9$ (corresponding to $Q_s \Delta \tau \approx 400$). If we take as average temperature $T_\varepsilon \approx 0.3Q_s$ from Tab. E.5, and $\hat{q} \approx 0.16T_\varepsilon^3 \approx 0.004Q_s^3$ from Fig. 4.11, this leads to $\omega \approx 640Q_s \approx 2000T_\varepsilon$, for which the formation time is of this order.

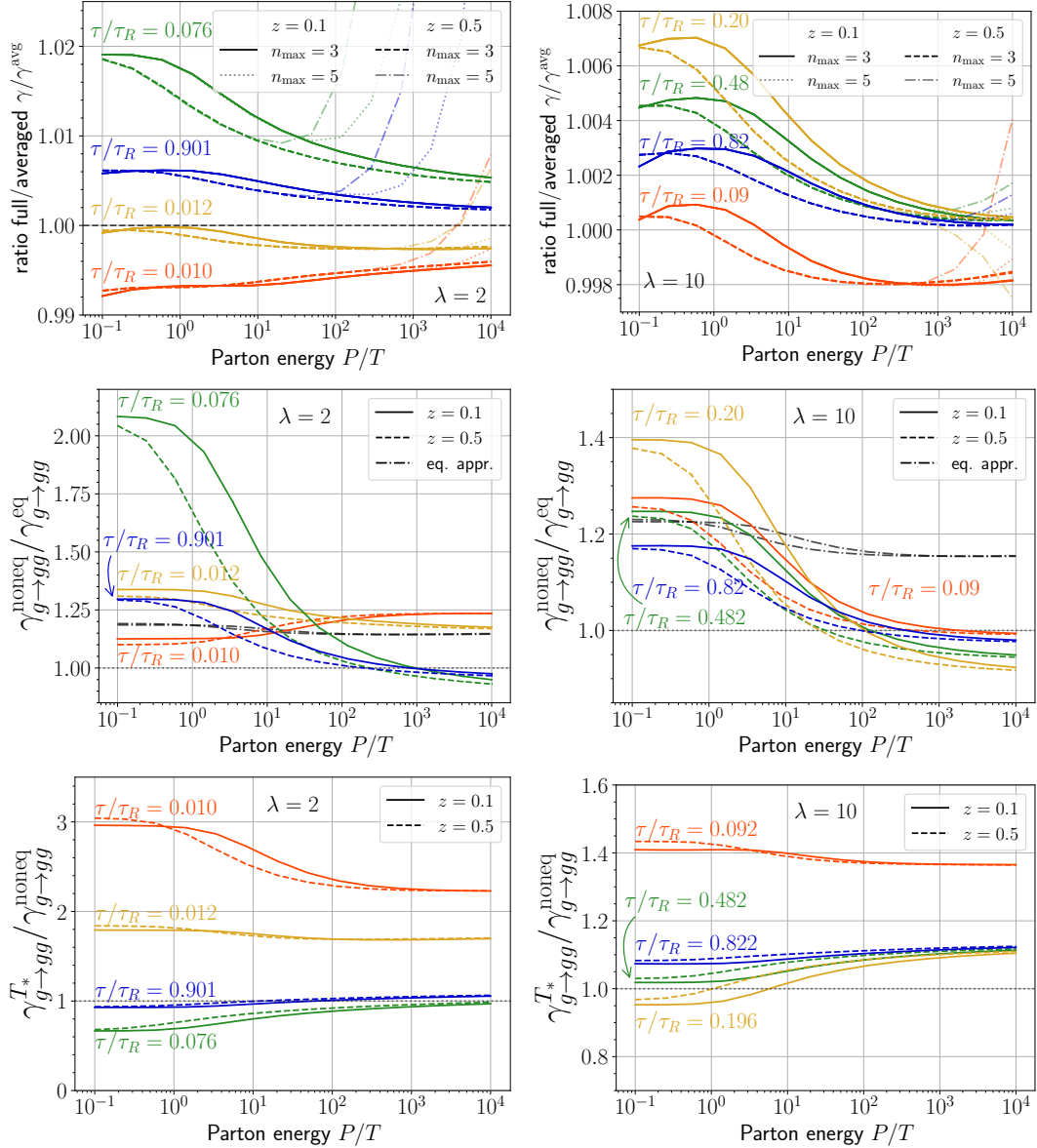


Figure 7.12: Gluon splitting rate for $\lambda = 2$ (left column) and $\lambda = 10$ (right column) in a Bjorken expanding gluonic plasma at different times (color-coded). The parameter z is the energy fraction of one of the emitted gluons. (Top): Ratio of the rate for the anisotropic collision kernel $C(\mathbf{q}_\perp)$ over the rate obtained from the angular averaged one $\langle C(\mathbf{q}_\perp) \rangle_\phi$. (Middle): Rate for the nonequilibrium kernel over the Landau-matched equilibrium one. Additionally shown is the rate obtained from the approximated thermal dipole cross section (7.29) as a black dash-dotted line. (Bottom): Rate using the T^* approximated dipole cross section as input (7.28) to the thermal one.

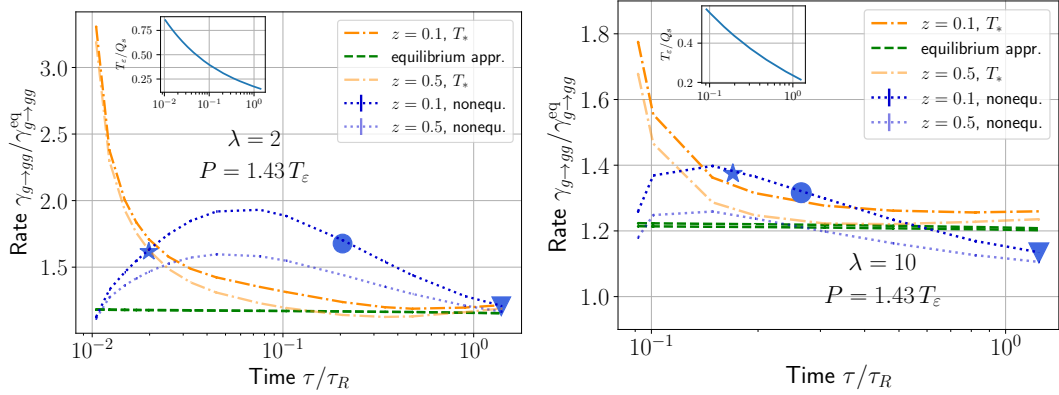


Figure 7.13: Comparison of the rate γ obtained from the nonequilibrium collision kernel $C(\mathbf{q}_\perp)$ (blue dotted line), the equilibrium approximated cross section (7.29) (green dashed line) and the isotropic approximated cross section (7.28) (orange dash-dotted line) for a parton with energy $P = 1.43 T_\epsilon$ as a function of time τ . The left panel shows the results for coupling $\lambda = 2$, the right panel for $\lambda = 10$.

For $\lambda = 10$, we can consider the right center panel of Fig. 7.12. Taking the time between the red and yellow curve corresponding to $Q_s \Delta \tau \approx 2$ with $T_\epsilon / Q_s \approx 0.5$ from Tab. E.6, and taking $\hat{q} \approx 2T_\epsilon^3 \approx 0.25Q_s^3$ from Fig. 4.13, we can estimate $\omega \lesssim Q_s \approx 2T_\epsilon$, which implies that for $z = 0.1$, the formation time is smaller or of that order for $P/T \lesssim 20$.

If we are less restrictive and consider the rate (or rather ratio) between the green ($\tau/\tau_R = 0.48$) and blue curve ($\tau/\tau_R = 0.82$) to be almost constant, this corresponds to roughly $\Delta \tau \approx 10/Q_s$, and take $T_\epsilon = 0.2Q_s$ and $\hat{q} \approx 2T_\epsilon^3 \approx 0.08Q_s^3$, we obtain $\omega = 8Q_s \approx 40T_\epsilon$, leading to a maximum parton energy of $P \approx 400T_\epsilon$, where the rate is still larger than its thermal equilibrium counterpart.

These simple estimates verify that the rates cannot be used for very energetic particles at all times, but can be used for particles with momenta of the order of the effective plasma temperature T_ϵ , for example, in kinetic theory simulations.

In the bottom row, we compare the rate γ^{T_*} obtained from the isotropic approximation to the dipole cross section $C_{\text{iso}}^{\text{appr.}}$ in (7.28) to the nonequilibrium one. We find that at early times the rate γ^{T_*} significantly overestimates the nonequilibrium rate. In particular for $\lambda = 2$, we find that initially the rate is overestimated by more than a factor of two. Even for $\lambda = 10$, γ^{T_*} is about 40% larger than the nonequilibrium rate.

Finally, in Fig. 7.13, we compare the splitting rate γ at a specific constant parton energy over effective temperature P/T_ϵ , obtained from the full anisotropic nonequilibrium collision kernel $C(\mathbf{q}_\perp, \tau)$ (blue dotted line), and for various approximations: The rate from the approximated thermal cross section (7.29) is shown as a green dashed curve, and the rate from the approximated isotropic cross section (7.28) is shown as an orange dash-dotted line. All of the values are normalized to the thermal values. The left panel shows the results for $\lambda = 2$, the right panel for $\lambda = 10$. In both cases, all of the curves are above unity, implying that the splitting rate for this parton energy is larger than expected from a Landau-matched thermal equilibrium. The thermal approximated rate in green is constant, at a value of 20% above the thermal rate. The nonequilibrium rate (blue dotted curves) initially

grows up to 20% above the thermal rate (50% for $\lambda = 2$) and then decreases, but at the triangle marker, the differences to thermal equilibrium are still larger than 10%. Surprisingly, the rate for the isotropic approximation (7.28) that is used in QCD kinetic theory simulations exhibits a qualitatively different behavior. It peaks at initial times with up to 60% above the thermal values (300% in the case of $\lambda = 2$), then drops below the nonthermal rate, crossing it approximately at the star marker, where the system becomes under-occupied. It then approaches the approximated thermal rate (which it should approach at late times). The failure to exactly approach the thermal rate at the very end is due to discretization artifacts.

This qualitative and quantitative different behavior of the rate γ^{T_*} obtained from the isotropic cross section (7.28) poses several questions regarding QCD kinetic theory simulations, in which this rate is commonly applied. In particular, at weak couplings, the deviations seem to become even larger. Since the bottom-up thermalization process relies crucially on the splitting rate, through which a soft thermal bath is formed, a modification of this rate in simulations can have sizable consequences. The rate obtained from the nonequilibrium kernel seems to be initially smaller during the over-occupied stage, which implies that fewer soft gluons are initially emitted. In the under-occupied stage (after the star marker), for $\lambda = 2$, the nonequilibrium rate becomes larger than γ^{T_*} , possibly affecting the second and third stage in the bottom-up equilibration simulations. Clearly, only further simulations using this nonequilibrium rate can clarify whether the equilibration and hydrodynamization process is substantially modified, which will be an exciting opportunity in the future.

7.4 CONCLUDING REMARKS

In this chapter, we studied the elastic collision kernel $C(\mathbf{q}_\perp, \tau)$, which generalizes the jet quenching parameter. The results obtained from numerical QCD kinetic theory simulations of the bottom-up equilibration process reveal an effectively angle-dependent screening scale and indicate that the jet quenching parameter \hat{q} receives larger contributions from small-momentum exchanges than in a corresponding thermal equilibrium, particularly in regions below the Debye mass. The anisotropy and magnitude of the kernel are consistent with the evaluation of the jet quenching parameter \hat{q} in Chapter 4.4.

We then moved on to study the dipole cross section, which can be obtained from the collision kernel using a (one-subtracted) Fourier transform (7.3). Its small distance behavior is relevant for calculating the gluon emission probability of a highly energetic parton, and, thus, the relevant region for jet quenching. This small distance behavior of the dipole cross section can be well described by the analytic formula (7.41), which needs as medium input only the jet quenching parameter as a function of the cutoff $\hat{q}(\Lambda_\perp)$. We found that this formula also reproduces very well the angular information. Furthermore, for calculating gluon emission rates of softer partons, the whole form of the dipole cross section is important. We have discussed the analytic limits of this quantity and compared it to its equilibrium estimates at various times. We find that while the nonequilibrium dipole cross section at large $|\mathbf{x}|$ is significantly larger than in equilibrium, at small distances $|\mathbf{x}|$, it is slightly smaller, indicating a suppression of jet quenching.

In the final part of this chapter, we considered the AMY gluon splitting rates obtained from the dipole cross section. For the first time, a numerical method is developed to obtain this quantity for an anisotropic dipole cross section. Remarkably, the rate obtained from the anisotropic cross section is well approximated by the rate obtained from the angular averaged cross section. However, it is still substantially different from the rate for an equilibrium collision kernel, especially at early times (up to 50% for $\lambda = 2$). Additionally, we have discussed that the approximation for the collision kernel used in QCD kinetic theory simulations leads to significantly larger rates at early times (up to 300% for $\lambda = 2$), which potentially impacts QCD kinetic theory simulations of the bottom-up equilibration and hydrodynamization process in heavy-ion collisions.

 SUMMARY, CONCLUSIONS AND OUTLOOK

This thesis focuses on the initial nonequilibrium stages in heavy-ion collisions, which can be described and modeled using QCD kinetic theory. Potential experimental probes of these initial stages are high-energy particles which are measured as jets in the detectors. Their energy loss can—in the harmonic approximation—be described by a single medium parameter, the jet quenching parameter \hat{q} .

In Chapter 4.4, we discussed how this jet quenching parameter \hat{q} can be obtained for a nonequilibrium QCD plasma using QCD kinetic theory, particularly for a Bjorken expanding system relevant for the initial stages in heavy-ion collisions. We studied this parameter for several toy models of different parts of these initial stages, and then extracted and obtained its value numerically using QCD kinetic theory for such expanding systems. The parameter is found to be similar in magnitude to calculations and simulations from the earlier Glasma stage, as well as in its qualitative properties, including increased broadening along the beam axis for a jet moving perpendicular to it. This first extraction using QCD kinetic theory marks an important step in understanding pre-equilibrium jet quenching.

We also discussed the jet quenching parameter and the related *heavy-quark diffusion coefficient* in the context of hydrodynamic attractors in Chapter 6. While for their anisotropy ratio, the commonly used time scaling associated with the hydrodynamic attractor seems to be less useful than for other observables, we identified a new feature in these transport coefficients. When time is rescaled with the parametric estimate for the bottom-up thermalization of weakly-coupled expanding systems, we observe that these anisotropy ratios admit an extrapolation to vanishing couplings, which we refer to as *limiting attractors*. We also observe this weak-coupling bottom-up limiting attractor in the pressure ratio, which additionally allows an extrapolation to the strong-coupling hydrodynamic limiting attractor. While the hydrodynamic limiting attractor is also visible for the jet quenching parameter and heavy-quark diffusion coefficient ratio, it offers less predictive power since even moderate values of the couplings quantitatively and qualitatively deviate from this attractor.

In Chapter 6.4.8, we then moved on to discuss in detail screening approximations which are typically employed in QCD kinetic theory simulations. In particular, we investigated how including the fully resummed HTL propagator in the elastic collision term modifies previous results on QCD thermalization obtained with a simpler Debye-like screening prescription. While for isotropic systems the effects are negligible, large and significant deviations can be observed in several quantities for expanding systems, which are relevant for the initial stages in heavy-ion collisions. For instance, the maximum pressure anisotropy is significantly reduced

when employing HTL screening. The approach to hydrodynamics is less affected when the different screening prescriptions are accounted for with different numerical values of the hydrodynamic transport parameter η/s . For this parameter, we found that the HTL screening prescription consistently leads to smaller values, which are closer to their perturbative estimate than when employing Debye-like screening. Furthermore, we studied the impact of this screening prescription on the jet quenching parameter \hat{q} , which was found to be only mildly influenced by different screening prescriptions. However, it should be noted that similar to all other previous treatments in QCD kinetic theory, we still lack a proper understanding of the effect of plasma instabilities in these simulations, which are currently neglected by employing an isotropic screening approximation.

Finally, we generalized the jet quenching parameter to obtain the elastic collision kernel $C(\mathbf{q}_\perp, \tau)$ in Chapter 8. We found that it is anisotropic and the contribution to the jet quenching parameter is peaked at the Debye mass for late times and for broadening transverse to the beam axis. For early times and broadening along the beam axis, the peak is shifted to smaller momentum exchanges, which could be interpreted as an emerging angle-dependent effective screening mass. This contribution to \hat{q} is significantly enhanced at early times for small momenta and suppressed for large momenta when compared to a corresponding thermal system, while at late times, it approaches its thermal form. We then moved on to obtain the dipole cross section as a Fourier transform of the collision kernel. We first verified that its small distance behavior is accurately described by the formula obtained in Section 7.2.1, and then studied and compared its nonequilibrium and angularly averaged form to the thermal form. There, we found that the dipole cross section is smaller than in thermal equilibrium for small distances throughout the whole evolution for larger couplings (and most of the evolution for coupling $\lambda = 2$). In contrast, for large distances, it significantly exceeds its thermal form and continuously decreases to thermal equilibrium throughout the hydrodynamization process. Finally, we also considered the dipole cross section as input to calculate the gluon splitting rates used in QCD kinetic theory simulations. There, we found that the rates obtained from an anisotropic collision kernel can be well approximated by the rate from an angular averaged kernel. However, these nonequilibrium rates significantly differ from those obtained in a corresponding thermal system. In particular, they are 20 – 50% enhanced. Moreover, the rate obtained from an isotropic approximated collision kernel employed in QCD kinetic theory simulations exhibits a significantly different behavior than the actual nonequilibrium rate, both in magnitude and functional time dependence, with possible and as of yet unexplored consequences for QCD kinetic theory simulations.

This first extraction of both the jet quenching parameter \hat{q} and the collision kernel during the initial stages in heavy-ion collisions using QCD kinetic theory marks an important step in increasing our understanding of pre-equilibrium jet quenching in heavy-ion collisions. In particular, many features found in these quantities, such as anisotropies and deviations from equilibrium, are unaccounted for in current simulations of heavy-ion collisions and will be even more important in the upcoming collisions of light ions at the LHC.

While this thesis thus constitutes an important theoretical and conceptual improvement of medium properties relevant for jet quenching studies during the

initial stages, further studies are needed to quantify the effect of these initial nonequilibrium stages. In particular, the effect of using the isotropic approximated kernel for obtaining the nonequilibrium splitting rates in QCD kinetic theory simulations will need to be explored in further simulations, to investigate if qualitative or quantitative changes arise from this approximation. Moreover, it will be interesting to study the new concept of limiting attractors proposed in this thesis, in particular, to identify other observables that exhibit a weak-coupling bottom-up limiting attractor. Studying how this bottom-up limiting attractor interferes and interplays with the hydrodynamic limiting attractor may improve our understanding of the hydrodynamization and equilibration process of QCD in heavy-ion collisions and beyond. Furthermore, the anisotropy and evolution of the jet quenching parameter and collision kernel during the nonequilibrium evolution should be included in the phenomenological modeling of heavy-ion collisions to assess their impact on jet quenching. This will enable finding, identifying, and proposing new experimental observables that may be sensitive to the initial stages and, thus, may offer the exciting opportunity of probing the nonequilibrium evolution of the QCD plasma in heavy-ion collisions.

A

QCD AND NONEQUILIBRIUM QUANTUM FIELD THEORY

In this appendix, we discuss details about QCD, correlation functions and nonequilibrium field theory. We start in Section A.1 by discussing the QCD Lagrangian and its building blocks. In Section A.2, we discuss aspects of nonthermal quantum field theory such as the closed time path and different types of propagators and correlation functions. In Section A.3, we discuss how the self-energy arises, and in A.4, the various propagators and correlation functions are listed, together with some convenient properties. In Section A.5.4, we discuss the hard thermal loop propagators, how they can be used in the isoHTML screening for the jet quenching parameter and elastic collision term, and in particular how to use the sum rule from Ref. [100] to obtain an analytic result for the collision kernel in isotropic systems. In Section B, we verify that for soft-gluon exchange, the AMY screening prescription (3.21a) is leading-order accurate by considering explicitly quark and gluon scatterings with soft momentum transfer.

A.1 QCD LAGRANGIAN AND NOTATION

Quantum chromodynamics is the quantum field theory describing the strong interaction. It is a nonabelian gauge theory with gauge group $SU(N_c)$ with $N_c = 3$ for QCD (but we can leave it arbitrary for the moment since it does not further complicate the discussion). This implies that the Lagrangian

$$\mathcal{L} = \sum_f \bar{\psi}_i^f (i\gamma^\mu D_{\mu,ij} - m_f) \psi_j^f - \frac{1}{2} \text{Tr} (F^{\mu\nu} F_{\mu\nu}) \quad (\text{A.1})$$

is invariant under the gauge transformation

$$\psi_i^f(X) \rightarrow U_{ij}(X) \psi_j^f(X), \quad A_\mu(X) \rightarrow U(X) A_\mu(X) U^\dagger(X) + \frac{i}{g} U(X) \partial_\mu U^\dagger(X), \quad (\text{A.2})$$

where $U \in SU(N_c)$ with components U_{ij} is a unitary $N_c \times N_c$ matrix with unit determinant, $\det U(X) = 1$. The Dirac field $\psi_{i,\alpha}^f(X)$ is a spinor field with color (i), flavor (f) and spinor (α) index. The gamma matrices $(\gamma^\mu)_{\alpha\beta}$ are matrices in spinor space (i.e., they act on the spinor index of ψ) and satisfy the Clifford algebra relation

$$\{\gamma^\mu, \gamma^\nu\} = \gamma^\mu \gamma^\nu + \gamma^\nu \gamma^\mu = -2\eta^{\mu\nu}. \quad (\text{A.3})$$

The adjoint spinor can be obtained via $\bar{\psi} = \psi^\dagger \gamma^0$.

The index f runs over the number of n_f quark flavors with mass m_f . For this thesis, the typical momenta of particles will be much larger than their rest mass (for the light flavors), making $m_f = 0$ a good approximation.

The gauge field $A_\mu(X) \in \mathfrak{su}(N_c)$ is an element of the Lie Algebra $\mathfrak{su}(N_c)$, and as such, can be represented by a traceless hermitian matrix. If we want to explicitly expand in the degrees of freedom, we can expand it in terms of the $d_A = N_c^2 - 1$ basis vectors (or *generators*) t_a ,

$$A_\mu(X) = A_\mu^a(X) t^a. \quad (\text{A.4})$$

It enters the covariant derivative

$$D_\mu = \partial_\mu - ig A_\mu(X), \quad (\text{A.5})$$

describing how a vector rotates in color space when it is parallel transported.

The *generators* t_a fulfill the commutation relations

$$[t^a, t^b] = if^{abc} t^c, \quad (\text{A.6})$$

and can be represented as $d_R \times d_R$ matrices, where R labels different representations. For our purposes, the *fundamental* ($R = F$) and *adjoint* ($R = A$) representation are of importance. Their dimensions are

$$d_F = N_c, \quad d_A = N_c^2 - 1. \quad (\text{A.7a})$$

Furthermore, in every representation, there is the invariant object $t_a t_a = \sum_a t_a t_a = C_R \mathbb{I}$, where C_R is called the *quadratic Casimir*. Their values for different representations are given by

$$C_F = \frac{N_c^2 - 1}{2N_c}, \quad C_A = N_c. \quad (\text{A.7b})$$

The coupling g often appears combined with N_c as the 't Hooft coupling λ , or α_s ,

$$\lambda = g^2 N_c, \quad \alpha_s = \frac{g^2}{4\pi}. \quad (\text{A.8})$$

The field strength tensor $F_{\mu\nu}$ is a generalization of the field strength tensor of classical electromagnetism, and is given by

$$F_{\mu\nu} = \frac{i}{g} [D_\mu, D_\nu] = \partial_\mu A_\nu - \partial_\nu A_\mu - ig [A_\mu, A_\nu]. \quad (\text{A.9})$$

A.2 CORRELATION FUNCTIONS AND CLOSED TIME PATH

In this subsection, we discuss aspects of quantum field theories out of equilibrium. The presentation here follows Ref. [183] but with the conventions from Ref. [177]. In a quantum field theory at finite temperature and out of equilibrium, it is useful to define several correlation functions. For a general quantum system, the expectation value of an operator \mathcal{O} is given by

$$\langle \mathcal{O} \rangle = \text{Tr} (\hat{\rho} \mathcal{O}), \quad (\text{A.10})$$

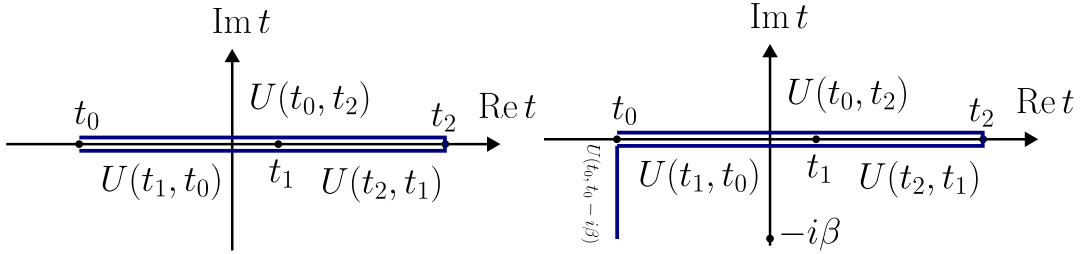


Figure A.1: The closed time path of the path integral (A.14).

where $\hat{\rho}$ is the density matrix ($\hat{\rho} = e^{-\beta H}/Z$ in thermal equilibrium). If $\hat{\rho}(t_0)$ is known at a given time t_0 and the operator \mathcal{O} has several time arguments but is not time ordered, e.g., $\mathcal{O} = \mathcal{O}(t_1)\mathcal{O}(t_2)$, suitable time translation operators $U(t_f, t_i)$ need to be inserted in (A.10). Representing them as a path integral is more tricky than for time-ordered operators since a path integral naturally introduces a time ordering along its path. For a product of operators of two different times $t_1 \neq t_2$, this can be achieved effectively by introducing two sets of fields, one set living on a forward while the other on the backward time path.

To illustrate this, take the correlation function

$$\langle \mathcal{O}(t_1)\mathcal{O}(t_2) \rangle = \text{Tr} (\hat{\rho}(t_0)\mathcal{O}(t_1)\mathcal{O}(t_2)) \quad (\text{A.11})$$

$$\begin{aligned} &= \sum_{ijklmn} \langle \phi_i | \hat{\rho}(t_0) | \phi_j \rangle \langle \phi_j | U(t_0, t_1) | \phi_k \rangle \langle \phi_k | \mathcal{O}(t_1) | \phi_l \rangle \langle \phi_l | U(t_1, t_2) | \phi_m \rangle \\ &\quad \times \langle \phi_m | \mathcal{O}(t_2) | \phi_n \rangle \langle \phi_n | U(t_2, t_0) | \phi_i \rangle. \end{aligned} \quad (\text{A.12})$$

Next, note that the time evolution operator can be represented as a path integral

$$\langle \phi_i | U(t_1, t_0) | \phi_i \rangle = \langle \phi_i | e^{-i\hat{H}(t_1-t_0)} | \phi_j \rangle = \int_{\phi_1(t_0)=\phi_i}^{\phi_1(t_1)=\phi_j} \mathcal{D}\phi_1(t) e^{iS(\phi_1)}, \quad (\text{A.13})$$

representing the time evolution from initial time t_0 to t_1 . It naturally satisfies the composition rule $U(t_0, t_1)U(t_1, t_2) = U(t_0, t_2)$. Eq. (A.12) can then be written as a path integral (assuming $t_0 < t_1 < t_2$)

$$\begin{aligned} \langle \mathcal{O}(t_1)\mathcal{O}(t_2) \rangle &= \sum_{ijklmn} \langle \phi_i | \hat{\rho}(t_0) | \phi_j \rangle \int_{\phi_2(t_0)=\phi_j}^{\phi_2(t_1)=\phi_k} \mathcal{D}\phi_2(t) e^{-iS(\phi_2)} \langle \phi_k | \mathcal{O}(t_1) | \phi_l \rangle \\ &\quad \times \int_{\phi_2(t_1)=\phi_l}^{\phi_2(t_2)=\phi_m} \mathcal{D}\phi_2(t) e^{-iS(\phi_2)} \langle \phi_m | \mathcal{O}(t_2) | \phi_n \rangle \\ &\quad \times \int_{\phi_1(t_0)=\phi_i}^{\phi_1(t_2)=\phi_n} \mathcal{D}\phi_1(t) e^{iS(\phi_1)} \end{aligned} \quad (\text{A.14})$$

and represented graphically in Fig. A.1. Effectively, we first evolve forward in time to reach the maximum time extent t_2 (using the fields on the forward path ϕ_1) and then backward to reach t_1 and back to t_0 using the fields on the backward path ϕ_2 . Going back to the initial time t_0 is a consequence of the trace in Eq. (A.10). Note that the action in the exponent of Eq. (A.14) in the path integral involving the fields ϕ_2 has a negative sign, which is a consequence of the backward time evolution. For a thermal system, the density operator $\hat{\rho} = e^{-\beta H}/Z$ can be interpreted as a time evolution operator in imaginary time up to time extent $\beta = 1/T$, together

with a periodicity condition at the boundary $\phi_i(t_0) = \phi_i(t_0 - i\beta)$. The thermal case is depicted in the left panel of Fig. A.1.

Considering the fields on the forward (ϕ_1) and backward (ϕ_2) to be different objects allows for a path integral representation of correlation functions, which are not time ordered. These types of correlation functions appear in thermal and nonthermal situations quite naturally. For instance, the Wightman functions are the (not time-ordered) correlators,

$$G^>(t_1, t_0) = \langle \phi(t_1) \phi(t_0) \rangle, \quad G^<(t_1, t_0) = \langle \phi(t_0) \phi(t_1) \rangle \quad (\text{A.15})$$

They can be obtained more generally by introducing the generating functional using the closed path integral using the two fields ϕ_1 and ϕ_2 and corresponding sources,

$$Z[J_1, J_2] = \sum_{ij} \langle \phi_i | \hat{\rho} | \phi_j \rangle \int_{\phi_i}^{\phi_j} \mathcal{D}\phi_1 \mathcal{D}\phi_2 e^{iS(\phi_1) - iS(\phi_2) - \int d^4x (J_1(x)\phi_1(x) - J_2(x)\phi_2(x))}. \quad (\text{A.16})$$

Using this, the various correlation functions can be obtained using functional derivatives,

$$\mathbf{D}_{ij} = \left. \frac{\delta}{\delta J_i} \frac{\delta}{\delta J_j} Z[J_1, J_2] \right|_{J=0} = \begin{pmatrix} \langle \phi_1 \phi_1 \rangle & \langle \phi_1 \phi_2 \rangle \\ \langle \phi_2 \phi_1 \rangle & \langle \phi_2 \phi_2 \rangle \end{pmatrix} = \begin{pmatrix} G & G^< \\ G^> & G^{\bar{F}} \end{pmatrix}, \quad (\text{A.17})$$

where $G^>$ and $G^<$ are the Wightman functions (A.15), D is the time-ordered (Feynman) propagator,

$$G(t_1, t_0) = \Theta(t_1 - t_0) G^>(t_1, t_0) + \Theta(t_0 - t_1) G^<(t_1, t_0), \quad (\text{A.18})$$

and $G^{\bar{F}}$ is the anti time-ordered (Dyson) propagator.

It is often useful to perform a basis transformation to the r/a basis, which is obtained by the linear transformation

$$\phi_r = \frac{1}{2}(\phi_1 + \phi_2), \quad \phi_a = \phi_1 - \phi_2, \quad \phi_1 = \phi_r + \frac{1}{2}\phi_a, \quad \phi_2 = \phi_r - \frac{1}{2}\phi_a, \quad (\text{A.19})$$

in which the propagator matrix has the form

$$\mathbf{G} = \begin{pmatrix} \langle \phi_r \phi_r \rangle & \langle \phi_r \phi_a \rangle \\ \langle \phi_a \phi_r \rangle & \langle \phi_a \phi_a \rangle \end{pmatrix} = \begin{pmatrix} G^{rr} & -iG^R \\ -iG^A & 0 \end{pmatrix}, \quad (\text{A.20})$$

where $G^{rr} = G^> + G^<$ is called the statistical two-point function or Hadamard propagator, and D^R and D^A are the retarded and advanced propagators¹,

$$G^R(t_1, t_0) = i\Theta(t_1 - t_0)\rho(t_1, t_0), \quad G^A(t_1, t_0) = -i\Theta(t_0 - t_1)\rho(t_1, t_0), \quad (\text{A.21})$$

where the spectral function or Jordan propagator ρ is given by

$$\rho(t_1, t_0) = G^> - G^< = -i(G^R - G^A). \quad (\text{A.22})$$

An important feature of the r/a basis is that the correlation function of two a fields vanishes $\langle \phi_a \phi_a \rangle = 0$, which simplifies calculations. Additionally, because of the

¹ We follow here the conventions of [177], which differ by a factor of i from the one in Ref. [183] for the retarded and advanced propagator.

step functions in (A.21), any closed loop containing only retarded or advanced propagators vanishes as well.

Physically, the retarded propagator represents causality flow, and we represent them pictorially by an arrow that points towards the r -field,

$$G_{ra}(t_0, t_1) = G^R(t_0, t_1) = \begin{array}{c} \text{---} \\ r \end{array} \xleftarrow{a} \begin{array}{c} \text{---} \\ a \end{array} . \quad (\text{A.23})$$

In this basis, the vertices can be obtained from Eq. (A.16) by taking the difference of the interaction part of the action with ϕ_1 fields and ϕ_2 fields and using the transformation (A.19),

$$S_I(\phi_1) - S_I(\phi_2) = S_I(\phi_r + \phi_a/2) - S_I(\phi_r - \phi_a/2), \quad (\text{A.24})$$

which implies that there are only vertices with an odd number of a fields.

The propagators and correlation functions are often used in momentum space. More generally, if the system is not translational invariant (e.g., inhomogeneous), one may instead perform a Wigner transform and expand in gradients for slowly varying fields. This is sketched in Section 3.4.5 to obtain the Boltzmann equation from a quantum field theory.

The Wigner transform of a function $f(X, Y)$ is given by

$$\tilde{f}(K, \bar{X}) = \int d^4S e^{-iK \cdot S} f(X(s, \bar{X}), Y(s, \bar{X})), \quad (\text{A.25})$$

with the difference S and central coordinates X given by

$$S^\mu = X^\mu - Y^\mu, \quad \bar{X}^\mu = \frac{X^\mu + Y^\mu}{2}. \quad (\text{A.26})$$

Note that the Wigner transform (A.25) reduces to an ordinary Fourier transform when the system is translational invariant (does not depend on \bar{X}).

A more detailed review of nonequilibrium quantum field theory can be found, e.g., in Refs. [179, 232].

A.3 PERTURBATION THEORY AND SELF-ENERGY

In perturbation theory, one separates the action into an action for a free theory, which is typically analytically solvable, and an interaction part, which is suppressed by a small dimensionless parameter $g \ll 1$ (which for QCD is satisfied at high energies due to *asymptotic freedom*). The full propagators are obtained from Eq. (A.10) with the full action, while the free propagators (indicated by an additional index 0) are obtained using only the free action. The interaction part gives rise to vertices, while the free theory part gives rise to the free propagators G_0 . Any quantities of interest are then expanded in terms of vertices and free propagators G_0 to obtain corrections proportional to the coupling g, g^2, \dots . This is typically represented graphically as an expansion in loops.

An important concept is the concept of a self energy, which determines the difference between the full and free propagator,²

$$G^{-1}(X, Y) = G_0^{-1}(X, Y) + \Pi(X, Y), \quad (\text{A.27})$$

² Different conventions exist that differ in signs or whether or not to also put an imaginary unit i there.

where the inverse propagators are defined via

$$\int d^4Z G^{-1}(X, Z)G(Z, Y) = \delta^4(X - Y), \quad \int d^4Z G_0^{-1}(X, Z)G_0(Z, Y) = \delta^4(X - Y). \quad (\text{A.28})$$

Similar to the Wightman functions and their relation to the propagator in Eq. (A.18), one may also decompose the self-energy into

$$\Pi(t_1, t_0) = \Theta(t_1 - t_0)\Pi^>(t_1, t_0) + \Theta(t_0 - t_1)\Pi^<(t_1, t_0) - i\delta(t_1 - t_0)\Pi^\delta(t_1), \quad (\text{A.29})$$

where we have included the possibility of a singular term Π^δ , see, e.g., [177]. Similar as with the propagators (A.21), we may introduce a retarded self-energy

$$\Pi^R(t_1, t_0) = -i\Theta(t_1 - t_0)\Gamma(t_1, t_0), \quad \Pi^A(t_1, t_0) = i\Theta(t_0 - t_1)\Gamma(t_1, t_0), \quad (\text{A.30})$$

with

$$\Gamma = -(\Pi^> - \Pi^<). \quad (\text{A.31})$$

A.4 CORRELATOR RELATIONS AND PROPERTIES

To summarize, the different propagators and correlators are given by

$$G_{\mu\nu}^{>ab}(X, Y) = \langle A_\mu^a(X)A_\nu^b(Y) \rangle, \quad (\text{A.32a})$$

$$G_{\mu\nu}^{<ab}(X, Y) = \langle A_\nu^b(Y)A_\mu^a(X) \rangle = G_{\nu\mu}^{>ba}(Y, X), \quad (\text{A.32b})$$

$$G_{\mu\nu}^{ab}(X, Y) = \Theta(X^0 - Y^0)G_{\mu\nu}^{>ab}(X, Y) + \Theta(Y^0 - X^0)G_{\mu\nu}^{<ab}(X, Y) \quad (\text{A.32c})$$

$$\rho_{\mu\nu}^{ab}(X, Y) = \langle [A_\mu^a(X), A_\nu^b(Y)] \rangle \quad (\text{A.32d})$$

$$G_{\mu\nu}^{Rab}(X, Y) = i\Theta(X^0 - Y^0)\rho_{\mu\nu}^{ab}(X, Y), \quad (\text{A.32e})$$

$$G_{\mu\nu}^{Aab}(X, Y) = -i\Theta(Y^0 - X^0)\rho_{\mu\nu}^{ab}(X, Y) = G_{\nu\mu}^{Rba}(Y, X) \quad (\text{A.32f})$$

Here, $\Theta(x)$ is the usual step function,

$$\Theta(x) = \begin{cases} 1, & x \geq 0, \\ 0, & x < 0 \end{cases} \quad (\text{A.32g})$$

Several useful properties of these correlators and the self-energies are listed in the following:

$$\left(\tilde{G}^<(Y, X) \right)^* = \tilde{G}^>(X, Y) \quad (\text{A.33})$$

$$G^A(X, Y) = G^R(Y, X), \quad \Pi^R(X, Y) = \Pi^A(Y, X) \quad (\text{A.34})$$

$$\left(\tilde{G}^A(K, X) \right)^* = \tilde{G}^R(K, X) \quad (\text{A.35})$$

$$\tilde{\rho}(K, X) = 2\text{Im}\tilde{G}^R(K, X), \quad \tilde{\Gamma}(K, X) = -2\text{Im}\tilde{\Gamma}^R(K, X) \quad (\text{A.36})$$

$$\tilde{G}^>(-K, X) = \tilde{G}^<(K, X) \quad (\text{A.37})$$

$$\tilde{\rho}(-K, X) = -\tilde{\rho}(K, X) \quad (\text{A.38})$$

$$G^R(-K, X) = G^A(K, X) \quad (\text{A.39})$$

$$\rho = G^> - G^< = -i(G^R - G^A), \quad -\Gamma = \Pi^> - \Pi^< = -i(\Pi^R - \Pi^A) \quad (\text{A.40})$$

The definitions for the correlation functions (A.32) hold generically for any bosonic fields. For fermions, additional minus signs have to be considered, and the commutators are replaced by anticommutators.

A.5 HARD THERMAL LOOPS

It is well-known in thermal field theory that to cure infrared problems, the propagators for the soft modes have to be resummed [225, 233, 234]. At a fixed order in the coupling g , it turns out that more diagrams contribute than what would be expected from a naïve loop expansion. In fact, for diagrams with soft external momenta, it is needed to integrate out the hard loop momenta, which is formalized in the hard thermal loop (HTL) theory [163–165].

Parts of the following discussion are based on Appendix B in [2].

A.5.1 Hard thermal loop resummed gluon propagator

The HTL retarded propagator in strict Coulomb gauge³ is given by⁴ [177, 183]

$$G^{00}(Q) = \frac{-1}{q^2 + \Pi^{00}(\omega/q)}, \quad (\text{A.41a})$$

$$G_R^{ij}(Q) = \left(\delta^{ij} - \frac{q^i q^j}{q^2} \right) G^T(Q) = \frac{\delta^{ij} - \frac{q^i q^j}{q^2}}{q^2 - \omega^2 + \Pi^T(\omega/q)} \quad (\text{A.41b})$$

with $x = \omega/q$ and the self-energies

$$\text{Re}\Pi^{00}(x) = m_D^2 \left(1 - \frac{x}{2} \ln \left| \frac{x+1}{x-1} \right| \right), \quad \text{Im}\Pi^{00}(x) = \frac{x m_D^2 \pi}{2} \Theta(1-|x|) \quad (\text{A.42a})$$

$$\text{Re}\Pi^T(x) = \frac{m_D^2}{2} - \frac{1}{2}(1-x^2)\text{Re}\Pi^{00}, \quad \text{Im}\Pi^T(x) = -\frac{1}{2}(1-x^2)\text{Im}\Pi^{00}. \quad (\text{A.42b})$$

The Debye mass can be obtained via the integral (3.11) and in equilibrium has the value (3.13),

$$m_D^2 = g^2 T^2 \left(\frac{N_c}{3} + \frac{n_f}{6} \right). \quad (\text{A.43})$$

For later use, let us also list here the spectral function $\rho(Q) = 2\text{Im}G^R(Q)$ (see Eq. (A.36)),

$$\rho^{00}(Q) = \frac{2\text{Im}\Pi^{00}(Q)}{(q^2 + \text{Re}\Pi^{00}(Q))^2 + (\text{Im}\Pi^{00}(Q))^2}, \quad (\text{A.44a})$$

$$\rho^T(Q) = \frac{-2\text{Im}\Pi^T(Q)}{(q^2 - \omega^2 + \text{Re}\Pi^T(Q))^2 + (\text{Im}\Pi^T(Q))^2}. \quad (\text{A.44b})$$

In the next subsections, we will use the propagators to obtain explicitly the isoHTL screened matrix element used for evaluating the jet quenching parameter and the elastic collision term. Additionally, we will discuss how to perform a certain integral over these propagators, where the spectral function will appear.

³ By Coulomb gauge we mean using $\partial_i A^i$ as the gauge function and by strict we mean enforcing it strictly, i.e. $\partial_i A^i = 0$, which amounts to setting $\xi = 0$ in the Faddeev-Popov procedure [225].

⁴ We take the explicit expression from Ref. [177] (BI), but write it in the form of [183] (GKSV). As mentioned before, different authors use different conventions of factors of $\pm i$. The conventions used by these authors are related by $G_R^{\text{BI}} = i G_R^{\text{GKSV}}$ for the retarded (and advanced) propagators.

A.5.2 IsoHTL screening in the jet quenching parameter

Here, we want to explicitly derive the expression (including all the kinematic contractions) for the full isotropic HTL matrix element (4.47) needed for the jet quenching parameter \hat{q} in Chapter 4.4. We start with the AMY screening prescription Eq. (4.31) (see also Eq. (3.21a)),

$$\mathcal{M}_{\text{HTL}} = |G_R(P - P')_{\mu\nu}(P + P')^\mu(K + K')^\nu|^2, \quad (\text{A.45})$$

Due to the kinematic constraint $|\omega| < q$ (see (4.11)), the variable x appearing in the self-energies (A.42) is always $|x| < 1$, and thus the imaginary parts of the self energies (A.42) always contribute. Note that $G_R(-Q)$ corresponds to the advanced propagator (see Eq. (A.39)), which has a different imaginary part in the self-energy, $\text{Im}\Pi_R(-Q) = -\text{Im}\Pi_R(Q)$. Let us further abbreviate

$$G^{00}(-Q) =: z_L = \frac{-1}{A + Bi}, \quad G^T(-Q) =: z_T = \frac{1}{C + Di}, \quad (\text{A.46})$$

$$A = q^2 + \text{Re}\Pi^{00}(x), \quad B = \text{Im}\Pi^{00}(-x), \quad (\text{A.47})$$

$$C = q^2 - \omega^2 + \text{Re}\Pi^T(x), \quad D = \text{Im}\Pi^T(-x). \quad (\text{A.48})$$

It will turn out that B and D only appear quadratically or as a product, i.e., we can consider the internal propagator to have momentum Q or $(-Q)$. Thus, we do not need to distinguish them from $\text{Im}\Pi_R(x)$. We can now split the retarded propagator in (A.45) into its temporal and spatial parts and use the expressions for \mathbf{p} , \mathbf{q} , and \mathbf{k} in the q -frame, i.e., using their parametrizations (4.15a), (4.15b) and (4.15c),

$$Q = P' - P = \begin{pmatrix} \omega \\ 0 \\ 0 \\ q \end{pmatrix}, \quad P = p \begin{pmatrix} 1 \\ \sin \theta_{qp} \\ 0 \\ \cos \theta_{qp} \end{pmatrix}, \quad K = k \begin{pmatrix} 1 \\ \sin \theta_{qk} \cos \phi_{qk} \\ \sin \theta_{qk} \sin \phi_{qk} \\ \cos \theta_{qk} \end{pmatrix}. \quad (\text{A.49})$$

to obtain

$$\mathcal{M}_{\text{HTL}} = |c_1 z_L + c_2 z_T|^2 = c_1^2 |z_L|^2 + c_2^2 |z_T|^2 + c_1 c_2 (z_L \bar{z}_T + \bar{z}_L z_T), \quad (\text{A.50})$$

where \bar{z} means taking the complex conjugate of z and $c_1 = (2p + \omega)(2k - \omega)$ and $c_2 = 4pk \sin \theta_{qp} \sin \theta_{qk} \cos \phi_{qk}$.

This leads to $|z_L|^2 = |G^{00}(Q)|^2 = (A^2 + B^2)^{-1}$, $|z_T|^2 = |G^T(Q)|^2 = (C^2 + D^2)^{-1}$ and

$$\bar{z}_L z_T + z_L \bar{z}_T = -2(AC + BD)|z_L|^2|z_T|^2, \quad (\text{A.51})$$

and eventually we obtain

$$\mathcal{M}_{\text{HTL}} = \frac{c_1^2}{A^2 + B^2} + \frac{c_2^2}{C^2 + D^2} - \frac{2c_1 c_2 (AC + BD)}{(A^2 + B^2)(C^2 + D^2)}. \quad (\text{A.52})$$

The last term is proportional to $\cos \phi_{qk}$ and may, therefore, be dropped for isotropic distributions $f(k)$.

The rescaled matrix element $\tilde{M} = \lim_{p \rightarrow \infty} \mathcal{M}_{\text{HTL}}/p^2$ in the limit $p \rightarrow \infty$ can be obtained easily by scaling out p (see Eq. (4.48))

$$\tilde{c}_1 = \lim_{p \rightarrow \infty} c_1/p = 2(2k - \omega), \quad \tilde{c}_2 = \lim_{p \rightarrow \infty} c_2/p = 4k \sin \theta_{qp} \sin \theta_{qk} \cos \phi_{qk}, \quad (\text{A.53})$$

which yields

$$\tilde{M}_{\text{HTL}} = \frac{\tilde{c}_1^2}{A^2 + B^2} + \frac{\tilde{c}_2^2}{C^2 + D^2} - \frac{2\tilde{c}_1\tilde{c}_2(AC + BD)}{(A^2 + B^2)(C^2 + D^2)}. \quad (\text{A.54})$$

Similarly, as before, for isotropic distributions, $f(k)$, the last term does not contribute and may be dropped.

A.5.3 IsoHTL screening in the elastic collision kernel

In Chapter 6.4.8, we consider isoHTL screening in the elastic collision term $\mathcal{C}^{2\leftrightarrow 2}$. The difference to the previous Section A.5.2 is that Eq. (A.49) is replaced by (B.13), in which the momentum \mathbf{p} is parametrized differently, including an additional angle ϕ_{qp} . This is because for \hat{q} , as explained in Section 4.1.2, the incoming parton specifies a specific direction \mathbf{p} , and one performs the \mathbf{q} integral in a frame, in which \mathbf{p} points in the z direction and the \mathbf{k} integration in a frame in which \mathbf{q} points in the z direction. For QCD kinetic theory simulations, however, one needs to solve the more general integration measure (3.16), performing the \mathbf{q} integration in the “lab frame” (in which also the distribution function is stored), and both the \mathbf{p} and \mathbf{k} integrations in the frame in which \mathbf{q} points in the z direction. This leads to the different parameterizations (A.49) and (B.13).

Effectively, the only change is in the coefficient c_2 in (A.52), with

$$c_2 = 4pk \sin \theta_{qp} \sin \theta_{qk} \cos(\phi_{qk} - \phi_{qp}). \quad (\text{A.55})$$

A.5.4 Sum rule

In this appendix, we show that one can analytically perform the integral over ω over the HTL matrix element (A.54),

$$\int_{-\infty}^{\infty} \frac{d\omega}{q} \tilde{M}_{\text{HTL}}, \quad (\text{A.56})$$

using the sum rule from Ref. [100]. This sum rule simplifies the evaluation of an integral over a “spectral function”

$$\int_0^1 \frac{dx}{x} \frac{2\text{Im}\Pi(x)}{(z + \text{Re}\Pi(x))^2 + (\text{Im}\Pi(x))^2} = \pi \left[\frac{1}{z + \text{Re}\Pi(\infty)} - \frac{1}{z + \text{Re}\Pi(0)} \right], \quad (\text{A.57})$$

provided that the function $\Pi(x)$ fulfills the conditions $\text{Im}\Pi(0) = 0$, $\text{Im}\Pi(x) = 0$ for $x \geq 1$ and $\text{Re}\Pi(x) \geq 0$ for $x \geq 1$.

Let us now calculate the collision kernel $C(\mathbf{q}_\perp)$ for small $q_\perp \ll k \ll p$. Thus, effectively, we can take the formalism developed in Section 4.4 for the jet quenching parameter \hat{q} (related to the collision kernel via Eq. (1.4)), and employ the approximations $q_\perp \ll k \ll p$. Effectively, we can thus work in the limit $p \rightarrow \infty$ discussed in Section 4.1.7. We consider isotropic systems and may thus drop the last term in the isoHTL screened matrix element (4.47). Recall that in this limit $\cos \theta_{qp} = \cos \theta_{qk} = \omega/q$, and then (4.47) reduces to

$$\langle \tilde{M}_{\text{HTL}} \rangle_\phi = \int_0^{2\pi} \frac{d\phi_{qk}}{2\pi} \tilde{M}_{\text{HTL}} = 16k^2 \left(|G^{00}|^2 + \frac{1}{2} \left(1 - \frac{\omega^2}{q^2} \right)^2 |G^T|^2 \right), \quad (\text{A.58})$$

where we have inserted back the more physical quantities $|G^{00}(Q)|^2 = (A^2 + B^2)^{-1}$ and $|G^T(Q)|^2 = (C^2 + D^2)^{-1}$, and already integrated out the angle ϕ_{qk} . Importantly, the collision kernel then reads (see Eq. (4.61))

$$C(\mathbf{q}_\perp) = \left(C_R \sum_{\pm} \Xi_{\pm} \frac{g^4}{2^8 \pi^4} \int_0^\infty dk k^2 f_{\pm}(k) (1 \pm f_{\pm}(k)) \right) \int_0^{2\pi} d\phi_{qk} \int_{-\infty}^\infty \frac{d\omega \tilde{M}_{\text{HTL}}}{k^2 q}, \quad (\text{A.59})$$

where, importantly, we have factored out the k -dependence and the distribution functions. As we will see, the integral over ω can now be performed using the sum rule (A.57),

for which we write $|G_R|^2$ in terms of the self-energy Π_R , and expand the fraction with the imaginary part of the self-energy,

$$|G^{00}|^2 = \frac{2q}{\omega m_D^2 \pi} \frac{\text{Im}\Pi^{00}(x)}{(q^2 + \text{Re}\Pi^{00})^2 + (\text{Im}\Pi^{00})^2} \quad (\text{A.60a})$$

$$|G^T|^2 = -\frac{4q}{\omega m_D^2 \pi (1-x^2)} \frac{\text{Im}\Pi^T(x)}{(q_\perp^2 + \text{Re}\Pi^T)^2 + (\text{Im}\Pi^T)^2}, \quad (\text{A.60b})$$

where we can immediately recognise the spectral functions (A.44),

$$\langle \tilde{M}_{\text{HTL}} \rangle_\phi = \frac{16k^2 q}{\omega m_D^2 \pi} (\rho^{00}(x) + \rho^{33}(x)) = \frac{16k^2 q}{\omega m_D^2 \pi} (\rho^{00}(x) + (1-x^2)\rho^T(x)). \quad (\text{A.61})$$

A similar trick is also used in [20].

Together with the substitution $\frac{d\omega}{\omega} = \frac{dx}{x(1-x^2)}$, this results in

$$\int_{-\infty}^\infty \frac{d\omega}{q} \langle \tilde{M}_{\text{HTL}} \rangle_\phi = 2 \int_0^\infty \frac{d\omega}{q} \langle \tilde{M}_{\text{HTL}} \rangle_\phi = \frac{32k^2}{m_D^2} \left[\frac{1}{q_\perp^2 + \frac{m_D^2}{3}} - \frac{1}{q_\perp^2 + m_D^2} - \frac{1}{q_\perp^2 + \frac{m_D^2}{3}} + \frac{1}{q_\perp^2} \right]. \quad (\text{A.62})$$

For the longitudinal propagator $|G^{00}|^2$ the factor $(1-x^2)$ from the coordinate transformation needs to be absorbed into the self-energy $\tilde{\Pi}^{00}(x) = (1-x^2)\Pi^{00}(x)$. The relevant limits read

$$\text{Re}\Pi^T(0) = 0, \quad \text{Re}\tilde{\Pi}^{00}(0) = m_D^2, \quad (\text{A.63a})$$

$$\text{Re}\Pi^T(\infty) = \frac{m_D^2}{3}, \quad \text{Re}\tilde{\Pi}^{00}(\infty) = \frac{m_D^2}{3}. \quad (\text{A.63b})$$

This leads to the familiar result

$$\frac{m_D^2}{32k^2} \int_0^{2\pi} \frac{d\phi_{qk}}{2\pi} \int_{-\infty}^\infty \frac{d\omega}{q} \tilde{M}_{\text{HTL}} = \frac{m_D^2}{q_\perp^2 (q_\perp^2 + m_D^2)} \quad (\text{A.64})$$

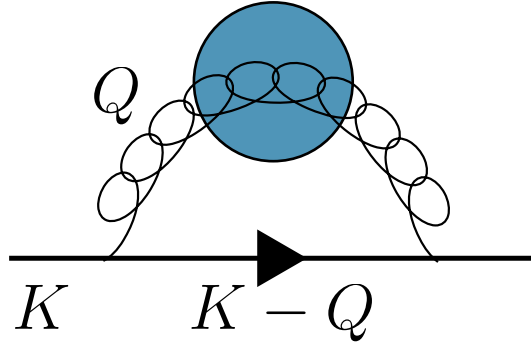


Figure A.2: Self-energy of an energetic quark, representing Eq. (A.66).

A similar result is obtained in [100, 102] in thermal equilibrium, where also the integral over the distribution functions $f(k)(1+f(k))$ is automatically included. Here, we have shown explicitly that the matrix element itself gives rise to the form (A.64). In the soft limit, this enables us to perform the integral over the distribution function separately, allowing a straightforward generalization to nonequilibrium systems. Finally, we note that this sum rule is used in Section 4.1.5 to set the parameter ξ_g^\perp in the Debye-like screening prescription.

An interested reader might wonder what this has to do with the Wightman function appearing in the integral equation (2.11). Another interested reader might wonder if the approach taken here was perhaps overly complicated. Perhaps, using a different approach, the spectral function (A.36) would appear more naturally. Indeed, both of these questions are answered by the following short discussion following the introduction of Ref. [133].

Let us consider a quark moving through the plasma with large momentum $K^\mu = (k, \mathbf{k})$, which has the decay rate [225] (or scattering rate)

$$\Gamma = \frac{1}{4k} \text{Tr} [\gamma^\mu K_\mu \Pi^>(K)] \quad (\text{A.65})$$

Calculating the self-energy via (see Fig. A.2)

$$\Pi^>(K) = g^2 C_F \int \frac{d^4 Q}{(2\pi)^4} G_{\text{gluon}}^{>\mu\nu}(Q) \gamma_\mu \gamma_\nu G_{\text{quark}}^>(K - Q), \quad (\text{A.66})$$

where we used the vertex factors $(ig) \times (-ig) = g^2$, and have the additional minus sign for the 2 vertex. We may now use Eq. (3.46) to write the Wightman functions $G^>(K) = \rho(K)(1 \pm N(K))$ as spectral density ρ and off-shell distribution function N . For the quark, since it is highly energetic $K \gg Q$, we may use the quasiparticle approximation, representing the spectral function as a delta function [225]

$$\rho_{\text{quark}}(P) = 2\pi \text{sign}(P^0) \gamma^\mu P_\mu \delta(P^2). \quad (\text{A.67})$$

With the trace identity

$$K_\alpha(K - Q)_\beta \text{Tr} [\gamma^\alpha \gamma^\mu \gamma^\beta \gamma^\nu] = 4(K^\mu(K - Q)^\nu + K^\nu(K - Q)^\mu - K \cdot (K - Q)\eta^{\mu\nu}) \approx 8K^\mu K^\nu - 4K^2\eta^{\mu\nu}, \quad (\text{A.68})$$

where we used the symmetry of the propagator $G^{>\mu\nu}$, we obtain

$$\Gamma = \frac{\pi}{2k} g^2 C_F \int \frac{d^4 Q}{(2\pi)^4} G_{\text{gluon}}^{>\mu\nu}(Q) (8K_\mu K_\nu - 4K^2 \eta_{\mu\nu}) \text{sign}(K^0 - Q^0) \delta((K - Q)^2) (1 - N(K - Q)). \quad (\text{A.69})$$

The delta function sets the distribution function on-shell $N(K - Q) = f(\mathbf{k} - \mathbf{q})$ (see Eq. (3.48)), and setting the self-energy on-shell (as in Eq. (3.50)), we obtain

$$\Gamma = 2\pi g^2 C_F \int \frac{d^4 Q}{(2\pi)^4} G_{\text{gluon}}^{>\mu\nu}(Q) v_\mu v_\nu \delta(v \cdot Q) (1 - f(\mathbf{k} - \mathbf{q})), \quad (\text{A.70})$$

where we have neglected $Q^2 \ll 2K \cdot Q$. Since the scale separation $k \gg$ medium scale $\gg q$, we can set $f(\mathbf{k} - \mathbf{q}) \rightarrow 0$. Therefore, the differential scattering rate is given by

$$\frac{d\Gamma}{d^4 Q} = \frac{2\pi g^2 C_F}{(2\pi)^4} G_{\text{gluon}}^{>\mu\nu}(Q) v_\mu v_\nu \delta(v \cdot Q) \quad (\text{A.71})$$

This expression is exactly what enters in the AMY integral equation (2.11). If we take the particle to be moving in the z direction, we have $v^\mu = (1, 0, 0, 1)$, and the delta function enforces $Q^0 = q_z$. We may now use the relation of the Wightman function to the spectral function (3.46),

$$G_{\text{gluon}}^{>\mu\nu}(Q) = \rho^{\mu\nu}(Q) (1 + f(Q^0)) \approx \frac{T_*}{Q^0} \rho^{\mu\nu}(Q), \quad (\text{A.72})$$

where we have approximated the distribution function for very soft momenta using the infrared temperature T_* . Contracting this with $v^\mu v^\nu$, we obtain

$$\frac{d\Gamma}{d^2 \mathbf{q}_\perp} = \frac{g^2 C_F T_*}{(2\pi)^3} \int \frac{d\omega}{\omega} (\rho^{00} + \rho^{33}) = \frac{C_F g^2 T_*}{(2\pi)^2} \frac{m_D^2}{q_\perp^2 (q_\perp^2 + m_D^2)}, \quad (\text{A.73})$$

where we used the sum rule result (A.62). This is exactly, up to prefactors, the collision kernel

$$C(\mathbf{q}_\perp) = (2\pi)^2 \frac{d\Gamma}{d^2 \mathbf{q}_\perp} = g^2 C_F \int \frac{dQ^0 dQ^z}{(2\pi)^2} 2\pi \delta(v \cdot Q) G_{\text{gluon}}^{>\mu\nu}(Q) v_\mu v_\nu \stackrel{\text{isotropic}}{\underset{\text{soft}}{\equiv}} \frac{C_F g^2 T_* m_D^2}{q_\perp^2 (q_\perp^2 + m_D^2)} \quad (\text{A.74})$$

Thus, we have seen that the collision kernel can be represented via a Wightman function, and how the spectral function appears.

A.5.5 An analytic results for the dipole cross section

Here we show how to obtain the dipole cross section (1.2),

$$C(\mathbf{x}) = \int \frac{d^2 \mathbf{q}_\perp}{(2\pi)^2} C(\mathbf{q}_\perp) (1 - e^{i\mathbf{x} \cdot \mathbf{q}_\perp}), \quad (\text{A.75})$$

using the small q_\perp form of the collision kernel for an isotropic system (A.74),

$$C(\mathbf{q}_\perp) = \frac{C_R g^2 T_* m_D^2}{q_\perp^2 (q_\perp^2 + m_D^2)}. \quad (\text{A.76})$$

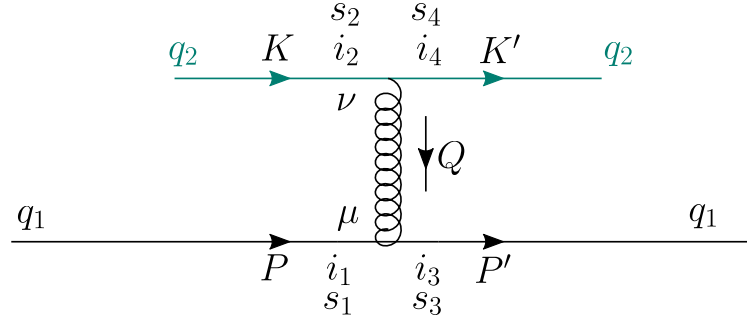


Figure A.3: Feynman diagram of a quark with momentum q_1 scattering off another quark (q_2) with two distinct quark flavors. The color, spin, and Lorentz indices are shown explicitly for illustration. Figure from [4].

First, the \mathbf{q}_\perp integral is split into modulus and angle, and the angular integral can be performed to yield the Bessel function J_0 ,

$$C(\mathbf{x}) = \frac{C_R g^2 T_*}{(2\pi)^2} \int_0^\infty dq_\perp q_\perp \int_0^{2\pi} d\phi \left(1 - e^{iq|\mathbf{x}| \cos \phi}\right) \frac{m_D^2}{q_\perp^2 (q_\perp^2 + m_D^2)} \quad (\text{A.77})$$

$$= C_R g^2 T_* \int_0^\infty \frac{dq_\perp}{2\pi} (1 - J_0(|\mathbf{x}| q_\perp)) \frac{m_D^2}{q_\perp (q_\perp^2 + m_D^2)}. \quad (\text{A.78})$$

Using $\frac{dJ_0(|\mathbf{x}| q)}{dq} = -|\mathbf{x}| J_1(|\mathbf{x}| q)$ and $\int dq \frac{m_D^2}{q(q^2 + m_D^2)} = \frac{1}{2} \log \frac{q^2}{q^2 + m_D^2}$, we obtain by partial integration (the boundary terms vanish because $J_0(0) = 1$)

$$C(\mathbf{x}) = -C_R g^2 T_* \frac{|\mathbf{x}|}{2} \int_0^\infty \frac{dq_\perp}{2\pi} J_1(|\mathbf{x}| q_\perp) \log \frac{q_\perp^2}{q_\perp^2 + m_D^2} \quad (\text{A.79})$$

$$= \frac{C_R g^2 T_*}{2\pi} \left(\gamma_E + K_0(|\mathbf{x}| m_D) + \log \frac{|\mathbf{x}| m_D}{2} \right), \quad (\text{A.80})$$

where γ_E is the Euler-Mascheroni constant, and K_0 is the modified Bessel function of the second kind. This expression can be expanded for small $|\mathbf{x}|$,

$$C(\mathbf{x}) = \frac{C_R g^2 T_* m_D^2}{8\pi} \mathbf{x}^2 \left(1 - \gamma_E - \log \frac{|\mathbf{x}| m_D}{2} \right) + \mathcal{O}(\mathbf{x}^4, \mathbf{x} \mathbf{x}^4 \log |\mathbf{x}|). \quad (\text{A.81})$$

It should be noted that Eq. (A.80) is not the correct form of the dipole cross section in thermal equilibrium, because we started off with only the small q_\perp form of the collision kernel.

A.6 SCATTERING WITH SOFT GLUON EXCHANGE

In this Appendix, we verify that quark or gluon scatterings with soft-gluon exchange are equivalent to scalar scatterings as in Eq. (3.27) up to $\mathcal{O}(Q/P)$. Or, put differently, that for soft-gluon exchange the matrix elements are at leading order independent of the spin of the hard particles.

This presentation follows Ref. [4].

A.6.1 Quark scattering

First, we calculate the square of the matrix element for quark scattering with a general internal gluon propagator. The amplitude for quark scattering of two different flavors with incoming momenta P and K (spin states s_1, s_2 and colors i_1, i_2) to the outgoing momenta P' and K' (spin states s_3 and s_4 , colors i_3 and i_4), as depicted in Fig. A.3, is given by⁵

$$i\mathcal{M}_{s_3 i_3, s_4 i_4}^{s_1 i_1, s_2 i_2} = -g^2 (\bar{u}^{s_3}(P') \gamma^\mu u^{s_1}(P)) (\bar{u}^{s_4}(K') \gamma^\nu u^{s_2}(K)) (-i G_{\mu\nu}^{ab}(Q)) t_{i_3 i_1}^a t_{i_4 i_2}^b. \quad (\text{A.82})$$

To calculate the square $|\mathcal{M}|^2 = \sum_{s_j, i_j} (\mathcal{M}_{s_3 i_3, s_4 i_4}^{s_1 i_1, s_2 i_2})^* \mathcal{M}_{s_3 i_3, s_4 i_4}^{s_1 i_1, s_2 i_2}$, we need to sum over the color indices and use

$$(t_{i_3 i_1}^a t_{i_4 i_2}^b)^* t_{i_3 i_1}^c t_{i_4 i_2}^d = \text{Tr}(t^a t^c) \text{Tr}(t^b t^d) = n_F^2 \delta^{ac} \delta^{bd}, \quad (\text{A.83})$$

where $n_F = 1/2 = C_F N_c / d_A$ is the index of the fundamental representation of $\text{SU}(N_c)$. Summing over all spins, we obtain

$$\begin{aligned} |\mathcal{M}|^2 &= \sum_{s_1 s_2 s_3 s_4} n_F^2 \delta^{ac} \delta^{bd} g^4 G_{\mu\nu}^{ab}(Q) (G_{\rho\sigma}^{cd}(Q))^* \\ &\times (\bar{u}^{s_3}(P') \gamma^\mu u^{s_1}(P)) (\bar{u}^{s_1}(P) \gamma^\rho u^{s_3}(P')) \\ &\times (\bar{u}^{s_4}(K') \gamma^\nu u^{s_2}(K)) (\bar{u}^{s_2}(K) \gamma^\sigma u^{s_4}(K')) \end{aligned} \quad (\text{A.84})$$

Using the identity $\sum_{s_1} u_i^{s_1}(P) \bar{u}_j^{s_1}(P) = -P_\mu (\gamma^\mu)_{ij} = -\not{P}_{da}$, we obtain

$$|\mathcal{M}|^2 = n_F^2 g^4 G_{\mu\nu}^{ab}(Q) (G_{\rho\sigma}^{ab}(Q))^* \text{Tr}(\gamma^\mu \not{P} \gamma^\rho \not{P}') \text{Tr}(\gamma^\nu \not{K} \gamma^\sigma \not{K}').$$

With

$$\text{Tr}(\not{P} \gamma^\mu \not{P}' \gamma^\nu) = 4(P^\mu P'^\nu + P^\nu P'^\mu - g^{\mu\nu} P \cdot P'), \quad (\text{A.85})$$

we finally arrive at

$$|\mathcal{M}|^2 = 16n_F^2 g^4 G_{\mu\nu}^{ab}(Q) (G_{\rho\sigma}^{ab}(Q))^* (Q) [P^\mu P'^\rho + P^\rho P'^\mu - g^{\mu\rho} P \cdot P'] [K^\nu K'^\sigma + K^\sigma K'^\nu - g^{\nu\sigma} K \cdot K']. \quad (\text{A.86})$$

This expression is independent of the precise form of the gluon propagator G . Note that all terms in the propagator $G_{\mu\nu}$ proportional to Q_μ or Q_ν (which we argue in Section 6.2.1 are the terms that depend on the specific gauge choice) do not contribute, i.e.,

$$Q_\mu [P^\mu (P+Q)^\nu + P^\nu (P+Q)^\mu - g^{\mu\nu} P \cdot Q] = P^\nu (2(Q \cdot P) + Q^2) = P^\nu (P+Q)^2 = P^\nu P'^2 = 0.$$

To expand for small Q , we use $P' = P + Q$, $K' = K - Q$. To lowest order, the only Q -dependence remains in the propagator and we obtain

$$|\mathcal{M}|^2 = 16n_F^2 g^4 G_{\mu\nu} G_{\rho\sigma}^* 4P^\mu P^\rho K^\nu K^\sigma \left(1 + \mathcal{O}\left(\frac{Q}{P}\right)\right). \quad (\text{A.87})$$

To the lowest order in Q , this is equivalent to

$$|\mathcal{M}|^2 = 4n_F^2 g^4 G_{\mu\nu} G_{\rho\sigma}^* \times (P+P')^\mu (P+P')^\rho (K+K')^\nu (K+K')^\sigma \times (1 + \mathcal{O}(Q/P)),$$

which at the same order is the same as the scalar quark result (3.27).

⁵ The Feynman rules can be found in any standard QFT textbook, e.g. see [235] for the mostly plus metric convention.

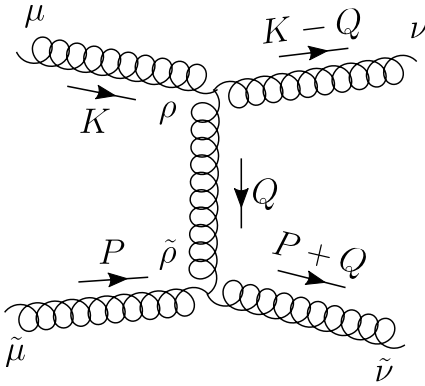


Figure A.4: t-channel diagram for gluon scattering. Figure from [4].

A.6.2 Gluon scattering

After having considered the case of quark scattering, we turn to gluon scattering. In this subsection, we show that in the soft limit, medium effects in gluon scattering enter in the same way.

Gluon-gluon scattering is depicted pictorially in Fig. A.4. The dominant process for screening effects is the *t*-channel, where $|t| \ll s$, or—equivalently—the *u*-channel, which can be readily obtained by exchanging $u \leftrightarrow t$ in the collision kernel.

Using the Feynman rules, we can write (suppressing color factors)

$$\begin{aligned} \mathcal{M}^{\mu\tilde{\mu}\nu\tilde{\nu}} &\propto G_{\rho\tilde{\rho}}(Q) [g^{\mu\rho}(K+Q)^\nu + g^{\rho\nu}(K-2Q)^\mu + g^{\nu\mu}(Q-2K)^\rho] \\ &\quad \times [g^{\tilde{\mu}\tilde{\nu}}(2P+Q)^\tilde{\rho} + g^{\tilde{\nu}\tilde{\rho}}(-P-2Q)^\tilde{\mu} + g^{\tilde{\rho}\tilde{\mu}}(Q-P)^\tilde{\nu}]. \end{aligned} \quad (\text{A.88})$$

In the soft limit, for small Q , we can, to a first approximation, neglect all Q dependence except for the propagator. Additionally, when summing over polarizations, we need to contract the “same” external lines $(\mathcal{M}^{\mu\tilde{\mu}\nu\tilde{\nu}})^* \mathcal{M}_{\mu\tilde{\mu}\nu\tilde{\nu}}$, and then the first line simplifies to

$$[g^{\mu\rho}K^\nu + g^{\rho\nu}K^\mu - 2g^{\nu\mu}K^\rho] [g_{\mu\rho'}K_\nu + g_{\rho'\nu}K_\mu - 2g_{\nu\mu}K_{\rho'}] = 2K^2\delta_{\rho'}^\rho + (4D-6)K^\rho K_{\rho'}, \quad (\text{A.89})$$

where $D = g_\mu^\mu$ is the space-time dimension. With $P^2 = K^2 = 0$, we obtain

$$|\mathcal{M}|^2 \propto K^\rho K_{\rho'} P^{\tilde{\rho}} P_{\tilde{\rho}'} G_{\rho\tilde{\rho}}(Q) \bar{G}^{\rho'\tilde{\rho}'}(Q) \times \left(1 + \mathcal{O}\left(\frac{Q}{K}, \frac{Q}{P}\right)\right) \quad (\text{A.90})$$

$$= |(K+K')^\rho (P+P')^{\tilde{\rho}} G_{\rho\tilde{\rho}}(Q)|^2 \times \left(1 + \mathcal{O}\left(\frac{Q}{K}, \frac{Q}{P}\right)\right). \quad (\text{A.91})$$

Again, to the lowest order in Q , this is the same as the scalar quark result (3.27).

B

NUMERICAL AND KINEMATIC DETAILS ON KINETIC THEORY SIMULATIONS

In this appendix, we discuss several numerical and kinematic aspects relevant for QCD kinetic theory simulations. In particular, we discuss how the distribution function is discretized, and how the collision terms are rewritten in a symmetrized form to solve the Boltzmann equation for the discretized distribution function. We discuss the coordinate systems that are used for the integral measure of the elastic collision term and discuss how the collision terms are evaluated using Monte Carlo sampling. We also discuss the adaptive step size algorithm used for the isoHTL-screened simulations.

B.1 DISCRETIZATION

In kinetic theory, all medium information is encoded in the distribution function $f(t, \mathbf{p})$. In our case, for a given time t (or proper time τ), it depends only on two parameters (see the discussion in section 3.6.1), the magnitude of the momentum p and its polar angle θ_p . How the distribution function $f(\mathbf{p})$ is stored on a finite grid follows the *discrete momentum* method of Ref. [169], where we store the number density per bin,

$$n_{ij} = \lambda \int \frac{d^3 \mathbf{p}}{(2\pi)^3} f(\mathbf{p}) w_i(p) \tilde{w}_j(\cos \theta), \quad (\text{B.1})$$

with the piecewise linear wedge functions w , defined for the momentum case as

$$w_i(p) = \begin{cases} \frac{p - p_{i-1}}{p_i - p_{i-1}}, & p_{i-1} < p < p_i \\ \frac{p_{i+1} - p}{p_{i+1} - p_i}, & p_i < p < p_{i+1} \\ 0 & \text{else,} \end{cases} \quad (\text{B.2})$$

and for the polar angle similarly with the grid points substituted by $p_i \rightarrow \cos \theta_i$. The distribution function $f(\mathbf{p})$ can be (approximately) recovered from the moments n_{ij} by linear interpolation between the grid points, using the simple relation

$$f(p_i, \cos \theta_j) = \frac{(2\pi)^3 n_{ij}}{\lambda p_i^2 4\pi \Delta V_i^p \Delta V_j^\theta}, \quad (\text{B.3})$$

with the volume factors defined via

$$\Delta V_i^p = \int_{-\infty}^{\infty} dx w_i(x), \quad \Delta V_i^\theta = \int_{-1}^1 d\cos \theta \tilde{w}_i(\cos \theta). \quad (\text{B.4})$$

Description	Chapter(s)	N_p	N_θ	p_{\min}	p_{\max}
Runs with Bjorken expansion for \hat{q}	4.4, 6	100	180	0.03	6
Runs extracting κ	6	100	180	0.05	6
Additional runs with $\lambda \in \{0.25, 0.75, 1.5\}$	6	180	250	0.03	6
Bjorken expanding isoHTML/Debye-like	6.4.8	200	180	0.03	8
Over-occupied, with $\lambda = 0.5$	6.4.8	300	1	0.01	25
Over-occupied, with $\lambda = 2$	6.4.8	200	1	0.01	12
Over-occupied, with $\lambda = 10$	6.4.8	200	1	0.01	10
Under-occupied runs	6.4.8	500	1	0.03	100
Runs with Bjorken expansion	8	200	180	0.03	8

Table B.1: Discretization parameters for the simulations used in this thesis.

This simplifies obtaining observables because the integral for an observable (3.80) can be computed via

$$n\langle O(\mathbf{p}) \rangle = \int \frac{d^3 \mathbf{p}}{(2\pi)^3} \mathcal{O}(\mathbf{p}) f(\mathbf{p}) \approx \sum_{ij} n_{ij} \mathcal{O}(\mathbf{p}_{ij}), \quad (\text{B.5})$$

which is exact for the number and energy density

$$n = \sum_{ij} n_{ij}, \quad \varepsilon = \sum_{ij} n_{ij} p_i, \quad (\text{B.6})$$

because we can insert (B.1) and use

$$\sum_i w_i(p) = 1, \quad \sum_i w_i(p) p_i = p. \quad (\text{B.7})$$

See also Appendix A of Ref. [25] for a more detailed discussion about the discretization.

The discretization parameters used for simulations in this thesis are summarized in Table B.1.

B.2 SYMMETRIZATION OF THE COLLISION TERMS

For the numerical evaluation, it is convenient to rewrite Eq. (3.15) in a symmetric form. For pure gluons, it then reads

$$\begin{aligned} \mathcal{C}^{2\leftrightarrow 2}[f(\tilde{\mathbf{p}})] &= \frac{(2\pi)^3}{4\pi\tilde{p}^2} \frac{1}{8\nu_g} \int d\Gamma_{\text{PS}} |\mathcal{M}(\mathbf{p}, \mathbf{k}; \mathbf{p}', \mathbf{k}')|^2 \\ &\times \left(f(\mathbf{p})f(\mathbf{k})(1+f(\mathbf{p}'))(1+f(\mathbf{k}')) - f(\mathbf{p}')f(\mathbf{k}')(1+f(\mathbf{p}))(1+f(\mathbf{k})) \right) \\ &\times \left(\delta^3(\tilde{\mathbf{p}} - \mathbf{p}) + \delta^3(\tilde{\mathbf{p}} - \mathbf{k}) - \delta^3(\tilde{\mathbf{p}} - \mathbf{p}') - \delta^3(\tilde{\mathbf{p}} - \mathbf{k}') \right), \end{aligned} \quad (\text{B.8})$$

with the integration measure

$$\begin{aligned} \int d\Gamma_{\text{PS}} &= \int_{\mathbf{p}\mathbf{k}\mathbf{p}'\mathbf{k}'} (2\pi)^4 \delta^4(P + K - P' - K') \\ &= \frac{1}{2^{12}\pi^8} \int_0^\infty dq \int_{-q}^q d\omega \int_{\frac{q-\omega}{2}}^\infty dp \int_{\frac{q+\omega}{2}}^\infty dk \int_{-1}^1 d\cos\theta_q \int_0^{2\pi} d\phi_q \int_0^{2\pi} d\phi_{pq} \int_0^{2\pi} d\phi_{qk}. \end{aligned} \quad (\text{B.9})$$

We will discuss the integration variables in more detail in the next section B.3.

As discussed in Section 3.3.2, the integrand is symmetric under the exchange of the outgoing particles with momenta $k' \leftrightarrow p'$, which exchanges the u - and t -channel. This shifts the dominating integration region from small $|u|$ and small $|t|$ to the small $|t|$ region only, which greatly simplifies the screening prescription and importance sampling.

The inelastic collision term (3.3) accounts for collinear splitting and merging. In its symmetrized form, and for pure gluons, it is given by

$$\begin{aligned} \mathcal{C}^{1 \leftrightarrow 2}[f(\mathbf{\tilde{p}})] &= \frac{(2\pi)^3}{4\pi\tilde{p}^2} \frac{1}{\nu} \int_0^\infty dp \int_0^{p/2} dk' 4\pi \gamma_{p'k'}^p \\ &\times \left\{ f(\mathbf{p})(1 + f(p'\hat{\mathbf{p}}))(1 + f(k'\hat{\mathbf{p}})) \right. \\ &\quad \left. - f(p'\hat{\mathbf{p}})f(k'\hat{\mathbf{p}})(1 + f(\mathbf{p})) \right\} \\ &\times [\delta(\tilde{p} - p) - \delta(\tilde{p} - p') - \delta(\tilde{p} - k')] \end{aligned} \quad (\text{B.10})$$

B.3 COORDINATE SYSTEM AND MANDELSTAM VARIABLES

The elastic collision term, after symmetrization (B.8) features an integration over \mathbf{p} , \mathbf{k} , and \mathbf{q} . Similarly to Ref. [206], the integrals over \mathbf{p} and \mathbf{k} are performed in a frame, in which \mathbf{q} defines the z -direction with the original z -axis lying in the xz plane. However, contrary to Ref. [206], \mathbf{p} is not required to be in the xz plane, since it is also integrated. This is also different to how the jet quenching parameter \hat{q} is obtained in Section 4.1.2, where the jet direction \mathbf{p} was fixed. As integration variables it is convenient to choose the exchange momentum \mathbf{q} , parametrized by its magnitude q , polar and azimuthal angle $\cos\theta_q$, and ϕ_q , the exchange energy ω , the magnitude of the vectors p and k , and the azimuthal angles of \mathbf{p} and \mathbf{k} in a frame (q -frame), in which \mathbf{q} points in the z direction and the original z -axis lies in the xz plane. This fixes the kinematics completely. We denote these azimuthal angles by θ_{qp} and θ_{qk} . Energy conservation results in the kinematic conditions

$$|\omega| < q, \quad p > \frac{q - \omega}{2}, \quad k > \frac{q + \omega}{2}, \quad (\text{B.11})$$

and fixes the polar angles θ_{qp} and θ_{qk} of \mathbf{p} and \mathbf{k} in the q -frame (see, e.g., [206] or the discussion in Section 4.1.2),

$$\cos\theta_{qp} = \frac{\omega}{q} + \frac{\omega^2 - q^2}{2pq}, \quad \cos\theta_{qk} = \frac{\omega}{q} - \frac{\omega^2 - q^2}{2kq}. \quad (\text{B.12})$$

In terms of these integration variables, we parameterize the relevant vectors (in the q -frame) using these variables as

$$Q = P' - P = \begin{pmatrix} \omega \\ 0 \\ 0 \\ q \end{pmatrix}, \quad P = p \begin{pmatrix} 1 \\ \sin\theta_{qp} \cos\phi_{qp} \\ \sin\theta_{qp} \sin\phi_{qp} \\ \cos\theta_{qp} \end{pmatrix}, \quad K = k \begin{pmatrix} 1 \\ \sin\theta_{qk} \cos\phi_{qk} \\ \sin\theta_{qk} \sin\phi_{qk} \\ \cos\theta_{qk} \end{pmatrix}. \quad (\text{B.13})$$

In terms of the integration variables, the Mandelstam variables needed for the matrix elements are given by

$$t = \omega^2 - q^2, \quad (\text{B.14})$$

$$s = -\frac{t}{2q^2} \left((p + p')(k + k') + q^2 - \sqrt{(4pp' + t)(4k'k + t)} \cos(\phi_{qk} - \phi_{qp}) \right), \quad (\text{B.15})$$

$$u = \frac{t}{2q^2} \left((p + p')(k + k') - q^2 - \sqrt{(4pp' + t)(4k'k + t)} \cos(\phi_{qk} - \phi_{qp}) \right). \quad (\text{B.16})$$

B.4 INELASTIC COLLISION TERM

For the inelastic collision term, the splitting rate γ_{gg}^s from Section 2.2 has to be evaluated. This is done using the method described in Ref. [169] following Ref. [231]. The integral equation (2.11) is solved in impact parameter space, where the dipole cross section (A.8o) is used. We do not discuss this method here in detail, but discuss a general method for obtaining the splitting rate for an arbitrary collision kernel $C(\mathbf{q}_\perp)$ in Appendix E.

B.5 MONTE CARLO EVALUATION OF THE COLLISION TERMS

To derive the differential equations for the moments n_{ij} , one needs to rewrite the Boltzmann equation (3.2) in terms of n_{ij} ,

$$v^\mu \partial_\mu n_{ijk} = \lambda \int \frac{d^3 \tilde{\mathbf{p}}}{(2\pi)^3} w_i(\tilde{p}) \tilde{w}_j(\cos \tilde{\theta}) v^\mu \partial_\mu f(\tilde{\mathbf{p}}) = -\lambda \int \frac{d^3 \tilde{\mathbf{p}}}{(2\pi)^3} w_i(\tilde{\mathbf{p}}) \tilde{w}_j(\cos \tilde{\theta}) \mathcal{C}[f](\tilde{\mathbf{p}}). \quad (\text{B.17})$$

This replaces the delta functions in the collision terms (B.8) and (B.10) by the wedge functions w_i and \tilde{w}_j . The collision terms are then computed using Monte Carlo importance sampling.

For the elastic collision term $\mathcal{C}^{2 \leftrightarrow 2}$, points from the integration measure (B.9) are sampled using Monte Carlo importance sampling. For finite grid boundaries, we need to require that all momenta sampled lie within the grid. For the q , ω , p , and k integration, the grid boundaries p_{\min} and p_{\max} have to be considered, and these integrals become

$$\int_0^{p_{\max}} dq \int_{\max(-q, p_{\min} - p_{\max})}^{\min(q, p_{\max} - p_{\min})} d\omega \int_{\max(\frac{q-\omega}{2}, p_{\min}, p_{\min} - \omega)}^{\min(p_{\max}, p_{\max} - \omega)} dp \int_{\max(\frac{q+\omega}{2}, p_{\min}, p_{\min} + \omega)}^{\min(p_{\max}, p_{\max} + \omega)} dk,$$

which ensures that all momenta $k, k' = k - \omega, p, p' = p + \omega$ lie within the grid. The second boundaries for ω come from the requirement that $p_{\max} > p_{\min} + \omega$ and $p_{\max} + \omega > p_{\min}$ in the k integral.

For the q -integral, we sample from a $dq/(q + \xi m_D)^4$ distribution, with $\xi_g = e^{5/6}/\sqrt{8}$ (see section 3.3.2), although its precise value is not important for the sampling process. While ω is sampled uniformly, both k and p are sampled from a dk/k distribution.

B.6 ADAPTIVE STEP SIZE

Here, the adaptive step size is described, which is used for simulations with the isoHTML screened matrix element in Chapter¹ 6.4.8. The philosophy of the adaptive timestep is to set it such that the relative change of specific observables is smaller than a predefined constant $\epsilon^{\text{errgoal}}$. This is similar to the stepsize employed in Ref. [25], but the method here goes beyond linearization by calculating the exact change in the considered observables. It is found that this approach is better stabilizes simulations with isoHTML screening.

To be more concrete, in every timestep $t_{k+1} = t_k + \Delta t$, the stored values of n_{ij} are changed (defined in (B.1)) such that

$$n_{ij}(t_{k+1}) = n_{ij}(t_k) + \Delta t c_{ij}, \quad (\text{B.18})$$

and c_{ij} are numerical estimates (from Monte Carlo integrals) of the sum of all collision terms in Eq. (3.2).

With the discretization choice (B.1), several quantities can be easily calculated,

$$\epsilon = \int \frac{d^3 \mathbf{p}}{(2\pi)^3} p f(\mathbf{p}) = \sum_{ij} \frac{n_{ij} p}{\lambda} \quad (\text{B.19a})$$

$$n = \int \frac{d^3 \mathbf{p}}{(2\pi)^3} f(\mathbf{p}) = \sum_{ij} \frac{n_{ij}}{\lambda} \quad (\text{B.19b})$$

$$n\langle p_z^2 \rangle = \int \frac{d^3 \mathbf{p}}{(2\pi)^3} p^2 \cos^2 \theta f(\mathbf{p}) \approx \sum_{ij} \frac{n_{ij}}{\lambda} p^2 \cos^2 \theta \quad (\text{B.19c})$$

$$n\langle f \rangle = \int \frac{d^3 \mathbf{p}}{(2\pi)^3} f^2(\mathbf{p}) \approx \sum_{ij} \frac{n_{ij}^2}{\lambda^2} \frac{(2\pi)^3}{\Delta V_i^p \Delta V_j^\theta p_i^2 4\pi} \quad (\text{B.19d})$$

$$n\langle pf \rangle = \int \frac{d^3 \mathbf{p}}{(2\pi)^3} p f^2(\mathbf{p}) \approx \sum_{ij} \frac{n_{ij}^2}{\lambda^2} p_i \frac{(2\pi)^3}{\Delta V_i^p \Delta V_j^\theta p_i^2 4\pi} \quad (\text{B.19e})$$

$$m^2 = 2\lambda \int \frac{d^3 \mathbf{p}}{(2\pi)^3} \frac{f(\mathbf{p})}{p} \approx 2 \sum_{ij} \frac{n_{ij}}{p_i}. \quad (\text{B.19f})$$

Note that, except for $n\langle f \rangle$ and $n\langle pf \rangle$, these quantities are linear in n_{ij} . After having evaluated the collision terms c_{ij} , we can accurately predict how these observables change in a single timestep and adjust the timestep such that their relative change does not exceed the parameter $\epsilon^{\text{errgoal}}$.

For quantities that are linear in n_{ij} (e.g., ϵ , m^2 , n , $n\langle p_z^2 \rangle$), their exact change per unit time can be obtained by replacing $n_{ij} \rightarrow c_{ij}$ in Eq. (B.19). For instance, the energy density ϵ changes by

$$\delta\epsilon := \frac{\Delta\epsilon}{\Delta t} = \sum_{ij} c_{ij} p_i. \quad (\text{B.20})$$

With the relative change $\frac{\Delta\epsilon}{\epsilon} = \frac{\delta\epsilon\Delta t}{\epsilon}$, the new time step can then be set according to

$$\Delta t = \frac{\epsilon^{\text{errgoal}}}{\left| \frac{\delta\epsilon}{\epsilon} \right|}. \quad (\text{B.21})$$

¹ The presentation here follows Ref. [4].

The change of the quadratic quantities (e.g., $n\langle f \rangle$ and $n\langle pf \rangle$), could be approximated linearly, e.g., for $\langle f \rangle$,

$$\Delta(n\langle f \rangle) \approx \sum_{ij} 2n_{ij}c_{ij}V_{ij} \quad (\text{B.22})$$

with

$$V_{ij} = \frac{(2\pi)^3}{\Delta V_i^p \Delta V_j^\theta p_i^2 4\pi} \quad (\text{B.23})$$

but this is only a crude estimate of the change and it turns out that using the correct change leads to a more stable evolution. The exact change $\Delta n\langle f \rangle = (n\langle f \rangle)_{i+1} - (n\langle f \rangle)_i$ can easily be obtained via

$$\Delta n\langle f \rangle = \sum_{ij} V_{ij} \left((n_{ij} + c_{ij}\Delta t)^2 - n_{ij}^2 \right) \quad (\text{B.24})$$

$$= \sum_{ij} V_{ij} \left(2n_{ij}c_{ij}\Delta t + c_{ij}^2(\Delta t)^2 \right). \quad (\text{B.25})$$

Enforcing a maximum relative change $|\Delta n\langle f \rangle/n\langle f \rangle| \leq \epsilon^{\text{errorgoal}}$ leads to a quadratic equation in Δt ,

$$|a\Delta t + b\Delta t^2| = \epsilon^{\text{errorgoal}}, \quad (\text{B.26})$$

with $b > 0$ and

$$a = \frac{\sum_{ij} V_{ij} 2n_{ij}c_{ij}}{n\langle f \rangle}, \quad b = \frac{\sum_{ij} V_{ij} (c_{ij})^2}{n\langle f \rangle}. \quad (\text{B.27})$$

To solve this quadratic equation for the most restrictive (i.e., smallest) Δt , we need to consider the two cases:

1. $a > 0$:

Here, $a\Delta t + b\Delta t^2$ monotonically increases and is always positive, thus the timestep is given by

$$\Delta t = -\frac{a}{2b} + \sqrt{\frac{a^2}{4b^2} + \frac{\epsilon^{\text{errorgoal}}}{b}}. \quad (\text{B.28})$$

2. For $a < 0$, the parabola (B.26) is sketched in Fig. B.1. Its minimum is at $\Delta t_{\min} = -a/(2b)$, with the minimum value $A_{\min} = -a^2/(4b)$.

When $|A_{\min}| < \epsilon^{\text{errorgoal}}$ as in Fig. B.1, we need to solve for positive ϵ , which yields the same result as above (again, we need the positive square root, as can be easily seen from the figure)

$$\Delta t = -\frac{a}{2b} + \sqrt{\frac{a^2}{4b^2} + \frac{\epsilon^{\text{errorgoal}}}{b}}. \quad (\text{B.29})$$

For $|A_{\min}| > \epsilon^{\text{errorgoal}}$, we need to equate to negative $\epsilon^{\text{errorgoal}}$, i.e., solve $a\Delta t + b\Delta t^2 = -\epsilon^{\text{errorgoal}}$, which yields

$$\Delta t = -\frac{a}{2b} - \sqrt{\frac{a^2}{4b^2} - \frac{\epsilon^{\text{errorgoal}}}{b}}. \quad (\text{B.30})$$

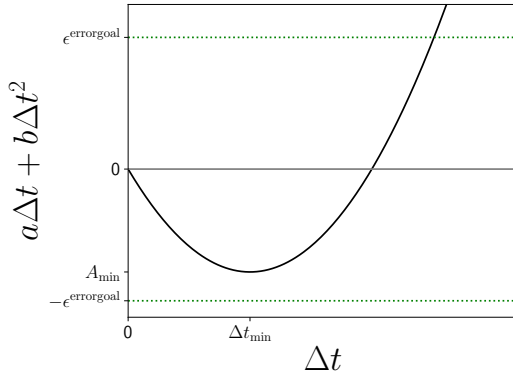


Figure B.1: Sketch of the quadratic equation (B.26) for $a < 0$. Figure from [4].

The new goal for the timestep is then set by determining the minimum of these

$$\Delta t^{\text{goal}} = \min_{i \in \{\varepsilon, n, n(p_z^2), n(f), n(pf), m^2\}} \Delta t_i \quad (\text{B.31})$$

and then adjusting it smoothly to the old one via

$$\Delta t^{\text{new}} = \sqrt{(\Delta t^{\text{goal}})^{2\alpha} (\Delta t^{\text{old}})^{2-2\alpha}}, \quad (\text{B.32})$$

where α is a constant $0 < \alpha < 1$ that ensures an interpolation between the previous value and the goal timestep. While $\alpha = 1$ corresponds to always choosing the goal timestep, $\alpha = 0$ corresponds to a constant time step (i.e., never choosing the goal timestep). Choosing α between these limits prevents large variations of this timestep due to statistical fluctuations. In practice, a value of $\alpha = 0.9$ is used for the simulations performed here.

B.7 KINEMATIC CONSIDERATIONS

In this section, we discuss why s is always the largest Mandelstam variable, and that if Q^2 is small, also q, ω are necessarily small. This section follows Ref. [4].

Why s is always the largest Mandelstam variable

Here, we want to show that s is always the largest Mandelstam variable. This has the consequence that no s -channel processes need to be screened in Section 3.3.2.

The Mandelstam variable s corresponds to the square of the center-of-mass energy. Since the Mandelstam variables are Lorentz invariant, we may compute them in any frame.

For simplicity, let us choose the center-of-mass frame, where

$$P = (p, p, 0, 0), \quad K = (p, -p, 0, 0), \quad (\text{B.33a})$$

$$P' = (p, p \mathbf{e}_x + \mathbf{q}), \quad K' = (p, -p \mathbf{e}_x - \mathbf{q}), \quad (\text{B.33b})$$

and rotate the frame such that $q_z = 0$. Note that in this frame, the energy of each particle is conserved separately in an elastic scattering process.

From $P'^2 = 0$ we can compute $2pq_x + q^2 = 2pq_x + q_x^2 + q_y^2 = 0$, and thus $q_x = -p \pm \sqrt{p^2 - q_y^2}$. Therefore, $|q_y| \leq p$, and $|q_x| \leq 2p$. Additionally, $q_x = -\frac{q^2}{2p}$.

The Mandelstam variable t is given by $t = -q^2$, which is thus bounded by $|t| \leq 4p^2 = s$. Therefore, s is always the largest Mandelstam variable, and no s -channel process will need to be screened.

Kinematic considerations: From Q^2 small follows q, ω small

Here, we show that the condition $0 < -t \ll s$, or $Q^2 \ll -(P + K)^2$ implies that all components of Q , i.e., $|\omega|$ and q , are small. For that, we consider a plasma with typical excitations at momentum T ,

$$P = T(1, 1, 0, 0), \quad K = T(1, \mathbf{n}), \quad (\text{B.34a})$$

$$P' = (T + \omega, T + q_x, q_y, q_z), \quad K' = (T - \omega, T\mathbf{n} - \mathbf{q}), \quad (\text{B.34b})$$

with $\mathbf{n} = (n_x, n_y, 0)$ being a unit vector in the $x - y$ plane, i.e., $n_x^2 + n_y^2 = 1$. The condition $|t| = |Q^2| \ll s$ is equivalent to

$$q^2 - \omega^2 \ll 2T^2(1 - n_x), \quad (\text{B.35})$$

where we used that $q^2 > \omega^2$.

We show in the following that Eq. (B.35) implies $|\mathbf{q}| \gtrsim |\omega| \ll T$.

Let us assume

$$|\mathbf{q}| \approx T \quad (\text{B.36})$$

and show that this leads to a contradiction. Eq. (B.36) requires $|\omega| \approx T$ for Eq. (B.35) to be fulfilled. We will show in the following that this is kinematically forbidden, and thus $|\mathbf{q}| \ll T$.

We thus assume $|\omega| \approx T$ and introduce a parameter $\alpha \ll 1 - n_x$ to rewrite Eq. (B.35) to $q^2 - \omega^2 = \mathcal{O}(\alpha T^2)$. From $P'^2 = 0$ we can obtain² an expression for $q_x = \omega + \mathcal{O}(\alpha^2 T)$. Similarly, from $K'^2 = 0$, we obtain³ $q_y = \frac{1-n_x}{n_y} \omega + \mathcal{O}(\alpha T)$. Inserting back into Eq. (B.35) and using $\frac{(1-n_x)^2}{1-n_x^2} = \frac{1-n_x}{1+n_x}$ yields an equation for q_z ,

$$q^2 - \omega^2 = \frac{1-n_x}{1+n_x} \omega^2 + q_z^2 + \mathcal{O}(\alpha T^2) = 0, \quad (\text{B.37})$$

which has no solution for which $q_z^2 > 0$. Therefore, the assumption $q^2 \approx \omega^2 \approx T^2$ leads to a contradiction, and we have shown that $|\mathbf{q}|, |\omega| \ll q \ll T$.

B.8 DOMINANCE OF SMALL ANGLE SCATTERINGS

Here, it is demonstrated that $|t| \ll |s| \sim |u|$ is the dominant regime for elastic processes in the collision term. This implies that the different screening prescriptions that we discussed in Eq. (6.20) in Chapter 6.4.8 agree for $|t|/s \ll 1$ and $|t/u| \ll 1$.

² Using $P'^2 = q^2 - \omega^2 - 2T(\omega - q_x)$

³ Using $K'^2 = (K - Q)^2 = q^2 - \omega^2 - 2T[-\omega + q_x n_y + q_y n_y]$ and then using $q_x = \omega - \frac{q^2 - \omega^2}{2T}$

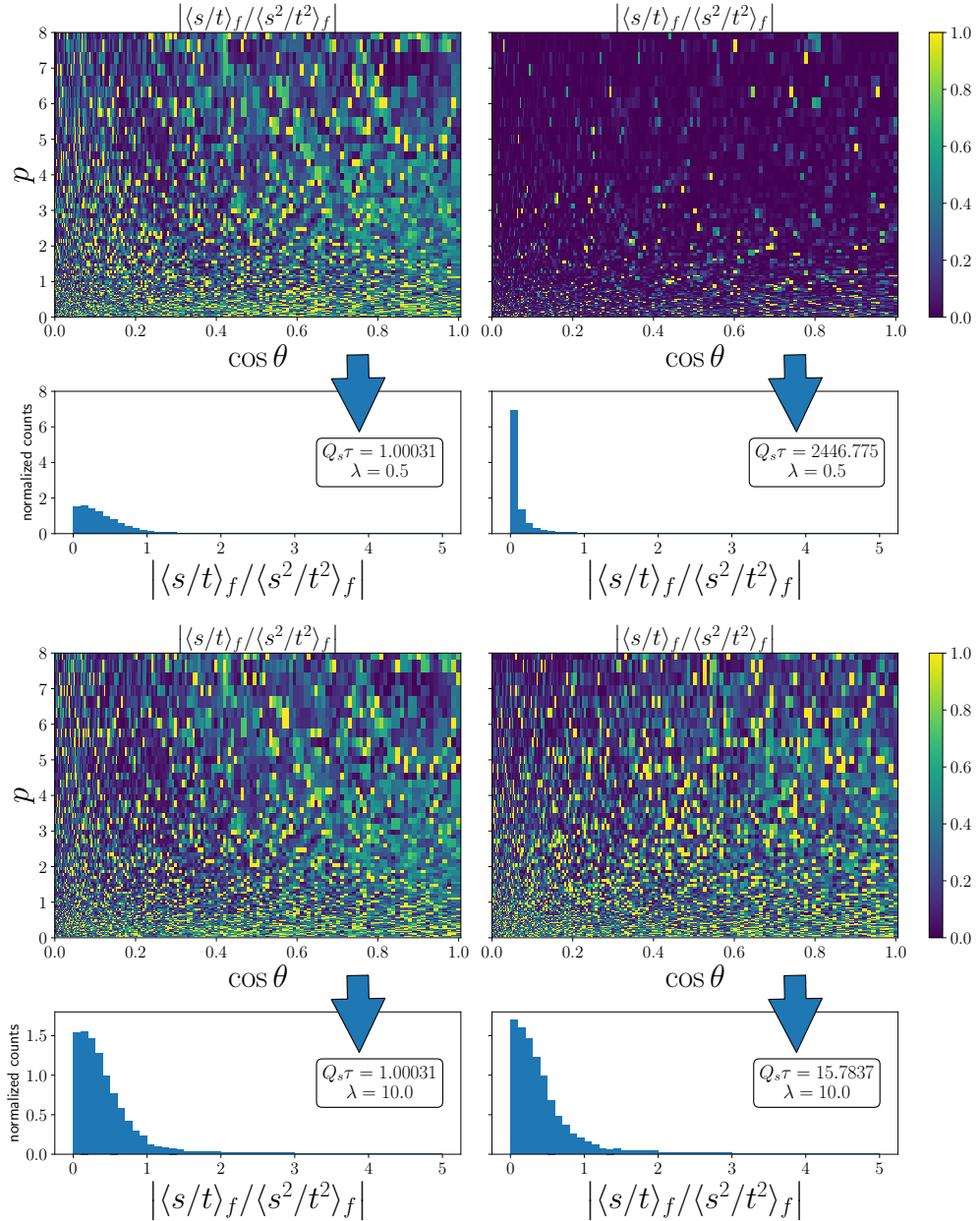


Figure B.2: Ratio of contributions of the elastic collision term with only s/t as matrix element over s^2/t^2 , denoted $|\langle s/t \rangle_f / \langle s^2/t^2 \rangle_f|$, which is defined in Eq. (B.38). All four panels show $|\langle s/t \rangle_f / \langle s^2/t^2 \rangle_f|$ as a function of the momentum p , parametrized by its length p and angle θ_p with respect to the beam axis. The histograms show the distribution of values in the plots above. The left column corresponds to the initial time and the right column to a later time for the couplings $\lambda = 0.5$ (top) and $\lambda = 10$ (bottom). Figure from [4].

To show this, typical distribution functions $f(\mathbf{p})$ are considered during simulations of the equilibration process in expanding systems, and the “expectation” value of s/t and s^2/t^2 is calculated by integrating over phase-space and the statistical factors. More concretely, kinetic theory simulations using the Debye-like screened matrix element (6.20a) are performed, and the distribution function $f(\mathbf{p})$ is extracted at two distinct times. Then the contribution to the collision term from the small $|t| \ll s$ contributions are calculated,

$$\left| \frac{\frac{\partial f(\mathbf{p})}{\partial \tau}}{\frac{\partial f(\mathbf{p})}{\partial \tau}} \right|_{\text{el. coll. with } s/t} = \left| \frac{\int d\Gamma \frac{s}{t} F^{2 \leftrightarrow 2}}{\int d\Gamma \frac{s^2}{t^2} F^{2 \leftrightarrow 2}} \right| = \left| \frac{\langle s/t \rangle_f}{\langle s^2/t^2 \rangle_f} \right|, \quad (\text{B.38})$$

where we have introduced the short notation $\langle \dots \rangle_f$ to denote the phase-space average including the distribution functions $F^{2 \leftrightarrow 2} = f_p f_k (1 + f_{p'}) (1 + f_{k'}) - f_{p'} f_{k'} (1 + f_p) (1 + f_k)$. Note that the result still depends on the vector \mathbf{p} , which is the argument of the initial distribution function.

The results of this procedure are presented for two distinct times in Fig. B.2 for couplings $\lambda = 0.5$ and $\lambda = 10$. We observe that the values of $|\langle s/t \rangle / \langle s^2/t^2 \rangle|$ fluctuate depending on the momentum bin, coupling, and time. However, when plotted within a histogram below (indicated by blue arrows), we find consistently dominating values below 1. Therefore, we conclude that indeed $\langle s/t \rangle$ terms are suppressed as compared to $\langle s^2/t^2 \rangle$ terms, and the results with the different Debye-like screening prescriptions coincide not only for weak coupling, as argued in Chapter 6.4.8.

B.9 STATISTICAL AVERAGES

The method for obtaining the collision integrals described here is based on Monte Carlo integration, which is based on random numbers. There, the value of an integral is estimated based on random samples in the integration region. Thus, the resulting estimate of the integral is inherently stochastic. In Chapter 6.4.8, different simulations with different seeds for the random number generators are performed. Every simulation, thus, will yield slightly different results. An estimate for the error of the mean, or the standard error [236] can be given by taking n samples of a considered quantity, \mathcal{O}_i , and calculating the sample average $\bar{\mathcal{O}}$ and sample variance s^2 ,

$$\bar{\mathcal{O}} = \frac{1}{n} \sum_{i=1}^n \mathcal{O}_i, \quad s^2 = \frac{1}{n-1} \sum_{i=1}^n (\mathcal{O}_i - \bar{\mathcal{O}})^2. \quad (\text{B.39})$$

The standard error $\bar{\sigma}$ is then calculated as

$$\bar{\sigma} = \sqrt{\frac{s^2}{n}}. \quad (\text{B.40})$$

This is the method for calculating the error bars in the time evolution in Chapter 6.4.8. The same method is also used to estimate the error from the Monte Carlo evaluation of the integral for the jet quenching parameter \hat{q} in Chapter 4.4.

C

LARGE MOMENTUM LIMITS OF THE JET QUENCHING PARAMETER

In this appendix, we study the behavior of the jet quenching parameter \hat{q} for large jet momentum p and, in particular, how to correctly perform the limit $p \rightarrow \infty$. We verify that taking the term which is leading order in $1/p$ in the integrand of \hat{q}^{ij} is indeed sufficient to obtain the correct leading-order contribution. This is not trivial since p also appears in the integration boundaries. Thus, there are two possible sources for large- p contributions to \hat{q} : the integrand and the integral boundaries. Our strategy here is to expand the integrand in orders of $1/p$ and then perform the integrals. This Appendix is based on Appendix C in [2].

We illustrate the large p behavior of \hat{q} using the gluonic matrix element,

$$\hat{q} \sim \int_0^\infty dk \int_{-\frac{p-k}{2}}^k d\omega \int_{|\omega|}^{\min(p+p',k+k')} dq q^2 (1 - \cos^2 \theta_{qp}) \frac{|\mathcal{M}_{gg}^{gg}|^2}{p^2} f_b(\mathbf{k}) (1 \pm f_d(\mathbf{k}')). \quad (\text{C.1})$$

The distribution function $f(\mathbf{k})$ provides a natural upper limit for the momentum of the plasma constituent k , which we assume to be much smaller than the jet momentum p , thus $k \ll p$. Hence, the minimum of $(p + p', k + k') = (2p + \omega, 2k - \omega)$ is always $2k - \omega$, because $2k - \omega < 2p + \omega$ for $\omega > k - p$, which is always fulfilled due to the lower boundary of the ω -integral, $\omega > \frac{k-p}{2}$. Then the only p -dependence in the integration boundaries of Eq. (C.1) comes from the lower limit of the ω integral.

Therefore, we will be interested in the region $\omega < 0$, where $|\omega|$ is very large. In particular, we will assume $|\omega| > \Lambda_\omega \gg k$ with a new scale Λ_ω , which will lead to simplifications in the matrix element. Additionally, the *Bose-enhanced* term \hat{q}_{ff} that includes $f(\mathbf{k})f(\mathbf{k}')$ does not contribute in this limit, since $f(\mathbf{k}') \approx 0$. Focusing only on relevant terms, i.e., disregarding the k -integral since it cannot contribute to any large p behavior, we analyze

$$\hat{q} \sim \int_{-\frac{p-k}{2}}^{-\Lambda_\omega} d\omega \int_{|\omega|}^{2k-\omega} dq q^2 (1 - \cos^2 \theta_{qp}) \frac{|\mathcal{M}_{gg}^{gg}|^2}{p^2}. \quad (\text{C.2})$$

C.1 THE INTEGRAND OF \hat{q} FOR LARGE p

Now let us expand the integrand in (C.2) for large p explicitly.

C.1.1 The large p limit of $\cos \theta_{qp}$

First, we consider $\cos \theta_{qp}$ in the limit $p \rightarrow \infty$. Our starting point is Eq. (4.19b),

$$\cos \theta_{qp} = \frac{1}{q} \left(\omega + \frac{\omega^2 - q^2}{2p} \right). \quad (\text{C.3})$$

Using Eq. (4.11), i.e., $q < 2k - \omega$, one has

$$\frac{q^2 - \omega^2}{2p} < \frac{4k(k - \omega)}{2p} \ll |\omega|, \quad (\text{C.4})$$

which leads for $p \rightarrow \infty$ to,

$$\cos \theta_{qp} = \frac{\omega}{q}, \quad (\text{C.5})$$

where the neglected terms are $\mathcal{O}(k/p)$. However, considering the term $1 - \cos^2 \theta_{qp}$ that appears in (C.2) is more subtle, because the seemingly leading term in a $1/p$ expansion, ω/q , can get close to unity, $|\omega| < q$. This leads to the corrections

$$\begin{aligned} 1 - \cos^2 \theta_{qp} &= 1 - \frac{\omega^2}{q^2} + \frac{\omega(q^2 - \omega^2)}{pq^2} + \dots \\ &= \left(1 - \frac{\omega^2}{q^2}\right) \left(1 + \frac{\omega}{p} + \dots\right), \end{aligned} \quad (\text{C.6})$$

and the correction term ω/p could possibly become large at the lower boundary of the ω integral, $\omega > -(p - k)/2$. Thus, in the limit $k/p \rightarrow 0$, $\cos \theta_{qp} \rightarrow \omega/q$, but $1 - \cos^2 \theta_{qp} \not\rightarrow 1 - \omega^2/q^2$.

C.1.2 Matrix element for large $|\omega|$

For large $|\omega|$, and therefore also large q (from Eq. (C.2)), we do not need to take into account screening effects $\mathcal{O}(m_D)$ in the matrix element, such that (4.33) reduces to $M_{\text{screen}} \approx M_0 = (s - u)^2/t^2$. The contribution from the transverse propagator in the sum in (4.33) is negligible for large $|\omega|$, and we are left with

$$\frac{|\mathcal{M}_{gg}^{gg}|^2}{g^4 p^2} = 16d_A C_A^2 \frac{\omega^2}{q^4} \left(1 + \frac{\omega}{p} + \dots\right). \quad (\text{C.7})$$

Collecting the pieces, we can rewrite the relevant integrand in (C.2) as

$$q^2(1 - \cos^2 \theta_{qp}) \frac{|\mathcal{M}_{gg}^{gg}|^2}{g^4 p^2} = 16d_A C_A^2 \frac{(q^2 - \omega^2)\omega^2}{q^4} \left(1 + \frac{2\omega}{p} + \dots\right). \quad (\text{C.8})$$

C.1.3 Integral over a more generic integrand

The integrand, which is relevant for determining the large p dominant behavior for \hat{q} , is a sum of terms $q^n \omega^m$, as can be seen from (C.8). Therefore, let us analyze

a general integrand of this form and define the integral I_{nm} (which should not be confused with Eq. (4.74) in Section 4.2.1),

$$I_{nm}(p) = \int_{-\frac{p-k}{2}}^{-\Lambda_\omega} d\omega \int_{-\omega}^{2k-\omega} dq q^n \omega^m. \quad (\text{C.9})$$

Although $|\omega| \gg 2k$, we cannot neglect $2k$ in the upper integration boundary of the q -integral (because it will be important later on), which additionally complicates the analysis. Using $\tilde{\omega} = -\omega > 0$ to get rid of additional minus signs, we obtain for $n \neq -1$

$$I_{nm}(p) = (-1)^m \int_{\Lambda_\omega}^{\frac{p-k}{2}} d\tilde{\omega} \int_{\tilde{\omega}}^{2k+\tilde{\omega}} dq q^n x^m, \quad (\text{C.10})$$

$$= \frac{(-1)^m}{n+1} \int_{\Lambda_\omega}^{\frac{p-k}{2}} d\tilde{\omega} x^m [(2k+\tilde{\omega})^{n+1} - \tilde{\omega}^{n+1}]. \quad (\text{C.11})$$

We expand the first term in a power series using the Binomial series

$$(x+y)^r = \sum_{k=0}^{\infty} \binom{r}{k} x^{r-k} y^k, \quad x, y \in \mathbb{R}, \quad (\text{C.12})$$

with $|x| > |y|$ and $r \in \mathbb{C}$. We thus obtain

$$I_{nm} = \frac{(-1)^m}{n+1} \int_{\Lambda_\omega}^{\frac{p-k}{2}} d\tilde{\omega} \tilde{\omega}^m \left[\sum_{j=0}^{\infty} \binom{n+1}{j} \tilde{\omega}^{n+1-j} (2k)^j - \tilde{\omega}^{n+1} \right] \\ = \frac{(-1)^m}{n+1} \int_{\Lambda_\omega}^{\frac{p-k}{2}} d\tilde{\omega} \sum_{j=1}^{\infty} \binom{n+1}{j} \tilde{\omega}^{n+m+1-j} (2k)^j \quad (\text{C.13})$$

$$= \frac{(-1)^m}{n+1} \left(\sum_{\substack{j=1 \\ j \neq n+m+2}}^{\infty} \binom{n+1}{j} \frac{\tilde{\omega}^{n+m+2-j}}{n+m+2-j} \bigg|_{\tilde{\omega}=\Lambda_\omega}^{p-k} (2k)^j + \binom{n+1}{n+m+2} \ln \left(\frac{p-k}{2\Lambda_\omega} \right) (2k)^{n+m+2} \right). \quad (\text{C.14})$$

Since we are interested in the behavior at large p , we drop the lower boundary $\tilde{\omega} = \Lambda_\omega$ and take only the leading-order (LO) terms with the largest powers of p into account. Those are obtained for $j = 1$, for which the (generalized) binomial coefficient yields $n+1$. It will be useful to also consider the next-to-leading order (NLO) terms in p . We obtain, up to an additive constant,

$$I_{nm}^{\text{LO}} \simeq \begin{cases} \frac{(-1)^m (2k)}{n+m+1} \left(\frac{p-k}{2} \right)^{n+m+1}, & n+m+1 \neq 0 \\ (-1)^m (2k) \ln(p), & n+m+1 = 0 \end{cases} \quad (\text{C.15a})$$

$$I_{nm}^{\text{NLO}} \simeq \begin{cases} \frac{(-1)^m (2k)^2}{(n+1)(n+m)} \binom{n+1}{2} \left(\frac{p-k}{2} \right)^{n+m}, & n+m \neq 0 \\ \frac{(-1)^m}{n+1} \binom{n+1}{2} (2k)^2 \ln(p), & n+m = 0. \end{cases} \quad (\text{C.15b})$$

Note that the inclusion of k in $(p-k)^{n+m+1}$ in the LO term is because it will contribute at NLO.

C.2 BEHAVIOR OF \hat{q} FOR LARGE p

Gathering the results of the previous sections and applying them to the integral of \hat{q} in (C.2) with the integrand (C.8), we obtain

$$\hat{q}^{\text{LO}} \sim I_{-2,2} - I_{-4,4} = (2k)^2 \ln p + \text{const}, \quad (\text{C.16a})$$

$$\hat{q}^{\text{NLO}} \sim \frac{1}{p} (I_{-2,3} - I_{-4,5}) = \text{const} + \mathcal{O}\left(\frac{1}{p}\right). \quad (\text{C.16b})$$

Note that here NLO denotes the terms proportional to $1/p$ in the integrand. For both cases, $n + m$ is constant, thus the leading terms (C.15a) cancel and we need the next-to-leading terms (C.15b). We observe that, due to the logarithmic enhancement of the leading-order contributions \hat{q}^{LO} , the next-to-leading order contributions \hat{q}^{NLO} become negligible¹ for sufficiently large p , and \hat{q} can be written in the form of Eq. (4.42),

$$\hat{q}(p \gg Q) \simeq a_p \ln p + b_p. \quad (\text{C.17})$$

Therefore, for sufficiently large jet momenta p , it is in principle enough to expand the matrix element and the integrand for large p and take only the leading-order contribution in p . Note, however, that to obtain the constant term it is not enough to use the leading large p behavior, but one must use the full matrix element.

Let us now calculate the coefficient of the logarithm, a_p . Until now, we have not considered the exact form of the distribution function $f(\mathbf{k})$ and merely used that it provides an upper cutoff for the k integral. The numerical value of the coefficient a_p will depend on the exact form of $f(\mathbf{k})$.

Let us consider a gluon jet scattering off a gluon in the plasma and start with Eq. (4.21),

$$\hat{q} \simeq \frac{16g^4 C_A^2}{2^{10} \pi^5} \int_0^{2\pi} d\phi_{pq} \int_0^{2\pi} d\phi_{qk} \int_0^\infty dk \int_{-\frac{p-k}{2}}^k d\omega \int_{|\omega|}^{2k-\omega} dq f(\mathbf{k}) \frac{\omega^2 (q^2 - \omega^2)}{q^4}, \quad (\text{C.18})$$

where we have taken the leading term in the large p integrand (C.8) that leads to the logarithmic behavior. Additionally, as explained below Eq. (C.1), it is sufficient to use $2k - \omega$ as the upper boundary of the q -integral.

In comparison to the general integrand we analysed in Eq. (C.9), there appears also the distribution function $f(\mathbf{k}) = f(k, \cos \theta_k)$, and the angle depends on $\cos \theta_{qk}$ and $\cos \theta_{qp}$ as well, which are functions of ω and q . For the large p behavior, we are interested in the region $|\omega| \gg k$ and $q \sim |\omega|$, which renders $v_{pq} \rightarrow -1$. For v_{kq} , however, we cannot make a definite statement, since it changes from -1 to 1 when q varies between its integration boundaries $|\omega| < q < 2k - \omega$. Therefore, we will restrict to isotropic distributions $f(k)$ here that only depend on the magnitude of \mathbf{k} . Then, the ω and q integrations in Eq. (C.18) are given by Eq. (C.16a).

¹ This is not a trivial statement: for an integrand $q^n \omega^m (1 + \omega/p)$ with $n + m > 0$, we would obtain $\frac{\hat{q}^{\text{NLO}}}{\hat{q}^{\text{LO}}} = \frac{\frac{1}{p} (a p^{n+m+2} + b)}{c p^{n+m+1} + e} \sim \frac{a}{c} + \mathcal{O}\left(\frac{1}{p}\right)$, thus the ratio NLO/LO does not tend to 0 for $p \rightarrow \infty$. This implies that multiplying the LO term with ω/p and integrating over it yields a term of the same order as the LO term.

For an isotropic plasma consisting of quarks and gluons with distributions f_q and f_g , the coefficient a_p is then given by Eq. (4.43),

$$a_p/C_R = \frac{C_A g^4}{4\pi^3} \int_0^\infty dk k^2 f_g(k) + \sum_f \frac{g^4}{8\pi^3} \int_0^\infty dk k^2 f_q(k). \quad (\text{C.19})$$

In thermal equilibrium, this reduces to

$$\frac{a_p^{\text{eq}}}{C_R} = \frac{g^4 \zeta(3) T^3}{2\pi^3} \left(N_c + \frac{3}{4} n_f \right). \quad (\text{C.20})$$

This logarithmic behavior of \hat{q}^{LO} implies that the limit $p \rightarrow \infty$ requires a UV cutoff to render \hat{q} finite. This is typically done by restricting the transverse momentum transfer, $q_\perp < \Lambda_\perp$. We will verify in the next section that in this limit, \hat{q} is finite, and we only need to consider the leading-order term in p in the integrand.

C.2.1 Large p behavior combined with a transverse momentum cutoff

Using a transverse momentum cutoff, $q_\perp < \Lambda_\perp \ll p$, we can retrace the steps in the previous sections. For large p , apart from factors $\mathcal{O}(1/p)$, this amounts to $q_\perp^2 = q^2 - \omega^2 < \Lambda_\perp^2$ (c.f., (4.44)), and thus we modify I_{nm} to

$$I_{nm}(p) = \int_{-\frac{p-k}{2}}^{-\Lambda_\omega} d\omega \int_{-\omega}^{\sqrt{\omega^2 + \Lambda_\perp^2}} dq q^n \omega^m. \quad (\text{C.21})$$

The upper limit in the q integral replaces $2k - \omega$ in Eq. (C.9) for sufficiently large Λ_ω because $\sqrt{\omega^2 + \Lambda_\perp^2} < 2k - \omega$ for $-\omega > \frac{\Lambda_\perp^2}{4k} - k$, which, since $-\omega > \Lambda_\omega$, can always be fulfilled by choosing

$$\Lambda_\omega > \frac{\Lambda_\perp^2}{4k} - k. \quad (\text{C.22})$$

Similarly as before, with $\tilde{\omega} = -\omega$ and for $n \neq -1$, we obtain

$$I_{nm}(p) = \frac{(-1)^m}{n+1} \int_{\Lambda_\omega}^{\frac{p-k}{2}} d\tilde{\omega} \tilde{\omega}^m \left[(\tilde{\omega}^2 + \Lambda_\perp^2)^{\frac{n+1}{2}} - \tilde{\omega}^{n+1} \right]. \quad (\text{C.23})$$

For the convergence of the Binomial series (C.12), we need to check that $\Lambda_\perp^2 < \tilde{\omega}^2$, which follows from (C.22),² and thus,

$$\begin{aligned} I_{nm} &= \frac{(-1)^m}{n+1} \int_{\Lambda_\omega}^{\frac{p-k}{2}} d\tilde{\omega} \sum_{j=1}^{\infty} \binom{(n+1)/2}{j} \tilde{\omega}^{n+m+1-2j} (\Lambda_\perp)^{2j} \\ &= \frac{(-1)^m}{n+1} \left[\sum_{\substack{j=1 \\ j \neq (n+m+2)/2}}^{\infty} \binom{(n+1)/2}{j} \frac{\tilde{\omega}^{n+m+2-2j}}{n+m+2-2j} \Big|_{\tilde{\omega}=\Lambda_\omega}^{\frac{p-k}{2}} \Lambda_\perp^{2j} + \binom{(n+1)/2}{(n+m+2)/2} \ln \left(\frac{p-k}{2\Lambda_\omega} \right) \Lambda_\perp^{n+m+2} \right]. \end{aligned} \quad (\text{C.24})$$

² We know that $\Lambda_\perp^2 < 4k\Lambda_\omega \left(1 + \frac{k}{\Lambda_\omega} \right) \approx 4k\Lambda_\omega$ and thus $\Lambda_\perp^2/\Lambda_\omega^2 < \frac{4k}{\Lambda_\omega} \ll 1$, which makes $\Lambda_\perp < \Lambda_\omega$ and thus $\Lambda_\perp < \tilde{\omega}$.

We now obtain, up to an additive constant (in p),

$$I_{nm}^{\text{LO}} = \begin{cases} \frac{(-1)^m \Lambda_\perp^2}{2(n+m)} \left(\frac{p-k}{2}\right)^{n+m}, & n+m \neq 0 \\ (-1)^m \Lambda_\perp^2 \ln(p), & n+m = 0 \end{cases} \quad (\text{C.26})$$

$$I_{nm}^{\text{NLO}} = \begin{cases} \frac{(-1)^m \Lambda_\perp^4 B}{(n+1)(n+m-2)} \left(\frac{p-k}{2}\right)^{n+m-2}, & n+m-2 \neq 0 \\ \frac{(-1)^m}{n+1} B \Lambda_\perp^4 \ln(p), & n+m-2 = 0, \end{cases} \quad (\text{C.27})$$

where $B = \binom{(n+1)/2}{2}$. In this case, denoting again with NLO the terms proportional to $1/p$ in the integrand, we obtain

$$\hat{q}^{\text{LO}} \sim I_{-2,2} - I_{-4,4} \sim \text{const} + \mathcal{O}\left(\frac{1}{p^2}\right), \quad (\text{C.28a})$$

$$\hat{q}^{\text{NLO}} \sim \frac{1}{p} (I_{-2,3} - I_{-4,5}) \sim \frac{\text{const}}{p} + \mathcal{O}\left(\frac{1}{p^2}\right). \quad (\text{C.28b})$$

Thus, with a transverse momentum cutoff Λ_\perp in place, we can explicitly take the limit of infinite jet momentum, $p \rightarrow \infty$, and obtain a finite jet quenching parameter \hat{q} . Moreover, it is then sufficient to take the leading-order terms in the integrand (in particular the matrix elements) in an expansion in $1/p$.

C.2.2 Large momentum cutoff Λ_\perp behavior

Removing the momentum cutoff, i.e. taking $\Lambda_\perp \rightarrow \infty$, leads to a divergent jet quenching parameter \hat{q} . It is reasonable to assume that this divergence will be logarithmic, as it is for finite but large jet momentum. We will now show this explicitly and calculate the coefficient of the logarithm.

We continue working in the limit $p \rightarrow \infty$, and thus take only the leading-order terms in p in the integrand into account. For that we start with Eq. (4.12) with explicit step-functions and perform the coordinate transformation in Eq. (4.59) to integrate over \mathbf{q}_\perp ,

$$\hat{q} \sim \int_0^\infty dk \int_{q_\perp < \Lambda_\perp} d^2 \mathbf{q}_\perp \int_{-\infty}^{k - \frac{q_\perp^2}{4k}} d\omega q_\perp^2 f(\mathbf{k}) (1 \pm f(\mathbf{k}')) \frac{|\mathcal{M}_{gg}^{\text{gg}}|^2}{p^2 \sqrt{q_\perp^2 + \omega^2}}, \quad (\text{C.29})$$

where we have not included the angular integrals.

The behavior for large Λ_\perp is of course dominated by the upper integration boundary of the q_\perp integral. For large Λ_\perp , we now split the integral into a part $0 < q_\perp < \Lambda_\omega$ and $\Lambda_\omega < q_\perp < \Lambda_\perp$. We can choose the scale $\Lambda_\omega \gg k$, such that $q_\perp \gg k$, since the momentum k has a natural upper cutoff coming from the distribution function $f(\mathbf{k})$. Then, also $|\omega| > \frac{q_\perp^2}{4k} - k$ must be very large and thus $f(\mathbf{k}') \approx 0$. Hence we arrive at the scale separation

$$|\omega| \gg q_\perp \gg k. \quad (\text{C.30})$$

Using this for the integrand (C.8), we obtain

$$\hat{q} \sim \int_{\Lambda_\omega}^{\Lambda_\perp} dq_\perp q_\perp \int_{-\infty}^{k - \frac{q_\perp^2}{4k}} d\omega q_\perp^2 \frac{1}{|\omega|^3} \approx 8k^2 \int_{\Lambda_\omega}^{\Lambda_\perp} dq_\perp \frac{q_\perp^3}{q_\perp^4} = 8k^2 \ln \Lambda_\perp + \text{const} \quad (\text{C.31})$$

We have thus shown that we can write \hat{q} in that limit as in Eq. (4.50),

$$\hat{q}(\Lambda_\perp \gg Q) \simeq a_{\Lambda_\perp} \ln \Lambda_\perp + b_{\Lambda_\perp}. \quad (\text{C.32})$$

It is also possible to determine the coefficient of $\ln \Lambda_\perp$, similarly as in Appendix D. While in Ref. [2], this was only done for isotropic systems, it is actually quite straightforward to generalize this to anisotropic system if one starts from the collision kernel, which we consider in more detail in Chapter 8.

Starting from the general expression (7.5),

$$C(\mathbf{q}_\perp) = \frac{1}{2p\nu} \sum_{bcd} \int \frac{d^3\mathbf{k}}{(2\pi)^3} dq_z \frac{|\mathcal{M}_{cd}^{ab}(\mathbf{p}, \mathbf{k}; \mathbf{p} + \mathbf{q}, \mathbf{k} - \mathbf{q})|^2}{8|\mathbf{k}||\mathbf{k} - \mathbf{q}||\mathbf{p} + \mathbf{q}|} \times f(\mathbf{k})(1 + f(\mathbf{k} - \mathbf{q}))\delta(p + |\mathbf{k}| - |\mathbf{p} + \mathbf{q}| - |\mathbf{k} - \mathbf{q}|), \quad (\text{C.33})$$

we take the limit of large q_\perp following Section 7.1.3. Using

$$\delta(k - q_z - |\mathbf{k} - \mathbf{q}|) \rightarrow \frac{q_\perp^2}{2(k - k_z)^2} \delta(q_z - \frac{\mathbf{q}_\perp \cdot \mathbf{k}_\perp - q_\perp^2/2}{k - k_z}), \quad (\text{C.34})$$

and the form for the matrix elements

$$|\mathcal{M}_{gg}^{gg}|^2 = 16g^4 d_A C_A^2 \frac{4p^2(k - k_z)^2}{q_\perp^4}, \quad |\mathcal{M}_{gq}^{gq}|^2 = 16g^4 d_F C_F C_A \frac{4p^2(k - k_z)^2}{q_\perp^4}, \quad (\text{C.35})$$

we obtain

$$C(q_\perp \gg T_\varepsilon) = \frac{2C_R g^4}{q_\perp^4} \int \frac{d^3\mathbf{k}}{(2\pi)^3} \left(1 - \frac{k_z}{k}\right) \left(N_c f_g(\mathbf{k}) + \frac{1}{2} \sum_f f_f(\mathbf{k})\right), \quad (\text{C.36})$$

where, according to our symmetry arguments (3.72), the term proportional to k_z/k vanishes. Integrating this to obtain \hat{q} , we obtain

$$\hat{q}(\Lambda_\perp \gg T_\varepsilon) \simeq \frac{C_R g^4}{\pi} \int \frac{d^3\mathbf{k}}{(2\pi)^3} \left(N_c f_g(\mathbf{k}) + \frac{1}{2} \sum_f f_f(\mathbf{k})\right) \log \Lambda_\perp + \text{const} \quad (\text{C.37})$$

For a plasma consisting of quarks and gluons with distributions f_q and f_g .

For isotropic systems, we obtain

$$\frac{a_{\Lambda_\perp}}{C_R} = \frac{N_c g^4}{2\pi^3} \int_0^\infty dk k^2 f_g(k) + \sum_f \frac{g^4}{4\pi^3} \int_0^\infty dk k^2 f_f(k), \quad (\text{C.38})$$

which reduces for thermal distributions to

$$\frac{a_{\Lambda_\perp}^{\text{eq}}}{C_R} = \frac{g^4 \zeta(3) T^3}{\pi^3} \left(N_c + \frac{3}{4} n_f\right). \quad (\text{C.39})$$

This nicely agrees with Eq. (4.77a) that stems from [101].

D

NUMERICAL DETAILS ON SOLVING THE AMY RATE EQUATIONS

In this Appendix, more details are provided on the numerical method used to solve the integral equation (7.55),

$$2\mathbf{h} = i\delta E(\mathbf{h})\mathbf{F}(\mathbf{h}) + \frac{1}{2} \int \frac{d^2\mathbf{q}_\perp}{(2\pi)^2} C(\mathbf{q}_\perp) \times [(3\mathbf{F}(\mathbf{h}) - \mathbf{F}(\mathbf{h} - p\mathbf{q}_\perp) - \mathbf{F}(\mathbf{h} - k\mathbf{q}_\perp) - \mathbf{F}(\mathbf{h} + p'\mathbf{q}_\perp)], \quad (\text{D.1})$$

with $\delta E(\mathbf{h}) = m_D^2/4 \times (1/k + 1/p - 1/p') + h^2/(2pkp')$. This needs to be solved for the function $F(\mathbf{h})$, which enters the rate via Eq. (7.54)

$$\gamma = \frac{p^4 + p'^4 + k'^4}{p^3 p'^3 k'^3} \frac{d_A \alpha_s}{2(2\pi)^3} \int \frac{d^2\mathbf{h}}{(2\pi)^2} 2\mathbf{h} \cdot \text{Re}\mathbf{F}, \quad (\text{D.2})$$

While in this thesis, the purely gluonic case is considered, quarks can be included by taking different color factors in (D.1) and different vacuum splitting functions in (D.2).

D.1 EQUATIONS AND BOUNDARY CONDITIONS

First, we transform the integral equation to impact parameter space using the Fourier transformed quantities,

$$\mathbf{F}(\mathbf{x}) = \int \frac{d^2\mathbf{h}}{(2\pi)^2} e^{i\mathbf{x} \cdot \mathbf{h}} \mathbf{F}(\mathbf{h}), \quad \mathbf{F}(\mathbf{h}) = \int d^2\mathbf{x} e^{-i\mathbf{x} \cdot \mathbf{h}} \mathbf{F}(\mathbf{x}), \quad (\text{D.3})$$

$$\tilde{C}(\mathbf{x}) = \int \frac{d^2\mathbf{q}_\perp}{(2\pi)^2} e^{i\mathbf{x} \cdot \mathbf{q}_\perp} C(\mathbf{q}_\perp). \quad (\text{D.4})$$

Here, I have introduced a tilde on the Fourier-transformed collision kernel because it is more convenient to think of the object

$$C(\mathbf{x}) = \tilde{C}(0) - \tilde{C}(\mathbf{x}) = \int \frac{d^2\mathbf{q}_\perp}{(2\pi)^2} (1 - e^{i\mathbf{x} \cdot \mathbf{q}_\perp}) C(\mathbf{q}_\perp). \quad (\text{D.5})$$

With the abbreviations

$$A = im(z, P) = i \left(\frac{m_{\infty, z}^2}{2zP} + \frac{m_{\infty, (1-z)}^2}{2(1-z)P} - \frac{m_{\infty, 1}^2}{2P} \right), \quad B = \frac{i}{2Pz(1-z)} \quad (\text{D.6})$$

we may rewrite the integral equation (D.1) into the shorter form

$$2\mathbf{h} = \mathbf{F}(\mathbf{h})(A + B\mathbf{h}^2) + \frac{1}{2} \int \frac{d^2\mathbf{q}}{(2\pi)^2} C(\mathbf{q}) \{3\mathbf{F}(\mathbf{h}) - \mathbf{F}(\mathbf{h} - \mathbf{q}) - \mathbf{F}(\mathbf{h} - z\mathbf{q}) - \mathbf{F}(\mathbf{h} - (1-z)\mathbf{q})\}. \quad (\text{D.7})$$

Note that $A, B \in \mathbb{C}$ but purely imaginary such that $iA \in \mathbb{R}$, $A/B \in \mathbb{R}$.

Inserting now the Fourier transforms (D.3), we obtain Eq. (7.56) in impact parameter space,

$$(A - D(z, \mathbf{x}) - B\nabla^2)\mathbf{F}(\mathbf{x}) = -2i\nabla\delta(\mathbf{x}), \quad (\text{D.8})$$

where we have introduced the function

$$D(z, \mathbf{x}) = -\frac{1}{2}(C(\mathbf{x}) + C((1-z)\mathbf{x}) + C((1-z)\mathbf{x})). \quad (\text{D.9})$$

Methods to solve this equation for isotropic $D(z, b)$ have been described in Refs. [110, 231]. Building on these previous methods, I describe here the method used in this thesis to solve this equation for any anisotropic $D(\mathbf{b}) = D(b, \phi)$.

First, note that the delta function can be seen as imposing a boundary condition on \mathbf{F} , which can be seen by considering the most singular terms

$$-2i\nabla\delta(\mathbf{x}) = -B\nabla^2\mathbf{F}(\mathbf{x}). \quad (\text{D.10})$$

This is solved by going to Fourier space, where we can use

$$\delta(\mathbf{x}) = \int \frac{d^2\mathbf{q}_\perp}{(2\pi)^2} e^{i\mathbf{q}_\perp \cdot \mathbf{x}}, \quad (\text{D.11})$$

such that $\mathbf{F}(q_\perp) = 2\frac{\mathbf{q}_\perp}{Bq_\perp^2}$. The backward Fourier transform can be done using the parameterization $\mathbf{x} = |\mathbf{x}|(\cos\phi_x, \sin\phi_x)$, $\mathbf{q}_\perp = q_\perp(\cos\phi_q, \sin\phi_q)$,

$$\int d^2\mathbf{q}_\perp \frac{\mathbf{q}_\perp}{q_\perp^2} e^{i\mathbf{x} \cdot \mathbf{q}_\perp} = |\mathbf{x}| \int_0^{2\pi} d\phi_q \int_0^\infty dq_\perp \begin{pmatrix} \cos\phi_q \\ \sin\phi_q \end{pmatrix} e^{i|\mathbf{x}|q_\perp \cos(\phi_q - \phi_x)} \quad (\text{D.12})$$

$$= |\mathbf{x}| \int_0^{2\pi} d\tilde{\phi}_q \int_0^\infty dq_\perp \begin{pmatrix} \cos(\tilde{\phi}_q + \phi_x) \\ \sin(\tilde{\phi}_q + \phi_x) \end{pmatrix} e^{i|\mathbf{x}|q_\perp \cos\tilde{\phi}_q} \quad (\text{D.13})$$

$$= |\mathbf{x}| \int_0^{2\pi} d\tilde{\phi}_q \int_0^\infty dq_\perp \begin{pmatrix} \cos\phi_x \cos\tilde{\phi}_q - \sin\phi_x \sin\tilde{\phi}_q \\ \sin\phi_x \cos\tilde{\phi}_q + \cos\phi_x \sin\tilde{\phi}_q \end{pmatrix} e^{i|\mathbf{x}|q_\perp \cos\tilde{\phi}_q}, \quad (\text{D.14})$$

$$= 2\pi i \frac{\mathbf{x}}{\mathbf{x}^2} \quad (\text{D.15})$$

where we used

$$\int_0^{2\pi} d\phi \cos\phi e^{i|\mathbf{x}|q_\perp \cos\phi} = 2\pi i J_1(q_\perp |\mathbf{x}|), \quad \int_0^{2\pi} d\phi \sin\phi e^{i|\mathbf{x}|q_\perp \cos\phi} = 0. \quad (\text{D.16})$$

Eq. (D.10) (and the full differential equation (D.8)) is thus solved by

$$\lim_{|\mathbf{x}| \rightarrow 0} \mathbf{F}(\mathbf{x}) = \frac{i}{B\pi} \frac{\mathbf{x}}{\mathbf{b}^2}. \quad (\text{D.17})$$

This we can take as a boundary condition and solve Eq. (D.8) for $|\mathbf{x}| > 0$.

Next, we redefine $\mathbf{F} = |\mathbf{x}|\mathbf{g} = |\mathbf{x}|(g_x, g_y)$, for which the differential equation becomes

$$\left[\frac{A - D(|\mathbf{x}|, \phi)}{B} - \partial_{|\mathbf{x}|}^2 - \frac{3}{|\mathbf{x}|} \partial_{|\mathbf{x}|} - \frac{1}{\mathbf{x}^2} - \frac{1}{\mathbf{x}^2} \partial_\phi^2 \right] \mathbf{g}(|\mathbf{x}|, \phi) = 0. \quad (\text{D.18})$$

This redefinition has the advantage that the real part of the integral appearing in (D.2) can be obtained by the function \mathbf{g} evaluated at $\mathbf{x} \rightarrow 0$.

$$\int \frac{d^2 \mathbf{h}}{(2\pi)^2} \text{Re}(\mathbf{h} \cdot \mathbf{F}(\mathbf{h})) = \text{Re} \int \frac{d^2 \mathbf{h}}{(2\pi)^2} \int d^2 \mathbf{x} e^{-i\mathbf{x} \cdot \mathbf{h}} \mathbf{F}(\mathbf{x}) \cdot \mathbf{h} \quad (\text{D.19})$$

$$= \text{Re} \int \frac{d^2 \mathbf{h}}{(2\pi)^2} \int d^2 \mathbf{x} (i\nabla_x) e^{-i\mathbf{x} \cdot \mathbf{h}} \cdot \mathbf{F}(\mathbf{x}) \quad (\text{D.20})$$

$$= \text{Re} \int \frac{d^2 \mathbf{h}}{(2\pi)^2} \int d^2 \mathbf{x} e^{-i\mathbf{x} \cdot \mathbf{h}} (-i\nabla \cdot \mathbf{F}(\mathbf{x})) \quad (\text{D.21})$$

$$= \text{Re} (-i\nabla \cdot \mathbf{F}(\mathbf{x}))_{\mathbf{x}=0} \quad (\text{D.22})$$

$$= \text{Im} (\nabla \cdot \mathbf{F}(\mathbf{x}))_{\mathbf{x}=0} \quad (\text{D.23})$$

$$= \text{Im} \left[\frac{g_x(0)}{\cos \phi} + \frac{g_y(0)}{\sin \phi} \right]. \quad (\text{D.24})$$

For the angular information, we decompose \mathbf{g} in its Fourier modes,

$$\mathbf{g}(|\mathbf{x}|, \phi) = \sum_n \mathbf{g}_n(|\mathbf{x}|) e^{in\phi}, \quad (\text{D.25})$$

$$D(|\mathbf{x}|, \phi) = \sum_m D_m(|\mathbf{x}|) e^{im\phi}, \quad (\text{D.26})$$

$$D_m(|\mathbf{x}|) = \frac{1}{2\pi} \int_0^{2\pi} d\phi e^{-im\phi} D(|\mathbf{x}|, \phi). \quad (\text{D.27})$$

In terms of these Fourier modes \mathbf{g}_n , the differential equation becomes

$$\left[\frac{A}{B} - \partial_b^2 - \frac{3}{|\mathbf{x}|} \partial_b + \frac{n^2 - 1}{\mathbf{x}^2} \right] \mathbf{g}_n(|\mathbf{x}|) = \sum_m \frac{D_m(|\mathbf{x}|)}{B} \mathbf{g}_{n-m}(|\mathbf{x}|) \quad (\text{D.28})$$

Note that the boundary condition (D.17) only affects the modes $n = \pm 1$, which can be seen by rewriting Eq. (D.17) using exponential functions,

$$\lim_{|\mathbf{x}| \rightarrow 0} \mathbf{g}(|\mathbf{x}|, \phi) = \frac{1}{2B\pi} \frac{1}{\mathbf{x}^2} \begin{pmatrix} i(e^{i\phi} + e^{-i\phi}) \\ e^{i\phi} - e^{-i\phi} \end{pmatrix}. \quad (\text{D.29})$$

This fixes the small $|\mathbf{x}|$ limit of $\mathbf{g}_{\pm 1}$. In the isotropic limit, $D_m \sim \delta_{m0}$ and does not couple different Fourier modes. Therefore, in this isotropic limit, only the modes for $m = \pm 1$ need to be solved for.

Let us now consider the case of small $|\mathbf{x}|$, where $D \sim \mathbf{x}^2 \log |\mathbf{x}|$ can be neglected against A , i.e., $|D_m(|\mathbf{x}|)| \ll |A|$. In this region, Eq. (D.28) can be solved analytically,

$$\mathbf{g}_n(|\mathbf{x}|) = \frac{\mathbf{c}_1 I_{|n|}(|\mathbf{x}| \sqrt{A/B}) + \mathbf{c}_2 K_{|n|}(|\mathbf{x}| \sqrt{A/B})}{|\mathbf{x}|}, \quad (\text{D.30})$$

where I_n and K_n are the modified Bessel functions of the first and second kind. Thus, at small x , the general solution is given by the linear combination

$$\mathbf{g}(|\mathbf{x}|, \phi) = \sum_n e^{in\phi} \frac{\mathbf{c}_I^n I_{|n|}(|\mathbf{x}| \sqrt{A/B}) + \mathbf{c}_K^n K_{|n|}(|\mathbf{x}| \sqrt{A/B})}{|\mathbf{x}|}. \quad (\text{D.31})$$

In practice, we will need to truncate the series, and only consider modes with $-n_{\max} \leq n \leq n_{\max}$, leading to $n_{\text{fourier}} = 2n_{\max} + 1$ different Fourier modes for every component of $\mathbf{g} = (g_x, g_y)$. We then have $2(2n_{\max} + 1)$ linearly independent solutions at small $|\mathbf{x}|$. For a general solution, we thus need $2(2n_{\max} + 1)$ boundary conditions.

Eq. (D.28) is a coupled system of $2n_{\max} + 1$ ordinary second-order differential equations, for which we need $2(2n_{\max} + 1)$ boundary conditions, which fix all the c_I^n and c_K^n uniquely. One natural boundary condition to impose is regularity at infinity [231],

$$\lim_{|\mathbf{x}| \rightarrow \infty} \mathbf{g}_n(|\mathbf{x}|) = 0, \quad (\text{D.32})$$

which yields $2n_{\max} + 1$ conditions for every component of \mathbf{g} . We also have the boundary condition (D.29) at small $|\mathbf{x}|$. To achieve that, we expand the Bessel functions for small $|\mathbf{x}|$,

$$I_n(|\mathbf{x}|)/|\mathbf{x}| \sim |\mathbf{x}|^{n-1}(1 + \mathcal{O}(|\mathbf{x}|)), \quad K_n(|\mathbf{x}|)/|\mathbf{x}| \sim |\mathbf{x}|^{n-1}(1 + \mathcal{O}(|\mathbf{x}|)) + \#|\mathbf{x}|^{-n-1}(1 + \mathcal{O}(|\mathbf{x}|)). \quad (\text{D.33})$$

Comparing with (D.17), we conclude that this fixes $c_K^{\pm 1}$ (2 additional conditions per component of \mathbf{g}). Furthermore, no function may diverge more quickly than $1/x^2$ at the origin, which fixes $c_K^m = 0$ for $m \geq 2$, resulting in $2(n_{\max} - 1)$ additional conditions per component of \mathbf{g} . With that we are missing one (complex) boundary condition to determine the system completely¹. Since we are interested in the imaginary part of the constant to which \mathbf{g}_n converges (see Eq. (D.24)) for $|\mathbf{x}| \rightarrow 0$, and since both $K_0/|\mathbf{x}|$ and $I_0/|\mathbf{x}|$ diverge in that limit, we can use one complex (or two real) boundary conditions to set $\text{Im } \mathbf{c}_I^0 = \text{Im } \mathbf{c}_K^0 = 0$. To summarize, the boundary conditions are given by

$$\lim_{|\mathbf{x}| \rightarrow \infty} \mathbf{g}_n(\mathbf{x}) = \mathbf{0}, \quad (\text{D.34a})$$

$$\mathbf{c}_K^1 = \frac{\sqrt{A/B}}{2B\pi} \begin{pmatrix} i \\ 1 \end{pmatrix}, \quad (\text{D.34b})$$

$$\mathbf{c}_K^{-1} = \frac{\sqrt{A/B}}{2B\pi} \begin{pmatrix} i \\ -1 \end{pmatrix}, \quad (\text{D.34c})$$

$$\text{Re } \mathbf{c}_I^0 = \mathbf{0}, \quad (\text{D.34d})$$

$$\text{Re } \mathbf{c}_K^0 = \mathbf{0}, \quad (\text{D.34e})$$

where the \mathbf{c}_I and \mathbf{c}_K coefficients are given by the small x approximation of the full solution.

¹ An interested reader might ask if excluding the $n = 0$ modes would solve the problem: This would reduce the number of independent solutions by 2, and the system would then be overdetermined.

To solve the differential equation with these boundary conditions, we make use of the fact that since it is a linear homogeneous equation, any linear combination also solves the equation. We thus solve m linearly independent systems $\{\mathbf{g}_n^{(m)}\}$ with m linearly independent initial conditions

$$\mathbf{c}_K^n = 0, \quad |n| \geq 2, \quad (\text{D.35})$$

and initialize every system with exactly one nonzero coefficient. This leads to $2(2n_{\max} + 1) - 2(n_{\max} - 2) = 2n_{\max} + 6$ linearly independent sets of solutions $\{\mathbf{g}_n^{(m)}\}$. The full solution may be obtained by superimposing

$$\mathbf{g}(|\mathbf{x}|, \phi) = \sum_m \mathbf{a}_m g_n^{(m)}(|\mathbf{x}|, \phi), \quad (\text{D.36})$$

by choosing the coefficients \mathbf{a}_m such that the boundary condition (D.34) is fulfilled. We have now put the information of the vector components of \mathbf{g} into the coefficients \mathbf{a}_m . The advantage of that is that we only need to solve the m systems once, and can then obtain two different sets of coefficients $\{a_m^x, a_m^y\}$. In practice, this leads to a linear system for \mathbf{a}_m ,

$$\sum_m \mathbf{a}_m \lim_{|\mathbf{x}| \rightarrow \infty} g_n^{(m)}(|\mathbf{x}|) = 0, \quad (\text{D.37})$$

which can be solved for a sufficiently large x_{\max} , and supplemented by (D.34),

$$\sum_m \mathbf{a}_m g_n^{(m)}(x_{\max}) = 0 \quad (\text{D.38a})$$

$$\sum_m \mathbf{a}_m c_K^{1(m)} = \frac{\sqrt{A/B}}{2B\pi} \begin{pmatrix} i \\ 1 \end{pmatrix}, \quad (\text{D.38b})$$

$$\sum_m \mathbf{a}_m c_K^{-1(m)} = \frac{\sqrt{A/B}}{2B\pi} \begin{pmatrix} i \\ -1 \end{pmatrix}, \quad (\text{D.38c})$$

$$\sum_m \operatorname{Re} \mathbf{a}_m c_I^{0(m)} = \mathbf{0}, \quad (\text{D.38d})$$

$$\sum_m \operatorname{Re} \mathbf{a}_m c_K^{0(m)} = \mathbf{0}, \quad (\text{D.38e})$$

I have checked explicitly that the results are independent of the choice of x_{\max} .

Every system with index (m) is initialized at a value $x = x_{\min}$, chosen such that $D(x_{\min}, \phi)/A < 0.00001$ with exactly one coefficient $c_{I,K}^n$ (taken to be a scalar not a vector) in Eq. (D.31) nonzero (except for those in Eq. (D.35)). For every system (m) , the system (D.28) is then integrated outwards using a fourth-fifth order Runge Kutta with time stepping until the absolute value of one of the solutions becomes larger than a threshold. Of all the systems, we then take the smallest of the maximum x , and solve the linear system (D.38). For larger n_{\max} , the linear system becomes increasingly difficult to solve numerically, as the `scipy`² routine used to solve the linear system encounters an almost singular matrix. Finally, the solution can be written as

$$\mathbf{g}(|\mathbf{x}|, \phi) = \sum_m \mathbf{a}_m \sum_n e^{in\phi} \frac{c_I^{n(m)} I_{|n|}(|\mathbf{x}| \sqrt{A/B}) + c_K^{n(m)} K_{|n|}(|\mathbf{x}| \sqrt{A/B})}{|\mathbf{x}|}, \quad (\text{D.39})$$

² [237]

where the $c_{I,K}^{n(m)}$ are the initial conditions.

Eventually, the prefactor of the I_1 solution is needed, because in the limit $|\mathbf{x}| \rightarrow 0$, only the $I_1(|\mathbf{x}| \sqrt{A/B}) = \frac{\sqrt{A/B}}{2} + \mathcal{O}(\mathbf{x}^2)$ contribute. Thus, at small $|\mathbf{x}|$,

$$\mathbf{g}(|\mathbf{x}|, \phi) = \sum_m \mathbf{a}_m \frac{\sqrt{A/B}}{2} \left(c_I^{1(m)} e^{i\phi} + c_I^{-1(m)} e^{-i\phi} \right). \quad (\text{D.40})$$

Comparing with (D.24), this clearly induces additional requirements³ on the coefficients $(a_m)_x$ and $(a_m)_y$, which we take as an uncertainty measure for our method. We thus obtain

$$\text{Im } g_x(0)/\cos \phi = \sqrt{A/B} \text{Im} \sum_m (a_m)_x c_I^{1(m)} = \sqrt{A/B} \text{Im} \sum_m (a_m)_x c_I^{-1(m)} \quad (\text{D.41a})$$

$$\text{Im } g_y(0)/\cos \phi = \sqrt{A/B} \text{Im} \left(i \sum_m (a_m)_x c_I^{1(m)} \right) = -\sqrt{A/B} \text{Im} \left(i \sum_m (a_m)_x c_I^{-1(m)} \right). \quad (\text{D.41b})$$

Now I want to briefly discuss that these additional requirements on the coefficients are actually not an additional equation but follow from the system (D.38). To do that, we consider as a toy model the simplified case of first having only 4 sets and only considering the modes $n = \pm 1$. With that assumption, the function $g^{(m)}$ for one set of initial conditions $c_i^{(m)}$ can be written as

$$g^{(m)} = e^{i\phi} (c_1^{(m)} f_1(|\mathbf{x}|) + c_2^{(m)} f_2(|\mathbf{x}|)) + e^{-i\phi} (c_3^{(m)} f_1(|\mathbf{x}|) + c_4^{(m)} f_2(|\mathbf{x}|)). \quad (\text{D.42})$$

As initial conditions, we assume that we use $c_i^{(m)} = \delta_i^m$. In that simplified case, the requirement of vanishing at infinity leads to

$$\begin{aligned} c_1 a_1 + c_2 a_2 + c_3 a_3 + c_4 a_4 &= 0 \\ c_3 a_1 + c_4 a_2 + c_1 a_3 + c_2 a_4 &= 0, \end{aligned} \quad (\text{D.43})$$

where we have used that $g^{(1)}$ and $g^{(3)}$ are similar because they are both initialized with the f_1 function. As an additional boundary condition, we need to have $a_1 = \pm a_3$, enforcing symmetric or antisymmetric boundary condition (corresponding to the cosine or sine in (D.29), and additionally fixing the value of one coefficient, e.g., $a_1 = 1$. Thus, we have the additional conditions (mimicking (D.38b) and (D.38c))

$$a_3 = \pm a_1, \quad a_1 = 1. \quad (\text{D.44})$$

Inserting this into (D.43), we can subtract (or add) those two equations to obtain

$$a_2(c_2 \mp c_4) + a_4(c_4 \mp c_2) = 0, \quad (\text{D.45})$$

which leads to $a_2 = \pm a_4$, i.e., the symmetry condition for (D.44) enforces the same symmetry on the other coefficients a_2 and a_4 .

³ These requirements amount to the whole function $g(\phi)$ to be odd or even.

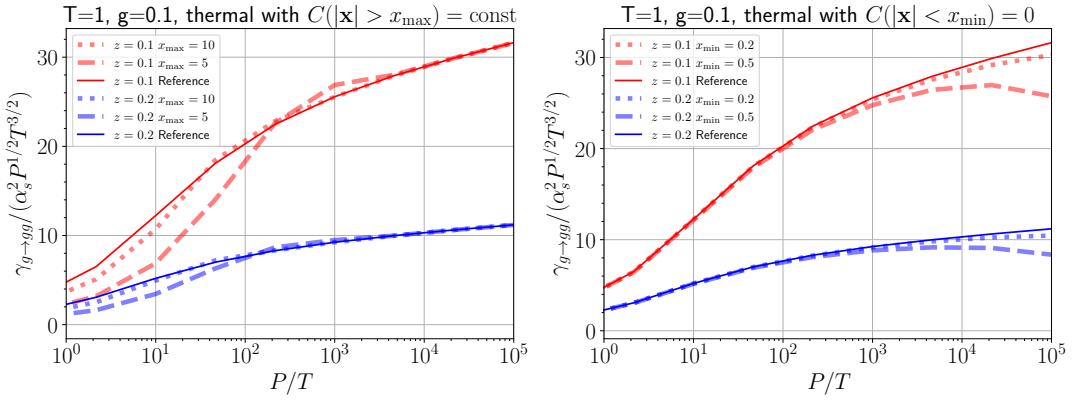


Figure D.1: Numerically obtaining the rate γ for Eq. (D.50) with small $|\mathbf{x}|$ (left) or large $|\mathbf{x}|$ (right) behavior modified.

While this holds for only considering two modes, $n = \pm 1$, this is also true for adding higher modes. For instance, let us consider now adding additionally $n = \pm 2$, such that Eq. (D.43) then reads

$$c_1 a_1 + c_2 a_2 + c_3 a_3 + c_4 a_4 + c_5 a_5 + c_6 a_6 = 0 \quad (\text{D.46a})$$

$$c_3 a_1 + c_4 a_2 + c_1 a_3 + c_2 a_4 + c_6 a_5 + c_5 a_6 = 0 \quad (\text{D.46b})$$

$$c_7 a_1 + c_8 a_2 + c_9 a_3 + c_{10} a_4 + c_{11} a_5 + c_{12} a_6 = 0 \quad (\text{D.46c})$$

$$c_9 a_1 + c_{10} a_2 + c_7 a_3 + c_8 a_4 + c_{12} a_5 + c_{11} a_6 = 0 \quad (\text{D.46d})$$

which, with the condition (D.44) leads to

$$0 = a_2(c_2 \mp c_4) + a_4(c_4 \mp c_2) + a_5(c_5 \mp c_6) + a_6(c_6 \mp c_5) \quad (\text{D.47})$$

$$0 = a_2(c_8 \mp c_{10}) + a_4(c_{10} \mp c_8) + a_5(c_{11} \mp c_{12}) + a_6(c_{12} \mp c_{11}), \quad (\text{D.48})$$

which, similar than before, upon eliminating a_5 and a_6 , leads to

$$0 = a_2 \left(\frac{c_2 \mp c_4}{c_5 \mp c_6} - \frac{c_8 \mp c_{10}}{c_{11} \mp c_{12}} \right) + a_4 \left(\frac{c_4 \mp c_2}{c_5 \mp c_6} - \frac{c_{10} \mp c_8}{c_{11} \mp c_{12}} \right). \quad (\text{D.49})$$

Similar as before, this leads to $a_2 = \pm a_4$, and thus to the same symmetry condition as for the other coefficients a_2 and a_4 .

Thus, the symmetry between $c_I^{1(m)}$ and $c_I^{-1(m)}$ in Eq. (D.41) is not an additional input but a consequence of the linear system (D.38).

D.2 NUMERICAL CROSS-CHECKS

As a numerical crosscheck, the rate is calculated for an isotropic dipole cross section (7.29),

$$C_{\text{eq}}^{\text{appr.}}(|\mathbf{x}|) = \frac{C_A g^2 T}{2\pi} \left(\gamma_E + K_0(m_D |\mathbf{x}|) + \log \frac{m_D |\mathbf{x}|}{2} \right). \quad (\text{D.50})$$

This is compared with a variation in the small or large $|\mathbf{x}|$ region. In the left panel of Fig. D.1, the large $|\mathbf{x}|$ behavior is modified such that it remains constant for $|\mathbf{x}| > x_{\text{max}}$. In the right panel the small $|\mathbf{x}|$ behavior is modified, such that $C(|\mathbf{x}| < x_{\text{min}}) = 0$. We

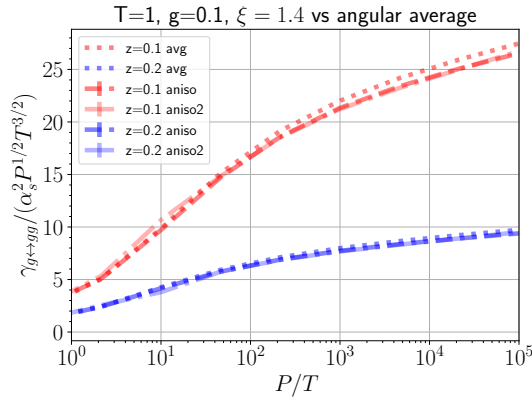


Figure D.2: Splitting rate for an anisotropic dipole cross section (D.50) with (D.51) and comparison to the rate from the angular averaged kernel.

find that modifying the small $|x|$ behavior changes the rate for large parton energies P , while changing the large $|x|$ behavior results in modifications for small parton energies.

In Fig. D.2, the anisotropic method is tested using (D.50), but an anisotropic Debye mass

$$m_D^2(\phi) = \left(1 - \frac{2\xi}{3} + \xi \cos^2 \phi\right) m_D, \quad (\text{D.51})$$

also used in Ref. [230] based on Ref. [36]. This model is used as a numerical cross-check. Its physical origin stems from a simple anisotropic plasma model using a squeezed thermal distribution, where this relation for the dominant mass m_+ is found in Ref. [36] in the static limit for small anisotropies. Using this model, T does no longer represent the actual effective temperature T_ϵ from (3.84), but it is still used here as a dimensionful scale. The results for the rather large anisotropy $\xi = 1.4$ are shown in Fig. D.2, which we compare with the rate from the angular averaged kernel (7.25). Two different sets of parameters are used for the number of Fourier modes, and grid values $|x_i|$ where the Fourier modes are calculated, and are shown as different line styles in Fig. D.2. Both anisotropic evaluations agree very well. As in the main text in Chapter 8, we find that the angular averaged kernel provides a good approximation of the anisotropic kernel when considering the rate. Note the small deviations for $z = 0.1$ despite the extremely anisotropic kernel with $\xi = 1.4$.

E

ADDITIONAL NUMERICAL RESULTS FOR BOTTOM-UP THERMALIZATION

In this Appendix, further results and plots for the simulations performed for this thesis are provided.

Fig. E.1 shows the time evolution of an expanding system in the anisotropy-occupancy plane, similar to Fig. 3.2, but with more couplings and initial conditions. Fig. E.2 depicts the temperature of an expanding system with the Debye-like screening prescription. For couplings $\lambda \in \{0.5, 2, 10\}$, several results are also tabulated in Tabs. E.1 - E.6. There, one may easily obtain numerical values for the effective temperature T_ε (Eq. (3.84)), infrared temperature T_* (Eq. (3.10)), screening mass (3.11), occupancy $\langle pf \rangle / \langle p \rangle$ and pressure ratio P_L / P_T . The energy density ε can be obtained from the effective temperature T_ε via Eq. (3.84). For the relaxation time τ_R , the values of η/s from Tab. 6.2 are used. In the left column, the times corresponding to the star, circle and triangle marker are indicated with the corresponding symbol. For $\lambda = 10$, the time is additionally given in fm/c and the effective temperature in GeV using $Q_s = 1.4$ GeV.

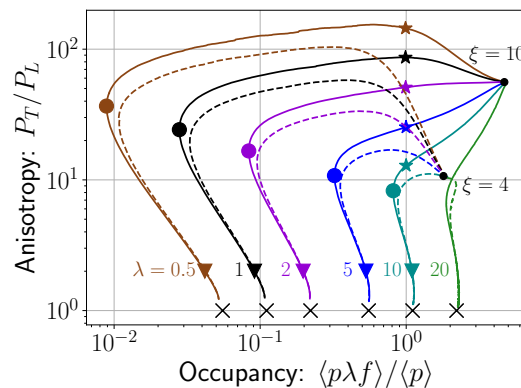


Figure E.1: Time evolution of expanding systems in the anisotropy-occupancy plane for various couplings for a Debye-like screening prescription.

		$\lambda = 0.5$,		Screening: Debye-like				
	$Q_s \tau$	τ/τ_R	τ/τ_{BMSS}	T_ε/Q_s	T_*/Q_s	m_D/Q_s	$\langle pf \rangle/\langle p \rangle$	P_L/P_T
	1.0	0.0013	0.000013	1.2	9.5	0.52	9.7	0.018
	1.3	0.0015	0.000017	1.1	5.7	0.38	5.5	0.014
	1.7	0.0019	0.000023	1.1	4.5	0.31	4.1	0.011
	2.3	0.0024	0.000030	0.98	3.6	0.26	3.1	0.0086
	3.0	0.0029	0.000040	0.92	3.1	0.22	2.5	0.0075
★	4.0	0.0035	0.000052	0.86	2.6	0.18	2	0.0069
	5.2	0.0043	0.000068	0.8	2.3	0.16	1.6	0.0066
	6.8	0.0053	0.000090	0.75	2	0.14	1.2	0.0065
	8.9	0.0065	0.00012	0.7	1.7	0.12	0.96	0.0066
	11.6	0.0079	0.00015	0.65	1.4	0.1	0.72	0.0068
	15.2	0.0097	0.00020	0.61	1.2	0.089	0.53	0.0069
	19.8	0.012	0.00026	0.57	1.1	0.079	0.38	0.0072
	25.8	0.014	0.00034	0.54	0.92	0.07	0.26	0.0077
	33.6	0.017	0.00044	0.5	0.81	0.062	0.18	0.008
	43.7	0.021	0.00058	0.47	0.73	0.056	0.13	0.0086
	56.9	0.026	0.00075	0.44	0.67	0.051	0.09	0.0092
	74.3	0.032	0.00098	0.41	0.61	0.046	0.066	0.0099
	96.6	0.039	0.0013	0.38	0.56	0.042	0.05	0.011
	125.7	0.047	0.0017	0.36	0.51	0.039	0.039	0.012
	164.1	0.057	0.0022	0.34	0.47	0.036	0.031	0.013
	213.8	0.07	0.0028	0.31	0.42	0.034	0.026	0.014
	278.9	0.085	0.0037	0.29	0.38	0.031	0.022	0.016
	363.1	0.1	0.0048	0.28	0.35	0.03	0.02	0.019
	472.9	0.13	0.0062	0.26	0.31	0.028	0.018	0.022
	615.8	0.15	0.0081	0.24	0.28	0.027	0.018	0.025
○	801.2	0.19	0.011	0.23	0.26	0.025	0.018	0.03
	1043.9	0.23	0.014	0.21	0.23	0.024	0.018	0.036
	1360.3	0.28	0.018	0.2	0.21	0.024	0.02	0.045
	1768.4	0.34	0.023	0.18	0.2	0.023	0.022	0.056
	2302.8	0.41	0.030	0.17	0.18	0.022	0.024	0.071
	2999.8	0.5	0.039	0.16	0.17	0.021	0.028	0.091
	3904.5	0.61	0.051	0.15	0.15	0.021	0.033	0.12
	5085.0	0.74	0.067	0.14	0.14	0.02	0.039	0.15
	6630.1	0.9	0.087	0.13	0.13	0.02	0.047	0.2
	8630.3	1.1	0.11	0.12	0.13	0.019	0.056	0.27
	11250.5	1.3	0.15	0.11	0.12	0.019	0.067	0.35
	14675.9	1.6	0.19	0.1	0.11	0.018	0.078	0.45
▽	19127.1	1.9	0.25	0.096	0.1	0.017	0.088	0.55
	24886.6	2.3	0.33	0.088	0.097	0.016	0.096	0.65
	32404.6	2.7	0.43	0.081	0.091	0.015	0.1	0.74
	42160.0	3.3	0.55	0.075	0.084	0.014	0.1	0.8

Table E.1: Simulation results of an expanding system with $\lambda = 0.5$ and Debye-like screening prescription.

		$\lambda = 2.0,$		Screening: Debye-like				
	$Q_s \tau$	τ/τ_R	τ/τ_{BMSS}	T_ϵ/Q_s	T_*/Q_s	m_D/Q_s	$\langle pf \rangle/\langle p \rangle$	P_L/P_T
★	1.0	0.0091	0.00048	0.86	2.7	0.52	2.4	0.018
	1.3	0.011	0.00064	0.8	1.7	0.38	1.3	0.018
	1.7	0.014	0.00084	0.75	1.4	0.31	0.89	0.018
	2.3	0.017	0.0011	0.7	1.2	0.26	0.64	0.019
	3.0	0.021	0.0015	0.65	1.1	0.23	0.48	0.02
	3.9	0.025	0.0019	0.61	0.94	0.2	0.35	0.021
	5.2	0.031	0.0025	0.57	0.83	0.17	0.26	0.022
	6.8	0.038	0.0033	0.53	0.75	0.15	0.18	0.023
	8.8	0.046	0.0043	0.5	0.67	0.14	0.13	0.025
	11.5	0.056	0.0055	0.46	0.61	0.13	0.099	0.027
○	15.0	0.069	0.0073	0.43	0.55	0.12	0.075	0.03
	19.6	0.084	0.0095	0.4	0.5	0.11	0.061	0.033
	25.4	0.1	0.012	0.38	0.46	0.1	0.051	0.037
	33.3	0.12	0.016	0.35	0.42	0.095	0.046	0.043
	43.4	0.15	0.021	0.33	0.38	0.09	0.043	0.05
	56.6	0.19	0.027	0.31	0.34	0.086	0.042	0.059
	73.8	0.23	0.036	0.29	0.31	0.082	0.042	0.07
	96.5	0.27	0.047	0.27	0.29	0.079	0.044	0.086
	125.8	0.33	0.061	0.25	0.26	0.076	0.048	0.11
	164.5	0.41	0.079	0.23	0.24	0.073	0.053	0.13
▽	214.5	0.49	0.10	0.22	0.23	0.071	0.059	0.17
	279.3	0.6	0.13	0.2	0.21	0.068	0.066	0.21
	363.7	0.73	0.18	0.19	0.2	0.065	0.075	0.27
	474.3	0.88	0.23	0.17	0.18	0.062	0.083	0.34
	617.8	1.1	0.30	0.16	0.17	0.059	0.092	0.42
	803.6	1.3	0.39	0.15	0.16	0.056	0.099	0.51
	1046.4	1.5	0.51	0.14	0.15	0.052	0.1	0.59
	1360.6	1.8	0.66	0.13	0.14	0.048	0.11	0.66
	1779.4	2.2	0.86	0.12	0.13	0.044	0.11	0.73
	2328.5	2.6	1.1	0.11	0.12	0.04	0.11	0.77
△	3034.0	3.2	1.5	0.098	0.11	0.037	0.11	0.81
	3959.8	3.8	1.9	0.09	0.1	0.034	0.11	0.84
	5171.6	4.5	2.5	0.083	0.092	0.031	0.11	0.87
	6741.4	5.4	3.3	0.076	0.085	0.028	0.11	0.89
	8767.8	6.5	4.2	0.07	0.079	0.025	0.11	0.91
	11433.4	7.8	5.5	0.064	0.074	0.023	0.1	0.93

Table E.2: Simulation results of an expanding system with $\lambda = 2$ and Debye-like screening prescription.

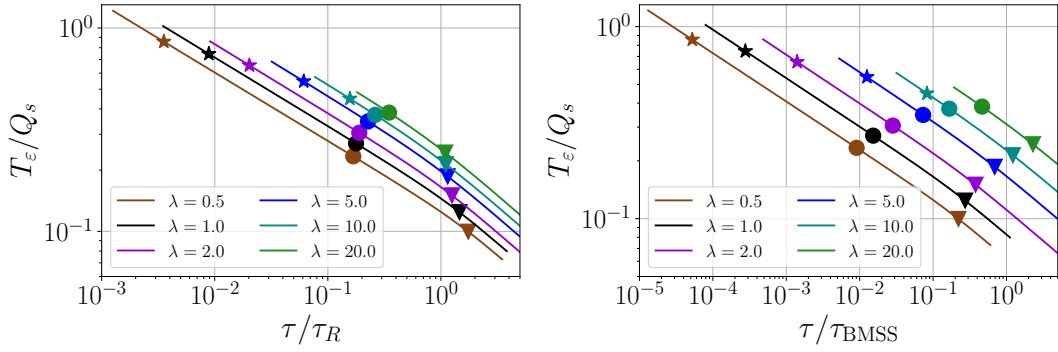


Figure E.2: Time evolution of the effective temperature T_ϵ from Eq. (3.84) of an expanding system. (Left): Time is rescaled with the relaxation time (3.85b). (Right): Time is rescaled with the bottom-up timescale (3.67).

$\lambda = 10.0$,			Screening: Debye-like							
	$Q_s \tau$	$\frac{\tau}{\text{fm}/c}$	τ/τ_R	$\frac{\tau}{\tau_{\text{BMSS}}}$	T_ϵ/Q_s	$\frac{T_\epsilon}{\text{GeV}}$	T_*/Q_s	m_D/Q_s	$\langle pf \rangle / \langle p \rangle$	P_L/P_T
	1.0	0.14	0.077	0.032	0.57	0.8	0.89	0.52	0.48	0.018
	1.3	0.18	0.094	0.042	0.54	0.75	0.71	0.41	0.23	0.041
	1.7	0.24	0.12	0.054	0.5	0.7	0.62	0.37	0.15	0.057
	2.2	0.32	0.14	0.071	0.47	0.65	0.55	0.34	0.11	0.071
\star	2.9	0.41	0.17	0.093	0.44	0.61	0.5	0.32	0.093	0.084
	3.8	0.54	0.21	0.12	0.41	0.57	0.45	0.3	0.085	0.099
	5.0	0.7	0.25	0.16	0.38	0.53	0.41	0.28	0.082	0.12
\circ	6.5	0.92	0.31	0.21	0.35	0.49	0.38	0.27	0.082	0.14
	8.5	1.2	0.37	0.27	0.33	0.46	0.35	0.26	0.085	0.17
	11.1	1.6	0.45	0.35	0.31	0.43	0.32	0.25	0.089	0.21
	14.4	2	0.55	0.46	0.28	0.4	0.3	0.23	0.095	0.26
	18.8	2.6	0.66	0.60	0.26	0.37	0.28	0.22	0.1	0.31
	24.6	3.5	0.8	0.78	0.24	0.34	0.26	0.21	0.1	0.38
	32.2	4.5	0.97	1.0	0.23	0.32	0.24	0.19	0.11	0.45
\triangleright	42.2	5.9	1.2	1.3	0.21	0.29	0.22	0.18	0.11	0.52
	54.9	7.7	1.4	1.7	0.19	0.27	0.2	0.17	0.11	0.59
	71.8	10	1.7	2.3	0.18	0.25	0.19	0.15	0.11	0.65
	93.9	13	2	3.0	0.16	0.23	0.17	0.14	0.11	0.71
	122.2	17	2.4	3.9	0.15	0.21	0.16	0.13	0.11	0.75
	159.2	22	2.9	5.1	0.14	0.19	0.15	0.12	0.11	0.79
	207.7	29	3.5	6.6	0.13	0.18	0.14	0.11	0.11	0.83
	271.0	38	4.2	8.6	0.12	0.16	0.13	0.099	0.11	0.86

Table E.3: Simulation results of an expanding system with $\lambda = 10$ and Debye-like screening prescription. Values in GeV and fm/c are obtained by using $Q_s = 1.4$ GeV.

$Q_s \tau$	$\lambda = 0.5,$		Screening: isoHTL					
	τ/τ_R	τ/τ_{BMSS}	T_ϵ/Q_s	T_*/Q_s	m_D/Q_s	$\langle pf \rangle/\langle p \rangle$	P_L/P_T	
★	1.0	0.0014	0.000013	1.2	9.5	0.52	9.7	0.018
	1.3	0.0017	0.000017	1.1	5.1	0.39	5.1	0.017
	1.7	0.002	0.000022	1.1	3.8	0.32	3.5	0.015
	2.2	0.0025	0.000029	1	3.1	0.28	2.6	0.014
	2.9	0.003	0.000038	0.93	2.5	0.24	1.9	0.013
	3.7	0.0037	0.000049	0.87	2.1	0.2	1.5	0.012
	4.8	0.0044	0.000064	0.82	1.7	0.18	1.1	0.011
	6.3	0.0054	0.000083	0.76	1.5	0.15	0.84	0.011
	8.2	0.0066	0.00011	0.72	1.3	0.13	0.63	0.011
	10.6	0.008	0.00014	0.67	1.1	0.12	0.48	0.011
	13.8	0.0098	0.00018	0.63	0.97	0.1	0.36	0.011
	17.9	0.012	0.00024	0.59	0.87	0.092	0.27	0.011
	23.3	0.014	0.00031	0.55	0.78	0.082	0.21	0.012
	30.3	0.018	0.00040	0.51	0.72	0.073	0.16	0.012
○	39.5	0.021	0.00052	0.48	0.66	0.065	0.12	0.013
	51.3	0.026	0.00067	0.45	0.61	0.059	0.092	0.013
	66.7	0.032	0.00088	0.42	0.56	0.053	0.071	0.014
	86.7	0.039	0.0011	0.4	0.52	0.049	0.056	0.015
	112.8	0.047	0.0015	0.37	0.48	0.045	0.045	0.016
	146.6	0.057	0.0019	0.35	0.44	0.041	0.037	0.018
	190.7	0.07	0.0025	0.32	0.41	0.038	0.031	0.019
	247.9	0.085	0.0033	0.3	0.37	0.035	0.027	0.021
	322.5	0.1	0.0042	0.28	0.34	0.033	0.024	0.024
	419.5	0.13	0.0055	0.27	0.31	0.031	0.022	0.027
	545.4	0.15	0.0072	0.25	0.28	0.029	0.021	0.031
	709.0	0.19	0.0093	0.23	0.26	0.028	0.02	0.037
	922.0	0.23	0.012	0.22	0.24	0.026	0.021	0.043
	1199.3	0.27	0.016	0.2	0.22	0.025	0.022	0.052
▽	1559.9	0.33	0.021	0.19	0.2	0.024	0.023	0.063
	2028.4	0.41	0.027	0.18	0.18	0.023	0.026	0.078
	2637.5	0.49	0.035	0.17	0.17	0.023	0.029	0.098
	3429.2	0.6	0.045	0.15	0.16	0.022	0.034	0.12
	4458.0	0.72	0.059	0.14	0.15	0.021	0.039	0.16
	5795.5	0.88	0.076	0.13	0.14	0.021	0.046	0.2
	7534.5	1.1	0.099	0.12	0.13	0.02	0.054	0.26
	9799.1	1.3	0.13	0.12	0.12	0.019	0.064	0.34
	12745.3	1.5	0.17	0.11	0.11	0.018	0.074	0.42
	16573.2	1.9	0.22	0.099	0.11	0.017	0.083	0.52

Table E.4: Simulation results of an expanding system with $\lambda = 0.5$ and isoHTL screening prescription.

$Q_s \tau$	$\lambda = 2.0,$		Screening: isoHTL				
	τ/τ_R	τ/τ_{BMSS}	T_ϵ/Q_s	T_*/Q_s	m_D/Q_s	$\langle pf \rangle/\langle p \rangle$	P_L/P_T
★	1.0	0.01	0.00048	0.86	2.7	0.52	2.4
	1.3	0.013	0.00063	0.8	1.6	0.39	1.2
	1.7	0.015	0.00082	0.75	1.3	0.33	0.74
	2.2	0.019	0.0011	0.7	1.1	0.28	0.51
	2.9	0.023	0.0014	0.66	0.92	0.25	0.36
	3.7	0.028	0.0018	0.62	0.82	0.22	0.26
	4.8	0.034	0.0023	0.58	0.74	0.19	0.19
	6.3	0.041	0.0030	0.54	0.67	0.17	0.15
	8.2	0.05	0.0039	0.5	0.62	0.16	0.11
	10.6	0.06	0.0051	0.47	0.57	0.14	0.09
○	13.8	0.073	0.0067	0.44	0.52	0.13	0.073
	18.0	0.089	0.0087	0.41	0.48	0.12	0.062
	23.4	0.11	0.011	0.39	0.44	0.11	0.054
	30.4	0.13	0.015	0.36	0.41	0.1	0.049
	39.5	0.16	0.019	0.34	0.37	0.098	0.046
	51.4	0.2	0.025	0.32	0.34	0.092	0.045
	66.8	0.24	0.032	0.29	0.31	0.088	0.045
	86.9	0.29	0.042	0.27	0.29	0.083	0.046
	113.0	0.35	0.055	0.26	0.27	0.08	0.049
	146.9	0.42	0.071	0.24	0.25	0.076	0.053
▽	191.0	0.51	0.092	0.22	0.23	0.073	0.059
	248.4	0.62	0.12	0.21	0.21	0.07	0.065
	323.0	0.75	0.16	0.19	0.2	0.067	0.072
	420.0	0.91	0.20	0.18	0.19	0.064	0.08
	546.2	1.1	0.26	0.17	0.17	0.06	0.088
	710.3	1.3	0.34	0.15	0.16	0.057	0.095
	923.4	1.6	0.45	0.14	0.15	0.053	0.1
	1200.7	1.9	0.58	0.13	0.14	0.049	0.1
	1561.0	2.3	0.75	0.12	0.13	0.045	0.11
	2030.2	2.7	0.98	0.11	0.12	0.042	0.11
△	2639.6	3.2	1.3	0.1	0.11	0.038	0.11
	3431.9	3.9	1.7	0.094	0.1	0.035	0.11
	4462.6	4.6	2.2	0.086	0.096	0.032	0.11
	5802.8	5.5	2.8	0.079	0.089	0.029	0.11
	7545.7	6.6	3.6	0.073	0.082	0.026	0.1
	9811.5	7.9	4.7	0.067	0.076	0.024	0.1
	12758.2	9.4	6.2	0.061	0.071	0.022	0.1
	16587.0	11	8.0	0.056	0.066	0.02	0.099
							0.95

Table E.5: Simulation results of an expanding system with $\lambda = 2$ and isoHTL screening prescription.

		Screening: isoHTL									
$\lambda = 10.0$,		$Q_s \tau$	$\frac{\tau}{\text{fm}/c}$	τ/τ_R	$\frac{\tau}{\tau_{\text{BMSS}}}$	T_ϵ/Q_s	$\frac{T_\epsilon}{\text{GeV}}$	T_*/Q_s	m_D/Q_s	$\langle pf \rangle/\langle p \rangle$	P_L/P_T
	1.0	0.14	0.091	0.032	0.57	0.8	0.89	0.52	0.48	0.018	
	1.3	0.18	0.11	0.041	0.54	0.75	0.66	0.42	0.18	0.054	
	1.7	0.24	0.13	0.054	0.5	0.7	0.58	0.38	0.12	0.076	
\star	2.2	0.31	0.16	0.070	0.47	0.66	0.52	0.36	0.096	0.094	
	2.9	0.4	0.2	0.091	0.44	0.61	0.48	0.33	0.086	0.11	
	3.7	0.52	0.24	0.12	0.41	0.57	0.44	0.31	0.081	0.13	
\circ	4.9	0.68	0.29	0.15	0.38	0.53	0.4	0.29	0.081	0.15	
	6.3	0.89	0.35	0.20	0.35	0.5	0.37	0.28	0.082	0.18	
	8.2	1.2	0.43	0.26	0.33	0.46	0.34	0.26	0.085	0.21	
	10.7	1.5	0.52	0.34	0.31	0.43	0.32	0.25	0.089	0.25	
	13.9	2	0.62	0.44	0.28	0.4	0.3	0.24	0.093	0.3	
	18.1	2.6	0.75	0.58	0.26	0.37	0.27	0.22	0.098	0.36	
	23.6	3.3	0.91	0.75	0.24	0.34	0.25	0.21	0.1	0.42	
	30.7	4.3	1.1	0.97	0.23	0.32	0.24	0.19	0.1	0.49	
\triangledown	40.0	5.6	1.3	1.3	0.21	0.29	0.22	0.18	0.11	0.56	
	51.9	7.3	1.6	1.6	0.19	0.27	0.2	0.17	0.11	0.62	
	67.5	9.5	1.9	2.1	0.18	0.25	0.19	0.15	0.11	0.68	
	87.9	12	2.3	2.8	0.16	0.23	0.17	0.14	0.11	0.73	
	114.4	16	2.7	3.6	0.15	0.21	0.16	0.13	0.11	0.77	
	148.9	21	3.2	4.7	0.14	0.19	0.15	0.12	0.11	0.8	
	193.7	27	3.9	6.1	0.13	0.18	0.14	0.11	0.11	0.84	
	251.9	35	4.6	8.0	0.12	0.16	0.13	0.099	0.11	0.86	

Table E.6: Simulation results of an expanding system with $\lambda = 10$ and isoHTL screening prescription. Values in GeV and fm/c are obtained by using $Q_s = 1.4$ GeV.

 NOTES ON NOTATIONAL CONVENTIONS HERE AND IN THE PAPERS

- $v_{...}$ in Ref. [2] is written as $\cos \theta_{...}$ here.

In Ref. [2], the cosine of angles is usually abbreviated with the letter $v_{...} = \cos \theta_{...}$. In this thesis, I choose to always write the cosine explicitly. For the angle between \mathbf{p} and \mathbf{q} , θ_{qp} , I write here for the cosine $\cos \theta_{qp} = v_{pq}$.

- The parameter ξ used in Ref. [1, 3] labels the anisotropy in the initial condition (3.77), which we denote as ξ_0 here. The parameter ξ is used in this thesis to denote the gauge parameter in the Fadeev-Popov procedure. Furthermore, the same letter ξ was used in Ref. [2] to denote the constant used in the Debye-like screening prescription. We denote this here by ξ_g for Debye-like screening in the elastic collision term (3.15), and ξ_g^\perp for Debye-like screening for the jet quenching parameter \hat{q} .
- The convention for the HTL propagators (A.41) differs from the one used in Ref. [2, 4] by a factor i and correspond here to the convention used by Blaizot and Iancu [177] to be consistent with the propagators defined throughout the thesis. In both references, the propagators enter only via the AMY replacement (3.21a) using the absolute value, so there are no other differences.
- The angle ϕ_{kq} from Ref. [2] is written ϕ_{qk} here, because it measures the azimuthal angle of \mathbf{k} in a frame which is defined by \mathbf{q} .

G

TOOLS USED

While working on my thesis, I used several scientific tools and libraries which I would like to acknowledge. I would like to acknowledge the use of Mathematica [238], Scipy [237], Numpy [239], Matplotlib [240], mpmath [241], sympy [242], and, of course, various large language model (LLM) tools such as ChatGPT¹, Mistral², copilot³ or others, which I mainly used when getting stuck in a coding question and to help me write code more efficiently.

¹ <https://chatgpt.com/>

² <https://mistral.ai/>

³ <https://copilot.microsoft.com>

BIBLIOGRAPHY

- [1] Kirill Boguslavski, Aleksi Kurkela, Tuomas Lappi, Florian Lindenbauer, and Jarkko Peuron. “Jet momentum broadening during initial stages in heavy-ion collisions”. In: *Phys. Lett. B* 850 (2024), p. 138525. doi: [10.1016/j.physletb.2024.138525](https://doi.org/10.1016/j.physletb.2024.138525). arXiv: [2303.12595 \[hep-ph\]](https://arxiv.org/abs/2303.12595).
- [2] Kirill Boguslavski, Aleksi Kurkela, Tuomas Lappi, Florian Lindenbauer, and Jarkko Peuron. “Jet quenching parameter in QCD kinetic theory”. In: *Phys. Rev. D* 110.3 (2024), p. 034019. doi: [10.1103/PhysRevD.110.034019](https://doi.org/10.1103/PhysRevD.110.034019). arXiv: [2312.00447 \[hep-ph\]](https://arxiv.org/abs/2312.00447).
- [3] Kirill Boguslavski, Aleksi Kurkela, Tuomas Lappi, Florian Lindenbauer, and Jarkko Peuron. “Limiting attractors in heavy-ion collisions”. In: *Phys. Lett. B* 852 (2024), p. 138623. doi: [10.1016/j.physletb.2024.138623](https://doi.org/10.1016/j.physletb.2024.138623). arXiv: [2312.11252 \[hep-ph\]](https://arxiv.org/abs/2312.11252).
- [4] Kirill Boguslavski and Florian Lindenbauer. “Soft-gluon exchange matters: Isotropic screening in QCD kinetic theory”. In: *Phys. Rev. D* 110.7 (2024), p. 074017. doi: [10.1103/PhysRevD.110.074017](https://doi.org/10.1103/PhysRevD.110.074017). arXiv: [2407.09605 \[hep-ph\]](https://arxiv.org/abs/2407.09605).
- [5] Kirill Boguslavski, Aleksi Kurkela, Tuomas Lappi, Florian Lindenbauer, and Jarkko Peuron. “Limiting attractors in heavy-ion collisions—The interplay between bottom-up and hydrodynamic attractors”. In: *EPJ Web Conf.* 296 (2024), p. 10004. doi: [10.1051/epjconf/202429610004](https://doi.org/10.1051/epjconf/202429610004). arXiv: [2401.09088 \[hep-ph\]](https://arxiv.org/abs/2401.09088).
- [6] Alois Altenburger, Kirill Boguslavski, and Florian Lindenbauer. In preparation.
- [7] K. Boguslavski, A. Kurkela, T. Lappi, F. Lindenbauer, and J. Peuron. “Heavy quark diffusion coefficient in heavy-ion collisions via kinetic theory”. In: *Phys. Rev. D* 109.1 (2024), p. 014025. doi: [10.1103/PhysRevD.109.014025](https://doi.org/10.1103/PhysRevD.109.014025). arXiv: [2303.12520 \[hep-ph\]](https://arxiv.org/abs/2303.12520).
- [8] Kirill Boguslavski, Aleksi Kurkela, Tuomas Lappi, Florian Lindenbauer, and Jarkko Peuron. “Heavy quark diffusion coefficient during hydrodynamization - non-equilibrium vs. equilibrium”. In: *PoS HardProbes2023* (2024), p. 091. doi: [10.22323/1.438.0091](https://doi.org/10.22323/1.438.0091). arXiv: [2308.07169 \[hep-ph\]](https://arxiv.org/abs/2308.07169).
- [9] Kirill Boguslavski, Aleksi Kurkela, Tuomas Lappi, Florian Lindenbauer, and Jarkko Peuron. “Heavy quark momentum diffusion coefficient during hydrodynamization via effective kinetic theory”. In: *EPJ Web Conf.* 296 (2024), p. 09001. doi: [10.1051/epjconf/202429609001](https://doi.org/10.1051/epjconf/202429609001). arXiv: [2312.12200 \[hep-ph\]](https://arxiv.org/abs/2312.12200).
- [10] Franz Gross et al. “50 Years of Quantum Chromodynamics”. In: *Eur. Phys. J. C* 83 (2023), p. 1125. doi: [10.1140/epjc/s10052-023-11949-2](https://doi.org/10.1140/epjc/s10052-023-11949-2). arXiv: [2212.11107 \[hep-ph\]](https://arxiv.org/abs/2212.11107).

- [11] Wit Busza, Krishna Rajagopal, and Wilke van der Schee. "Heavy Ion Collisions: The Big Picture, and the Big Questions". In: *Ann. Rev. Nucl. Part. Sci.* 68 (2018), pp. 339–376. doi: [10.1146/annurev-nucl-101917-020852](https://doi.org/10.1146/annurev-nucl-101917-020852). arXiv: [1802.04801 \[hep-ph\]](https://arxiv.org/abs/1802.04801).
- [12] P. Achenbach et al. "The present and future of QCD". In: *Nucl. Phys. A* 1047 (2024), p. 122874. doi: [10.1016/j.nuclphysa.2024.122874](https://doi.org/10.1016/j.nuclphysa.2024.122874). arXiv: [2303.02579 \[hep-ph\]](https://arxiv.org/abs/2303.02579).
- [13] Jürgen Berges, Michal P. Heller, Aleksas Mazeliauskas, and Raju Venugopalan. "QCD thermalization: Ab initio approaches and interdisciplinary connections". In: *Rev. Mod. Phys.* 93.3 (2021), p. 035003. doi: [10.1103/RevModPhys.93.035003](https://doi.org/10.1103/RevModPhys.93.035003). arXiv: [2005.12299 \[hep-th\]](https://arxiv.org/abs/2005.12299).
- [14] J. Eisert, M. Friesdorf, and C. Gogolin. "Quantum many-body systems out of equilibrium". In: *Nature Phys.* 11 (2015), p. 124. doi: [10.1038/nphys3215](https://doi.org/10.1038/nphys3215). arXiv: [1408.5148 \[quant-ph\]](https://arxiv.org/abs/1408.5148).
- [15] Christof Gattringer and Kurt Langfeld. "Approaches to the sign problem in lattice field theory". In: *Int. J. Mod. Phys. A* 31.22 (2016), p. 1643007. doi: [10.1142/S0217751X16430077](https://doi.org/10.1142/S0217751X16430077). arXiv: [1603.09517 \[hep-lat\]](https://arxiv.org/abs/1603.09517).
- [16] Andrei Alexandru, Gokce Basar, Paulo F. Bedaque, and Neill C. Warrington. "Complex paths around the sign problem". In: *Rev. Mod. Phys.* 94.1 (2022), p. 015006. doi: [10.1103/RevModPhys.94.015006](https://doi.org/10.1103/RevModPhys.94.015006). arXiv: [2007.05436 \[hep-lat\]](https://arxiv.org/abs/2007.05436).
- [17] Francois Gelis, Edmond Iancu, Jamal Jalilian-Marian, and Raju Venugopalan. "The Color Glass Condensate". In: *Ann. Rev. Nucl. Part. Sci.* 60 (2010), pp. 463–489. doi: [10.1146/annurev.nucl.010909.083629](https://doi.org/10.1146/annurev.nucl.010909.083629). arXiv: [1002.0333 \[hep-ph\]](https://arxiv.org/abs/1002.0333).
- [18] Alex Krasnitz and Raju Venugopalan. "Nonperturbative computation of gluon minijet production in nuclear collisions at very high-energies". In: *Nucl. Phys. B* 557 (1999), p. 237. doi: [10.1016/S0550-3213\(99\)00366-1](https://doi.org/10.1016/S0550-3213(99)00366-1). arXiv: [hep-ph/9809433](https://arxiv.org/abs/hep-ph/9809433).
- [19] Peter Brockway Arnold, Guy D. Moore, and Laurence G. Yaffe. "Effective kinetic theory for high temperature gauge theories". In: *JHEP* 01 (2003), p. 030. doi: [10.1088/1126-6708/2003/01/030](https://doi.org/10.1088/1126-6708/2003/01/030). arXiv: [hep-ph/0209353](https://arxiv.org/abs/hep-ph/0209353).
- [20] Jacopo Ghiglieri, Guy D. Moore, and Derek Teaney. "Jet-Medium Interactions at NLO in a Weakly-Coupled Quark-Gluon Plasma". In: *JHEP* 03 (2016), p. 095. doi: [10.1007/JHEP03\(2016\)095](https://doi.org/10.1007/JHEP03(2016)095). arXiv: [1509.07773 \[hep-ph\]](https://arxiv.org/abs/1509.07773).
- [21] Aleksi Kurkela and Egang Lu. "Approach to Equilibrium in Weakly Coupled Non-Abelian Plasmas". In: *Phys. Rev. Lett.* 113.18 (2014), p. 182301. doi: [10.1103/PhysRevLett.113.182301](https://doi.org/10.1103/PhysRevLett.113.182301). arXiv: [1405.6318 \[hep-ph\]](https://arxiv.org/abs/1405.6318).
- [22] Aleksi Kurkela and Yan Zhu. "Isotropization and hydrodynamization in weakly coupled heavy-ion collisions". In: *Phys. Rev. Lett.* 115.18 (2015), p. 182301. doi: [10.1103/PhysRevLett.115.182301](https://doi.org/10.1103/PhysRevLett.115.182301). arXiv: [1506.06647 \[hep-ph\]](https://arxiv.org/abs/1506.06647).

- [23] Aleksi Kurkela and Aleksas Mazeliauskas. "Chemical equilibration in weakly coupled QCD". In: *Phys. Rev. D* 99.5 (2019), p. 054018. DOI: [10.1103/PhysRevD.99.054018](https://doi.org/10.1103/PhysRevD.99.054018). arXiv: [1811.03068 \[hep-ph\]](https://arxiv.org/abs/1811.03068).
- [24] Aleksi Kurkela and Aleksas Mazeliauskas. "Chemical Equilibration in Hadronic Collisions". In: *Phys. Rev. Lett.* 122 (2019), p. 142301. DOI: [10.1103/PhysRevLett.122.142301](https://doi.org/10.1103/PhysRevLett.122.142301). arXiv: [1811.03040 \[hep-ph\]](https://arxiv.org/abs/1811.03040).
- [25] Xiaojian Du and Sören Schlichting. "Equilibration of weakly coupled QCD plasmas". In: *Phys. Rev. D* 104.5 (2021), p. 054011. DOI: [10.1103/PhysRevD.104.054011](https://doi.org/10.1103/PhysRevD.104.054011). arXiv: [2012.09079 \[hep-ph\]](https://arxiv.org/abs/2012.09079).
- [26] Xiaojian Du and Sören Schlichting. "Equilibration of the Quark-Gluon Plasma at Finite Net-Baryon Density in QCD Kinetic Theory". In: *Phys. Rev. Lett.* 127.12 (2021), p. 122301. DOI: [10.1103/PhysRevLett.127.122301](https://doi.org/10.1103/PhysRevLett.127.122301). arXiv: [2012.09068 \[hep-ph\]](https://arxiv.org/abs/2012.09068).
- [27] Aleksi Kurkela, Aleksas Mazeliauskas, Jean-François Paquet, Sören Schlichting, and Derek Teaney. "Matching the Nonequilibrium Initial Stage of Heavy Ion Collisions to Hydrodynamics with QCD Kinetic Theory". In: *Phys. Rev. Lett.* 122.12 (2019), p. 122302. DOI: [10.1103/PhysRevLett.122.122302](https://doi.org/10.1103/PhysRevLett.122.122302). arXiv: [1805.01604 \[hep-ph\]](https://arxiv.org/abs/1805.01604).
- [28] Aleksi Kurkela, Aleksas Mazeliauskas, Jean-François Paquet, Sören Schlichting, and Derek Teaney. "Effective kinetic description of event-by-event pre-equilibrium dynamics in high-energy heavy-ion collisions". In: *Phys. Rev. C* 99.3 (2019), p. 034910. DOI: [10.1103/PhysRevC.99.034910](https://doi.org/10.1103/PhysRevC.99.034910). arXiv: [1805.00961 \[hep-ph\]](https://arxiv.org/abs/1805.00961).
- [29] Giuliano Giacalone, Aleksas Mazeliauskas, and Sören Schlichting. "Hydrodynamic attractors, initial state energy and particle production in relativistic nuclear collisions". In: *Phys. Rev. Lett.* 123.26 (2019), p. 262301. DOI: [10.1103/PhysRevLett.123.262301](https://doi.org/10.1103/PhysRevLett.123.262301). arXiv: [1908.02866 \[hep-ph\]](https://arxiv.org/abs/1908.02866).
- [30] Maurice Coquet, Michael Winn, Xiaojian Du, Jean-Yves Ollitrault, and Soeren Schlichting. "Dilepton Polarization as a Signature of Plasma Anisotropy". In: *Phys. Rev. Lett.* 132.23 (2024), p. 232301. DOI: [10.1103/PhysRevLett.132.232301](https://doi.org/10.1103/PhysRevLett.132.232301). arXiv: [2309.00555 \[nucl-th\]](https://arxiv.org/abs/2309.00555).
- [31] Oscar Garcia-Montero, Aleksas Mazeliauskas, Philip Plaschke, and Sören Schlichting. "Pre-equilibrium photons from the early stages of heavy-ion collisions". In: *JHEP* 03 (2024), p. 053. DOI: [10.1007/JHEP03\(2024\)053](https://doi.org/10.1007/JHEP03(2024)053). arXiv: [2308.09747 \[hep-ph\]](https://arxiv.org/abs/2308.09747).
- [32] Oscar Garcia-Montero, Philip Plaschke, and Sören Schlichting. "Scaling of pre-equilibrium dilepton production in QCD kinetic theory". In: *Phys. Rev. D* 111.3 (2025), p. 034036. DOI: [10.1103/PhysRevD.111.034036](https://doi.org/10.1103/PhysRevD.111.034036). arXiv: [2403.04846 \[hep-ph\]](https://arxiv.org/abs/2403.04846).
- [33] Fabian Zhou, Jasmine Brewer, and Aleksas Mazeliauskas. "Minijet quenching in non-equilibrium quark-gluon plasma". In: *JHEP* 06 (2024), p. 214. DOI: [10.1007/JHEP06\(2024\)214](https://doi.org/10.1007/JHEP06(2024)214). arXiv: [2402.09298 \[hep-ph\]](https://arxiv.org/abs/2402.09298).

- [34] Stanislaw Mrowczynski. "Stream Instabilities of the Quark - Gluon Plasma". In: *Phys. Lett. B* 214 (1988). [Erratum: *Phys.Lett.B* 656, 273 (2007)], p. 587. doi: [10.1016/0370-2693\(88\)90124-4](https://doi.org/10.1016/0370-2693(88)90124-4).
- [35] S. Mrowczynski. "Plasma instability at the initial stage of ultrarelativistic heavy ion collisions". In: *Phys. Lett. B* 314 (1993), pp. 118–121. doi: [10.1016/0370-2693\(93\)91330-P](https://doi.org/10.1016/0370-2693(93)91330-P).
- [36] Paul Romatschke and Michael Strickland. "Collective modes of an anisotropic quark gluon plasma". In: *Phys. Rev. D* 68 (2003), p. 036004. doi: [10.1103/PhysRevD.68.036004](https://doi.org/10.1103/PhysRevD.68.036004). arXiv: [hep-ph/0304092](https://arxiv.org/abs/hep-ph/0304092).
- [37] Paul Romatschke and Michael Strickland. "Collective modes of an anisotropic quark-gluon plasma II". In: *Phys. Rev. D* 70 (2004), p. 116006. doi: [10.1103/PhysRevD.70.116006](https://doi.org/10.1103/PhysRevD.70.116006). arXiv: [hep-ph/0406188](https://arxiv.org/abs/hep-ph/0406188).
- [38] Aleksi Kurkela and Guy D. Moore. "Bjorken Flow, Plasma Instabilities, and Thermalization". In: *JHEP* 11 (2011), p. 120. doi: [10.1007/JHEP11\(2011\)120](https://doi.org/10.1007/JHEP11(2011)120). arXiv: [1108.4684 \[hep-ph\]](https://arxiv.org/abs/1108.4684).
- [39] Stanislaw Mrowczynski, Bjoern Schenke, and Michael Strickland. "Color instabilities in the quark-gluon plasma". In: *Phys. Rept.* 682 (2017), pp. 1–97. doi: [10.1016/j.physrep.2017.03.003](https://doi.org/10.1016/j.physrep.2017.03.003). arXiv: [1603.08946 \[hep-ph\]](https://arxiv.org/abs/1603.08946).
- [40] Bjoern Schenke, Michael Strickland, Carsten Greiner, and Markus H. Thoma. "A Model of the effect of collisions on QCD plasma instabilities". In: *Phys. Rev. D* 73 (2006), p. 125004. doi: [10.1103/PhysRevD.73.125004](https://doi.org/10.1103/PhysRevD.73.125004). arXiv: [hep-ph/0603029](https://arxiv.org/abs/hep-ph/0603029).
- [41] Ruizhe Zhao, Luhua Qiu, Yun Guo, and Michael Strickland. "Collective modes of a collisional anisotropic quark-gluon plasma". In: *Phys. Rev. D* 108.3 (2023), p. 034023. doi: [10.1103/PhysRevD.108.034023](https://doi.org/10.1103/PhysRevD.108.034023). arXiv: [2306.12851 \[hep-ph\]](https://arxiv.org/abs/2306.12851).
- [42] J. Berges, K. Boguslavski, S. Schlichting, and R. Venugopalan. "Turbulent thermalization process in heavy-ion collisions at ultrarelativistic energies". In: *Phys. Rev. D* 89.7 (2014), p. 074011. doi: [10.1103/PhysRevD.89.074011](https://doi.org/10.1103/PhysRevD.89.074011). arXiv: [1303.5650 \[hep-ph\]](https://arxiv.org/abs/1303.5650).
- [43] Juergen Berges, Kirill Boguslavski, Soeren Schlichting, and Raju Venugopalan. "Universal attractor in a highly occupied non-Abelian plasma". In: *Phys. Rev. D* 89.11 (2014), p. 114007. doi: [10.1103/PhysRevD.89.114007](https://doi.org/10.1103/PhysRevD.89.114007). arXiv: [1311.3005 \[hep-ph\]](https://arxiv.org/abs/1311.3005).
- [44] Luciano Rezzolla and Olindo Zanotti. *Relativistic Hydrodynamics*. Oxford University Press, Sept. 2013. ISBN: 978-0-19-174650-5, 978-0-19-852890-6. doi: [10.1093/acprof:oso/9780198528906.001.0001](https://doi.org/10.1093/acprof:oso/9780198528906.001.0001).
- [45] Charles Gale, Sangyong Jeon, and Bjoern Schenke. "Hydrodynamic Modeling of Heavy-Ion Collisions". In: *Int. J. Mod. Phys. A* 28 (2013), p. 1340011. doi: [10.1142/S0217751X13400113](https://doi.org/10.1142/S0217751X13400113). arXiv: [1301.5893 \[nucl-th\]](https://arxiv.org/abs/1301.5893).
- [46] Paul Romatschke and Ulrike Romatschke. *Relativistic Fluid Dynamics In and Out of Equilibrium*. Cambridge Monographs on Mathematical Physics. Cambridge University Press, May 2019. ISBN: 978-1-108-48368-1, 978-1-108-75002-8. doi: [10.1017/9781108651998](https://doi.org/10.1017/9781108651998). arXiv: [1712.05815 \[nucl-th\]](https://arxiv.org/abs/1712.05815).

- [47] Ulrich Heinz and Björn Schenke. "Hydrodynamic Description of the Quark-Gluon Plasma". In: Dec. 2024. arXiv: [2412.19393 \[nucl-th\]](https://arxiv.org/abs/2412.19393).
- [48] Hannah Elfner and Berndt Müller. "The exploration of hot and dense nuclear matter: introduction to relativistic heavy-ion physics". In: *J. Phys. G* 50.10 (2023), p. 103001. DOI: [10.1088/1361-6471/ace824](https://doi.org/10.1088/1361-6471/ace824). arXiv: [2210.12056 \[nucl-th\]](https://arxiv.org/abs/2210.12056).
- [49] Juan Martin Maldacena. "The Large N limit of superconformal field theories and supergravity". In: *Adv. Theor. Math. Phys.* 2 (1998), pp. 231–252. DOI: [10.4310/ATMP.1998.v2.n2.a1](https://doi.org/10.4310/ATMP.1998.v2.n2.a1). arXiv: [hep-th/9711200](https://arxiv.org/abs/hep-th/9711200).
- [50] Edward Witten. "Anti de Sitter space and holography". In: *Adv. Theor. Math. Phys.* 2 (1998), pp. 253–291. DOI: [10.4310/ATMP.1998.v2.n2.a2](https://doi.org/10.4310/ATMP.1998.v2.n2.a2). arXiv: [hep-th/9802150](https://arxiv.org/abs/hep-th/9802150).
- [51] S. S. Gubser, Igor R. Klebanov, and Alexander M. Polyakov. "Gauge theory correlators from noncritical string theory". In: *Phys. Lett. B* 428 (1998), pp. 105–114. DOI: [10.1016/S0370-2693\(98\)00377-3](https://doi.org/10.1016/S0370-2693(98)00377-3). arXiv: [hep-th/9802109](https://arxiv.org/abs/hep-th/9802109).
- [52] Paul M. Chesler and Laurence G. Yaffe. "Boost invariant flow, black hole formation, and far-from-equilibrium dynamics in $N = 4$ supersymmetric Yang-Mills theory". In: *Phys. Rev. D* 82 (2010), p. 026006. DOI: [10.1103/PhysRevD.82.026006](https://doi.org/10.1103/PhysRevD.82.026006). arXiv: [0906.4426 \[hep-th\]](https://arxiv.org/abs/0906.4426).
- [53] Paul M. Chesler and Laurence G. Yaffe. "Holography and colliding gravitational shock waves in asymptotically AdS_5 spacetime". In: *Phys. Rev. Lett.* 106 (2011), p. 021601. DOI: [10.1103/PhysRevLett.106.021601](https://doi.org/10.1103/PhysRevLett.106.021601). arXiv: [1011.3562 \[hep-th\]](https://arxiv.org/abs/1011.3562).
- [54] Wilke van der Schee. "Holographic thermalization with radial flow". In: *Phys. Rev. D* 87.6 (2013), p. 061901. DOI: [10.1103/PhysRevD.87.061901](https://doi.org/10.1103/PhysRevD.87.061901). arXiv: [1211.2218 \[hep-th\]](https://arxiv.org/abs/1211.2218).
- [55] Wilke van der Schee, Paul Romatschke, and Scott Pratt. "Fully Dynamical Simulation of Central Nuclear Collisions". In: *Phys. Rev. Lett.* 111.22 (2013), p. 222302. DOI: [10.1103/PhysRevLett.111.222302](https://doi.org/10.1103/PhysRevLett.111.222302). arXiv: [1307.2539 \[nucl-th\]](https://arxiv.org/abs/1307.2539).
- [56] Liam Keegan, Aleksi Kurkela, Paul Romatschke, Wilke van der Schee, and Yan Zhu. "Weak and strong coupling equilibration in nonabelian gauge theories". In: *JHEP* 04 (2016), p. 031. DOI: [10.1007/JHEP04\(2016\)031](https://doi.org/10.1007/JHEP04(2016)031). arXiv: [1512.05347 \[hep-th\]](https://arxiv.org/abs/1512.05347).
- [57] Aleksi Kurkela, Wilke van der Schee, Urs Achim Wiedemann, and Bin Wu. "Early- and Late-Time Behavior of Attractors in Heavy-Ion Collisions". In: *Phys. Rev. Lett.* 124.10 (2020), p. 102301. DOI: [10.1103/PhysRevLett.124.102301](https://doi.org/10.1103/PhysRevLett.124.102301). arXiv: [1907.08101 \[hep-ph\]](https://arxiv.org/abs/1907.08101).
- [58] Michal P. Heller and Michal Spalinski. "Hydrodynamics Beyond the Gradient Expansion: Resurgence and Resummation". In: *Phys. Rev. Lett.* 115.7 (2015), p. 072501. DOI: [10.1103/PhysRevLett.115.072501](https://doi.org/10.1103/PhysRevLett.115.072501). arXiv: [1503.07514 \[hep-th\]](https://arxiv.org/abs/1503.07514).

- [59] Alexander Soloviev. "Hydrodynamic attractors in heavy ion collisions: a review". In: *Eur. Phys. J. C* 82.4 (2022), p. 319. DOI: [10.1140/epjc/s10052-022-10282-4](https://doi.org/10.1140/epjc/s10052-022-10282-4). arXiv: [2109.15081 \[hep-th\]](https://arxiv.org/abs/2109.15081).
- [60] Jakub Jankowski and Michał Spaliński. "Hydrodynamic attractors in ultra-relativistic nuclear collisions". In: *Prog. Part. Nucl. Phys.* 132 (2023), p. 104048. DOI: [10.1016/j.ppnp.2023.104048](https://doi.org/10.1016/j.ppnp.2023.104048). arXiv: [2303.09414 \[nucl-th\]](https://arxiv.org/abs/2303.09414).
- [61] Michael Strickland, Jorge Noronha, and Gabriel Denicol. "Anisotropic nonequilibrium hydrodynamic attractor". In: *Phys. Rev. D* 97.3 (2018), p. 036020. DOI: [10.1103/PhysRevD.97.036020](https://doi.org/10.1103/PhysRevD.97.036020). arXiv: [1709.06644 \[nucl-th\]](https://arxiv.org/abs/1709.06644).
- [62] Michal P. Heller, Aleksi Kurkela, Michał Spaliński, and Viktor Svensson. "Hydrodynamization in kinetic theory: Transient modes and the gradient expansion". In: *Phys. Rev. D* 97.9 (2018), p. 091503. DOI: [10.1103/PhysRevD.97.091503](https://doi.org/10.1103/PhysRevD.97.091503). arXiv: [1609.04803 \[nucl-th\]](https://arxiv.org/abs/1609.04803).
- [63] Dekrayat Almaalol, Aleksi Kurkela, and Michael Strickland. "Nonequilibrium Attractor in High-Temperature QCD Plasmas". In: *Phys. Rev. Lett.* 125.12 (2020), p. 122302. DOI: [10.1103/PhysRevLett.125.122302](https://doi.org/10.1103/PhysRevLett.125.122302). arXiv: [2004.05195 \[hep-ph\]](https://arxiv.org/abs/2004.05195).
- [64] Xiaojian Du, Michal P. Heller, Sören Schlichting, and Viktor Svensson. "Exponential approach to the hydrodynamic attractor in Yang-Mills kinetic theory". In: *Phys. Rev. D* 106.1 (2022), p. 014016. DOI: [10.1103/PhysRevD.106.014016](https://doi.org/10.1103/PhysRevD.106.014016). arXiv: [2203.16549 \[hep-ph\]](https://arxiv.org/abs/2203.16549).
- [65] Vincenzo Nugara, Vincenzo Greco, and Salvatore Plumari. "Far-from-equilibrium attractors with Full Relativistic Boltzmann approach in 3+1D: moments of distribution function and anisotropic flows v_n ". In: *Eur. Phys. J. C* 85.3 (2025), p. 311. DOI: [10.1140/epjc/s10052-025-14029-9](https://doi.org/10.1140/epjc/s10052-025-14029-9). arXiv: [2409.12123 \[hep-ph\]](https://arxiv.org/abs/2409.12123).
- [66] Krishna Rajagopal, Bruno Scheihing-Hitschfeld, and Rachel Steinhorst. "Adiabatic Hydrodynamization and the emergence of attractors: a unified description of hydrodynamization in kinetic theory". In: *JHEP* 04 (2025), p. 028. DOI: [10.1007/JHEP04\(2025\)028](https://doi.org/10.1007/JHEP04(2025)028). arXiv: [2405.17545 \[hep-ph\]](https://arxiv.org/abs/2405.17545).
- [67] Michal P. Heller, David Mateos, Wilke van der Schee, and Diego Trancanelli. "Strong Coupling Isotropization of Non-Abelian Plasmas Simplified". In: *Phys. Rev. Lett.* 108 (2012), p. 191601. DOI: [10.1103/PhysRevLett.108.191601](https://doi.org/10.1103/PhysRevLett.108.191601). arXiv: [1202.0981 \[hep-th\]](https://arxiv.org/abs/1202.0981).
- [68] Michal P. Heller. "Holography, Hydrodynamization and Heavy-Ion Collisions". In: *Acta Phys. Polon. B* 47 (2016), p. 2581. DOI: [10.5506/APhysPolB.47.2581](https://doi.org/10.5506/APhysPolB.47.2581). arXiv: [1610.02023 \[hep-th\]](https://arxiv.org/abs/1610.02023).
- [69] Aleksas Mazeliauskas and Jürgen Berges. "Prescaling and far-from-equilibrium hydrodynamics in the quark-gluon plasma". In: *Phys. Rev. Lett.* 122.12 (2019), p. 122301. DOI: [10.1103/PhysRevLett.122.122301](https://doi.org/10.1103/PhysRevLett.122.122301). arXiv: [1810.10554 \[hep-ph\]](https://arxiv.org/abs/1810.10554).
- [70] Michal P. Heller, Aleksas Mazeliauskas, and Thimo Preis. "Prescaling Relaxation to Nonthermal Attractors". In: *Phys. Rev. Lett.* 132.7 (2024), p. 071602. DOI: [10.1103/PhysRevLett.132.071602](https://doi.org/10.1103/PhysRevLett.132.071602). arXiv: [2307.07545 \[hep-th\]](https://arxiv.org/abs/2307.07545).

- [71] Matisse De Lescluze and Michal P. Heller. "Quasinormal modes of nonthermal fixed points". In: (Feb. 2025). arXiv: [2502.01622 \[hep-th\]](https://arxiv.org/abs/2502.01622).
- [72] Jürgen Berges, Gabriel S. Denicol, Michal P. Heller, and Thimo Preis. "Far from equilibrium hydrodynamics of nonthermal fixed points". In: (Apr. 2025). arXiv: [2504.18754 \[hep-th\]](https://arxiv.org/abs/2504.18754).
- [73] Jasmine Brewer, Li Yan, and Yi Yin. "Adiabatic hydrodynamization in rapidly-expanding quark-gluon plasma". In: *Phys. Lett. B* 816 (2021), p. 136189. doi: [10.1016/j.physletb.2021.136189](https://doi.org/10.1016/j.physletb.2021.136189). arXiv: [1910.00021 \[nucl-th\]](https://arxiv.org/abs/1910.00021).
- [74] Jasmine Brewer, Bruno Scheihing-Hitschfeld, and Yi Yin. "Scaling and adiabaticity in a rapidly expanding gluon plasma". In: *JHEP* 05 (2022), p. 145. doi: [10.1007/JHEP05\(2022\)145](https://doi.org/10.1007/JHEP05(2022)145). arXiv: [2203.02427 \[hep-ph\]](https://arxiv.org/abs/2203.02427).
- [75] Aleksas Mazeliauskas and Tilman Enss. "Hydrodynamic attractor in periodically driven ultracold quantum gases". In: (Jan. 2025). arXiv: [2501.19240 \[cond-mat.quant-gas\]](https://arxiv.org/abs/2501.19240).
- [76] Carlota Andres, Néstor Armesto, Harri Niemi, Risto Paatelainen, and Carlos A. Salgado. "Jet quenching as a probe of the initial stages in heavy-ion collisions". In: *Phys. Lett. B* 803 (2020), p. 135318. doi: [10.1016/j.physletb.2020.135318](https://doi.org/10.1016/j.physletb.2020.135318). arXiv: [1902.03231 \[hep-ph\]](https://arxiv.org/abs/1902.03231).
- [77] Charles Gale, Jean-François Paquet, Björn Schenke, and Chun Shen. "Multimessenger heavy-ion collision physics". In: *Phys. Rev. C* 105.1 (2022), p. 014909. doi: [10.1103/PhysRevC.105.014909](https://doi.org/10.1103/PhysRevC.105.014909). arXiv: [2106.11216 \[nucl-th\]](https://arxiv.org/abs/2106.11216).
- [78] Dana Avramescu, Vincenzo Greco, Tuomas Lappi, Heikki Mäntysaari, and David Müller. "Heavy-Flavor Angular Correlations as a Direct Probe of the Glasma". In: *Phys. Rev. Lett.* 134.17 (2025), p. 172301. doi: [10.1103/PhysRevLett.134.172301](https://doi.org/10.1103/PhysRevLett.134.172301). arXiv: [2409.10565 \[hep-ph\]](https://arxiv.org/abs/2409.10565).
- [79] Z. Citron et al. "Report from Working Group 5: Future physics opportunities for high-density QCD at the LHC with heavy-ion and proton beams". In: *CERN Yellow Rep. Monogr.* 7 (2019). Ed. by Andrea Dainese, Michelangelo Mangano, Andreas B. Meyer, Aleandro Nisati, Gavin Salam, and Mika Anton Vesterinen, pp. 1159–1410. doi: [10.23731/CYRM-2019-007.1159](https://doi.org/10.23731/CYRM-2019-007.1159). arXiv: [1812.06772 \[hep-ph\]](https://arxiv.org/abs/1812.06772).
- [80] Jasmine Brewer, Aleksas Mazeliauskas, and Wilke van der Schee. "Opportunities of OO and p O collisions at the LHC". In: *Opportunities of OO and p O collisions at the LHC*. Mar. 2021. arXiv: [2103.01939 \[hep-ph\]](https://arxiv.org/abs/2103.01939).
- [81] Guang-You Qin and Xin-Nian Wang. "Jet quenching in high-energy heavy-ion collisions". In: *Int. J. Mod. Phys. E* 24.11 (2015). Ed. by Xin-Nian Wang, p. 1530014. doi: [10.1142/S0218301315300143](https://doi.org/10.1142/S0218301315300143). arXiv: [1511.00790 \[hep-ph\]](https://arxiv.org/abs/1511.00790).
- [82] Liliana Apolinário, Yen-Jie Lee, and Michael Winn. "Heavy quarks and jets as probes of the QGP". In: *Prog. Part. Nucl. Phys.* 127 (2022), p. 103990. doi: [10.1016/j.ppnp.2022.103990](https://doi.org/10.1016/j.ppnp.2022.103990). arXiv: [2203.16352 \[hep-ph\]](https://arxiv.org/abs/2203.16352).
- [83] B. G. Zakharov. "Fully quantum treatment of the Landau-Pomeranchuk-Migdal effect in QED and QCD". In: *JETP Lett.* 63 (1996), pp. 952–957. doi: [10.1134/1.567126](https://doi.org/10.1134/1.567126). arXiv: [hep-ph/9607440](https://arxiv.org/abs/hep-ph/9607440).

- [84] B. G. Zakharov. "Radiative energy loss of high-energy quarks in finite size nuclear matter and quark - gluon plasma". In: *JETP Lett.* 65 (1997), pp. 615–620. DOI: [10.1134/1.567389](https://doi.org/10.1134/1.567389). arXiv: [hep-ph/9704255](https://arxiv.org/abs/hep-ph/9704255).
- [85] B. G. Zakharov. "Light cone path integral approach to the Landau-Pomeranchuk-Migdal effect". In: *Phys. Atom. Nucl.* 61 (1998), pp. 838–854. arXiv: [hep-ph/9807540](https://arxiv.org/abs/hep-ph/9807540).
- [86] R. Baier, Yuri L. Dokshitzer, Alfred H. Mueller, S. Peigne, and D. Schiff. "Radiative energy loss of high-energy quarks and gluons in a finite volume quark - gluon plasma". In: *Nucl. Phys. B* 483 (1997), pp. 291–320. DOI: [10.1016/S0550-3213\(96\)00553-6](https://doi.org/10.1016/S0550-3213(96)00553-6). arXiv: [hep-ph/9607355](https://arxiv.org/abs/hep-ph/9607355).
- [87] R. Baier, Yuri L. Dokshitzer, Alfred H. Mueller, S. Peigne, and D. Schiff. "Radiative energy loss and p(T) broadening of high-energy partons in nuclei". In: *Nucl. Phys. B* 484 (1997), pp. 265–282. DOI: [10.1016/S0550-3213\(96\)00581-0](https://doi.org/10.1016/S0550-3213(96)00581-0). arXiv: [hep-ph/9608322](https://arxiv.org/abs/hep-ph/9608322).
- [88] R. Baier, D. Schiff, and B. G. Zakharov. "Energy loss in perturbative QCD". In: *Ann. Rev. Nucl. Part. Sci.* 50 (2000), pp. 37–69. DOI: [10.1146/annurev.nucl.50.1.37](https://doi.org/10.1146/annurev.nucl.50.1.37). arXiv: [hep-ph/0002198](https://arxiv.org/abs/hep-ph/0002198).
- [89] Miklos Gyulassy, Peter Levai, and Ivan Vitev. "Jet quenching in thin quark gluon plasmas. 1. Formalism". In: *Nucl. Phys. B* 571 (2000), pp. 197–233. DOI: [10.1016/S0550-3213\(99\)00713-0](https://doi.org/10.1016/S0550-3213(99)00713-0). arXiv: [hep-ph/9907461](https://arxiv.org/abs/hep-ph/9907461).
- [90] M. Gyulassy, P. Levai, and I. Vitev. "Reaction operator approach to non-Abelian energy loss". In: *Nucl. Phys. B* 594 (2001), pp. 371–419. DOI: [10.1016/S0550-3213\(00\)00652-0](https://doi.org/10.1016/S0550-3213(00)00652-0). arXiv: [nucl-th/0006010](https://arxiv.org/abs/nucl-th/0006010).
- [91] Miklos Gyulassy, Ivan Vitev, Xin-Nian Wang, and Ben-Wei Zhang. "Jet quenching and radiative energy loss in dense nuclear matter". In: (2004). Ed. by R. C. Hwa and X. N. Wang, pp. 123–191. DOI: [10.1142/9789812795533_0003](https://doi.org/10.1142/9789812795533_0003). arXiv: [nucl-th/0302077](https://arxiv.org/abs/nucl-th/0302077).
- [92] Urs Achim Wiedemann. "Gluon radiation off hard quarks in a nuclear environment: Opacity expansion". In: *Nucl. Phys. B* 588 (2000), pp. 303–344. DOI: [10.1016/S0550-3213\(00\)00457-0](https://doi.org/10.1016/S0550-3213(00)00457-0). arXiv: [hep-ph/0005129](https://arxiv.org/abs/hep-ph/0005129).
- [93] Carlos A. Salgado and Urs Achim Wiedemann. "Calculating quenching weights". In: *Phys. Rev. D* 68 (2003), p. 014008. DOI: [10.1103/PhysRevD.68.014008](https://doi.org/10.1103/PhysRevD.68.014008). arXiv: [hep-ph/0302184](https://arxiv.org/abs/hep-ph/0302184).
- [94] Peter Brockway Arnold, Guy D. Moore, and Laurence G. Yaffe. "Photon and gluon emission in relativistic plasmas". In: *JHEP* 06 (2002), p. 030. DOI: [10.1088/1126-6708/2002/06/030](https://doi.org/10.1088/1126-6708/2002/06/030). arXiv: [hep-ph/0204343](https://arxiv.org/abs/hep-ph/0204343).
- [95] Magdalena Djordjevic and Ulrich W. Heinz. "Radiative energy loss in a finite dynamical QCD medium". In: *Phys. Rev. Lett.* 101 (2008), p. 022302. DOI: [10.1103/PhysRevLett.101.022302](https://doi.org/10.1103/PhysRevLett.101.022302). arXiv: [0802.1230 \[nucl-th\]](https://arxiv.org/abs/0802.1230).
- [96] Peter Brockway Arnold. "Simple Formula for High-Energy Gluon Bremsstrahlung in a Finite, Expanding Medium". In: *Phys. Rev. D* 79 (2009), p. 065025. DOI: [10.1103/PhysRevD.79.065025](https://doi.org/10.1103/PhysRevD.79.065025). arXiv: [0808.2767 \[hep-ph\]](https://arxiv.org/abs/0808.2767).

- [97] Simon Caron-Huot and Charles Gale. "Finite-size effects on the radiative energy loss of a fast parton in hot and dense strongly interacting matter". In: *Phys. Rev. C* 82 (2010), p. 064902. DOI: [10.1103/PhysRevC.82.064902](https://doi.org/10.1103/PhysRevC.82.064902). arXiv: [1006.2379 \[hep-ph\]](https://arxiv.org/abs/1006.2379).
- [98] Jean-Paul Blaizot, Fabio Dominguez, Edmond Iancu, and Yacine Mehtar-Tani. "Medium-induced gluon branching". In: *JHEP* 01 (2013), p. 143. DOI: [10.1007/JHEP01\(2013\)143](https://doi.org/10.1007/JHEP01(2013)143). arXiv: [1209.4585 \[hep-ph\]](https://arxiv.org/abs/1209.4585).
- [99] Nestor Armesto et al. "Comparison of Jet Quenching Formalisms for a Quark-Gluon Plasma 'Brick'". In: *Phys. Rev. C* 86 (2012), p. 064904. DOI: [10.1103/PhysRevC.86.064904](https://doi.org/10.1103/PhysRevC.86.064904). arXiv: [1106.1106 \[hep-ph\]](https://arxiv.org/abs/1106.1106).
- [100] P. Aurenche, F. Gelis, and H. Zaraket. "A Simple sum rule for the thermal gluon spectral function and applications". In: *JHEP* 05 (2002), p. 043. DOI: [10.1088/1126-6708/2002/05/043](https://doi.org/10.1088/1126-6708/2002/05/043). arXiv: [hep-ph/0204146](https://arxiv.org/abs/hep-ph/0204146).
- [101] Peter Brockway Arnold and Wei Xiao. "High-energy jet quenching in weakly-coupled quark-gluon plasmas". In: *Phys. Rev. D* 78 (2008), p. 125008. DOI: [10.1103/PhysRevD.78.125008](https://doi.org/10.1103/PhysRevD.78.125008). arXiv: [0810.1026 \[hep-ph\]](https://arxiv.org/abs/0810.1026).
- [102] Simon Caron-Huot. "O(g) plasma effects in jet quenching". In: *Phys. Rev. D* 79 (2009), p. 065039. DOI: [10.1103/PhysRevD.79.065039](https://doi.org/10.1103/PhysRevD.79.065039). arXiv: [0811.1603 \[hep-ph\]](https://arxiv.org/abs/0811.1603).
- [103] Hong Liu, Krishna Rajagopal, and Urs Achim Wiedemann. "Calculating the jet quenching parameter from AdS/CFT". In: *Phys. Rev. Lett.* 97 (2006), p. 182301. DOI: [10.1103/PhysRevLett.97.182301](https://doi.org/10.1103/PhysRevLett.97.182301). arXiv: [hep-ph/0605178](https://arxiv.org/abs/hep-ph/0605178).
- [104] Hong Liu, Krishna Rajagopal, and Urs Achim Wiedemann. "Wilson loops in heavy ion collisions and their calculation in AdS/CFT". In: *JHEP* 03 (2007), p. 066. DOI: [10.1088/1126-6708/2007/03/066](https://doi.org/10.1088/1126-6708/2007/03/066). arXiv: [hep-ph/0612168](https://arxiv.org/abs/hep-ph/0612168).
- [105] Nestor Armesto, Jose D. Edelstein, and Javier Mas. "Jet quenching at finite 't Hooft coupling and chemical potential from AdS/CFT". In: *JHEP* 09 (2006), p. 039. DOI: [10.1088/1126-6708/2006/09/039](https://doi.org/10.1088/1126-6708/2006/09/039). arXiv: [hep-ph/0606245](https://arxiv.org/abs/hep-ph/0606245).
- [106] Francesco D'Eramo, Hong Liu, and Krishna Rajagopal. "Transverse Momentum Broadening and the Jet Quenching Parameter, Redux". In: *Phys. Rev. D* 84 (2011), p. 065015. DOI: [10.1103/PhysRevD.84.065015](https://doi.org/10.1103/PhysRevD.84.065015). arXiv: [1006.1367 \[hep-ph\]](https://arxiv.org/abs/1006.1367).
- [107] Zi-qiang Zhang, De-fu Hou, and Hai-cang Ren. "The finite 't Hooft coupling correction on jet quenching parameter in a $\mathcal{N} = 4$ Super Yang-Mills Plasma". In: *JHEP* 01 (2013), p. 032. DOI: [10.1007/JHEP01\(2013\)032](https://doi.org/10.1007/JHEP01(2013)032). arXiv: [1210.5187 \[hep-th\]](https://arxiv.org/abs/1210.5187).
- [108] Amit Kumar, Abhijit Majumder, and Johannes Heinrich Weber. "Jet transport coefficient q^{γ} in lattice QCD". In: *Phys. Rev. D* 106.3 (2022), p. 034505. DOI: [10.1103/PhysRevD.106.034505](https://doi.org/10.1103/PhysRevD.106.034505). arXiv: [2010.14463 \[hep-lat\]](https://arxiv.org/abs/2010.14463).
- [109] Marco Panero, Kari Rummukainen, and Andreas Schäfer. "Lattice Study of the Jet Quenching Parameter". In: *Phys. Rev. Lett.* 112.16 (2014), p. 162001. DOI: [10.1103/PhysRevLett.112.162001](https://doi.org/10.1103/PhysRevLett.112.162001). arXiv: [1307.5850 \[hep-ph\]](https://arxiv.org/abs/1307.5850).

- [110] Guy D. Moore, Soeren Schlichting, Niels Schluesser, and Ismail Soudi. "Non-perturbative determination of collisional broadening and medium induced radiation in QCD plasmas". In: *JHEP* 10 (2021), p. 059. doi: [10.1007/JHEP10\(2021\)059](https://doi.org/10.1007/JHEP10(2021)059). arXiv: [2105.01679 \[hep-ph\]](https://arxiv.org/abs/2105.01679).
- [111] Ilia Grishmanovskii, Taesoo Song, Olga Soloveva, Carsten Greiner, and Elena Bratkovskaya. "Exploring jet transport coefficients by elastic scattering in the strongly interacting quark-gluon plasma". In: *Phys. Rev. C* 106.1 (2022), p. 014903. doi: [10.1103/PhysRevC.106.014903](https://doi.org/10.1103/PhysRevC.106.014903). arXiv: [2204.01561 \[nucl-th\]](https://arxiv.org/abs/2204.01561).
- [112] Taesoo Song, Ilia Grishmanovskii, and Olga Soloveva. "Soft gluon emission from heavy quark scattering in strongly interacting quark-gluon plasma". In: *Phys. Rev. D* 107.3 (2023), p. 036009. doi: [10.1103/PhysRevD.107.036009](https://doi.org/10.1103/PhysRevD.107.036009). arXiv: [2210.04010 \[nucl-th\]](https://arxiv.org/abs/2210.04010).
- [113] Ilia Grishmanovskii, Olga Soloveva, Taesoo Song, Carsten Greiner, and Elena Bratkovskaya. "Jet transport coefficients by elastic and radiative scatterings in the strongly interacting quark-gluon plasma". In: *Phys. Rev. C* 110.1 (2024), p. 014908. doi: [10.1103/PhysRevC.110.014908](https://doi.org/10.1103/PhysRevC.110.014908). arXiv: [2402.04923 \[hep-ph\]](https://arxiv.org/abs/2402.04923).
- [114] Karen M. Burke et al. "Extracting the jet transport coefficient from jet quenching in high-energy heavy-ion collisions". In: *Phys. Rev. C* 90.1 (2014), p. 014909. doi: [10.1103/PhysRevC.90.014909](https://doi.org/10.1103/PhysRevC.90.014909). arXiv: [1312.5003 \[nucl-th\]](https://arxiv.org/abs/1312.5003).
- [115] S. Cao et al. "Determining the jet transport coefficient \hat{q} from inclusive hadron suppression measurements using Bayesian parameter estimation". In: *Phys. Rev. C* 104.2 (2021), p. 024905. doi: [10.1103/PhysRevC.104.024905](https://doi.org/10.1103/PhysRevC.104.024905). arXiv: [2102.11337 \[nucl-th\]](https://arxiv.org/abs/2102.11337).
- [116] Man Xie, Weiyao Ke, Hanzhong Zhang, and Xin-Nian Wang. "Information-field-based global Bayesian inference of the jet transport coefficient". In: *Phys. Rev. C* 108.1 (2023), p. L011901. doi: [10.1103/PhysRevC.108.L011901](https://doi.org/10.1103/PhysRevC.108.L011901). arXiv: [2206.01340 \[hep-ph\]](https://arxiv.org/abs/2206.01340).
- [117] R. Ehlers et al. "Bayesian inference analysis of jet quenching using inclusive jet and hadron suppression measurements". In: *Phys. Rev. C* 111.5 (2025), p. 054913. doi: [10.1103/PhysRevC.111.054913](https://doi.org/10.1103/PhysRevC.111.054913). arXiv: [2408.08247 \[hep-ph\]](https://arxiv.org/abs/2408.08247).
- [118] Yayun He, Tan Luo, Xin-Nian Wang, and Yan Zhu. "Linear Boltzmann Transport for Jet Propagation in the Quark-Gluon Plasma: Elastic Processes and Medium Recoil". In: *Phys. Rev. C* 91 (2015). [Erratum: *Phys. Rev. C* 97, 019902 (2018)], p. 054908. doi: [10.1103/PhysRevC.91.054908](https://doi.org/10.1103/PhysRevC.91.054908). arXiv: [1503.03313 \[nucl-th\]](https://arxiv.org/abs/1503.03313).
- [119] Soeren Schlichting and Ismail Soudi. "Medium-induced fragmentation and equilibration of highly energetic partons". In: *JHEP* 07 (2021), p. 077. doi: [10.1007/JHEP07\(2021\)077](https://doi.org/10.1007/JHEP07(2021)077). arXiv: [2008.04928 \[hep-ph\]](https://arxiv.org/abs/2008.04928).
- [120] Y. Mehtar-Tani, S. Schlichting, and I. Soudi. "Jet thermalization in QCD kinetic theory". In: *JHEP* 05 (2023), p. 091. doi: [10.1007/JHEP05\(2023\)091](https://doi.org/10.1007/JHEP05(2023)091). arXiv: [2209.10569 \[hep-ph\]](https://arxiv.org/abs/2209.10569).

- [121] Peter Brockway Arnold and Caglar Dogan. "QCD Splitting/Joining Functions at Finite Temperature in the Deep LPM Regime". In: *Phys. Rev. D* 78 (2008), p. 065008. DOI: [10.1103/PhysRevD.78.065008](https://doi.org/10.1103/PhysRevD.78.065008). arXiv: [0804.3359 \[hep-ph\]](https://arxiv.org/abs/0804.3359).
- [122] Yacine Mehtar-Tani. "Gluon bremsstrahlung in finite media beyond multiple soft scattering approximation". In: *JHEP* 07 (2019), p. 057. DOI: [10.1007/JHEP07\(2019\)057](https://doi.org/10.1007/JHEP07(2019)057). arXiv: [1903.00506 \[hep-ph\]](https://arxiv.org/abs/1903.00506).
- [123] Yacine Mehtar-Tani and Konrad Tywoniuk. "Improved opacity expansion for medium-induced parton splitting". In: *JHEP* 06 (2020), p. 187. DOI: [10.1007/JHEP06\(2020\)187](https://doi.org/10.1007/JHEP06(2020)187). arXiv: [1910.02032 \[hep-ph\]](https://arxiv.org/abs/1910.02032).
- [124] João Barata, Yacine Mehtar-Tani, Alba Soto-Ontoso, and Konrad Tywoniuk. "Medium-induced radiative kernel with the Improved Opacity Expansion". In: *JHEP* 09 (2021), p. 153. DOI: [10.1007/JHEP09\(2021\)153](https://doi.org/10.1007/JHEP09(2021)153). arXiv: [2106.07402 \[hep-ph\]](https://arxiv.org/abs/2106.07402).
- [125] Carlota Andres, Liliana Apolinário, and Fabio Dominguez. "Medium-induced gluon radiation with full resummation of multiple scatterings for realistic parton-medium interactions". In: *JHEP* 07 (2020), p. 114. DOI: [10.1007/JHEP07\(2020\)114](https://doi.org/10.1007/JHEP07(2020)114). arXiv: [2002.01517 \[hep-ph\]](https://arxiv.org/abs/2002.01517).
- [126] Soeren Schlichting and Ismail Soudi. "Splitting rates in QCD plasmas from a nonperturbative determination of the momentum broadening kernel $C(q_\perp)$ ". In: *Phys. Rev. D* 105.7 (2022), p. 076002. DOI: [10.1103/PhysRevD.105.076002](https://doi.org/10.1103/PhysRevD.105.076002). arXiv: [2111.13731 \[hep-ph\]](https://arxiv.org/abs/2111.13731).
- [127] Carlota Andres, Liliana Apolinário, Fabio Dominguez, and Marcos Gonzalez Martinez. "In-medium gluon radiation spectrum with all-order resummation of multiple scatterings in longitudinally evolving media". In: *JHEP* 11 (2024), p. 025. DOI: [10.1007/JHEP11\(2024\)025](https://doi.org/10.1007/JHEP11(2024)025). arXiv: [2307.06226 \[hep-ph\]](https://arxiv.org/abs/2307.06226).
- [128] Rouzbeh Modarresi Yazdi, Shuzhe Shi, Charles Gale, and Sangyong Jeon. "Leading order, next-to-leading order, and nonperturbative parton collision kernels: Effects in static and evolving media". In: *Phys. Rev. C* 106.6 (2022), p. 064902. DOI: [10.1103/PhysRevC.106.064902](https://doi.org/10.1103/PhysRevC.106.064902). arXiv: [2206.05855 \[hep-ph\]](https://arxiv.org/abs/2206.05855).
- [129] Rouzbeh Modarresi-Yazdi, Shuzhe Shi, Charles Gale, and Sangyong Jeon. "QCD jets in a hot and dense medium: A study of shower formation time and collision kernels". In: *Phys. Rev. C* 111.5 (2025), p. 054904. DOI: [10.1103/PhysRevC.111.054904](https://doi.org/10.1103/PhysRevC.111.054904). arXiv: [2407.19966 \[hep-ph\]](https://arxiv.org/abs/2407.19966).
- [130] Paul Romatschke and Michael Strickland. "Collisional energy loss of a heavy quark in an anisotropic quark-gluon plasma". In: *Phys. Rev. D* 71 (2005), p. 125008. DOI: [10.1103/PhysRevD.71.125008](https://doi.org/10.1103/PhysRevD.71.125008). arXiv: [hep-ph/0408275](https://arxiv.org/abs/hep-ph/0408275).
- [131] Paul Romatschke. "Momentum broadening in an anisotropic plasma". In: *Phys. Rev. C* 75 (2007), p. 014901. DOI: [10.1103/PhysRevC.75.014901](https://doi.org/10.1103/PhysRevC.75.014901). arXiv: [hep-ph/0607327](https://arxiv.org/abs/hep-ph/0607327).
- [132] Adrian Dumitru, Yasushi Nara, Bjoern Schenke, and Michael Strickland. "Jet broadening in unstable non-Abelian plasmas". In: *Phys. Rev. C* 78 (2008), p. 024909. DOI: [10.1103/PhysRevC.78.024909](https://doi.org/10.1103/PhysRevC.78.024909). arXiv: [0710.1223 \[hep-ph\]](https://arxiv.org/abs/0710.1223).

- [133] Sigtryggur Hauksson, Sangyong Jeon, and Charles Gale. "Momentum broadening of energetic partons in an anisotropic plasma". In: *Phys. Rev. C* 105.1 (2022), p. 014914. DOI: [10.1103/PhysRevC.105.014914](https://doi.org/10.1103/PhysRevC.105.014914). arXiv: [2109.04575](https://arxiv.org/abs/2109.04575) [hep-ph].
- [134] Andrey V. Sadofyev, Matthew D. Sievert, and Ivan Vitev. "Ab initio coupling of jets to collective flow in the opacity expansion approach". In: *Phys. Rev. D* 104.9 (2021), p. 094044. DOI: [10.1103/PhysRevD.104.094044](https://doi.org/10.1103/PhysRevD.104.094044). arXiv: [2104.09513](https://arxiv.org/abs/2104.09513) [hep-ph].
- [135] Carlota Andres, Fabio Dominguez, Andrey V. Sadofyev, and Carlos A. Salgado. "Jet broadening in flowing matter: Resummation". In: *Phys. Rev. D* 106.7 (2022), p. 074023. DOI: [10.1103/PhysRevD.106.074023](https://doi.org/10.1103/PhysRevD.106.074023). arXiv: [2207.07141](https://arxiv.org/abs/2207.07141) [hep-ph].
- [136] João Barata, Andrey V. Sadofyev, and Carlos A. Salgado. "Jet broadening in dense inhomogeneous matter". In: *Phys. Rev. D* 105.11 (2022), p. 114010. DOI: [10.1103/PhysRevD.105.114010](https://doi.org/10.1103/PhysRevD.105.114010). arXiv: [2202.08847](https://arxiv.org/abs/2202.08847) [hep-ph].
- [137] João Barata, Xoán Mayo López, Andrey V. Sadofyev, and Carlos A. Salgado. "Medium induced gluon spectrum in dense inhomogeneous matter". In: *Phys. Rev. D* 108.3 (2023), p. 034018. DOI: [10.1103/PhysRevD.108.034018](https://doi.org/10.1103/PhysRevD.108.034018). arXiv: [2304.03712](https://arxiv.org/abs/2304.03712) [hep-ph].
- [138] Matvey V. Kuzmin, Xoán Mayo López, Jared Reiten, and Andrey V. Sadofyev. "Jet quenching in anisotropic flowing matter". In: *Phys. Rev. D* 109.1 (2024), p. 014036. DOI: [10.1103/PhysRevD.109.014036](https://doi.org/10.1103/PhysRevD.109.014036). arXiv: [2309.00683](https://arxiv.org/abs/2309.00683) [hep-ph].
- [139] João Barata, Sigtryggur Hauksson, Xoán Mayo López, and Andrey V. Sadofyev. "Jet quenching in the glasma phase: Medium-induced radiation". In: *Phys. Rev. D* 110.9 (2024), p. 094055. DOI: [10.1103/PhysRevD.110.094055](https://doi.org/10.1103/PhysRevD.110.094055). arXiv: [2406.07615](https://arxiv.org/abs/2406.07615) [hep-ph].
- [140] Steffen A. Bass, Charles Gale, Abhijit Majumder, Chiho Nonaka, Guang-You Qin, Thorsten Renk, and Jorg Ruppert. "Systematic Comparison of Jet Energy-Loss Schemes in a realistic hydrodynamic medium". In: *Phys. Rev. C* 79 (2009), p. 024901. DOI: [10.1103/PhysRevC.79.024901](https://doi.org/10.1103/PhysRevC.79.024901). arXiv: [0808.0908](https://arxiv.org/abs/0808.0908) [nucl-th].
- [141] Bjoern Schenke, Charles Gale, and Sangyong Jeon. "MARTINI: An Event generator for relativistic heavy-ion collisions". In: *Phys. Rev. C* 80 (2009), p. 054913. DOI: [10.1103/PhysRevC.80.054913](https://doi.org/10.1103/PhysRevC.80.054913). arXiv: [0909.2037](https://arxiv.org/abs/0909.2037) [hep-ph].
- [142] Korinna C. Zapp, Frank Krauss, and Urs A. Wiedemann. "A perturbative framework for jet quenching". In: *JHEP* 03 (2013), p. 080. DOI: [10.1007/JHEP03\(2013\)080](https://doi.org/10.1007/JHEP03(2013)080). arXiv: [1212.1599](https://arxiv.org/abs/1212.1599) [hep-ph].
- [143] Jorge Casalderrey-Solana, Doga Can Gulhan, José Guilherme Milhano, Daniel Pablos, and Krishna Rajagopal. "A Hybrid Strong/Weak Coupling Approach to Jet Quenching". In: *JHEP* 10 (2014). [Erratum: *JHEP* 09, 175 (2015)], p. 019. DOI: [10.1007/JHEP09\(2015\)175](https://doi.org/10.1007/JHEP09(2015)175). arXiv: [1405.3864](https://arxiv.org/abs/1405.3864) [hep-ph].

- [144] Shanshan Cao, Tan Luo, Guang-You Qin, and Xin-Nian Wang. "Heavy and light flavor jet quenching at RHIC and LHC energies". In: *Phys. Lett. B* 777 (2018), pp. 255–259. DOI: [10.1016/j.physletb.2017.12.023](https://doi.org/10.1016/j.physletb.2017.12.023). arXiv: [1703.00822 \[nucl-th\]](https://arxiv.org/abs/1703.00822).
- [145] Alexander Huss, Aleksi Kurkela, Aleksas Mazeliauskas, Risto Paatelainen, Wilke van der Schee, and Urs Achim Wiedemann. "Discovering Partonic Rescattering in Light Nucleus Collisions". In: *Phys. Rev. Lett.* 126.19 (2021), p. 192301. DOI: [10.1103/PhysRevLett.126.192301](https://doi.org/10.1103/PhysRevLett.126.192301). arXiv: [2007.13754 \[hep-ph\]](https://arxiv.org/abs/2007.13754).
- [146] Alexander Huss, Aleksi Kurkela, Aleksas Mazeliauskas, Risto Paatelainen, Wilke van der Schee, and Urs Achim Wiedemann. "Predicting parton energy loss in small collision systems". In: *Phys. Rev. C* 103.5 (2021), p. 054903. DOI: [10.1103/PhysRevC.103.054903](https://doi.org/10.1103/PhysRevC.103.054903). arXiv: [2007.13758 \[hep-ph\]](https://arxiv.org/abs/2007.13758).
- [147] Dusan Zivic, Bojana Ilic, Marko Djordjevic, and Magdalena Djordjevic. "Exploring the initial stages in heavy-ion collisions with high- p_{\perp} R_{AA} and v_2 theory and data". In: *Phys. Rev. C* 101.6 (2020), p. 064909. DOI: [10.1103/PhysRevC.101.064909](https://doi.org/10.1103/PhysRevC.101.064909). arXiv: [1908.11866 \[hep-ph\]](https://arxiv.org/abs/1908.11866).
- [148] Carlota Andres, Liliana Apolinário, Fabio Dominguez, Marcos Gonzalez Martinez, and Carlos A. Salgado. "Medium-induced radiation with vacuum propagation in the pre-hydrodynamics phase". In: *JHEP* 03 (2023), p. 189. DOI: [10.1007/JHEP03\(2023\)189](https://doi.org/10.1007/JHEP03(2023)189). arXiv: [2211.10161 \[hep-ph\]](https://arxiv.org/abs/2211.10161).
- [149] A. Kumar et al. "Inclusive jet and hadron suppression in a multistage approach". In: *Phys. Rev. C* 107.3 (2023), p. 034911. DOI: [10.1103/PhysRevC.107.034911](https://doi.org/10.1103/PhysRevC.107.034911). arXiv: [2204.01163 \[hep-ph\]](https://arxiv.org/abs/2204.01163).
- [150] Shuzhe Shi, Rouzbeh Modarresi Yazdi, Charles Gale, and Sangyong Jeon. "Comparing the martini and cujet models for jet quenching: Medium modification of jets and jet substructure". In: *Phys. Rev. C* 107.3 (2023), p. 034908. DOI: [10.1103/PhysRevC.107.034908](https://doi.org/10.1103/PhysRevC.107.034908). arXiv: [2212.05944 \[hep-ph\]](https://arxiv.org/abs/2212.05944).
- [151] Y. Tachibana et al. "Hard jet substructure in a multistage approach". In: *Phys. Rev. C* 110.4 (2024), p. 044907. DOI: [10.1103/PhysRevC.110.044907](https://doi.org/10.1103/PhysRevC.110.044907). arXiv: [2301.02485 \[hep-ph\]](https://arxiv.org/abs/2301.02485).
- [152] Andreas Ipp, David I. Müller, and Daniel Schuh. "Anisotropic momentum broadening in the 2+1D Glasma: analytic weak field approximation and lattice simulations". In: *Phys. Rev. D* 102.7 (2020), p. 074001. DOI: [10.1103/PhysRevD.102.074001](https://doi.org/10.1103/PhysRevD.102.074001). arXiv: [2001.10001 \[hep-ph\]](https://arxiv.org/abs/2001.10001).
- [153] Andreas Ipp, David I. Müller, and Daniel Schuh. "Jet momentum broadening in the pre-equilibrium Glasma". In: *Phys. Lett. B* 810 (2020), p. 135810. DOI: [10.1016/j.physletb.2020.135810](https://doi.org/10.1016/j.physletb.2020.135810). arXiv: [2009.14206 \[hep-ph\]](https://arxiv.org/abs/2009.14206).
- [154] Margaret E. Carrington, Alina Czajka, and Stanislaw Mrowczynski. "Heavy Quarks Embedded in Glasma". In: *Nucl. Phys. A* 1001 (2020), p. 121914. DOI: [10.1016/j.nuclphysa.2020.121914](https://doi.org/10.1016/j.nuclphysa.2020.121914). arXiv: [2001.05074 \[nucl-th\]](https://arxiv.org/abs/2001.05074).
- [155] Margaret E. Carrington, Alina Czajka, and Stanislaw Mrowczynski. "Jet quenching in glasma". In: *Phys. Lett. B* 834 (2022), p. 137464. DOI: [10.1016/j.physletb.2022.137464](https://doi.org/10.1016/j.physletb.2022.137464). arXiv: [2112.06812 \[hep-ph\]](https://arxiv.org/abs/2112.06812).

- [156] Margaret E. Carrington, Alina Czajka, and Stanislaw Mrowczynski. "Transport of hard probes through glasma". In: *Phys. Rev. C* 105.6 (2022), p. 064910. doi: [10.1103/PhysRevC.105.064910](https://doi.org/10.1103/PhysRevC.105.064910). arXiv: [2202.00357 \[nucl-th\]](https://arxiv.org/abs/2202.00357).
- [157] Dana Avramescu, Virgil Băran, Vincenzo Greco, Andreas Ipp, David. I. Müller, and Marco Ruggieri. "Simulating jets and heavy quarks in the glasma using the colored particle-in-cell method". In: *Phys. Rev. D* 107.11 (2023), p. 114021. doi: [10.1103/PhysRevD.107.114021](https://doi.org/10.1103/PhysRevD.107.114021). arXiv: [2303.05599 \[hep-ph\]](https://arxiv.org/abs/2303.05599).
- [158] Soeren Schlichting and Derek Teaney. "The First fm/c of Heavy-Ion Collisions". In: *Ann. Rev. Nucl. Part. Sci.* 69 (2019), pp. 447–476. doi: [10.1146/annurev-nucl-101918-023825](https://doi.org/10.1146/annurev-nucl-101918-023825). arXiv: [1908.02113 \[nucl-th\]](https://arxiv.org/abs/1908.02113).
- [159] Aleksi Kurkela and Guy D. Moore. "Thermalization in Weakly Coupled Nonabelian Plasmas". In: *JHEP* 12 (2011), p. 044. doi: [10.1007/JHEP12\(2011\)044](https://doi.org/10.1007/JHEP12(2011)044). arXiv: [1107.5050 \[hep-ph\]](https://arxiv.org/abs/1107.5050).
- [160] Lev Davidovich Landau and I. Pomeranchuk. "The Limits of Applicability of the Theory of Bremsstrahlung by Electrons and of the Creation of Pairs at Large Energies". In: *Dokl. Akad. Nauk SSSR* 92 (1953). Ed. by D. ter Haar. doi: [10.1016/b978-0-08-010586-4.50080-8](https://doi.org/10.1016/b978-0-08-010586-4.50080-8).
- [161] A. B. Migdal. "Bremsstrahlung and pair production in condensed media at high-energies". In: *Phys. Rev.* 103 (1956), pp. 1811–1820. doi: [10.1103/PhysRev.103.1811](https://doi.org/10.1103/PhysRev.103.1811).
- [162] Liliana Apolinário, Néstor Armesto, José Guilherme Milhano, and Carlos A. Salgado. "Medium-induced gluon radiation and colour decoherence beyond the soft approximation". In: *JHEP* 02 (2015), p. 119. doi: [10.1007/JHEP02\(2015\)119](https://doi.org/10.1007/JHEP02(2015)119). arXiv: [1407.0599 \[hep-ph\]](https://arxiv.org/abs/1407.0599).
- [163] Eric Braaten and Robert D. Pisarski. "Soft Amplitudes in Hot Gauge Theories: A General Analysis". In: *Nucl. Phys. B* 337 (1990), pp. 569–634. doi: [10.1016/0550-3213\(90\)90508-B](https://doi.org/10.1016/0550-3213(90)90508-B).
- [164] Eric Braaten and Robert D. Pisarski. "Deducing Hard Thermal Loops From Ward Identities". In: *Nucl. Phys. B* 339 (1990), pp. 310–324. doi: [10.1016/0550-3213\(90\)90351-D](https://doi.org/10.1016/0550-3213(90)90351-D).
- [165] J. Frenkel and J. C. Taylor. "High Temperature Limit of Thermal QCD". In: *Nucl. Phys. B* 334 (1990), pp. 199–216. doi: [10.1016/0550-3213\(90\)90661-V](https://doi.org/10.1016/0550-3213(90)90661-V).
- [166] Stanislaw Mrowczynski and Markus H. Thoma. "Hard loop approach to anisotropic systems". In: *Phys. Rev. D* 62 (2000), p. 036011. doi: [10.1103/PhysRevD.62.036011](https://doi.org/10.1103/PhysRevD.62.036011). arXiv: [hep-ph/0001164](https://arxiv.org/abs/hep-ph/0001164).
- [167] Stanislaw Mrowczynski, Anton Rebhan, and Michael Strickland. "Hard loop effective action for anisotropic plasmas". In: *Phys. Rev. D* 70 (2004), p. 025004. doi: [10.1103/PhysRevD.70.025004](https://doi.org/10.1103/PhysRevD.70.025004). arXiv: [hep-ph/0403256](https://arxiv.org/abs/hep-ph/0403256).
- [168] Michael E. Peskin and Daniel V. Schroeder. *An Introduction to quantum field theory*. Reading, USA: Addison-Wesley, 1995. ISBN: 978-0-201-50397-5, 978-0-429-50355-9, 978-0-429-49417-8. doi: [10.1201/9780429503559](https://doi.org/10.1201/9780429503559).

- [169] Mark C. Abraao York, Aleksi Kurkela, Egang Lu, and Guy D. Moore. "UV cascade in classical Yang-Mills theory via kinetic theory". In: *Phys. Rev. D* 89.7 (2014), p. 074036. DOI: [10.1103/PhysRevD.89.074036](https://doi.org/10.1103/PhysRevD.89.074036). arXiv: [1401.3751](https://arxiv.org/abs/1401.3751) [hep-ph].
- [170] Aleksi Kurkela and Florian Lindenbauer. *EKTqhat - Effective kinetic theory solver with jet quenching parameter*. Dec. 2023. DOI: [10.5281/zenodo.10409474](https://doi.org/10.5281/zenodo.10409474). URL: <https://doi.org/10.5281/zenodo.10409474>.
- [171] Peter Brockway Arnold, Jonathan Lenaghan, and Guy D. Moore. "QCD plasma instabilities and bottom up thermalization". In: *JHEP* 08 (2003), p. 002. DOI: [10.1088/1126-6708/2003/08/002](https://doi.org/10.1088/1126-6708/2003/08/002). arXiv: [hep-ph/0307325](https://arxiv.org/abs/hep-ph/0307325).
- [172] K. Boguslavski, A. Kurkela, T. Lappi, and J. Peuron. "Spectral function for overoccupied gluodynamics from real-time lattice simulations". In: *Phys. Rev. D* 98.1 (2018), p. 014006. DOI: [10.1103/PhysRevD.98.014006](https://doi.org/10.1103/PhysRevD.98.014006). arXiv: [1804.01966](https://arxiv.org/abs/1804.01966) [hep-ph].
- [173] K. Boguslavski, A. Kurkela, T. Lappi, and J. Peuron. "Broad excitations in a 2+1D overoccupied gluon plasma". In: *JHEP* 05 (2021), p. 225. DOI: [10.1007/JHEP05\(2021\)225](https://doi.org/10.1007/JHEP05(2021)225). arXiv: [2101.02715](https://arxiv.org/abs/2101.02715) [hep-ph].
- [174] Kirill Boguslavski, Tuomas Lappi, Mark Mace, and Sören Schlichting. "Spectral function of fermions in a highly occupied non-Abelian plasma". In: *Phys. Lett. B* 827 (2022), p. 136963. DOI: [10.1016/j.physletb.2022.136963](https://doi.org/10.1016/j.physletb.2022.136963). arXiv: [2106.11319](https://arxiv.org/abs/2106.11319) [hep-ph].
- [175] Leo P. Kadanoff and Gordon Baym. *Quantum Statistical Mechanics*. New York: W.A. Benjamin, 1962.
- [176] E. Calzetta and B. L. Hu. "Nonequilibrium Quantum Fields: Closed Time Path Effective Action, Wigner Function and Boltzmann Equation". In: *Phys. Rev. D* 37 (1988), p. 2878. DOI: [10.1103/PhysRevD.37.2878](https://doi.org/10.1103/PhysRevD.37.2878).
- [177] Jean-Paul Blaizot and Edmond Iancu. "The Quark gluon plasma: Collective dynamics and hard thermal loops". In: *Phys. Rept.* 359 (2002), pp. 355–528. DOI: [10.1016/S0370-1573\(01\)00061-8](https://doi.org/10.1016/S0370-1573(01)00061-8). arXiv: [hep-ph/0101103](https://arxiv.org/abs/hep-ph/0101103).
- [178] Juergen Berges. "N-particle irreducible effective action techniques for gauge theories". In: *Phys. Rev. D* 70 (2004), p. 105010. DOI: [10.1103/PhysRevD.70.105010](https://doi.org/10.1103/PhysRevD.70.105010). arXiv: [hep-ph/0401172](https://arxiv.org/abs/hep-ph/0401172).
- [179] Juergen Berges. "Introduction to nonequilibrium quantum field theory". In: *AIP Conf. Proc.* 739.1 (2004). Ed. by Mirian Bracco, Marcelo Chiapparini, Erasmo Ferreira, and Takeshi Kodama, pp. 3–62. DOI: [10.1063/1.1843591](https://doi.org/10.1063/1.1843591). arXiv: [hep-ph/0409233](https://arxiv.org/abs/hep-ph/0409233).
- [180] Jean-Paul Blaizot and Edmond Iancu. "A Boltzmann equation for the QCD plasma". In: *Nucl. Phys. B* 557 (1999), pp. 183–236. DOI: [10.1016/S0550-3213\(99\)00341-7](https://doi.org/10.1016/S0550-3213(99)00341-7). arXiv: [hep-ph/9903389](https://arxiv.org/abs/hep-ph/9903389).
- [181] Jørgen Rammer. *Quantum Field Theory of Non-equilibrium States*. Cambridge University Press, 2007.
- [182] Simon Caron-Huot. "Heavy quark energy losses in the quark-gluon plasma : beyond leading order". MA thesis. McGill U., 2007.

- [183] Jacopo Ghiglieri, Aleksi Kurkela, Michael Strickland, and Aleksi Vuorinen. "Perturbative Thermal QCD: Formalism and Applications". In: *Phys. Rept.* 880 (2020), pp. 1–73. DOI: [10.1016/j.physrep.2020.07.004](https://doi.org/10.1016/j.physrep.2020.07.004). arXiv: [2002.10188 \[hep-ph\]](https://arxiv.org/abs/2002.10188).
- [184] Florian Lindenbauer. "Jet momentum broadening in a gluonic plasma from effective kinetic theory". MA thesis. TU Wien, 2022. DOI: [10.34726/hss.2022.97124](https://doi.org/10.34726/hss.2022.97124).
- [185] R. Baier, Alfred H. Mueller, D. Schiff, and D. T. Son. "'Bottom up' thermalization in heavy ion collisions". In: *Phys. Lett. B* 502 (2001), pp. 51–58. DOI: [10.1016/S0370-2693\(01\)00191-5](https://doi.org/10.1016/S0370-2693(01)00191-5). arXiv: [hep-ph/0009237](https://arxiv.org/abs/hep-ph/0009237).
- [186] Jean-Paul Blaizot, Francois Gelis, Jin-Feng Liao, Larry McLerran, and Raju Venugopalan. "Bose–Einstein Condensation and Thermalization of the Quark Gluon Plasma". In: *Nucl. Phys. A* 873 (2012), pp. 68–80. DOI: [10.1016/j.nuclphysa.2011.10.005](https://doi.org/10.1016/j.nuclphysa.2011.10.005). arXiv: [1107.5296 \[hep-ph\]](https://arxiv.org/abs/1107.5296).
- [187] Yu Fu, Jacopo Ghiglieri, Shahin Iqbal, and Aleksi Kurkela. "Thermalization of non-Abelian gauge theories at next-to-leading order". In: *Phys. Rev. D* 105.5 (2022), p. 054031. DOI: [10.1103/PhysRevD.105.054031](https://doi.org/10.1103/PhysRevD.105.054031). arXiv: [2110.01540 \[hep-ph\]](https://arxiv.org/abs/2110.01540).
- [188] Peter Brockway Arnold, Guy D. Moore, and Laurence G. Yaffe. "The Fate of non-Abelian plasma instabilities in 3+1 dimensions". In: *Phys. Rev. D* 72 (2005), p. 054003. DOI: [10.1103/PhysRevD.72.054003](https://doi.org/10.1103/PhysRevD.72.054003). arXiv: [hep-ph/0505212](https://arxiv.org/abs/hep-ph/0505212).
- [189] Peter Brockway Arnold and Guy D. Moore. "QCD plasma instabilities: The NonAbelian cascade". In: *Phys. Rev. D* 73 (2006), p. 025006. DOI: [10.1103/PhysRevD.73.025006](https://doi.org/10.1103/PhysRevD.73.025006). arXiv: [hep-ph/0509206](https://arxiv.org/abs/hep-ph/0509206).
- [190] Anton Rebhan, Paul Romatschke, and Michael Strickland. "Dynamics of quark-gluon-plasma instabilities in discretized hard-loop approximation". In: *JHEP* 09 (2005), p. 041. DOI: [10.1088/1126-6708/2005/09/041](https://doi.org/10.1088/1126-6708/2005/09/041). arXiv: [hep-ph/0505261](https://arxiv.org/abs/hep-ph/0505261).
- [191] Paul Romatschke and Anton Rebhan. "Plasma Instabilities in an Anisotropically Expanding Geometry". In: *Phys. Rev. Lett.* 97 (2006), p. 252301. DOI: [10.1103/PhysRevLett.97.252301](https://doi.org/10.1103/PhysRevLett.97.252301). arXiv: [hep-ph/0605064](https://arxiv.org/abs/hep-ph/0605064).
- [192] Dietrich Bodeker and Kari Rummukainen. "Non-abelian plasma instabilities for strong anisotropy". In: *JHEP* 07 (2007), p. 022. DOI: [10.1088/1126-6708/2007/07/022](https://doi.org/10.1088/1126-6708/2007/07/022). arXiv: [0705.0180 \[hep-ph\]](https://arxiv.org/abs/0705.0180).
- [193] Anton Rebhan, Michael Strickland, and Maximilian Attems. "Instabilities of an anisotropically expanding non-Abelian plasma: 1D+3V discretized hard-loop simulations". In: *Phys. Rev. D* 78 (2008), p. 045023. DOI: [10.1103/PhysRevD.78.045023](https://doi.org/10.1103/PhysRevD.78.045023). arXiv: [0802.1714 \[hep-ph\]](https://arxiv.org/abs/0802.1714).
- [194] Andreas Ipp, Anton Rebhan, and Michael Strickland. "Non-Abelian plasma instabilities: SU(3) vs. SU(2)". In: *Phys. Rev. D* 84 (2011), p. 056003. DOI: [10.1103/PhysRevD.84.056003](https://doi.org/10.1103/PhysRevD.84.056003). arXiv: [1012.0298 \[hep-ph\]](https://arxiv.org/abs/1012.0298).

- [195] Maximilian Attems, Anton Rebhan, and Michael Strickland. "Instabilities of an anisotropically expanding non-Abelian plasma: 3D+3V discretized hard-loop simulations". In: *Phys. Rev. D* 87.2 (2013), p. 025010. DOI: [10.1103/PhysRevD.87.025010](https://doi.org/10.1103/PhysRevD.87.025010). arXiv: [1207.5795 \[hep-ph\]](https://arxiv.org/abs/1207.5795).
- [196] Sigtryggur Hauksson, Sangyong Jeon, and Charles Gale. "Probes of the quark-gluon plasma and plasma instabilities". In: *Phys. Rev. C* 103 (2021), p. 064904. DOI: [10.1103/PhysRevC.103.064904](https://doi.org/10.1103/PhysRevC.103.064904). arXiv: [2012.03640 \[hep-ph\]](https://arxiv.org/abs/2012.03640).
- [197] Sergio Barrera Cabodevila, Carlos A. Salgado, and Bin Wu. "Thermalization of gluons in spatially homogeneous systems". In: *Phys. Lett. B* 834 (2022), p. 137491. DOI: [10.1016/j.physletb.2022.137491](https://doi.org/10.1016/j.physletb.2022.137491). arXiv: [2206.12376 \[hep-ph\]](https://arxiv.org/abs/2206.12376).
- [198] Sergio Barrera Cabodevila, Carlos A. Salgado, and Bin Wu. "Quark production and thermalization of the quark-gluon plasma". In: *JHEP* 06 (2024), p. 145. DOI: [10.1007/JHEP06\(2024\)145](https://doi.org/10.1007/JHEP06(2024)145). arXiv: [2311.07450 \[hep-ph\]](https://arxiv.org/abs/2311.07450).
- [199] Sergio Barrera Cabodevila, Xiaojian Du, Carlos A. Salgado, and Bin Wu. "Quark production in the bottom-up thermalization". In: (Mar. 2025). arXiv: [2503.24291 \[hep-ph\]](https://arxiv.org/abs/2503.24291).
- [200] Alfred H. Mueller. "The Boltzmann equation for gluons at early times after a heavy ion collision". In: *Phys. Lett. B* 475 (2000), pp. 220–224. DOI: [10.1016/S0370-2693\(00\)00084-8](https://doi.org/10.1016/S0370-2693(00)00084-8). arXiv: [hep-ph/9909388](https://arxiv.org/abs/hep-ph/9909388).
- [201] Moritz Greif, Carsten Greiner, Björn Schenke, Sören Schlichting, and Zhe Xu. "Importance of initial and final state effects for azimuthal correlations in p+Pb collisions". In: *Phys. Rev. D* 96.9 (2017), p. 091504. DOI: [10.1103/PhysRevD.96.091504](https://doi.org/10.1103/PhysRevD.96.091504). arXiv: [1708.02076 \[hep-ph\]](https://arxiv.org/abs/1708.02076).
- [202] Moritz Greif, Carsten Greiner, Simon Plätzer, Björn Schenke, and Sören Schlichting. "Hadronization of correlated gluon fields". In: *Phys. Rev. D* 103.5 (2021), p. 054011. DOI: [10.1103/PhysRevD.103.054011](https://doi.org/10.1103/PhysRevD.103.054011). arXiv: [2012.08493 \[hep-ph\]](https://arxiv.org/abs/2012.08493).
- [203] T. Lappi. "Gluon spectrum in the glasma from JIMWLK evolution". In: *Phys. Lett. B* 703 (2011), pp. 325–330. DOI: [10.1016/j.physletb.2011.08.011](https://doi.org/10.1016/j.physletb.2011.08.011). arXiv: [1105.5511 \[hep-ph\]](https://arxiv.org/abs/1105.5511).
- [204] Liam Keegan, Aleksi Kurkela, Aleksas Mazeliauskas, and Derek Teaney. "Initial conditions for hydrodynamics from weakly coupled pre-equilibrium evolution". In: *JHEP* 08 (2016), p. 171. DOI: [10.1007/JHEP08\(2016\)171](https://doi.org/10.1007/JHEP08(2016)171). arXiv: [1605.04287 \[hep-ph\]](https://arxiv.org/abs/1605.04287).
- [205] Peter Brockway Arnold, Guy D. Moore, and Laurence G. Yaffe. "Transport coefficients in high temperature gauge theories. 1. Leading log results". In: *JHEP* 11 (2000), p. 001. DOI: [10.1088/1126-6708/2000/11/001](https://doi.org/10.1088/1126-6708/2000/11/001). arXiv: [hep-ph/0010177](https://arxiv.org/abs/hep-ph/0010177).
- [206] Peter Brockway Arnold, Guy D Moore, and Laurence G. Yaffe. "Transport coefficients in high temperature gauge theories. 2. Beyond leading log". In: *JHEP* 05 (2003), p. 051. DOI: [10.1088/1126-6708/2003/05/051](https://doi.org/10.1088/1126-6708/2003/05/051). arXiv: [hep-ph/0302165](https://arxiv.org/abs/hep-ph/0302165).

- [207] W. Israel and J. M. Stewart. "Thermodynamics of nonstationary and transient effects in a relativistic gas". In: *Phys. Lett. A* 58.4 (1976), pp. 213–215. DOI: [10.1016/0375-9601\(76\)90075-X](https://doi.org/10.1016/0375-9601(76)90075-X).
- [208] G. S. Denicol, H. Niemi, E. Molnar, and D. H. Rischke. "Derivation of transient relativistic fluid dynamics from the Boltzmann equation". In: *Phys. Rev. D* 85 (2012). [Erratum: *Phys. Rev. D* 91, 039902 (2015)], p. 114047. DOI: [10.1103/PhysRevD.85.114047](https://doi.org/10.1103/PhysRevD.85.114047). arXiv: [1202.4551 \[nucl-th\]](https://arxiv.org/abs/1202.4551).
- [209] Guang-You Qin and Abhijit Majumder. "A pQCD-based description of heavy and light flavor jet quenching". In: *Phys. Rev. Lett.* 105 (2010), p. 262301. DOI: [10.1103/PhysRevLett.105.262301](https://doi.org/10.1103/PhysRevLett.105.262301). arXiv: [0910.3016 \[hep-ph\]](https://arxiv.org/abs/0910.3016).
- [210] Jiechen Xu, Alessandro Buzzatti, and Miklos Gyulassy. "Azimuthal jet flavor tomography with CUJET2.0 of nuclear collisions at RHIC and LHC". In: *JHEP* 08 (2014), p. 063. DOI: [10.1007/JHEP08\(2014\)063](https://doi.org/10.1007/JHEP08(2014)063). arXiv: [1402.2956 \[hep-ph\]](https://arxiv.org/abs/1402.2956).
- [211] Shanshan Cao, Chathuranga Sirimanna, and Abhijit Majumder. "The medium modification of high-virtuality partons". In: (Jan. 2021). arXiv: [2101.03681 \[hep-ph\]](https://arxiv.org/abs/2101.03681).
- [212] Aleksi Kurkela, Aleksas Mazeliauskas, and Robin Törnkvist. "Collective flow in single-hit QCD kinetic theory". In: *JHEP* 11 (2021), p. 216. DOI: [10.1007/JHEP11\(2021\)216](https://doi.org/10.1007/JHEP11(2021)216). arXiv: [2104.08179 \[hep-ph\]](https://arxiv.org/abs/2104.08179).
- [213] K. Boguslavski, A. Kurkela, T. Lappi, and J. Peuron. "Heavy quark diffusion in an overoccupied gluon plasma". In: *JHEP* 09 (2020), p. 077. DOI: [10.1007/JHEP09\(2020\)077](https://doi.org/10.1007/JHEP09(2020)077). arXiv: [2005.02418 \[hep-ph\]](https://arxiv.org/abs/2005.02418).
- [214] Florian Lindenbauer. *Data and analysis code for arXiv:2303.12595*. Zenodo, Dec. 2023. DOI: [10.5281/zenodo.10419537](https://doi.org/10.5281/zenodo.10419537). URL: <https://doi.org/10.5281/zenodo.10419537>.
- [215] Thomas Epelbaum and Francois Gelis. "Fluctuations of the initial color fields in high energy heavy ion collisions". In: *Phys. Rev. D* 88 (2013), p. 085015. DOI: [10.1103/PhysRevD.88.085015](https://doi.org/10.1103/PhysRevD.88.085015). arXiv: [1307.1765 \[hep-ph\]](https://arxiv.org/abs/1307.1765).
- [216] Jürgen Berges, Björn Schenke, Sören Schlichting, and Raju Venugopalan. "Turbulent thermalization process in high-energy heavy-ion collisions". In: *Nucl. Phys. A* 931 (2014). Ed. by Peter Braun-Munzinger, Bengt Friman, and Johanna Stachel, pp. 348–353. DOI: [10.1016/j.nuclphysa.2014.08.103](https://doi.org/10.1016/j.nuclphysa.2014.08.103). arXiv: [1409.1638 \[hep-ph\]](https://arxiv.org/abs/1409.1638).
- [217] T. Lappi. "Wilson line correlator in the MV model: Relating the glasma to deep inelastic scattering". In: *Eur. Phys. J. C* 55 (2008), pp. 285–292. DOI: [10.1140/epjc/s10052-008-0588-4](https://doi.org/10.1140/epjc/s10052-008-0588-4). arXiv: [0711.3039 \[hep-ph\]](https://arxiv.org/abs/0711.3039).
- [218] Sigtryggur Hauksson and Edmond Iancu. "Jet polarisation in an anisotropic medium". In: *JHEP* 08 (2023), p. 027. DOI: [10.1007/JHEP08\(2023\)027](https://doi.org/10.1007/JHEP08(2023)027). arXiv: [2303.03914 \[hep-ph\]](https://arxiv.org/abs/2303.03914).
- [219] João Barata, Carlos A. Salgado, and João M. Silva. "Gluon to $q\bar{q}$ antenna in anisotropic QCD matter: spin-polarized and azimuthal jet observables". In: *JHEP* 12 (2024), p. 023. DOI: [10.1007/JHEP12\(2024\)023](https://doi.org/10.1007/JHEP12(2024)023). arXiv: [2407.04774 \[hep-ph\]](https://arxiv.org/abs/2407.04774).

- [220] Guy D. Moore and Derek Teaney. “How much do heavy quarks thermalize in a heavy ion collision?” In: *Phys. Rev. C* 71 (2005), p. 064904. DOI: [10.1103/PhysRevC.71.064904](https://doi.org/10.1103/PhysRevC.71.064904). arXiv: [hep-ph/0412346](https://arxiv.org/abs/hep-ph/0412346).
- [221] Abraham. Savitzky and M. J. E. Golay. “Smoothing and Differentiation of Data by Simplified Least Squares Procedures.” In: *Analytical Chemistry* 36.8 (1964), pp. 1627–1639. DOI: [10.1021/ac60214a047](https://doi.org/10.1021/ac60214a047). eprint: <https://doi.org/10.1021/ac60214a047>. URL: <https://doi.org/10.1021/ac60214a047>.
- [222] R. Kobes, G. Kunstatter, and A. Rebhan. “Gauge dependence identities and their application at finite temperature”. In: *Nucl. Phys. B* 355 (1991), pp. 1–37. DOI: [10.1016/0550-3213\(91\)90300-M](https://doi.org/10.1016/0550-3213(91)90300-M).
- [223] R. Kobes, G. Kunstatter, and A. Rebhan. “QCD plasma parameters and the gauge dependent gluon propagator”. In: *Phys. Rev. Lett.* 64 (1990), pp. 2992–2995. DOI: [10.1103/PhysRevLett.64.2992](https://doi.org/10.1103/PhysRevLett.64.2992).
- [224] Anton Rebhan. “Comment on ‘Damping of energetic gluons and quarks in high temperature QCD’”. In: *Phys. Rev. D* 46 (1992), pp. 482–483. DOI: [10.1103/PhysRevD.46.482](https://doi.org/10.1103/PhysRevD.46.482). arXiv: [hep-ph/9203211](https://arxiv.org/abs/hep-ph/9203211).
- [225] Michel Le Bellac. *Thermal Field Theory*. Cambridge Monographs on Mathematical Physics. Cambridge University Press, Mar. 2011. ISBN: 978-0-511-88506-8, 978-0-521-65477-7. DOI: [10.1017/CBO9780511721700](https://doi.org/10.1017/CBO9780511721700).
- [226] Margaret E. Carrington, Bailey M. Forster, and Sofiya Makar. “Collective modes in anisotropic systems”. In: *Phys. Rev. C* 104.6 (2021), p. 064908. DOI: [10.1103/PhysRevC.104.064908](https://doi.org/10.1103/PhysRevC.104.064908). arXiv: [2107.08229 \[hep-ph\]](https://arxiv.org/abs/2107.08229).
- [227] R. Baier, G. Kunstatter, and D. Schiff. “Gauge dependence of the resummed thermal gluon selfenergy”. In: *Nucl. Phys. B* 388 (1992), pp. 287–314. DOI: [10.1016/0550-3213\(92\)90614-H](https://doi.org/10.1016/0550-3213(92)90614-H). arXiv: [hep-ph/9206239](https://arxiv.org/abs/hep-ph/9206239).
- [228] Kirill Boguslavski, Florian Lindenbauer, Aleksas Mazeliauskas, Adam Takacs, and Fabian Zhou. In preparation.
- [229] Jean-Paul Blaizot, Jinfeng Liao, and Larry McLerran. “Gluon Transport Equation in the Small Angle Approximation and the Onset of Bose-Einstein Condensation”. In: *Nucl. Phys. A* 920 (2013), pp. 58–77. DOI: [10.1016/j.nuclphysa.2013.10.010](https://doi.org/10.1016/j.nuclphysa.2013.10.010). arXiv: [1305.2119 \[hep-ph\]](https://arxiv.org/abs/1305.2119).
- [230] Sigtryggur Hauksson and Charles Gale. “Polarized photons from the early stages of relativistic heavy-ion collisions”. In: *Phys. Rev. C* 109.3 (2024), p. 034902. DOI: [10.1103/PhysRevC.109.034902](https://doi.org/10.1103/PhysRevC.109.034902). arXiv: [2306.10307 \[nucl-th\]](https://arxiv.org/abs/2306.10307).
- [231] P. Aurenche, F. Gelis, G. D. Moore, and H. Zaraket. “Landau-Pomeranchuk-Migdal resummation for dilepton production”. In: *JHEP* 12 (2002), p. 006. DOI: [10.1088/1126-6708/2002/12/006](https://doi.org/10.1088/1126-6708/2002/12/006). arXiv: [hep-ph/0211036](https://arxiv.org/abs/hep-ph/0211036).
- [232] Esteban A. Calzetta and Bei-Lok B. Hu. *Nonequilibrium Quantum Field Theory*. Cambridge Monographs on Mathematical Physics. Cambridge University Press, 2008.
- [233] Mikko Laine and Aleksi Vuorinen. *Basics of Thermal Field Theory*. Vol. 925. Springer, 2016. DOI: [10.1007/978-3-319-31933-9](https://doi.org/10.1007/978-3-319-31933-9). arXiv: [1701.01554 \[hep-ph\]](https://arxiv.org/abs/1701.01554).

- [234] J. I. Kapusta and Charles Gale. *Finite-temperature field theory: Principles and applications*. Cambridge Monographs on Mathematical Physics. Cambridge University Press, 2011. ISBN: 978-0-521-17322-3, 978-0-521-82082-0, 978-0-511-22280-1. DOI: [10.1017/CBO9780511535130](https://doi.org/10.1017/CBO9780511535130).
- [235] M. Srednicki. *Quantum field theory*. Cambridge University Press, Jan. 2007. ISBN: 978-0-521-86449-7, 978-0-511-26720-8. DOI: [10.1017/CBO9780511813917](https://doi.org/10.1017/CBO9780511813917).
- [236] Shirley Dowdy, Stanley Weardon, and Daniel Chilko. *Statistics for Research*. John Wiley & Sons, Inc., Jan. 2004. DOI: [10.1002/0471477435](https://doi.org/10.1002/0471477435). URL: <http://dx.doi.org/10.1002/0471477435>.
- [237] Pauli Virtanen et al. “SciPy 1.0: Fundamental Algorithms for Scientific Computing in Python”. In: *Nature Methods* 17 (2020), pp. 261–272. DOI: [10.1038/s41592-019-0686-2](https://doi.org/10.1038/s41592-019-0686-2).
- [238] Wolfram Research Inc. *Mathematica, Version 13.0*. Champaign, IL, 2021.
- [239] Charles R. Harris et al. “Array programming with NumPy”. In: *Nature* 585.7825 (Sept. 2020), pp. 357–362. DOI: [10.1038/s41586-020-2649-2](https://doi.org/10.1038/s41586-020-2649-2). URL: <https://doi.org/10.1038/s41586-020-2649-2>.
- [240] J. D. Hunter. “Matplotlib: A 2D graphics environment”. In: *Computing in Science & Engineering* 9.3 (2007), pp. 90–95. DOI: [10.1109/MCSE.2007.55](https://doi.org/10.1109/MCSE.2007.55).
- [241] The mpmath development team. *mpmath: a Python library for arbitrary-precision floating-point arithmetic (version 1.3.0)*. <http://mpmath.org/>. 2023.
- [242] Aaron Meurer et al. “SymPy: symbolic computing in Python”. In: *PeerJ Computer Science* 3 (Jan. 2017), e103. ISSN: 2376-5992. DOI: [10.7717/peerj-cs.103](https://doi.org/10.7717/peerj-cs.103). URL: <https://doi.org/10.7717/peerj-cs.103>.